University of Alberta Library
0 1620 2918351 2

University of Alberta

The Contribution of Altered Fatty Acid Metabolism to Insulin Resistance and Cardiac Function

by

John Edward Reyes Ussher

A thesis submitted to the Faculty of Graduate Studies and Research
in partial fulfillment of the requirements for the degree of

Doctor of Philosophy

Pharmacology

©John Edward Reyes Ussher
Spring 2010
Edmonton, Alberta

Permission is hereby granted to the University of Alberta Libraries to reproduce single copies of this thesis and to lend or sell such copies for private, scholarly or scientific research purposes only. Where the thesis is converted to, or otherwise made available in digital form, the University of Alberta will advise potential users of the thesis of these terms.

The author reserves all other publication and other rights in association with the copyright in the thesis and, except as herein before provided, neither the thesis nor any substantial portion thereof may be printed or otherwise reproduced in any material form whatsoever without the author's prior written permission.

UNIVERSITY LIBRARY
UNIVERSITY OF ALBERTA

Examining Committee

Dr. Gary Lopaschuk, Pediatrics

Dr. Sandy Clanachan, Pharmacology

Dr. Evangelos Michelakis, Medicine

Dr. Sandra Davidge, Physiology

Dr. Jeffrey Horowitz, Movement Science, University of Michigan

Digitized by the Internet Archive
in 2026 with funding from
University of Alberta Library

https://archive.org/details/0162029183512

Dedication

This thesis is dedicated to my parents, Edward and Agnes Ussher, my brothers, Christianne and MacGyver Ussher, my fiancée, Nancy Yan, and all my lifelong friends that I grew up with, Justin Lee, Daniel Heng, Justin Foo, Sherwin Mendoza, Justin Franko, Travis Franko, Leon Grayfer, Jensen Wong, Eddie Kim, and Geoffrey Reeves, all of whom were instrumental in shaping me into the individual I have become today.

Abstract

Obesity is now deemed to be the primary preventable cause of illness and premature death. Recent studies demonstrate that alterations in fatty acid metabolism contribute towards the pathology of many of the conditions associated with obesity, some of which include skeletal muscle insulin resistance, type 2 diabetes, and ischemic heart disease. It has been postulated that an impairment in skeletal muscle and cardiac fatty acid oxidation rates during obesity results in the intracellular accumulation of lipid metabolites such as diacylglycerol and ceramide, which contribute to the development of these obesity-associated diseases. With regards to ischemic heart disease, it has been proposed that inhibiting fatty acid oxidation during reperfusion can protect against the development of reperfusion injury by improving the efficiency of contractile function in the heart.

This thesis addresses these proposals by using a number of genetic and pharmacological approaches to alter fatty acid metabolism. Our results challenge current dogma by demonstrating that treatments which lower fatty acid oxidation rates in the muscle (genetic deletion of malonyl CoA decarboxylase (MCD) in mice) actually protect against insulin resistance associated with both obesity and age. Furthermore, we follow up on these observations by showing differences between the inhibition of mitochondrial fatty acid uptake and mitochondrial fatty acid oxidation in providing protection against insulin resistance. In subsequent studies, we demonstrate that pharmacological inhibition of serine palmitoyl

transferase 1 (SPT 1) prevents the obesity-induced rise in skeletal muscle ceramide content and reverses insulin resistance.

With regards to the development of cardiomyopathy during obesity, our results once again challenge current dogma and show that reduced myocardial fatty acid oxidation rates do not have negative consequences on contractile function, and can actually improve insulin-stimulated cardiac glucose utilization rates in MCD deficient mice. In addition, we show that the stimulation of glucose oxidation either directly, or secondary to an inhibition of fatty acid oxidation, reduces infarct size following *in vivo* ischemia/reperfusion.

Overall, the results of this thesis illustrate that modulating fatty acid metabolism (via either MCD or SPT 1 inhibition) is a promising target for the treatment of obesity-associated diseases.

Acknowledgements

First and foremost, I would like to thank my supervisor, Dr. Gary Lopaschuk, for allowing me to carry out my graduate studies in his laboratory, and mentoring me with the skills required to become a successful independent investigator in the future. I would especially like to thank Gary for allowing me creative freedom during my graduate studies and allowing me to carry out my own independent projects without inhibition.

I would also like to give a special thanks to the members of my supervisory committee, Drs. Sandy Clanachan and Evangelos Michelakis, for their constructive criticism throughout my graduate training, which has allowed me to become a better scientist and to design more elegant experiments.

I would like to give a special thanks to Cory Wagg, Thomas Panakkezhum, Donna Beker, Sandra Kelly, and Shannon Lang, who were pivotal in the completion of my studies, and for that I am eternally grateful. I would also like to thank each and every individual of the Lopaschuk laboratory, for experimental assistance and intellectual input with regards to my studies, as well as Dr. Jagdip Jaswal, Gopinath Sutendra, Peter Dromparis, and Dr. Sebastien Bonnet, for making sure the 4th floor of HMRC was always a fun place to be, and acknowledging that I know more about the NHL than they do.

Last, I would like to thank my fiancée, Nancy Yan, for proof reading my thesis, correcting my numerous grammatical errors, and encouraging me to not be so lazy during the final stages of my graduate training.

Table of Contents

VOLUME 1

CHAPTER 1: Introduction 1

Obesity 2

Fatty Acid Metabolism 3

-Fatty acid uptake 3

-Cytoplasmic control of fatty acid β-oxidation 4

-Mitochondrial fatty acid uptake and the AMPK-ACC-MCD malonyl CoA axis 5

-Mitochondrial fatty acid translocation 9

-Fatty acid oxidation 11

-Malonyl CoA decarboxylase 12

Glucose Metabolism 15

-Glucose uptake and glycolysis 15

-Glucose oxidation 16

-Other sources of glucose metabolism 17

-Insulin signaling and control of glucose metabolism 17

The "Randle" Cycle 21

Skeletal Muscle Insulin Resistance 22

-Impaired skeletal muscle fatty acid oxidation and intramyocellular lipid metabolite accumulation 24

-Ceramide and skeletal muscle insulin resistance 25

-Aging, skeletal muscle insulin resistance, and type 2 diabetes 27

Cardiac Lipotoxicity 28

-Impaired myocardial fatty acid oxidation and intra-myocardial lipid metabolite accumulation 29

-Controversy: The other side of the story of myocardial fatty acid oxidation rates in obesity 30

Acute Myocardial Infarction and Ischemia/Reperfusion Injury 32

-Ischemia-induced alterations in plasma FFA concentrations 34

-Ischemia-induced alterations in fatty acid oxidation 35

-Ischemia-induced alterations in the subcellular control of fatty acid oxidation and fatty acid oxidation in the post-ischemic period 36

-Production of H^+s and development of acidosis from uncoupled glucose metabolism 38

-Stimulating glucose oxidation to alleviate myocardial acidosis and improve cardiac efficiency 39

Hypothesis and Aims 41

-General Hypothesis 41

-Specific Hypotheses 41

CHAPTER 2: Materials and Methods **76**

Introduction 77

Materials 78

Methods 79

-Generation and Breeding of Malonyl CoA Decarboxylase Deficient Mice 80

-Generation and Breeding of Pyruvate Dehydrogenase Kinase 4 Deficient Mice 81

-Diet Induced Obesity Feeding Protocol 82

-Glucose/Insulin Tolerance Testing and Assessment of the Insulin Signaling Pathway 82

-Meal Tolerance Testing 83

-Exercise Tolerance Testing 83

-Whole Body *In Vivo* Metabolic Assessment 84

-Ultrasound Echocardiography 85

-Isolated Working Mouse Heart 86

-Mechanical Function Measurements in Isolated Working Mouse Hearts 87

-Measurement of Glycolysis, Glucose, and Palmitate Oxidation 88

-Calculation of H^+ Production From Glucose Utilization 89

-Calculation of Tricarboxylic Acid Cycle Activity and ATP Production 89

-*In vivo* Ischemia/Reperfusion Injury via Ligation of the Left Anterior Descending Coronary Artery in the Mouse 90

-Infarct Size Assessment 90

-Area at Risk Isolation 91

-Tissue Analysis 91

-Pyruvate Dehydrogenase Activity Assay 91

-5'AMP Activated Protein Kinase Activity Assay 92

-Citrate Synthase Activity Assay 93

-β-Hydroxyacyl CoA Dehydrogenase Activity Assay 94

-Metabolic Profiling 95

-Measurement of Adenine Nucleotides and Short Chain CoA Esters 96

-Measurement of Long Chain Acyl CoA Esters 97

-Measurement of Triacylglycerol 98

-Measurement of Ceramide 99

-Measurement of Diacylglycerol 99

-Plasma Insulin Determination 100

-Whole Cell Homogenate Preparation and Immunoblot Analysis 101

-Statistical Analysis 102

CHAPTER 3: Evidence for the Randle Cycle in skeletal muscle: Short term high fat feeding and fasting lead to an impairment in muscle pyruvate dehydrogenase activity **105**

Abstract 106

Introduction 108

Materials and Methods 111

-Animal Studies 111

Results 112

-Fasting and short-term high fat feeding lead to a reduction in gastrocnemius muscle PDH activity 112

-Short-term high fat feeding does not impair insulin sensitivity despite a dramatic shift in substrate preference 112

-Short-term high fat feeding or fasting do not impair the insulin signaling pathway at the level of Akt or GSK3 113

-Intramyocellular lipid metabolite accumulation in response to short-term high fat feeding or fasting 114

Discussion 136

CHAPTER 4: Malonyl CoA decarboxylase deficient mice are protected against obesity-induced skeletal muscle insulin resistance **143**

Abstract 144

Introduction 146

Materials and Methods 148

-Animal Studies 148

Results 149

-MCD-/- mice gain similar amounts of body weight during DIO but display improved glucose and insulin tolerance 149

-The protection against obesity-induced insulin resistance observed in MCD-/- mice is associated with increased glucose oxidation rates in isolated muscle and increased PDH activity 149

-*In vivo* metabolic profiles and exercise capacity in WT and MCD-/- mice subjected to DIO 150

-Intramyocellular lipid metabolite accumulation in lean and DIO WT and MCD-/- mice 151

-GC/MS metabolic profiling reveals dramatic changes in TCA cycle intermediates and long chain acylcarnitine levels in DIO mice that are consistent with the incomplete oxidation of fatty acids 151

Discussion 177

CHAPTER 5: Inhibition of 3-ketoacyl CoA thiolase is unable to reverse diet-induced insulin resistance, but does prevent diet-induced cardiac dysfunction and hypertrophy **183**

Abstract 184

Introduction 186

Materials and Methods 188

-Animal Studies 188

Results 189

-Treatment with trimetazidine has no effect on body weight or glucose tolerance of mice subjected to diet-induced insulin resistance 189

-Treatment with trimetazidine increases the reliance on carbohydrate oxidation as a fuel source in diet-induced insulin resistant mice 189

-Intramyocellular lipid metabolite accumulation in diet-induced insulin resistant mice treated with trimetazidine 190

-Treatment with trimetazidine prevents diet-induced cardiac hypertrophy and contractile dysfunction 191

Discussion 217

CHAPTER 6: Inhibition of *de novo* ceramide synthesis reverses diet-induced insulin resistance and restores whole body oxygen consumption 222

Abstract 223

Introduction 225

Materials and Methods 228

-Animal Studies 228

Results 229

-Chronic high fat feeding results in dramatic weight gain, whole body insulin resistance, and altered substrate preference 229

-Inhibition of *de novo* ceramide synthesis via pharmacological inhibition of SPT 1 reverses diet-induced insulin resistance 229

-Inhibition of *de novo* ceramide synthesis via pharmacological inhibition of SPT 1 reverses diet-induced impairments on exercise capacity, which coincide with a restoration of whole body oxygen consumption rates 230

-Inhibition of *de novo* ceramide synthesis via pharmacological inhibition of SPT 1 reverses diet-induced impairments on heat production with no effect on animal activity 231

-Inhibition of *de novo* ceramide synthesis via pharmacological inhibition of SPT 1 has no effect on the obesity-associated increase of long chain acyl CoA and DAG accumulation in muscle, but significantly elevates TAG levels 232

-Inhibition of *de novo* ceramide synthesis via pharmacological inhibition of SPT 1 has no effect on inflammatory protein expression or phosphorylation in muscle of diet-induced insulin resistant mice 233

-Inhibition of *de novo* ceramide synthesis via pharmacological inhibition of SPT 1 prevents the development of insulin resistance in leptin receptor deficient type 2 diabetic *db/db* mice 233

Discussion 297

CHAPTER 7: Accumulation of ceramide contributes to the development of skeletal muscle insulin resistance in the obese JCR:LA-cp rat **305**

Abstract 306

Introduction 308

Materials and Methods 310

-Animal Studies 310

Results 311

-JCR:LA-cp obese rats treated with L-cycloserine display improved insulin sensitivity during meal tolerance testing 311

-JCR:LA-cp obese rats display a severe impairment in whole body oxygen consumption rates that is not prevented via L-cycloserine treatment 311

-The improved insulin sensitivity in JCR:LA-cp obese rats treated with L-cycloserine is associated with an improvement in Akt and PDH phosphorylation 312

-The improved insulin sensitivity in JCR:LA-cp obese rats treated with L-cycloserine is associated with a reduction in skeletal muscle ceramide levels 313

Discussion 329

CHAPTER 8: Enhanced lifespan in mice deficient for malonyl CoA decarboxylase is associated with a switch in whole body energy metabolism fatty acid to carbohydrate utilization **333**

Abstract 334

Introduction 336

Materials and Methods 338

-Animal Studies 338

Results 339

-Aged MCD-/- mice have an enhanced lifespan that is associated with a reduction in whole body oxygen consumption rates and increased reliance on carbohydrates for energy metabolism 339

-Intramyocellular lipid metabolite accumulation in aged WT and MCD-/- mice 340

-Aged MCD-/- mice produce contractile work more efficiently and display no signs of cardiac dysfunction despite reduced fatty acid oxidative capacity 341

-Aged MCD-/- accumulate intrahepatic TAG, but not DAG, and show no signs of hepatic insulin resistance 342

Discussion 376

VOLUME 2

CHAPTER 9: Insulin-stimulated cardiac glucose oxidation is increased in high fat diet-induced obese mice lacking malonyl CoA decarboxylase **380**

Abstract 381

Introduction 383

Materials and Methods 386

-Animal Studies 386

Results 387

-Effects of DIO on cardiac fatty acid and glucose oxidation in isolated working mouse hearts 387

-Effects of DIO and fasting on cardiac malonyl CoA levels 388

-Effects of DIO and fasting on myocardial long chain acylcarnitine levels 389

-Myocardial TCA cycle intermediates are not depleted by DIO or fasting 390

-Intra-myocardial long chain acyl CoA and TAG profile following DIO or fasting 391

-Effects of DIO on expression and phosphorylation of proteins involved in regulating myocardial energy metabolism and insulin signaling 392

Discussion 421

CHAPTER 10: Inhibition of serine palmitoyl transferase 1 reduces cardiac ceramide levels and preserves glycolysis rates **429**

Abstract 430

Introduction 432

Materials and Methods 434

-Animal Studies 434

Results 435

-DIO does not cause cardiac dysfunction 435

-DIO and insulin resistance reduce myocardial glycolytic rates, which are restored by myriocin treatment 435

-Myriocin treatment improves myocardial Akt signaling following DIO and insulin resistance 436

-Myriocin treatment leads to a dramatic reduction in intra-myocardial ceramide levels and prevents the DIO-associated increase in DAG levels 436

-Myriocin treatment has no effect on cardiac function in obese leptin receptor deficient *db/db* mice 437

Discussion 459

CHAPTER 11: Glucose oxidation stimulation provides protection against *in vivo* ischemia reperfusion injury **464**

Abstract 465

Introduction 467

Materials and Methods 469

-Animal Studies 469

Results 470

-MCD-/- mice are protected against *in vivo* I/R 470

-The protection in MCD-/- mice against *in vivo* I/R is associated with increased malonyl CoA levels and PDH activity in the AAR 470

-Direct stimulation of PDH with DCA affords protection against *in vivo* I/R 471

-PDHK4-/- mice are protected against *in vivo* I/R 471

Discussion 484

CHAPTER 12: Discussion and Conclusions **488**

Summary 489

An Operating Randle Cycle in Skeletal Muscle 494

Mitochondrial Fatty Acid Uptake Versus Fatty Acid Oxidation in the Development of Skeletal Muscle Insulin Resistance 497

Ceramide Versus TAG, DAG, and Long Chain Acyl CoA in the Development of Skeletal Muscle Insulin Resistance 503

Life-Long Deficiency of Mitochondrial Fatty Acid Oxidation and the Development of Chronic Disease with Age 508

Mitochondrial Fatty Acid Oxidation, Intra-Myocardial Lipid Metabolite Accumulation, Cardiac Lipotoxicity, and Cardiac Insulin Sensitivity in Response to Obesity 509

Optimization of PDH and Glucose Oxidation in the Treatment Against AMI 513

Justification of Methodology and Experimental Limitations 515

-DIO Model of Insulin Resistance 515

-Assessment of Insulin Sensitivity via Glucose and Insulin Tolerance Testing 516

-*In Vivo* Assessment of Whole Body Oxygen Consumption Rates 517

-The Isolated Working Mouse Heart 517

-Direct Measurement of Glycolysis 519

-Myocardial Acidosis from the Uncoupling of Glycolysis from Glucose Oxidation 521

-*In Vivo* Temporary LAD Ligation Model for I/R in the Mouse 523

-Use of Genetically Modified Mouse Strains 524

-Lack of Cell Culture Experiments 524

Final Conclusions 525

Future Directions 527

CHAPTER 13: References **535**

List of Tables **Page Number**

Table 3-1: Body weight in mice subjected to a short-term high fat diet. 115

Table 4-1: Body weight gain in WT and MCD-/- mice following DIO. 153

Table 4-2: Gastrocnemius malonyl CoA levels (nmol/g wet weight) in DIO WT and MCD-/- mice. 154

Table 5-1: *In vivo* assessment of cardiac function and LV wall dimensions in DIO mice treated with trimetazidine. 192

Table 6-1: βHAD activity in gastrocnemius muscle of lean and obese mice treated with vehicle control or myriocin. 235

Table 6-2: Effect of myriocin on body and tissue weight, and plasma glucose and insulin levels in lean and obese mice. 236

Table 8-1: Plasma parameters in aged WT and MCD-/- mice. 344

Table 8-2: MCD deficiency does not cause *in vivo* cardiac dysfunction in aged mice. 345

Table 9-1: MCD deficiency does not result in *ex vivo* cardiac dysfunction following DIO. 394

Table 9-2: MCD deficiency does not result in *in vivo* cardiac dysfunction following DIO. 395

Table 9-3: MCD deficiency results in an improved myocardial insulin sensitivity index following DIO. 396

Table 9-4: Insulin-stimulated cardiac acetyl CoA production in WT and MCD-/- mice following DIO. 397

Table 9-5: Myocardial lactate and pyruvate content in WT and MCD LF and DIO mice. 398

Table 10-1: *In vivo* cardiac function and LV wall measurements in lean and obese mice treated with myriocin. 439

Table 10-2: *Ex vivo* cardiac function in lean and obese mice treated with myriocin. 440

Table 10-3: Cardiac malonyl CoA levels (nmol/g dry weight) in lean and obese mice treated with myriocin. 441

Table 10-4: Cardiac function and LV wall measurements in *db/db* mice treated with myriocin. 442

List of Figures **Page Number**

Figure 1-1: Fatty acid uptake and activation in the cell. 47

Figure 1-2: Metabolic pathways for metabolism of fatty acids into various intermediates. 49

Figure 1-3: Mitochondrial uptake of fatty acids. 51

Figure 1-4: Fatty acid β-oxidation. 53

Figure 1-5: Glycolysis. 55

Figure 1-6: Oxidation of pyruvate via the pyruvate dehydrogenase complex. 57

Figure 1-7: The tricarboxylic acid cycle. 59

Figure 1-8: The Randle cycle. 61

Figure 1-9: Insulin signaling. 63

Figure 1-10: Consequences of lipid metabolite accumulation in the skeletal muscle and heart. 65

Figure 1-11: Ceramide metabolism. 67

Figure 1-12: Subcellular changes in metabolism during ischemia/reperfusion. 69

Figure 1-13: Reduction in cardiac efficiency via increased H^+ production. 71

Figure 1-14: How does the H^+ originate from glycolysis. 73

Figure 2-1: *In vivo* model of ischemia/reperfusion. 104

Figure 3-1: Fasting and short-term high fat feeding inhibit 117

gastrocnemius PDH activity.

Figure 3-2: Short-term high fat feeding does not cause insulin resistance in mice. 123

Figure 3-3: *In vivo* metabolic profile in mice subjected to a short-term high fat diet. 125

Figure 3-4: Fasting and short-term high fat feeding has no effect on Akt and AMPK signaling. 129

Figure 3-5: Ceramide and long chain acyl CoA accumulate in gastrocnemius muscle of mice following 3 wks of high fat feeding, but not after 1 wk. 133

Figure 4-1: MCD-/- mice are protected against DIO-associated insulin resistance. 156

Figure 4-2: Increased skeletal muscle glucose oxidation rates and PDH activity in MCD-/- mice subjected to DIO. 160

Figure 4-3: *In vivo* metabolic parameters in DIO WT and MCD-/- mice. 164

Figure 4-4: Improved exercise capacity in MCD-/- mice subjected to DIO. 170

Figure 4-5: Skeletal muscle lipid metabolite content in WT and MCD-/- subjected to DIO. 174

Figure 4-6: Metabolic profiling reveals a reduction in incomplete fatty acid oxidation by-products in skeletal muscle of MCD-/- mice subjected to DIO. 176

Figure 5-1: Trimetazidine treatment has no effect on body weight gain, but significantly increases plasma triacylglycerol levels in diet-induced insulin resistant mice. 194

Figure 5-2: Trimetazidine treatment has no effect on glucose intolerance and insulin sensitivity in diet-induced insulin resistant mice. 198

Figure 5-3: Assessment of *in vivo* metabolic parameters in vehicle control and trimetazidine treated diet-induced insulin resistant mice. 202

Figure 5-4: Intramyocellular lipid metabolite accumulation and levels of tricarboxylic acid cycle intermediates in vehicle control and trimetazidine treated diet-induced insulin resistant mice. 208

Figure 6-1: The effect of chronic high fat feeding on body weight and insulin sensitivity. 238

Figure 6-2: High fat diet-induced insulin resistance is associated with a dramatic shift in substrate preference and an impairment of whole body oxygen consumption rates. 242

Figure 6-3: Inhibition of SPT 1 reverses high fat diet-induced insulin resistance and improves insulin signaling. 246

Figure 6-4: Substrate preference in lean and obese mice treated with myriocin. 252

Figure 6-5: L-cycloserine treatment reverses high-fat diet induced insulin resistance. 254

Figure 6-6: Myriocin treatment reverses the impairment in aerobic exercise capacity caused by DIO. 258

Figure 6-7: Myriocin treatment reverses the impairment in whole body oxygen consumption rates caused by DIO. 260

Figure 6-8: Heat production and activity in lean and DIO mice treated with myriocin. 264

Figure 6-9: Inhibition of SPT 1 reduces skeletal muscle ceramide levels without any effect on other lipid metabolites. 268

Figure 6-10: MCD-/- mice do not accumulate ceramide in their skeletal muscle following 12 wks of high fat feeding. 276

Figure 6-11: Expression and phosphorylation status of proteins involved in inflammation in skeletal muscle. 278

Figure 6-12: Prevention of insulin resistance in *db/db* mice via myriocin treatment. 282

Figure 6-13: *In vivo* metabolic parameters, intramyocellular lipid metabolite profile, and insulin signaling in *db/db* mice treated with myriocin. 286

Figure 6-14: Gluconeogenic capacity in obese-insulin resistant mice is not altered via myriocin treatment. 296

Figure 7-1: L-cycloserine treatment improves insulin sensitivity in JCR:LA-cp obese rats. 316

Figure 7-2: L-cycloserine treatment has no effect on whole body oxygen consumption rates and heat production in JCR:LA-cp obese rats. 320

Figure 7-3: L-cycloserine treatment improves glucose utilization signaling in JCR:LA-cp obese rats. 322

Figure 7-4: L-cycloserine treatment decreases the elevation of skeletal muscle ceramide levels observed in JCR:LA-cp obese rats. 326

Figure 8-1: MCD-/- mice have a prolonged lifespan. 347

Figure 8-2: Insulin sensitivity, oxygen consumption rates, and intramyocellular lipid metabolite accumulation in aged WT and MCD-/- mice. 351

Figure 8-3: Improved insulin tolerance in aged female MCD-/- mice. 359

Figure 8-4: Insulin signaling pathway in aged male WT and MCD-/- mice. 361

Figure 8-5: Improved efficiency of contractile work in hearts from aged male MCD-/- mice. 363

Figure 8-6: Improved efficiency of contractile work in hearts from aged female MCD-/- mice. 367

Figure 8-7: Intrahepatic lipid metabolite accumulation and hepatic insulin signaling in aged WT and MCD-/- mice. 371

Figure 9-1: MCD deficiency improves insulin-stimulated glucose oxidation in DIO mice. 400

Figure 9-2: MCD deficiency improves PDH activity in DIO mice despite an increased expression of PDK4. 402

Figure 9-3: MCD deficiency increases malonyl CoA levels in DIO mice. 404

Figure 9-4: MCD deficiency increases myocardial malonyl CoA levels and decreases the accumulation of fatty acid oxidative intermediates in fasted mice. 406

Figure 9-5: MCD deficiency decreases the accumulation of fatty acid oxidative intermediates in DIO mice without decreasing tricarboxylic acid cycle intermediates. 410

Figure 9-6: Improvement of insulin-sensitivity in MCD -/- mice subjected to DIO does not correlate with the accumulation of myocardial lipid intermediates. 416

Figure 9-7: Neither DIO or MCD deficiency alters the expression of proteins involved in energy metabolism and mitochondrial function. 418

Figure 9-8: Insulin stimulated Akt phosphorylation is increased in hearts from MCD-/- mice following DIO. 420

Figure 10-1: SPT 1 inhibition prevents the DIO-associated impairment of cardiac glycolysis rates. 444

Figure 10-2: Cardiac PDH activity is not impaired in DIO mice treated with myriocin. 446

Figure 10-3: H^+ production in hearts from DIO mice. 450

Figure 10-4: Cardiac Akt phosphorylation is increased in DIO myriocin treated mice. 452

Figure 10-5: Myriocin treatment of DIO mice decreases intra-myocardial ceramide levels and prevents the accumulation of intra-myocardial DAG. 456

Figure 11-1: MCD-/- mice are protected against *in vivo* ischemia/reperfusion. 473

Figure 11-2: Increased malonyl CoA levels and PDH activity in MCD-/- mice following ischemia/reperfusion. 475

Figure 11-3: DCA treated mice are protected against *in vivo* ischemia/reperfusion. 479

Figure 11-4: PDHK4-/- mice are protected against *in vivo* ischemia/reperfusion. 483

Figure 12-1: Overall thesis discussion summary figure. 534

Abbreviations

-/-	knock out/deficient
3-KAT	3-keto acyl CoA thiolase
AAR	area at risk
ACC	acetyl CoA carboxylase
ADP	adenosine diphosphate
AICAR	5-aminoimidazole-4-carboxamide1-β-D-ribofuranoside
Akt	protein kinase B
AMI	acute myocardial infarction
AMP	adenosine monophosphate
AMPK	5'-AMP activated protein kinase
ANOVA	analysis of variance
AS160	Akt substrate of 160 kDa
ATGL	adipose triacylglycerol lipase
ATP	adenosine triphosphate
AUC	area under the curve
BAC	bacterial artificial chromosome
βHAD	β-hydroxyacyl CoA dehydrogenase
BSA	bovine serum albumin
Ca^{2+}	calcium ion
CACT	carnitine:acylcarnitine translocase
CLAMS	comprehensive lab animal monitoring system
CO_2	carbon dioxide
CoA	coenzyme A
CPT	carnitine palmitoyl transferase
Cr	creatine
CS	citrate synthase
CT	carnitine:acylcarnitine translocase
CV	calorific value
d	diastole
DAG	diacylglycerol
db/db	leptin receptor deficient
DCA	dichloroacetate
DGAT	diacylglycerol acyl transferase
DIO	diet-induced obesity
DNA	deoxyribonucleic acid
DNTB	5,5'-dithiobis-(2-nitrobenzic acid)
DTT	dithiothreitol
EDL	extensor digitorum longus
EDTA	ethylenediaminetetraacetic acid
EF	ejection fraction
EGTA	ethylene glycol tetraacetic acid

ETC	electron transport chain
FABP	fatty acid binding protein
FACS	fatty acyl CoA synthetase
$FAD/FADH_2$	flavin adenine dinucleotide
FAS	fatty acid synthase
FAT/CD36	fatty acid translocase
FATP	fatty acid transport protein
FFA	free fatty acid
FS	fractional shortening
GC	gas chromatography
GLUT	glucose transporter
GSK3	glycogen synthase kinase 3
GTP	guanosine triphosphate
GTT	glucose tolerance test
H^+	proton
HF	high fat
HFD	high fat diet
HOMA	homeostatic model assessment
HPLC	high performance liquid chromatography
hr	hour(s)
IDCM	idiopathic dilated cardiomyopathy
IKK	inhibitor of kappa b kinase
IP	immunoprecipitation
IR	insulin receptor
IRS	insulin receptor substrate
I/R	ischemia/reperfusion
IS	infarct size
ITT	insulin tolerance test
IVS	intraventricular septum
JNK	Jun-N terminal kinase
K^+	potassium ion
LAD	left anterior descending coronary artery
LDH	lactate dehydrogenase
LF	low fat
LPM	litres per minute
LV	left ventricle/left ventricular
LVEDV	left ventricular end diastolic volume
LVEDD	left ventricular end diastolic dimensions
LVID	left ventricular internal diameter
LVPW	left ventricular posterior wall thickness
LVWT	left ventricular wall thickness
MAPK	mitogen activated protein kinase
MCD	malonyl CoA decarboxylase
MCT	monocarboxylic acid transporter
min	minute(s)
MRS	magnetic resonance spectroscopy

MS	mass spectrometry
MTT	meal tolerance test
NAD^+/NADH	nicotinamide adenine dinucleotide
NCX	sodium-calcium exchanger
NHE	sodium-hydrogen exchanger
NMR	nuclear magnetic resonance
ob/ob	leptin deficient
PCr	phosphocreatine
PDK	phosphoinositide-dependent kinase 1
PDH	pyruvate dehydrogenase
PDHK	pyruvate dehydrogenase kinase
PDP	pyruvate dehydrogenase phosphatase
PFK	phosphofructokinase
PGC-1	peroxisomal proliferator-activated receptor γ coactivator-1
PH	pleckstrin homology
PI3K	phosphatidylinositol-3-kinase
PIP_3	phosphatidylinositol (3,4,5) trisphosphate
PKC	protein kinase C
PPAR	peroxisome proliferator activated receptor
RER	respiratory exchange ratio
ROS	reactive oxygen species
RPM	revolutions per minute
s	systole
SDS	sodium dodecylsulfate
SDS-PAGE	SDS polyacrylamide gel electrophoresis
sec	second(s)
SEM	standard error of the mean
SH2	Src homology 2
SPT	serine palmitoyl transferase
TAG	triacylglycerol
TCA	tricarboxylic acid cycle
TTC	triphenyltetrazolium chloride
U	unit
UCP	uncoupling protein
VAMP2	vesicle associated membrane protein 2
VCO_2	carbon dioxide production
VLDL	very low density lipoprotein
VO_2	oxygen consumption
v/v	volume/volume
wk(s)	week(s)
wt	weight (only in figures)
WT	wild type
w/v	weight/volume

CHAPTER 1.

Introduction

CHAPTER 1

Introduction

Obesity

Obesity is defined as an excess amount of body fat in relation to lean body mass, such that adverse health consequences may occur, resulting in a reduced life expectancy (147, 239), whereas being overweight is defined as an increase in body weight in relation to height. The World Health Organization (WHO) describes obesity as one of the most obviously visible, yet widely neglected, public-health problems that threatens to overwhelm both developed and developing countries (420). The estimated number of deaths attributable to obesity is ~300,000 in the United States of America alone, and has overtaken smoking as the primary preventable cause of illness and premature death (269). These deaths result from obesity being a major risk factor for the development and progression of a multitude of diseases, which include insulin resistance, type 2 diabetes, and cardiovascular disease (147, 185, 407, 422). It is worth mentioning that insulin resistance is the number one predictor of developing type 2 diabetes later on in life (228, 411), and that the number one cause of death in a type 2 diabetic individual is cardiovascular disease (389).

Although the treatment and/or prevention of obesity is an issue of utmost importance that our primary health care systems must address, the aims of this thesis are not on the treatment of obesity itself, but to further understand how obesity contributes to the development of the aforementioned obesity-associated

diseases, and how they can be treated. As such, this thesis will explore how alterations in fatty acid metabolism contribute to the development of obesity-induced skeletal muscle insulin resistance, myocardial ischemia/reperfusion (I/R) injury, and diabetic cardiomyopathy. Because obesity-induced alterations in fatty acid metabolism are essential to the development of these diseases, a thorough description of how fatty acids are metabolized will first be described, and secondly, how they negatively impact glucose metabolism (a primary mechanism by which they contribute to disease development).

Fatty Acid Metabolism

Fatty acid uptake

Free fatty acids (FFAs) originating from either albumin or lipoprotein-triacylglycerol (TAG) enter the skeletal muscle or cardiac myocyte either by passive diffusion, or via a protein carrier mediated pathway (128, 360, 384, 406). These protein carriers include fatty acid translocase (FAT)/CD36, the plasma membrane isoform of fatty acid binding protein (FABPpm), and fatty acid transport protein (FATP) 1/6. A proposed mechanism for this protein-mediated uptake involves binding of the fatty acids to FABPpm, which concentrates the fatty acids for either passive diffusion or uptake via FAT/CD36- or FATP 1/6 (360). Of these potential carriers, FAT/CD36 has received the most attention, and plays a primary role in the translocation of fatty acid across the sarcolemmal membrane of both skeletal muscle and cardiac myocytes (138, 146, 245). Studies

involving either FAT/CD36 inhibition (245) or deletion (205) have shown that 50-60% of myocardial fatty acid uptake and oxidation occurs via FAT/CD36-mediated transport. Patients with CD36 deficiency have low rates of myocardial fatty acid tracer uptake (122, 289, 412), consistent with a key role for CD36 in regulating cardiac fatty acid metabolism *in vivo*. In skeletal muscle, FATP1 has also been shown to play a key role in fatty acid uptake, as genetic deletion of FATP1 prevents both lipid infusion- and high fat diet-induced elevations in intramyocellular lipid metabolites such as TAG and long chain acyl CoA (188).

Cytoplasmic control of fatty acid β-oxidation

Once in the cytoplasm, fatty acids are converted into long chain acyl CoA esters by fatty acyl CoA synthetase (FACS) (Figure 1-1). Long chain acyl CoA species' can then be used for synthesis of a number of intracellular lipid metabolites, or the fatty acid moiety can be transferred to carnitine and taken up into the mitochondria for subsequent oxidation. The conversion of fatty acids into complex lipids such as TAG, diacylglycerol (DAG), and ceramide (Figure 1-2) has recently received considerable interest, as the accumulation of these intermediates has been implicated in the development of skeletal muscle insulin resistance, cardiac dysfunction and heart failure (280, 305, 367, 385). Of importance is that fatty acid supply and the rate of long chain acyl CoA production can impact the level of these potentially harmful intracellular intermediates. For example, mice with cardiac specific overexpression of either FACS (222) or FATP1 (66) have increased rates of cardiac fatty acid uptake and

conversion to long chain acyl CoA, which results in the cytoplasmic accumulation of intra-myocardial lipid and development of a severe dilated cardiomyopathy. It is also possible that a decreased rate of long chain acyl CoA removal by fatty acid β-oxidation (will be referred to simply as fatty acid oxidation) may contribute to lipotoxicity (398). As such, mice deficient for acetyl CoA carboxylase (ACC) β have elevated rates of skeletal muscle fatty acid oxidation and are protected from high fat diet-induced insulin resistance (5, 69), effects associated with a significant reduction in intramyocellular levels of TAG, long chain acyl CoA, and DAG (69). In the normal heart, about 75% of the fatty acids taken up are immediately oxidized (237, 284, 426). As a result, a decrease in fatty acid oxidation could theoretically contribute to lipid-induced cardiac pathology, and the acceleration of fatty acid oxidation may lessen the potential for lipotoxicity. However, the role of fatty acid oxidation rates contributing to both lipid-induced skeletal muscle and cardiac pathology is controversial (21, 22, 238, 365, 436, 443, 444), and will be discussed later in this thesis (See Chapters 4, 5, 7, and 8).

Mitochondrial fatty acid uptake and the AMPK-ACC-MCD malonyl CoA axis

Carnitine palmitoyl transferase 1 (CPT 1) is a key enzyme in the mitochondria, and catalyzes the conversion of long chain acyl CoA to long chain acylcarnitine, which is subsequently transported into the mitochondria (Figure 1-3). Allosteric inhibition of CPT 1 by malonyl CoA is a key mechanism by which CPT 1 activity is regulated (257, 259-261, 263, 264, 302, 345). The turnover of malonyl CoA in the heart is quite rapid, with a $t_{1/2}$ of approximately 1.25 min

(319). Therefore, myocardial malonyl CoA concentrations are dependent upon the balance between its synthesis by acetyl CoA via ACC (24, 94, 240, 244, 342) and its degradation via malonyl CoA decarboxylase (MCD) (91, 96, 98, 212, 347, 406). Two cardiac isoforms of ACC exist, ACCα and ACCß, with ACCß predominating (4, 30, 74, 79, 80, 96, 292). A number of studies have provided direct evidence that ACC activity is inversely related to fatty acid oxidation rates in the heart (8, 124, 240, 244, 342). A role for ACC in regulating skeletal muscle fatty acid oxidation has also now been demonstrated (213, 423, 425), as ACCß deficient mice (5) have marked increases in muscle fatty acid oxidation rates, confirming the role of ACCß as a key regulator of fatty acid oxidation in muscle.

A key determinant of ACC activity in the heart is the activity of 5'AMP activated protein kinase (AMPK) (97, 144, 145). In rat heart it has been demonstrated that AMPK is able to phosphorylate both ACCα and ACCß, resulting in an almost complete loss of ACC activity (96, 207, 209). Moreover, heart ACC co-purifies with the α2 isoform of the catalytic subunit of AMPK (96), suggesting a tight association between AMPK and ACC in the heart. A close correlation also exists between increased AMPK activity, decreased ACC activity, and increased fatty acid oxidation in the heart (207, 209, 248), and in skeletal muscle (330, 424).

Studies have shown that the heart has a high activity and expression of MCD (91), which consists of a 50 kDa protein that forms a tetramer in the intact cell (92, 409). The human MCD cDNA has two putative 5' start sites that code for a 54 and 50 kDa protein and contains a mitochondrial targeting sequence on

the amino terminus (73, 92, 114, 167, 409). Both isoforms of MCD are expressed in the heart, with the 50 kDa isoform being localized to the mitochondria (349). Although originally reported to be solely a mitochondrial enzyme in mammalian cells (77, 197), MCD is also found in the cytoplasm and peroxisomes (8, 186, 349). Interestingly, it has recently been suggested that as much as 50% of the malonyl CoA in the heart is derived from peroxisomal acetyl CoA production (320). In support of this observation, recent work from our laboratory suggests that cardiac MCD is localized to peroxisomes, suggesting that both peroxisomal MCD and malonyl CoA have, as of yet, unidentified roles in controlling the rate of mitochondrial fatty acid oxidation (unpublished data). A number of studies have now shown that conditions associated with increased fatty acid oxidation are also associated with increased MCD activity, including fasting, diabetes, ischemia, and newborn heart development (24, 91, 131, 209). In skeletal muscle, liver, and pancreatic islet cells, increased MCD activity is also associated with increased fatty acid oxidation rates (16, 298, 330, 346). Moreover, it has recently been shown in human skeletal muscle myotubes that knock down of MCD with small interfering RNA inhibits fatty acid oxidation rates (41).

AMPK acts as a "fuel sensor" that increases fatty acid oxidation during times of increased energy demand, or decreased fatty acid oxidation in times of low demand, secondary to respective decreases and increases in ACC activity and malonyl CoA levels. In skeletal muscle, it has also been suggested that MCD is a direct target of AMPK (346), whereby AMPK-induced phosphorylation of MCD increases MCD activity and subsequently lowers malonyl CoA levels, however,

our laboratory and others have been unable to reproduce these findings (135, 349). AMPK is a serine/threonine kinase that responds to metabolic stresses that deplete cellular ATP, increase AMP, or increase the creatine/phospho-creatine (Cr/PCr ratio) (97, 142, 143, 145) and is very active in the heart with an important role in regulating both fatty acid oxidation (124, 207, 208, 244, 247, 248, 347), as well as glucose uptake and glycolysis (29, 113, 168-170, 225, 334, 387, 427, 432, 434). AMPK is a heterotrimeric protein, consisting of an α catalytic subunit, and ß and γ regulatory subunits. A number of different isoforms of each of these subunits exists, with variable tissue distribution (79, 97, 125, 139, 143, 428, 429). Skeletal muscle and heart express both the α1 and α2 catalytic subunits, with the α2 subunit predominating, as well as both the ß1 and ß2 subunits, and γ1 and γ2 subunits. The ß and γ subunits regulate the catalytic activity of the α subunit, with the γ subunit being important in conferring the AMP sensitivity of the AMPK complex (97). While AMPK activation usually requires changes in the ratio of AMP/ATP or Cr/PCr, it is now clear that both skeletal muscle and cardiac AMPK activity can also be altered without changes in nucleotide levels (10, 162, 207). For instance, insulin inhibits myocardial AMPK under conditions where AMP/ATP and Cr/PCr ratios do not change (29, 115, 124, 247), and in skeletal muscle, α2 adrenergic receptor stimulation increases AMPK activity independent of changes in both AMP and ATP levels (162). In addition, it has been shown that during low-flow ischemia where the AMP/ATP ratio does not change, the activation of the upstream AMPK kinase (AMPKK) also contributes significantly to the activation of AMPK (10, 27). However, to date, the AMPKK responsible

for AMPK activation during ischemia remains to be identified, as the identified AMPKKs, LKB1 and CAMKKß, are either not activated by ischemia (10), or expressed at very low levels in the heart (97), respectively. The most recent work in our laboratory has identified the myosin light chain kinase to potentially be an AMPKK responsible for the activation of AMPK during ischemia (unpublished data).

It is important to note that while ACC, MCD, and AMPK can all regulate fatty acid oxidation rates via controlling levels of malonyl CoA and subsequent CPT 1 activity, the majority of malonyl CoA is inaccessible to CPT 1. In the heart, the cytosolic concentration of malonyl CoA is approximately 5 μM, while the IC_{50} of CPT 1 inhibition via malonyl CoA is between 50 and 100 nM (262, 342). Therefore, if all the malonyl CoA in the heart were accessible to CPT 1, fatty acid oxidation would always be completely inhibited, which of course is not the case. The reason why the majority of malonyl CoA is not accessible to CPT 1 is not known, but may have to do with compartmentalization of malonyl CoA. Recent evidence supporting this may comes from the observation that a large proportion of MCD exists in the peroxisomes (341), and as mentioned, it has been suggested that the majority of malonyl CoA produced in the heart originates from the peroxisomes (320).

Mitochondrial fatty acid translocation

Following the formation of long chain acylcarnitine by CPT 1, the acylcarnitine is translocated across the inner mitochondrial membrane by a

carnitine:acylcarnitine translocase (CACT) that involves the exchange of carnitine for acylcarnitine (Figure 1-3). CACT is a small protein (32.5 kDa) that has a broad specificity in transporting carnitine esters across the mitochondrial membrane, including acetylcarnitine export from the mitochondria (235, 358). In addition to transporting acylcarnitine into the mitochondrial matrix, CACT also provides free carnitine for subsequent CPT 1 reactions. CACT is a critical step in the translocation of fatty acid moieties into the mitochondria, as evinced by the development of cardiomyopathies and irregular heart beats in individuals with CACT deficiencies (235).

Once in the matrix, acylcarnitine is converted back into long chain acyl CoA by CPT 2, a 70 kDa enzyme located on the matrix side of the inner mitochondrial membrane (358). The long chain acyl CoA produced by CPT 2 then enters the fatty acid oxidation pathway. Unlike CPT 1, CPT 2 is less sensitive to inhibition by malonyl CoA (259, 414, 415).

CD36 also resides in mitochondrial membranes in heart, and it has been suggested to be essential for mitochondrial long chain fatty acyl uptake and oxidation based on data using the putative CD36 inhibitor, sulfo-N-succinimidyl oleate, which decreases fatty acid oxidation in skeletal muscle mitochondria (52). On the other hand, isolated cardiac and skeletal muscle mitochondria from CD36 knock-out mice have normal fatty acid oxidation, and show a decrease in fatty acid oxidation with sulfo-N-succinimidyl oleate treatment that is similar to wild type (WT) mice (192), suggesting that the CD36 does not serve an essential role in mitochondrial fatty acid metabolism.

Fatty acid oxidation

The metabolism of long chain acyl CoA in the mitochondrial matrix occurs via the β-oxidation pathway, involving the sequential metabolism of acyl CoA by acyl CoA dehydrogenase, enoyl CoA hydratase, L-3-hydroxyacyl CoA dehydrogenase, and 3-ketoacyl CoA thiolase (3-KAT)(Figure 1-4)(358). Each cycle of fatty acid oxidation results in the shortening of the fatty acyl moiety by two carbons, as well as the production of acetyl CoA, nicotinamide adenine dinucleotide (NADH), and flavin adenine dinucleotide ($FADH_2$). The four enzymes of oxidation exist in multiple isoforms that have different chain length specificities. Each of these enzymes is sensitive to feedback inhibition by the products of the enzymatic reaction, including $FADH_2$ and NADH. Of particular importance is the feedback inhibition of 3-KAT by the accumulation of acetyl CoA. This is important in times of low metabolic demand, where a decrease in electron transport chain (ETC) and tricarboxylic acid (TCA) cycle activity results in the accumulation of acetyl CoA, NADH, and $FADH_2$ that feedback inhibits the enzymes of fatty acid oxidation (284). An increase in acetyl CoA and NADH production by the pyruvate dehydrogenase (PDH) complex can also directly inhibit fatty acid oxidation. As a result, flux through fatty acid oxidation is highly dependent on both cardiac energy demand, and the source of carbon substrate.

The enzymes of fatty acid oxidation are also under a high degree of transcriptional control (see (85) for excellent reviews on transcriptional regulation of fatty acid oxidation), and conditions that upregulate fatty acid oxidation are often associated with increases in the expression of a number of fatty acid

oxidation enzymes (238). These transcriptional changes are mediated to a large degree by the peroxisomal proliferator activated receptor (PPAR) α and peroxisomal proliferator-activated receptor γ coactivator-1 (PGC-1) α (85, 110-112, 161, 246).

The majority of fatty acids undergoing oxidation are not saturated fatty acids, but rather mono- or poly-unsaturated fatty acids. For instance, the most abundant fatty acid in the blood is oleate, a mono-unsaturated fatty acid (295). The oxidation of these fatty acids is facilitated by auxiliary enzymes, which include 2,4-dienoyl CoA reductase and enoyl CoA isomerase (358). These enzymes facilitate the formation of a *trans* double bond from a *cis* double bound, which is necessary for the oxidation of fatty acids by the enoyl CoA hydratase enzyme isoforms involved in fatty acid oxidation. To date, little is known as to whether these enzymes are important in determining the fate of saturated versus unsaturated fatty acids (i.e. oxidation or esterification into complex lipids). Importantly, at equivalent, non-competing concentrations, in isolated working rat hearts, the oxidation of unsaturated fatty acids such as oleate or arachidonic acid (344), occurs at similar rates to that of the saturated fatty acid, palmitate. Similar fractional β-oxidation rates are observed for palmitate and oleate in the human heart (426).

Malonyl CoA decarboxylase

As mentioned previously, MCD degrades malonyl CoA into acetyl CoA (190, 196, 197), and is thus a key player in the regulation of fatty acid oxidation

rates via regulation of malonyl CoA levels. Although originally reported to be solely a mitochondrial enzyme in mammalian cells (77, 197), MCD is also found in the cytoplasm and peroxisomes (8, 186, 349). The human MCD cDNA has also now been sequenced (73, 114, 167), and has two putative 5' start sites that code for a 54 and 50 kDa protein, with cardiac cells primarily expressing the 50 kDa isoform (92, 341, 409). Sequence analysis of MCD suggests that a mitochondrial targeting sequence exists on the amino terminus (92, 409). Our laboratory expressed MCD in cardiac cells and found that both isoforms of MCD are expressed, with the 50 kDa isoform localized to the mitochondria (349).

Since our initial identification of MCD in cardiac muscle (91, 209), a number of studies have shown that conditions where fatty acid oxidation increase are associated with high MCD activity, including fasting, diabetes, ischemia, increased work, and newborn heart development (24, 91, 131, 209). For example, perfusion of isolated working rat hearts with adrenaline to increase cardiac work resulted in a 40% increase in myocardial fatty acid oxidation rates, which was associated with a 55% increase in MCD activity and 33% decrease in malonyl CoA content (131). Furthermore, fatty acid oxidation rates are extremely low in the heart immediately after birth, but begin to mature by approximately 7 days after birth, which is also associated with a significant increase in MCD activity and a subsequent decline in malonyl CoA content (291). In human skeletal muscle, a prolonged exercise strength-training regimen is associated with an increase in MCD activity and a subsequent drop in malonyl CoA content, likely contributing to the exercise-induced alterations in fatty acid oxidation rates (210).

MCD is primarily regulated by chronic transcriptional control (78, 189, 220), and a number of studies have shown that cardiac MCD activity and expression are increased during diabetes, fasting, and high fat feeding (51, 92, 131, 209, 442). Part of this transcription control is regulated by PPARα (51, 131, 219, 220). In PPARα null mice, MCD expression and activity is decreased, which is accompanied by a significant decrease in fatty acid oxidation rates (51). Even in the hypothalamus, activation of PPARα is associated with an increased mRNA expression of MCD and a subsequent reduction in hypothalamic malonyl CoA content (58). In addition, our recent work shows a peroxisomal localization of cardiac MCD (unpublished data), suggesting that peroxisomal MCD may have a yet unidentified role in the regulation of mitochondrial fatty acid oxidation rates in the heart.

As will be discussed in following sections, a number of studies have now provided substantial data supporting a role for excessive myocardial fatty acid oxidation rates playing a role in mediating I/R injury (93, 95, 98, 171, 172, 402, 403, 405). Emerging evidence suggests that MCD inhibition is one approach to overcoming the detrimental effects of high levels of fatty acids in the ischemic heart. Mice with a genetic deficiency for MCD (MCD-/-) have significantly increased malonyl CoA levels and a complete lack of MCD (95). When subjected to reperfusion following a global no-flow ischemia, hearts from MCD-/- mice have an enhanced recovery of cardiac function compared to their wild type (WT) littermate controls, which is associated with a dramatic increase in glucose oxidation rates (95). Furthermore, using novel MCD inhibitors (61, 62), Dyck *et*

al. showed an enhanced recovery of cardiac function in rat hearts subjected to *ex vivo* I/R, and the Stanley laboratory replicated these findings in pig hearts subjected to an *in vivo* demand induced ischemia (93, 381). A key component of this thesis will explore how MCD may be a possible exciting novel target for the treatment of obesity-induced insulin resistance and acute myocardial infarction (AMI), likely due to its effects on stimulating glucose metabolism secondary to an inhibition of fatty acid oxidation rates.

Glucose Metabolism

Glucose uptake and glycolysis

The majority of glucose that the heart metabolizes is derived from the blood with its uptake being facilitated by glucose transporters (GLUT). GLUT1 is responsible for maintaining basal glucose uptake, whereas GLUT4 translocates from an intracellular pool to the sarcolemmal membrane in response to insulin, increased work demand or ischemia (440, 441).

In both the heart and skeletal muscle, glucose is then immediately phosphorylated by hexokinase, the first enzyme of the glycolytic pathway (see Figure 1-5 for overview of the glycolytic pathway). Glucose-6-phosphate undergoes a series of enzymatic reactions, until finally, it is converted into pyruvate via the enzymatic action of pyruvate kinase. Glycolysis produces a net gain of 2 ATP and 2 NADH molecules, and although glycolysis rates can increase dramatically during ischemia to provide ATP in the absence of oxygen (93, 382),

it will be discussed later how this may not necessarily be a desirable outcome for patients with ischemic heart disease. This is because the hydrolysis of glycolytically-derived ATP results in an increased proton (H^+) production, which causes myocardial acidosis, impairing cardiac efficiency (84, 233, 323).

Glucose oxidation

In order for glucose to be completely oxidized, the pyruvate formed from glycolysis must enter the mitochondria via the enzymatic activity of PDH. PDH is a multi-enzyme complex that decarboxylates pyruvate into acetyl CoA, CO_2, and NADH (Figure 1-6). The acetyl CoA generated by PDH subsequently enters the TCA cycle (Figure 1-7), where it produces the necessary reducing equivalents that become electron donors for the ETC, generating the H^+ motive force that drives ATP production during oxidative phosphorylation.

The PDH complex itself is under tight regulation by an upstream kinase, PDH kinase (PDHK), which acts to phosphorylate and inhibit the activity of the PDH complex (316). PDHK is positively regulated by acetyl CoA and NADH. Because the oxidation of fatty acids increases the acetyl CoA/CoA and $NADH/NAD^+$ ratios, increased rates of fatty acid oxidation lead to potent inhibition of PDH and glucose oxidation. This "glucose-fatty acid" cycle was first described by Sir Philip Randle and colleagues in the 1960s and is generally referred to as the "Randle cycle" (316) (Figure 1-8).

Other sources of glucose metabolism

Alternative sources for glucose metabolism outside of plasma glucose include endogenous glycogen stores and lactate. The mobilization of endogenous glycogen stores can generate glucose-6-phosphate, which bypasses the hexokinase reaction of glycolysis. Thus, glycolysis of glycogen-derived glucose-6-phosphate generates 3 molecules of ATP, as opposed to the 2 normally seen from glycolysis of glucose taken up from the plasma.

Lactate, is a major energy source of the heart (410), and is converted into pyruvate via the enzymatic activity of lactate dehydrogenase (LDH). The pyruvate molecule is then oxidized in the same manner that pyruvate generated from glycolysis is, via the enzymatic activity of PDH. It is important to note that although the heart is normally a lactate consumer, during times of metabolic stress, such as myocardial ischemia, the heart becomes a lactate producer (229, 230).

Insulin signaling and control of glucose metabolism

In the postprandial state, elevated blood glucose levels cause the pancreatic β-cells of the Islets of Langerhans to secrete insulin. Insulin signaling (Figure 1-9) begins with insulin binding to its receptor in target tissues. The insulin receptor (IR) and its related family members are tetrameric proteins consisting of two external α- and two internal β-subunits that function as allosteric enzymes. Binding of insulin to the α-subunit leads to derepression of the tyrosine kinase activity in the β-subunit, followed by autophosphorylation of

the β-subunits, resulting in a conformational change that further increases kinase activity (301). The activated IR phosphorylates tyrosine residues on intracellular substrates, some of which include the insulin receptor substrate (IRS) protein family. Upon phosphorylation, the IRS proteins interact with a number of different effector/adapter molecules that contain Src homology 2 (SH2) domains that recognize specific phosphotyrosine motifs (59).

Although there are many effector/adapter molecules that bind to IRS proteins, the phosphatidylinositol-3-kinase (PI3K) pathway is essential for the effects of insulin on glucose uptake and metabolism. Through binding of its p85α subunit to IRS-1/2, the catalytic p110 subunit of PI3K is activated and increases phosphatidylinositol (3,4,5) trisphosphate (PIP_3) production. Phosphoinositide-dependent kinase 1 (PDK1) is subsequently recruited to the plasma membrane through its pleckstrin homology (PH) domain that binds PIP_3.

From here, two pathways that result in increased GLUT4 translocation to the plasma membrane branch off PDK1 (Figure 1-9). In one branch, PDK1 recruits atypical protein kinase C zeta (PKCζ) to the membrane through interaction with the hydrophobic portion of the PKCζ kinase domain. This allows PDK1 to activate PKCζ by phosphorylation at its threonine 410 residue (150). Although studies have routinely demonstrated PKCζ involvement in insulin-mediated glucose uptake, the exact mechanisms by which it does so have not been clearly defined. Studies in L6 myotubes show that PKCζ overexpression results in an insulin-like effect on actin remodeling, which increases GLUT4 translocation to the plasma membrane (232). A study by Braiman and colleagues

demonstrated that insulin or PKCζ overexpression induces serine phosphorylation of vesicle-associated membrane protein 2 (VAMP2) in the GLUT4 compartment (43). Furthermore, dominant negative PKCζ prevented the effect of insulin on VAMP2 serine phosphorylation and GLUT4 translocation.

In the other branch, the serine/threonine kinase, Akt (protein kinase B), also possessing a PH domain, is recruited to the membrane within the vicinity of PDK1, which is capable of phosphorylating and activating Akt isoforms 1 through 3 (272). While many studies have implicated Akt involvement in mediating insulin's effects on glucose uptake, similar to PKCζ, only few targets involved in this response have been extensively studied. Of particular importance to this pathway is the Rab-GTPase activating protein, Akt substrate of 160 kDa (AS160), which undergoes insulin-dependent phosphorylation and contains multiple Akt phosphorylation sites (351). Overexpression of an AS160 mutant that cannot be phosphorylated blocks insulin stimulated GLUT4 translocation (446). In addition, insulin-stimulated AS160 phosphorylation is reduced in patients with type 2 diabetes (183).

Although PDK1 branches through PKCζ or Akt to mediate insulin-stimulated glucose uptake, it should be noted that there is the potential for intersection between these pathways. A recent study by Fritzius *et al.* demonstrated that the protein ProF co-localized in vesicular structures and bound both PKCζ and Akt in 3T3-L1 preadipocytes. Moreover, ProF interacted more strongly with PKCζ and Akt after insulin growth factor-1 stimulation (119). Other studies have shown that PKCζ can negatively regulate Akt in skeletal

muscle cells in response to high palmitate-induced insulin resistance (312). High levels of palmitate result in *de novo* ceramide synthesis through enzymatic action of serine palmitoyl transferase (SPT). Because ceramides can activate PKCζ (39, 277) and have been implicated as potential mediators in the development of insulin resistance (106, 173, 391), PKCζ over-activation may be maladaptive in insulin-sensitive tissues (312).

The net effect of insulin on glucose uptake results in an increased rate of glycolysis and glycogen synthesis. Insulin's effects on glycogen synthesis are mediated via Akt, which phosphorylates and inhibits glycogen synthase kinase 3α/β (GSK3α/β), leaving glycogen synthase in its dephosphorylated active form, increasing glycogen synthesis (175). The other major effects of insulin signaling on metabolism are to reduce fatty acid oxidation and to increase fatty acid synthesis. Insulin reduces fatty acid metabolism by decreasing the mobilization of fatty acids from the adipose tissue, thereby decreasing fatty acid delivery to peripheral tissues (211, 218). In regards to fatty acid synthesis, insulin activates sterol response element binding proteins, which are transcription factors that control a number of genes involved in the *de novo* synthesis of fatty acids, such as fatty acid synthase (FAS) and ACCα (107, 133, 254).

It is important to realize that the effects of insulin are still not completely understood, and that the insulin receptor is a pleiotropic receptor responsible for a wide range of effects that include not only metabolism, but also cell volume, cell growth, and potassium homeostasis amongst others. The signaling molecules involved in mediating insulin's pleiotropic effects may differ between insulin-

sensitive tissues, and the major studies responsible for uncovering the pathways involved in insulin-stimulated glucose uptake were established in either muscle or adipose tissue.

The "Randle" Cycle

As mentioned earlier, Sir Philip Randle and colleagues in 1963 discovered the existence of a "glucose-fatty acid" cycle in both the diaphragm and heart muscle (316) (Figure 1-8). This cycle involves an inverse relationship, whereby increasing concentrations of circulating FFAs lead to an increased uptake of fatty acids by the heart and muscle, which are subsequently oxidized in the mitochondria. The enhanced oxidation of fatty acids results in an elevation in fatty acid by-products, which feedback inhibit PDH activity and subsequent glucose oxidation. At the time, Randle and colleagues had concluded that this "glucose-fatty acid" cycle was responsible for the abnormalities in carbohydrate metabolism observed in muscle during diabetes, starvation, and hypersecretion of corticosteroids (316).

Even today, the Randle cycle is of prominent importance to both skeletal muscle insulin resistance and ischemic heart disease (305, 382, 405). Interestingly, in skeletal muscle, it has actually been proposed that the Randle cycle is non-operative, which has led to an explosion of studies suggesting that accelerating fatty acid oxidation in muscle is a novel target to ameliorate obesity-associated insulin resistance (69, 303-305, 447). However, the experiments

undertaken in this thesis will challenge this theory and hopefully shed some light on this very important issue. In regards to ischemic heart disease, the heart has an increased reliance on fatty acids as an energy substrate following successful reperfusion, and as will be discussed later, this dramatically inhibits glucose oxidation and reduces the recovery of cardiac efficiency (207, 233, 405). Studies undertaken in this thesis will also show that overcoming this fatty acid-induced inhibition of glucose oxidation has potent effects on protecting against an AMI.

Skeletal Muscle Insulin Resistance

Insulin resistance is a term that can be defined in more ways than one. It is commonly defined as the failure of insulin to mediate a normal insulin-type response from insulin-sensitive tissues. To be more specific, it is the failure of insulin to adequately regulate blood glucose homeostasis. This results in a decreased glucose uptake into the skeletal muscle and adipose tissue, and increases endogenous glucose production in the liver, both of which lead to an elevated blood glucose concentration. For the purposes of this thesis, we will simply refer to insulin resistance as the failure of insulin to increase glucose uptake in a target tissue.

As the skeletal muscle serves as the "sink" for glucose disposal in response to insulin, numerous studies investigating the molecular mechanisms responsible for causing insulin resistance have focused their efforts in this tissue. Although there has been no true discovery to date of what mediates insulin

resistance, there has been vast progress in regards to potential culprits of this devastating disease. Some of these include inflammatory responses associated with increased circulating tumor necrosis factor alpha and other cytokines (327, 329, 383), increased intramyocellular ceramide production (309, 451), oxidative stress (102, 103), intramyocellular lipid metabolite accumulation (TAG, long chain acyl CoA, and DAG) (188, 305), and elevated circulating levels of fatty acids (182). Although there are many different proposed candidates for what initially causes insulin resistance, common cellular mechanisms do exist, primarily involving a failure of insulin to increase IRS-associated PI3K activity (188, 383).

In the individual beginning to become insulin resistant, blood glucose levels are initially maintained due to the pancreatic β-cell's ability to increase insulin secretion by approximately 4 – 5 fold (182). As the individual develops a more severe insulin resistance, hepatic glucose production is increased as insulin can no longer inhibit gluconeogenesis, while glucose uptake is reduced in the skeletal muscle and adipose tissue. Both of these effects result in an elevated blood glucose level. In addition, insulin is able to reduce food intake via its actions on the hypothalamus, and thus a decreased response of the hypothalamus to insulin leads to hyperphagia and obesity (49, 359). A reduced response to insulin in the adipose tissue also results in increased lipolysis, which increases circulating fatty acids, adversely affecting β-cell function. Once β-cell function can no longer fully compensate for decreased insulin sensitivity, the insulin resistant individual is often considered to be type 2 diabetic (181).

Impaired skeletal muscle fatty acid oxidation and intramyocellular lipid metabolite accumulation

As mentioned in the previous section, one of the popular theories for how insulin resistance develops in the skeletal muscle involves the cytosolic accumulation of intramyocellular lipid metabolites, such as TAG, long chain acyl CoA, DAG, and ceramide, which impede insulin signaling and reduce insulin-stimulated glucose uptake via activation of the classical/novel protein kinase C signaling cascade (68, 69, 305, 367, 368, 447) (Figure 1-10). In fact, the accumulation of intramyocellular lipid correlates more closely with insulin resistance versus other commonly measured indices, such as body mass index, waist hip ratios, or total body fat (87, 204). While it is generally agreed upon that these lipid metabolites accumulate in the muscle during obesity-associated insulin resistance, the mechanisms by which they accumulate is not agreed upon. On one side, it is believed that the dramatic increase in fatty acid supply and delivery to the muscle seen with obesity is just too great for the mitochondrial fatty acid oxidative machinery to keep up with, and thus the metabolites accumulate in the cytosol (280). In contrast, and appearing to be ever more so prevalent in the literature, it is believed that an impaired ability of the skeletal muscle to oxidize fatty acids in the mitochondria is the primary factor responsible for the accumulation of these lipid metabolites (69, 447). Thus, it has been suggested that by enhancing the capacity of skeletal muscle to oxidize fatty acids, the cytosolic accumulation of these metabolites can be attenuated, thereby improving insulin

signaling and glucose uptake, ameliorating insulin resistance (68, 69, 305, 367, 368, 447).

A caveat of the proposal that impaired fatty acid oxidation contributes to insulin-resistance is that acceleration of fatty acid oxidation would decrease glucose oxidation via inhibition of PDH and phosphofructokinase 1 (PFK1), and thus reduce insulin stimulated glucose metabolism based on the Randle Cycle (313-315). Shulman and colleagues have proposed that this would not present a problem because the Randle Cycle is non-operative in skeletal muscle, based off recent studies utilizing ^{31}P-MRS in human offspring of patients with type 2 diabetes (304, 305).

Nonetheless, it is important to note that there has been a recent surge of studies showing that mitochondrial fatty acid oxidation is enhanced in numerous models of obesity and insulin resistance (140, 202, 396). A major goal of this thesis is to address the controversy of the Randle Cycle in skeletal muscle and its contribution to the development of insulin resistance.

Ceramide and skeletal muscle insulin resistance

Ceramide is a sphingolipid second messenger containing sphingosine, an amide-linked long chain fatty acid, and a hydroxyl group. Its two major sources of production are either from hydrolysis of plasma membrane sphingomyelin, via the action of sphingomyelinase, or from its *de novo* synthesis from palmitoyl CoA and serine, via the action of SPT (Figure 1-11) (385). Ceramide may also be produced from sphingosine, via the action of ceramide synthase, or from

deacylation or dephosphorylation of ceramide metabolites (Figure 1-11) (385). Of recent, ceramide has received increasing attention as a potential culprit in the development of skeletal muscle insulin resistance, as it is a key intermediate that may link two popular theories explaining this disease's development, over-nutrition and inflammation (385).

Numerous studies in both cell culture and animal models demonstrate that accumulation of ceramide inhibits insulin signaling and causes insulin resistance (153, 231, 310, 312). Moreover, Holland and colleagues have shown that inhibiting *de novo* synthesis of ceramide via pharmacological inhibition SPT 1 can prevent insulin resistance caused by corticosteroids, saturated fats, and in genetic models of obesity (153). Pharmacological inhibition of SPT 1 in human muscle cells has also been shown to prevent the inhibition of insulin stimulated glycogen synthesis induced by palmitic acid (310). Finally, the improvement in insulin sensitivity brought about by exercise training in obese individuals is associated with a significant reduction in skeletal muscle ceramide levels (48, 90). Interestingly, TAG and DAG, lipid metabolites implicated in skeletal muscle insulin resistance development, were either unchanged or only showed a trend towards a reduction (48, 90). A primary objective of this thesis will be to further investigate the contribution of ceramide to skeletal muscle insulin resistance, and to delineate and understand the potential mechanisms involved in this process.

Aging, skeletal muscle insulin resistance, and type 2 diabetes

Type 2 diabetes is the most common chronic metabolic disease of the elderly population, affecting nearly 30 million individuals 65 years of age or older in developed countries (191). The elderly population constitutes a significant proportion of the estimated $100 billion annual burden of diabetes in the United States of America (160). Epidemiological studies demonstrate that the transition to overt type 2 diabetes with age is associated with a deterioration in glucose tolerance (340, 352) that results from impaired insulin-stimulated glucose utilization in skeletal muscle (318, 328).

It has been proposed, similar to obesity-induced insulin resistance, that the aging associated decline in insulin-stimulated glucose utilization and development of eventual type 2 diabetes arises from an impairment in mitochondrial function and fatty acid oxidative capacity, which results in the accumulation of intramyocellular lipid metabolites that impede the insulin signaling cascade (303). Physical inactivity has been proposed to contribute to this impairment of muscle mitochondrial function in the elderly (141, 155). As such, increasing physical activity in elderly individuals has dramatic effects on health status and overall life expectancy, whereby men of 70 years of age or older who engaged in regular physical activity increased their chances of living until age 90 by 10% (437). Studies done in this thesis will challenge this proposal, as we observed controversial findings with regards to aging and the development of chronic disease in a mouse model of genetic deficiency for fatty acid oxidation.

In obesity, similar to the skeletal muscle, the heart is also exposed to elevated concentrations of circulating FFAs and TAGs, which lead to the intra-myocardial accumulation of the aforementioned described lipid metabolites (239, 365, 444). The accumulation of these lipid metabolites in the heart, and in particular, TAG and ceramide, is associated with increased cardiac myocyte apoptosis, myocardial fibrosis, left ventricular (LV) chamber expansion, contractile dysfunction, and impaired diastolic filling (109, 258, 354, 382, 398, 399, 433, 439, 450). This general phenomenon has been observed in several genetic models in mice and rats, and has been broadly defined as "cardiac lipotoxicity" (239). For example, obese Zucker diabetic rats develop cardiac dilatation and reduced contractility, effects that are associated with elevated intra-myocardial TAG, ceramide, and increased DNA laddering, a marker of apoptosis (450). Interestingly, treatment of these animals with the PPARγ agonist, troglitazone, suppresses plasma TAG levels and reduces intra-myocardial TAG and ceramide accumulation, which was associated with a complete prevention of apoptosis and restoration of cardiac function. In addition, cardiac overexpression of FACS results in lipid accumulation, cardiac hypertrophy, gradual progression to LV dysfunction, and ultimately premature death (65). Furthermore, cardiac overexpression of human lipoprotein lipase utilizing an anchoring sequence to localize the enzyme to the surface of cardiac myocytes causes LV chamber enlargement and impairs contractile function compared to WT counterparts (433).

Despite these findings in rodents, it is important to note that the term "cardiac lipotoxicity" remains poorly defined and continues to lack a true clinical equivalent condition. Regardless, the studies undertaken in this thesis will shed light on this very important area of metabolism and cardiovascular disease.

Impaired myocardial fatty acid oxidation and intra-myocardial lipid metabolite accumulation

The intra-myocardial accumulation of lipid metabolites houses the same debate with respect to the relative importance of an increase in fatty acid supply versus a decrease in fatty acid oxidative capacity as the major contributing factor. It has also been proposed that a downregulation of PPARα and decreased expression of fatty acid oxidation enzymes causes intra-myocardial lipid metabolite accumulation that contributes to the cardiac dysfunction that is sometimes observed with obesity, insulin resistance and diabetes (63, 443, 444). This idea was supported by the observation that obese and type 2 diabetic patients with heart failure have a dramatic increase in intra-myocardial lipid accumulation, which has been attributed to impaired fatty acid oxidation, due to a reduction in a number of PPARα target gene transcripts (364). However, it is important to note that this study lacked an obese group without heart failure. Furthermore, in support of an impaired myocardial fatty acid oxidation in obesity, studies in obese Zucker rats have shown that fatty acid oxidation rates are impaired following an overnight fast, which was associated with an increased lipid deposition in the heart and impaired contractile function (443).

These findings, in accordance with what has been observed in skeletal muscle, has led to the postulation, that identical to the skeletal muscle, an acceleration of fatty acid oxidation in the heart could prevent the accumulation of these toxic lipid metabolites during obesity, alleviating contractile dysfunction (239, 365, 443, 444). This proposal has recently been supported in the heart by findings from Essop *et al.* in mice deficient for ACC2 (ACC2-/-) (101). ACC2-/- mice have reduced malonyl CoA levels and elevated rates of myocardial fatty acid oxidation. Despite this elevation in fatty acid oxidation rates, ACC2-/- mice also had a significant increase in myocardial glucose oxidation rates and insulin stimulated 2-deoxyglucose uptake compared to their WT counterparts. Although these results suggest that accelerating fatty acid oxidation via inhibition of ACC may benefit the insulin-resistant heart in the setting of obesity and type 2 diabetes, the reported glucose oxidation rates were ~10-20 fold lower than the vast majority of reported rates in the literature. In addition, the authors observed an increase in both glucose oxidation and fatty acid oxidation rates, but interestingly, no increase in oxygen consumption.

Controversy: The other side of the story of myocardial fatty acid oxidation rates in obesity

As mentioned previously, there is debate at present as to whether the Randle Cycle operates in skeletal muscle (303, 305, 353). Nonetheless, numerous studies have clearly showed that the Randle Cycle is operative in cardiac muscle

(233, 291, 382), and argue against the notion that accelerating fatty acid oxidation would be a viable strategy to improve glucose metabolism and function in the heart (239). Furthermore, there are a large number of studies that have shown that myocardial fatty acid oxidation rates are actually elevated in models of obesity and diabetes (3, 50, 137, 158, 215, 253, 435). In contrast to the study in obese Zucker rats (443), results from our laboratory with JCR obese rats reveals that fatty acid oxidation rates are not impaired following an overnight fast, and that the doubling of myocardial TAGs observed is likely due to an excessive fatty acid supply (22). Moreover, fatty acid oxidation rates account for the majority of ATP production in hearts from JCR obese rats (241). These results are also supported in *db/db* mice, as the Severson laboratory has shown that the enhancement in fatty acid uptake in these mice is due to increases in the fatty acid transporters, CD36 and FABPpm (54). Moreover, mice with a cardiac specific overexpression of PPARα have a phenotype mimicking that seen in type 2 diabetes, and this is associated with a dramatic increase in myocardial fatty acid oxidation rates and a subsequent reduction in both glucose oxidation and glucose uptake (113). Supporting these findings, studies from Aasum and colleagues has also shown that fatty acid oxidation rates are enhanced in hearts from *db/db* mice or mice subjected to diet-induced obesity (DIO) (2, 3, 137, 158, 159, 215). Work from Abel and colleagues, as well as our laboratory, have also reproduced these findings in perfused hearts from *db/db* mice, as well as *ob/ob* mice (50, 55, 253). In addition, studies in humans from Peterson *et al.* using positron emission

tomography and ^{11}C-palmitate imaging showed that obese women and type 2 diabetic patients have an increased uptake and oxidation of fatty acids (148, 307).

Adding to this confusion are studies involving deletion of adipose TAG lipase (ATGL), which is expressed in the heart (136). Deletion of ATGL led to a marked increase in intra-myocardial TAG, which was associated with a decrease in contractile function and the development of cardiac fibrosis. However, these changes were also associated with an increase in cardiac glucose uptake, as well as an increase in whole body glucose utilization, presumably due to a decrease in fatty acid availability for potentially toxic lipid metabolites. Finally, consuming a high fat diet significantly increased body mass, intra-myocardial TAG, and ceramide content in rats with established infarct-induced heart failure, but did not negatively effect LV chamber dimensions, pressure or mass (273), suggesting that lipid accumulation in the heart is not detrimental to function in heart failure. Studies done in this thesis will attempt to address the important issue of fatty acid oxidation, lipid metabolites, insulin resistance, and lipotoxicity in the heart during obesity.

Acute Myocardial Infarction and Ischemia/Reperfusion Injury

Myocardial ischemia occurs when coronary blood flow is inadequate, and hence the oxygen supply to the myocardium is not sufficient to meet oxygen demand. Due to the hearts high demand for energy and thus high rates of

oxidative metabolism utilized to drive cardiac contraction, the manifestations of myocardial ischemia are dependent upon the nature, and severity of the ischemic episode and the subsequent re-establishment of flow (reperfusion). The consequences of myocardial ischemia are numerous, and if left untreated, will lead to a full fledged myocardial infarction encompassing the death of living myocardial tissue. Thus, it is vital that reperfusion of the ischemic myocardium be established in a timely manner, in order to the limit the amount of myocardial tissue death. As such, it has been demonstrated in human studies that the size of infarcted tissue is a major determinant in the progression to LV dysfunction and subsequent heart failure following an AMI (44). Unfortunately, upon successful reperfusion of ischemic myocardium, further damage can occur to the heart that impairs the recovery of contractile function, a phenomenon coined "reperfusion injury." In recent years, basic science research has led to the discovery of numerous potential mechanisms that contribute to the severity of reperfusion injury, some of which include enhanced rates of cardiac myocyte apoptosis, increased production of reactive oxygen species (ROS) and oxidative stress, and calcium overload of the reperfused myocardium (53, 438). In addition, metabolic perturbations with regards to the availability of circulating energy substrates, as well as the regulation of energy substrate metabolism, specifically fatty acids and fatty acid oxidation, have been shown to be an important factor contributing to these consequences of reperfusion injury (98, 402). Important factors regulating fatty acid oxidation include the concentration of circulating plasma FFAs and the intracellular content of malonyl CoA, which itself is primarily regulated by the

AMPK-ACC-MCD axis (98, 403, 405) (Figure 1-12).

Ischemia-induced alterations in plasma FFA concentrations

The concentration of FFAs is influenced by a variety of factors such as prandial and hormonal state. Fasting increases circulating plasma FFA concentrations; whilst there is a decrease in circulating plasma FFA concentrations in the post-prandial state due to the anti-lipolytic effects of insulin (314, 315). Ischemia rapidly increases catecholamine discharge, be it in response to myocardial ischemia arising from underlying pathophysiological alterations, or in response to elective ischemia employed in cardiac surgical procedures. Plasma norepinephrine concentrations increase within minutes and can remain elevated for periods of up to 20 hr (276) depending on the severity of the ischemic insult and ensuing stress response. This elevates circulating plasma FFA concentrations by promoting adipose tissue lipolysis (212), and suppresses pancreatic insulin secretion and peripheral insulin sensitivity (70, 224, 324). Furthermore, elevated plasma concentrations of hydrocortisone accompany the stress of ischemia, having permissive effects on adipose tissue lipolysis, and blunting insulin sensitivity (322). An increase in circulating plasma FFAs during and following ischemia thus increases the delivery of fatty acids to the myocardium and can alter fatty acid utilization during both the ischemic and post-ischemic period.

Ischemia-induced alterations in fatty acid oxidation

The primary effect of ischemia is a lack of oxygen and nutrient supply and decreased clearance of metabolic by-products from the affected region(s) of the myocardium (282). The obligate requirement for oxygen in the process of oxidative phosphorylation results in a rapid decrease in ATP production from the catabolism of fatty acids and pyruvate in proportion to the degree of ischemia. However, fatty acid oxidation remains the major source of residual oxidative metabolism (116, 227, 234, 419) with no increase in the relative contribution of carbohydrate oxidation (265, 297). There is a rapid acceleration in the conversion of pyruvate to lactate via LDH and the regeneration of NAD^+ from NADH in an effort to maintain anaerobic glycolysis. Although glycolysis can provide a limited amount of ATP during ischemia, the hydrolysis of glycolytically derived ATP in the absence of subsequent pyruvate oxidation leads to an accumulation of lactate and H^+ (84, 323), which can further aggravate ionic disturbances brought about by ischemia. Thus during ischemia, when glycolysis is accelerated, a greater proportion of ATP hydrolysis must be diverted towards performing chemical work (re-establishing ionic homeostasis). With total ischemia there is an accumulation of reducing equivalents in the form of NADH, and $FADH_2$ (282). Both the acyl CoA dehydrogenase and 3-hydroxyacyl CoA dehydrogenase enzyme reactions of fatty acid oxidation are sensitive to the redox state of the matrix (NAD^+/NADH and ratios FAD/$FADH_2$)(284). The inhibition of fatty acid oxidation secondary to the accumulation of reducing equivalents can result in the accumulation of fatty acid intermediates in distinct cellular

compartments. Long chain acylcarnitine species can accumulate in both the mitochondrial matrix and cytosol, whereas long chain acyl CoA species accumulate primarily in the mitochondrial matrix as this pool of CoA does not exchange with the relatively small cytosolic CoA pool (163). The accumulation of these acylcarnitine and acyl CoA esters promotes disruption of mitochondrial cristae and the formation of amorphous intramitochondrial densities, changes that may ultimately disrupt mitochondrial function (174).

Ischemia-induced alterations in the subcellular control of fatty acid oxidation and fatty acid oxidation in the post-ischemic period

Alterations in the subcellular control of fatty acid oxidation also contribute to changes in myocardial fatty acid metabolism brought about by ischemia (405) (Figure 1-12). Myocardial ischemia is accompanied by the rapid activation of AMPK, and the subsequent phosphorylation and inhibition of ACC (207, 208). These former changes coupled with the relative maintenance or increase in the activity of MCD, results in a decrease in myocardial malonyl CoA content during no-flow ischemia in *ex vivo* rat hearts (207), but not *in vivo* in pigs subjected to low flow ischemia (380) or ischemia caused by simultaneous flow constriction and dobutamine infusion (381). A reduction in malonyl CoA content relieves the inhibition of CPT 1, allowing fatty acid oxidation to increase by virtue of the increased entry of fatty acyl CoA moieties into the mitochondrial matrix. These effects contribute to the continued reliance on fatty acid oxidation for residual oxidative ATP generation during myocardial ischemia (116, 419).

The activation of AMPK persists during reperfusion following ischemia, and is associated with the changes in ACC and MCD activity described above, resulting therefore in a marked decrease in myocardial malonyl CoA content (207) (Figure 1-12). Thus during reperfusion the rates of fatty acid oxidation recover rapidly to pre-ischemic values at the expense of glucose oxidation, while contractile function remains depressed (266, 390). This results in a greater contribution of fatty acid oxidation to oxidative ATP production during reperfusion following ischemia. However, the recovery of fatty acid oxidation at the expense of glucose oxidation contributes to an uncoupling of glucose metabolism, whereby glycolysis is disproportionately greater than subsequent pyruvate oxidation, thus aggravating intracellular acidosis, and impairing the recovery of cardiac function and efficiency despite the restoration of coronary flow (233).

The marked decrease in ATP production during ischemia leads to the inhibition of the Na^+/K^+ ATPase, which is responsible for the extrusion of 3 Na^+ ions in exchange for 2 K^+ ions, and is crucial in regulating resting membrane potential (34). Impaired function of the Na^+/K^+ ATPase thus results in intracellular Na^+ overload. Impaired activity of the sarcoplasmic Ca^{2+} ATPase, which is responsible for the reuptake of Ca^{2+} following myocyte contraction, contributes to Ca^{2+} overload. As Ca^{2+} is required for cardiac muscle contraction, it is a major determinant of the pathophysiology of ischemic and post-ischemic contractile dysfunction, via mechanisms involving decreased responsiveness of the contractile proteins to activating Ca^{2+} (36). Intracellular acidosis itself impairs

the response of the contractile filaments to Ca^{2+}, thereby contributing to the impaired recovery of function during reperfusion. The increased contribution of fatty acid oxidation to myocardial energy requirements, again at the expense of pyruvate oxidation during reperfusion, in conjunction with the alterations in ionic homeostasis occurring during ischemia, prime the myocardium to further injury. The normalization of extracellular pH during the post-ischemic period produces a large pH gradient across the sarcolemmal membrane promoting Na^+/H^+ exchange, and further aggravating intracellular Na^+ overload. This in turn promotes reverse mode Na^+/Ca^{2+} exchange (25), and the sequence of events associated with intracellular Ca^{2+} overload, including contracture, mitochondrial dysfunction, the activation of Ca^{2+} dependent proteases, and cardiac myocyte cell death culminating in the impaired recovery of cardiac function and efficiency (Figure 1-13).

Production of H^+s and development of acidosis from uncoupled glucose metabolism

A popular misconception is that the acidosis observed during myocardial I/R arises from the increased production of lactate from pyruvate (323). However, as mentioned in the above sections, the acidosis observed during myocardial I/R does not arise from lactate accumulation, but rather the hydrolysis of glycolytically-derived ATP (84, 323). When the ATP molecules required for the hexokinase and (PFK1) enzymatic reactions of glycolysis are hydrolyzed, the liberated phosphate group attaches to the glucose molecule and replaces a

hydrogen molecule via electrophilic substitution (323) (Figure 1-14). The liberated hydrogen carries a positive charge and represents the produced H^+. If glycolysis is coupled to glucose oxidation, the pyruvate that enters the mitochondria takes a H^+ with it through a monocarboxylic acid transporter (MCT), and this H^+ is utilized for oxidative phosphorylation or to maintain the H^+ gradient in the mitochondrial intermembrane space (323). However, physiologically, in the heart, there is never 100% coupling between glycolysis and glucose oxidation, and thus there will always be net myocardial H^+ production, even in the aerobic setting. Although in the aerobic setting, this does not present a problem as the heart has energy in sufficient amounts to deal with these H^+s. As mentioned in the previous section, during myocardial I/R, the generation of a large pH gradient across the sarcolemmal membrane promotes Na^+/H^+ exchange, which in turn promotes reverse mode Na^+/Ca^{2+} exchange (25), and this impairs the recovery of cardiac function and efficiency (Figure 1-13).

Stimulating glucose oxidation to alleviate myocardial acidosis and improve cardiac efficiency

The modulation of myocardial energy substrate metabolism, particularly, shifting energy substrate preference from the use of fatty acids towards the use of glucose as an oxidative fuel, is a novel therapeutic intervention to enhance the preservation of mechanical function and efficiency in various forms of ischemic heart disease and heart failure. Pharmacological agents that inhibit fatty acid

oxidation and favor the use of glucose as an oxidative fuel have recently received considerable attention (71, 93, 95, 171, 214, 221, 236, 268, 379, 382, 397, 402, 436). Altering the balance between fatty acid and glucose use can be elicited through the use of pharmacological agents that act at a variety of levels on the pathways of fatty acid and glucose metabolism, and as such, alter the balance and contribution of these pathways to cardiac energetics and function by increasing the efficiency of both ATP generation and utilization. With regards to fatty acid metabolism, such effects can be obtained by altering the availability of circulating substrates, mitochondrial uptake of fatty acyl CoA, as well as through altering the process of fatty acid oxidation, either directly or indirectly via the stimulation of pyruvate oxidation. One of the goals of this thesis will be to determine whether stimulating glucose oxidation either directly, or indirectly via inhibition of fatty acid oxidation, can salvage myocardial tissue during an AMI.

Hypothesis and Aims

General Hypothesis

Alterations in fatty acid metabolism have now been shown to contribute to numerous forms of both skeletal muscle and cardiovascular disease, such as insulin resistance, cardiac lipotoxicity, and myocardial I/R injury. Historical observations by Sir Philip Randle and colleagues implicated a substrate-regulated cycle, whereby excessive use of fatty acids for energy metabolism reduces the use of carbohydrates, such as glucose, as an energy fuel. I hypothesize that optimizing fatty acid metabolism by either inhibiting its oxidation in the mitochondria, or partitioning it away from conversion into particular metabolites (i.e. ceramide) should therefore enhance glucose metabolism in both the skeletal muscle and heart, improving obesity-induced skeletal muscle insulin resistance and cardiac dysfunction, and reducing the burden of myocardial I/R injury, which will manifest in the form of a reduced infarct size.

Specific Hypothesis

The specific hypotheses of this thesis are described within the individual chapters pertaining to the experimental results.

Specific Aim 1

To address the controversy of whether the Randle Cycle exists in the skeletal muscle or not, which will be assessed by either fasting mice or subjecting them to a short term high fat diet, and measuring activity of PDH, the rate limiting enzyme of glucose oxidation.

Specific Aim 2

To determine whether inhibiting mitochondrial fatty acid uptake and subsequent oxidation can improve obesity-induced skeletal muscle insulin resistance by increasing glucose oxidation. This will be achieved by subjecting mice with a genetic deficiency of MCD (MCD-/-), which therefore have elevated levels of malonyl CoA and continual CPT 1 inhibition) and their WT littermates to a chronic high fat diet. Insulin resistance will be assessed via glucose and insulin tolerance testing, while whole body *in vivo* metabolism will be assessed via indirect calorimetry with a comprehensive laboratory animal monitoring system (CLAMS).

Specific Aim 3

To determine whether it is the inhibition of mitochondrial fatty acid oxidation itself, or the inhibition of mitochondrial fatty acid uptake that confers

protection against obesity-induced skeletal muscle insulin resistance. This will be determined by subjecting mice to DIO, then inhibiting 3-KAT, the final enzyme is mitochondrial fatty acid oxidation, with the pharmacological inhibitor, trimetazidine. Because only 3-KAT is being inhibited, fatty acids should still have unimpeded entry into the mitochondria via CPT 1. Insulin resistance will be assessed via glucose and insulin tolerance testing, while whole body *in vivo* metabolism will be assessed via indirect calorimetry with a CLAMS apparatus.

Specific Aim 4

To determine whether inhibiting *de novo* synthesis of ceramide in skeletal muscle offers protection against obesity-induced skeletal muscle insulin resistance. This will be determined by subjecting mice to DIO, then inhibiting SPT 1, the rate limiting in *de novo* ceramide synthesis, with pharmacological inhibitors (myriocin and L-cycloserine). Insulin resistance will be assessed via glucose and insulin tolerance testing, while whole body *in vivo* metabolism will be assessed via indirect calorimetry with a CLAMS apparatus.

Specific Aim 5

To determine whether genetic deficiency of MCD is associated with beneficial effects against aging and its associated conditions. This will be assessed by allowing MCD-/- mice and their WT littermates to age until death.

Insulin resistance will be assessed via glucose and insulin tolerance testing continually as the animals age, while whole body *in vivo* metabolism will be assessed via indirect calorimetry with a CLAMS apparatus. *In vivo* cardiac function will also be monitored in aged mice via ultrasound echocardiography.

Specific Aim 6

To determine whether inhibiting mitochondrial fatty acid uptake and subsequent oxidation exacerbates obesity-induced cardiac lipotoxicity. This will be achieved by subjecting MCD-/- mice and their WT littermates to a chronic high fat diet. *In vivo* and *ex vivo* cardiac function will be monitored in mice via ultrasound echocardiography and in an isolated working heart model, respectively. Furthermore, we will measure insulin stimulated glucose oxidation in the hearts as an index of myocardial insulin resistance, and determine the levels of intra-myocardial lipid metabolites.

Specific Aim 7

To determine whether inhibiting *de novo* synthesis of ceramide in the heart offers protection against obesity-induced cardiac lipotoxicity. This will be determined by subjecting mice to DIO, then inhibiting SPT 1 with the pharmacological inhibitor, myriocin. *In vivo* and *ex vivo* cardiac function will be monitored in mice via ultrasound echocardiography and in an isolated working

heart model, respectively. Furthermore, we will measure insulin stimulated glycolysis and glucose oxidation in the hearts as an index of myocardial insulin resistance, and determine the levels of intra-myocardial lipid metabolites.

Specific Aim 8

To determine if the beneficial effects of MCD inhibition on *ex vivo* I/R injury in the heart will translate into a reduction in infarct size, the more clinically relevant outcome. This will be achieved via temporary ligation of the left anterior descending coronary artery (LAD) in MCD-/- mice and their WT littermates.

Figure 1-1: *Fatty acid uptake and activation in the cell.*

Fatty acids enter the cell by passive diffusion, or via a protein carrier mediated pathway. These protein carriers include FAT/CD36 and the FATPs. The fatty acid is then activated by esterification to CoA via the enzymatic activity of FACS. The long chain acyl CoA/fatty acyl CoA molecule can then undergo metabolism to various intermediates (see Figure 1-2), or be taken up into the mitochondria and subsequently oxidized by the β-oxidative machinery (See Figure 1-4).

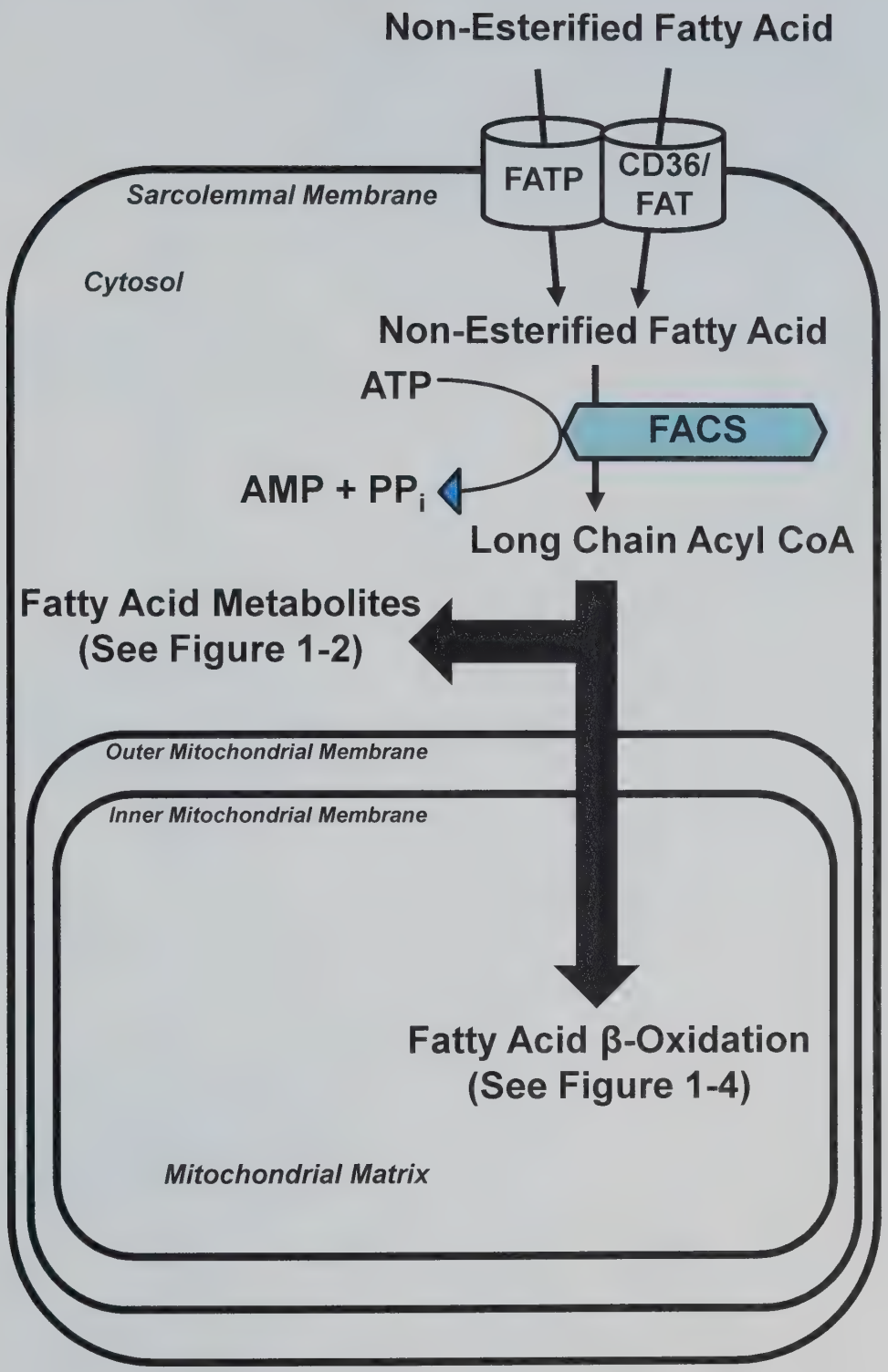
Non-Esterified Fatty Acid
FATP
CD36/
FAT
Sarcolemmal Membrane
Cytosol
Non-Esterified Fatty Acid
ATP
FACS
AMP + PPi
Long Chain Acyl CoA
Fatty Acid Metabolites
(See Figure 1-2)
Outer Mitochondrial Membrane
Inner Mitochondrial Membrane
Fatty Acid β-Oxidation
(See Figure 1-4)
Mitochondrial Matrix

FIGURE 1-1

Figure 1-2: *Metabolic pathways for metabolism of fatty acids into various intermediates.*

The following figure depicts the intracellular metabolism of activated fatty acid molecules into key lipid intermediates implicated in the pathogenesis of skeletal muscle insulin resistance and cardiac lipotoxicity, some of which include TAG, DAG, and ceramide (See Figure 1-11).

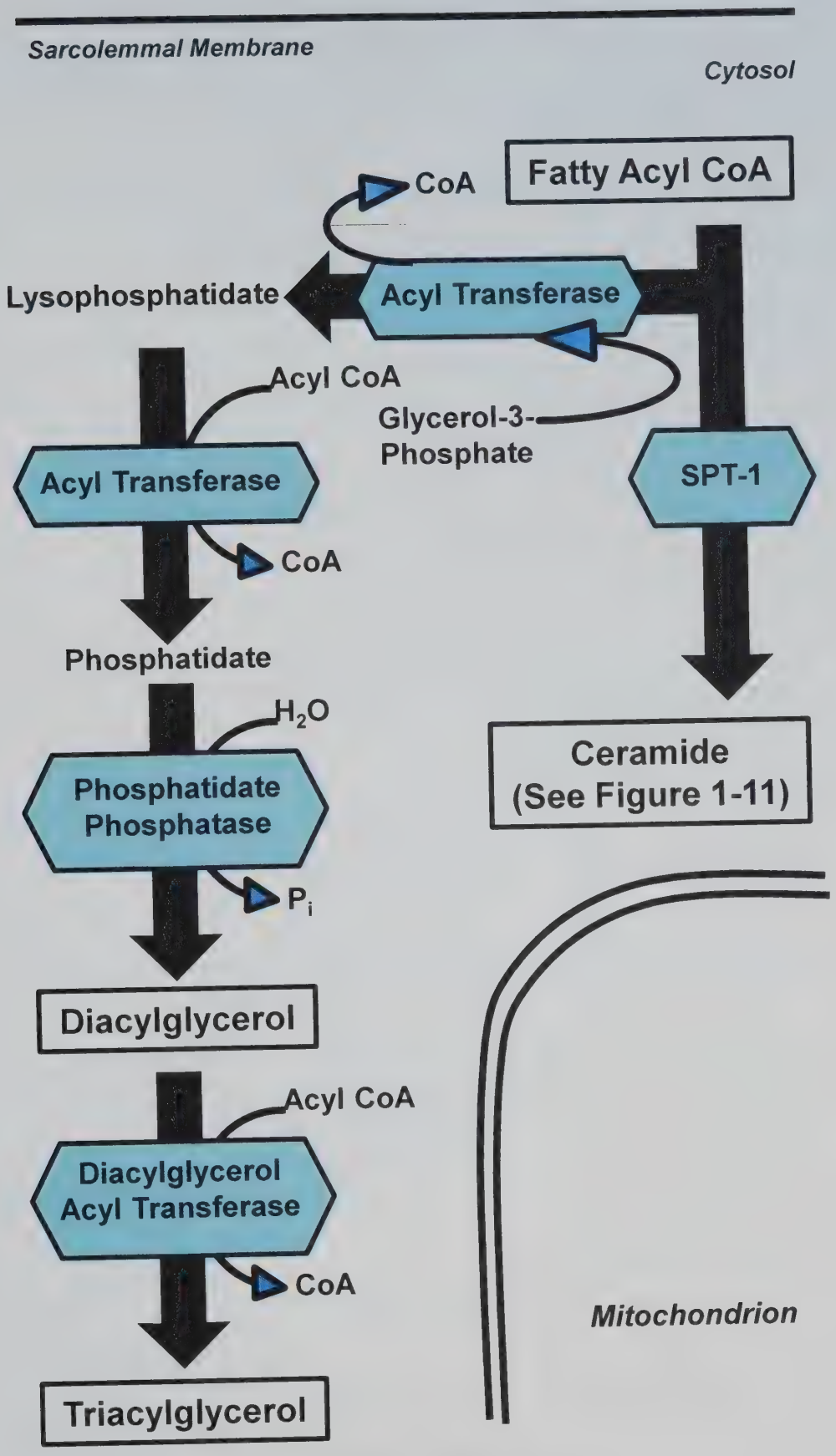
Sarcolemmal Membrane
Cytosol
Fatty Acyl CoA
CoA
Lysophosphatidate
Acyl Transferase
Acyl CoA
Glycerol-3-Phosphate
Acyl Transferase
SPT-1
CoA
Phosphatidate
H_2O
Phosphatidate Phosphatase
Ceramide (See Figure 1-11)
P_i
Diacylglycerol
Acyl CoA
Diacylglycerol Acyl Transferase
CoA
Mitochondrion
Triacylglycerol

FIGURE 1-2

Figure 1-3: *Mitochondrial uptake of fatty acids.*

Because activated fatty acids are impermeable to the mitochondrial membrane, they are taken up into the mitochondria via a carnitine shuttle consisting of 3 enzymes, which include an outer mitochondrial membrane CPT 1, an inner mitochondrial CPT 2, and a mitochondrial intermembrane space CACT.

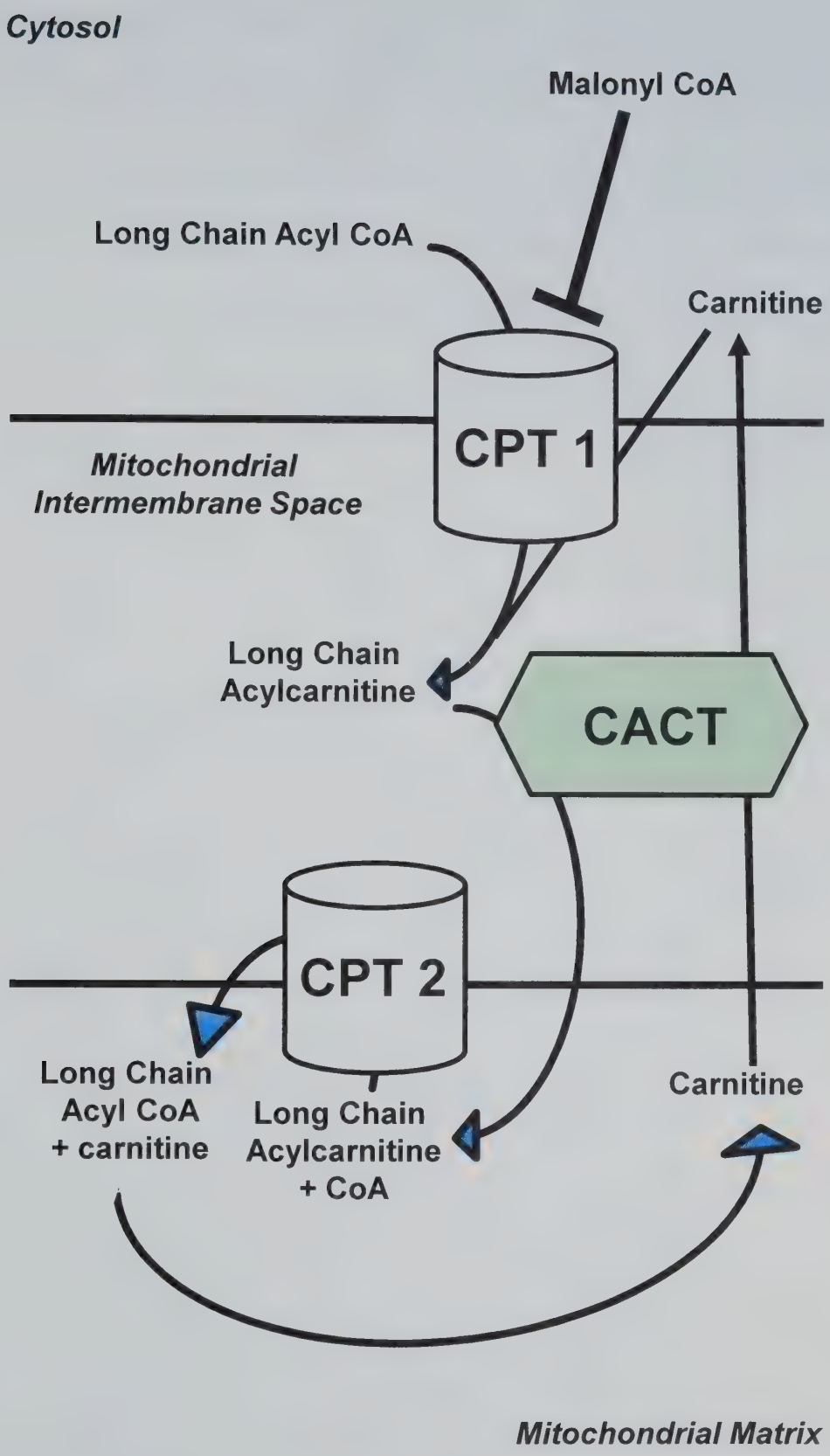
Cytosol
Malonyl CoA
Long Chain Acyl CoA
Carnitine
CPT 1
Mitochondrial
Intermembrane Space
Long Chain
Acylcarnitine
CACT
CPT 2
Long Chain
Acyl CoA
+ carnitine
Long Chain
Acylcarnitine
+ CoA
Carnitine
Mitochondrial Matrix

FIGURE 1-3

Figure 1-4: *Fatty acid β-oxidation.*

Figure depicts the 4 key enzymes involved in the oxidation of activated fatty acids in the mitochondria. The acyl CoA dehydrogenase and hydroxyacyl CoA dehydrogenase enzyme isoforms generate reducing equivalents for oxidative phosphorylation. It is also important to note that the oxidation of unsaturated fatty acids requires 2 auxiliary enzymes, 3,2-enoyl CoA isomerase and 2,4-dienoyl CoA reductase, which are not depicted here.

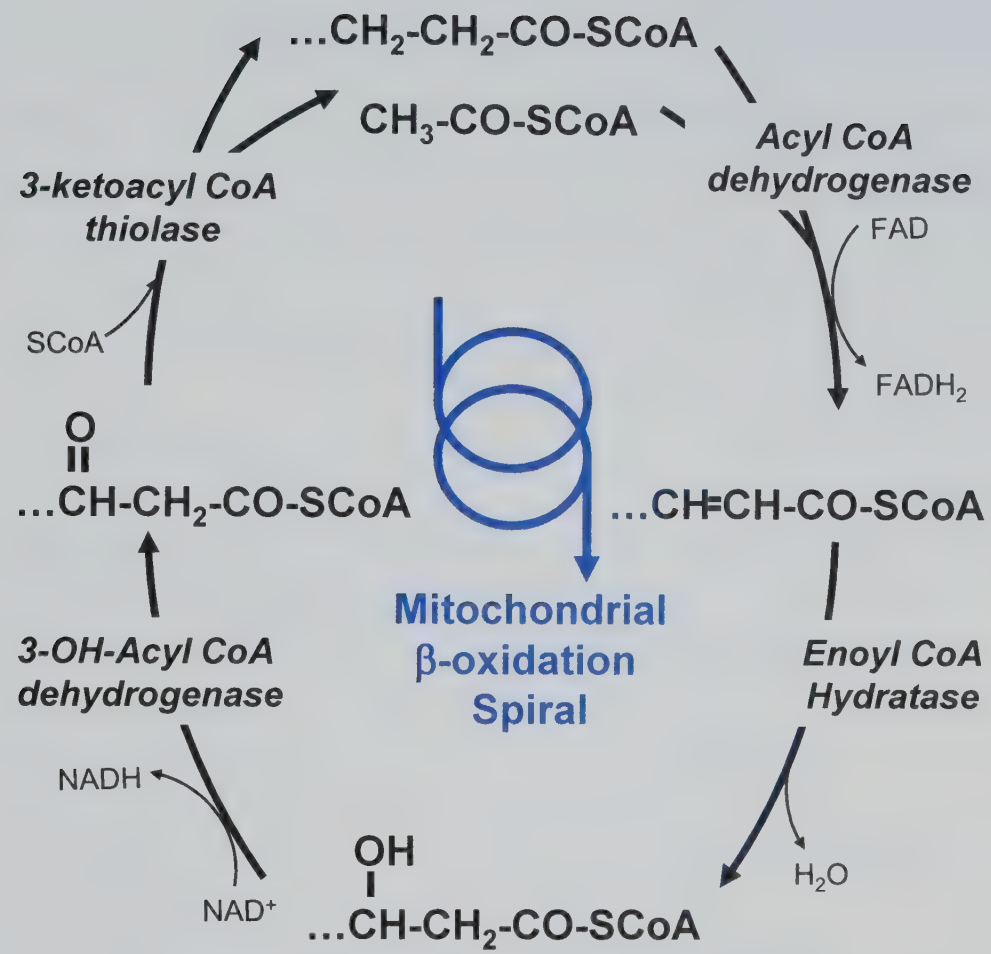
…CH2-CH2-CO-SCoA
CH3-CO-SCoA
3-ketoacyl CoA thiolase
Acyl CoA dehydrogenase
FAD
FADH2
SCoA
O
…CH-CH2-CO-SCoA
…CH=CH-CO-SCoA
Mitochondrial β-oxidation Spiral
3-OH-Acyl CoA dehydrogenase
Enoyl CoA Hydratase
NADH
NAD+
OH
…CH-CH2-CO-SCoA
H2O

FIGURE 1-4

Figure 1-5: *Glycolysis.*

Figure depicts the enzymes and intermediates involved in the metabolism of glucose via the glycolytic pathway. The glucose-6-phosphate can also be diverted away from glycolysis into 2 other significant pathways, that being glycogen metabolism and the pentose phosphate pathway. It is important to note that while PFK1 is naturally the rate-limiting enzyme during glycolysis, glyceraldehyde-3-phosphate dehydrogenase can become rate-limiting during metabolic stresses such as ischemia.

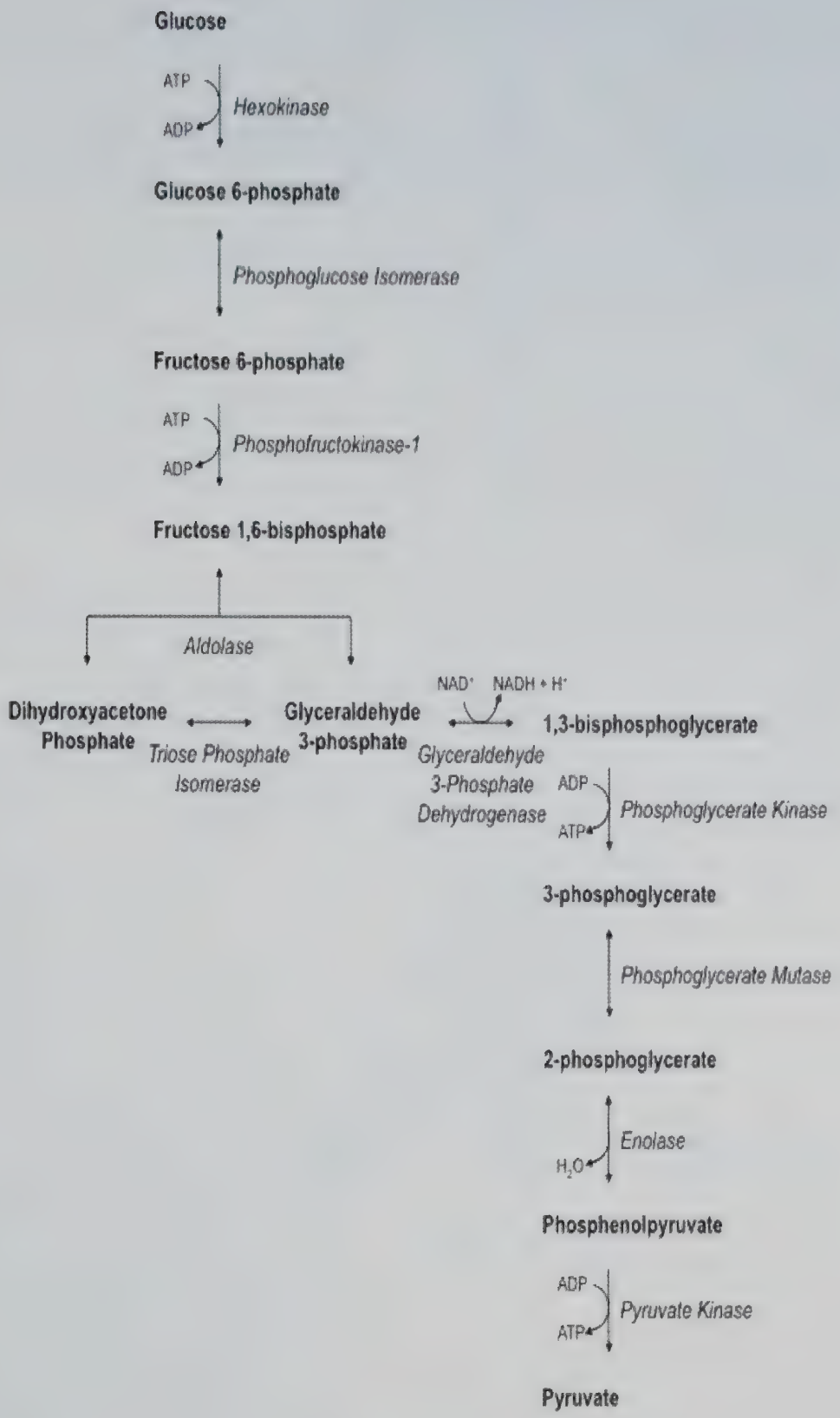
Glucose
ATP
ADP
Hexokinase
Glucose 6-phosphate
Phosphoglucose Isomerase
Fructose 6-phosphate
ATP
ADP
Phosphofructokinase-1
Fructose 1,6-bisphosphate
Aldolase
Dihydroxyacetone Phosphate
Triose Phosphate Isomerase
Glyceraldehyde 3-phosphate
NAD+
NADH + H+
1,3-bisphosphoglycerate
Glyceraldehyde 3-Phosphate Dehydrogenase
ADP
ATP
Phosphoglycerate Kinase
3-phosphoglycerate
Phosphoglycerate Mutase
2-phosphoglycerate
H2O
Enolase
Phosphenolpyruvate
ADP
ATP
Pyruvate Kinase
Pyruvate

FIGURE 1-5

Figure 1-6: *Oxidation of pyruvate via the pyruvate dehydrogenase complex.*

The PDH complex is the rate-limiting enzyme of carbohydrate oxidation, and consists of 3 enzymes, with the catalytic decarboxylating activity residing in the pyruvate dehydrogenase (enzyme 1) subunit. The PDH complex is negatively regulated by phosphorylation via PDHK, and activated by dephosphorylation via PDP. It is important to note that increased fatty acid by products arising from enhanced rates of fatty acid oxidation will activate PDHK to inhibit PDH and subsequent carbohydrate oxidation (See Figure 1-8), whereas increasing mitochondrial Ca^{2+} concentration, or insulin, will activate PDP to activate PDH and increase carbohydrate oxidation.

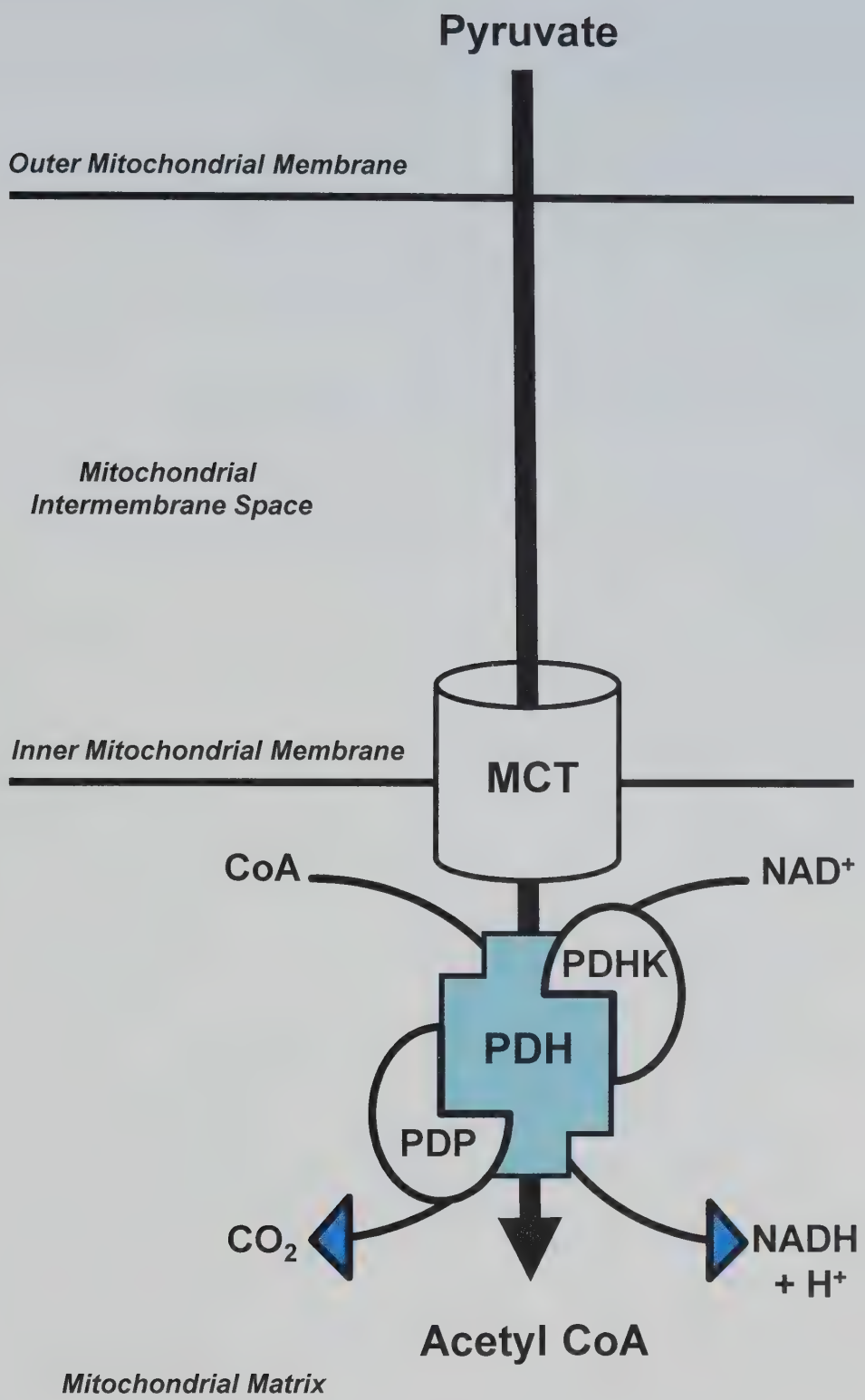
Pyruvate
Outer Mitochondrial Membrane
Mitochondrial
Intermembrane Space
Inner Mitochondrial Membrane
MCT
CoA
NAD+
PDHK
PDH
PDP
CO2
NADH
+ H+
Acetyl CoA
Mitochondrial Matrix

FIGURE 1-6

Figure 1-7: *The tricarboxylic acid cycle.*

Figure depicts the enzymes and intermediates involved in the TCA cycle. The oxidation of any type of fuel source (i.e. glucose, amino acids, fatty acids, ketone bodies) will results in the generation of acetyl CoA for the TCA cycle.

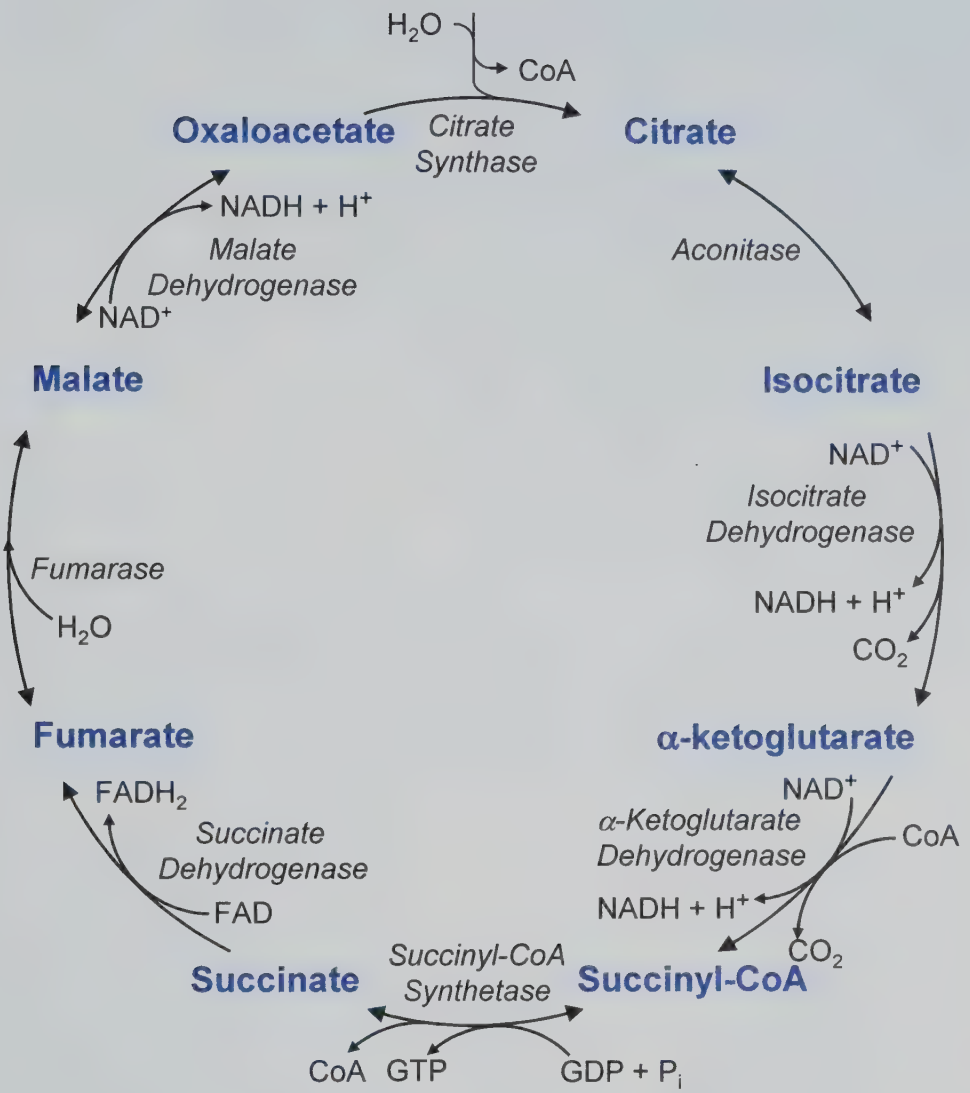
H2O
CoA
Oxaloacetate
Citrate Synthase
Citrate
NADH + H+
Malate Dehydrogenase
NAD+
Aconitase
Malate
Isocitrate
NAD+
Isocitrate Dehydrogenase
NADH + H+
CO2
Fumarase
H2O
Fumarate
α-ketoglutarate
FADH2
Succinate Dehydrogenase
FAD
NAD+
α-Ketoglutarate Dehydrogenase
CoA
NADH + H+
CO2
Succinate
Succinyl-CoA Synthetase
Succinyl-CoA
CoA
GTP
GDP + Pi

FIGURE 1-7

Figure 1-8: *The Randle cycle.*

Figure depicts the premise of the Randle Cycle, whereby increasing rates of fatty acid oxidation increases the availability of fatty acid by-products, such as acetyl CoA and NADH. This results in elevated acetyl CoA/CoA and NADH/NAD^+ ratios, which activated PDHK isoforms to phosphorylate and inhibit PDH, subsequently reducing pyruvate (carbohydrate) oxidation. The graph below shows evidence for the Randle Cycle in the isolated working rat heart, whereby increasing the concentration of palmitate delivered to the heart increased palmitate oxidation, and subsequently reduces glucose oxidation.

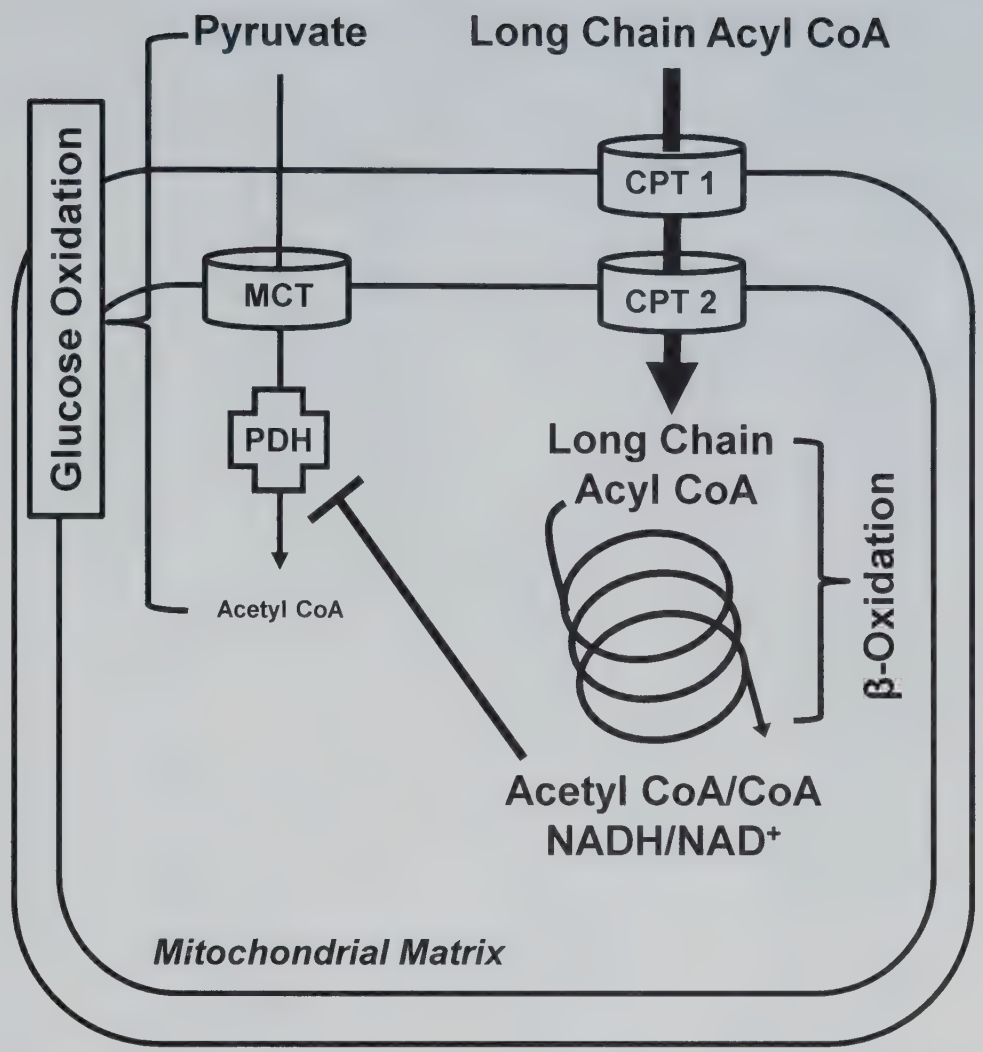
Pyruvate
Long Chain Acyl CoA
Glucose Oxidation
CPT 1
MCT
CPT 2
PDH
Long Chain
Acyl CoA
β-Oxidation
Acetyl CoA
Acetyl CoA/CoA
NADH/NAD+
Mitochondrial Matrix

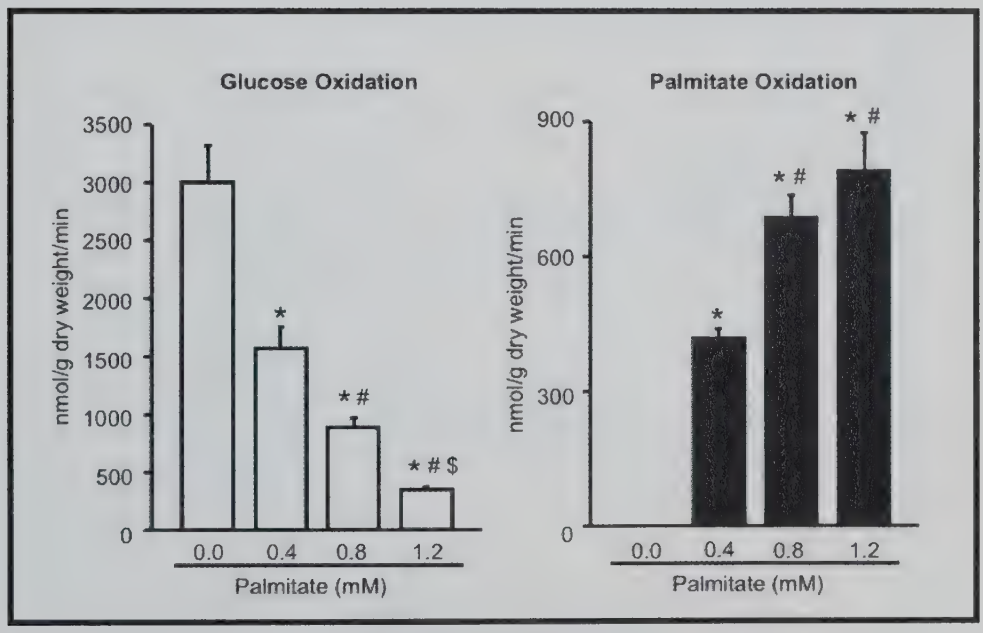
Glucose Oxidation
nmol/g dry weight/min
3500
3000
2500
2000
1500
1000
500
0
* # $
0.0
0.4
0.8
1.2
Palmitate (mM)
Palmitate Oxidation
nmol/g dry weight/min
900
600
300
0
* #
0.0
0.4
0.8
1.2
Palmitate (mM)

FIGURE 1-8

Figure 1-9: *Insulin signaling.*

Figures depicts the cellular events involved in insulin signaling via the insulin receptor. It is important to note that there are two key kinases believed to play a key role in mediating GLUT4 translocation and subsequent glucose uptake in response to insulin, Akt and PKCζ, both of which are activated by PI3K in response to insulin.

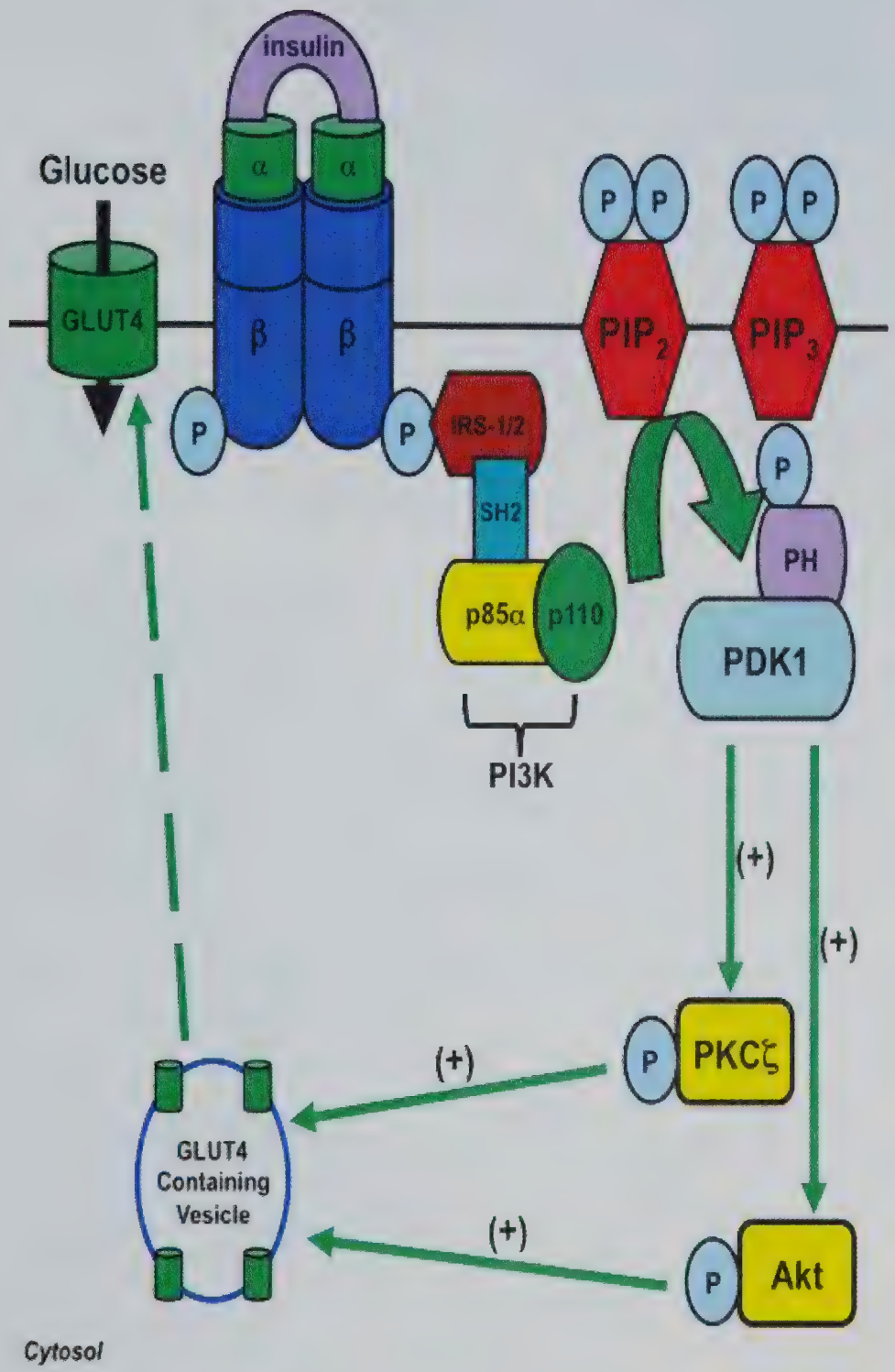
insulin
Glucose
α
α
β
β
GLUT4
P
P
IRS-1/2
SH2
p85α
p110
PI3K
P
P
P
P
PIP2
PIP3
P
PH
PDK1
(+)
(+)
(+)
(+)
P
PKCζ
P
Akt
GLUT4
Containing
Vesicle
Cytosol

FIGURE 1-9

Figure 1-10: *Consequences of lipid metabolite accumulation in the skeletal muscle and heart.*

During obesity, an increased fatty acid supply to the skeletal muscle, in combination with an impaired ability to oxidize fatty acids in the mitochondria, results in the intracellular accumulation of TAG, long chain acyl CoA, DAG, and/or ceramide. These metabolites, and in particular, long chain acyl CoA and DAG, can act as ligands activating isoforms of the classical/novel PKC family, which subsequently phosphorylate IRS proteins on serine residues. Phosphorylation at serine residues prevents tyrosine phosphorylation and subsequent activation of the IRS proteins, which inhibits PI3K and subsequent Akt activation, preventing GLUT4 translocation and glucose uptake into the cell, ultimately leading to skeletal muscle insulin resistance. This sequence of events is believed to also contribute to the development of cardiac insulin resistance. In addition, it is believed that the accumulation of ceramide in the cardiac myocyte induces apoptosis, leading to contractile dysfunction and contributing towards the progression to heart failure in patients with obesity.

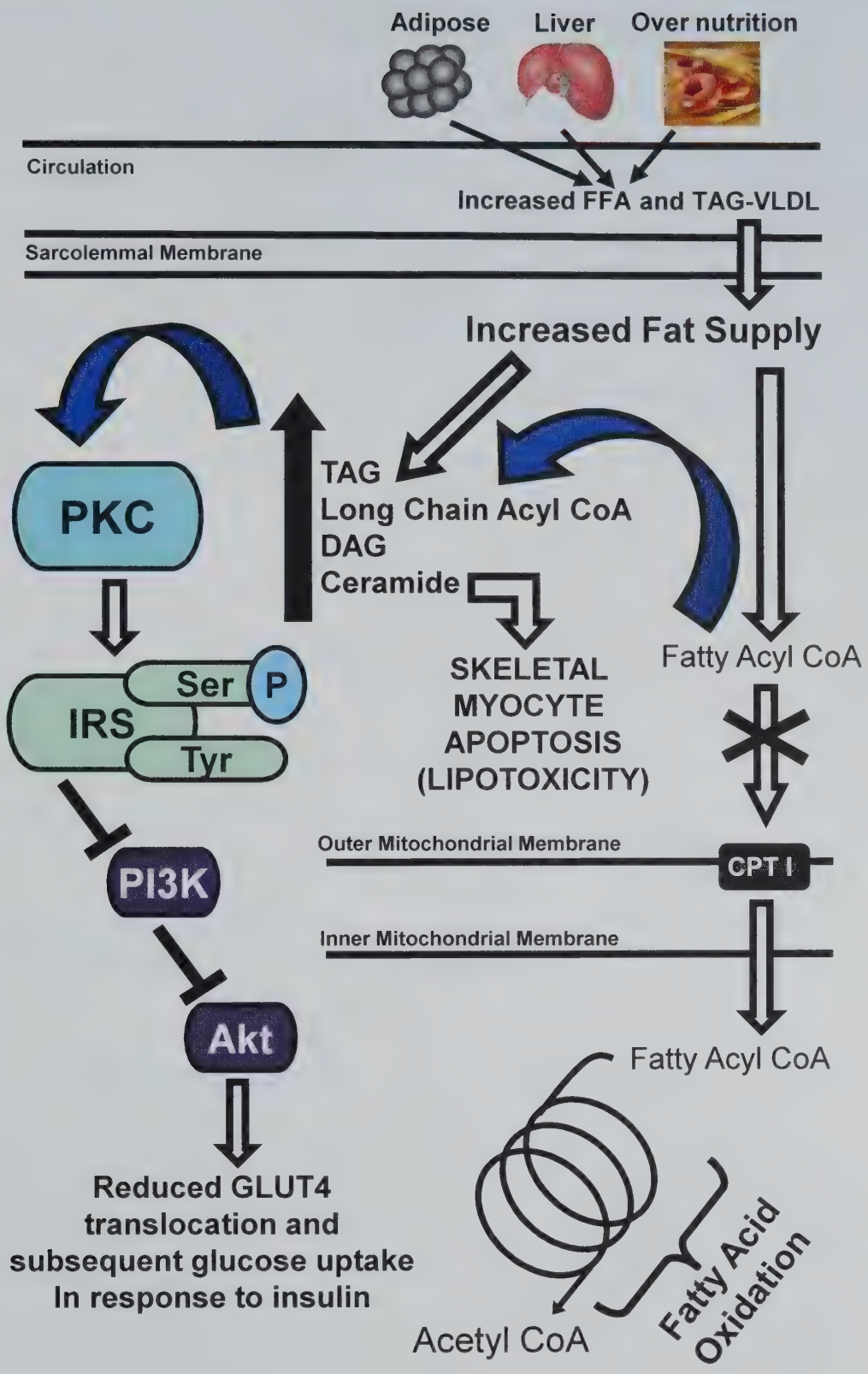
Adipose
Liver
Over nutrition
Circulation
Increased FFA and TAG-VLDL
Sarcolemmal Membrane
Increased Fat Supply
PKC
TAG
Long Chain Acyl CoA
DAG
Ceramide
Ser
P
IRS
Tyr
SKELETAL
MYOCYTE
APOPTOSIS
(LIPOTOXICITY)
Fatty Acyl CoA
Outer Mitochondrial Membrane
CPT I
PI3K
Inner Mitochondrial Membrane
Akt
Fatty Acyl CoA
Reduced GLUT4
translocation and
subsequent glucose uptake
In response to insulin
Acetyl CoA
Fatty Acid
Oxidation

FIGURE 1-10

Figure 1-11: *Ceramide metabolism.*

Figure depicts the synthesis of ceramide from *de novo* precursors, or from membrane phospholipids such as sphingomyelin. Figure also depicts the metabolism of ceramide into various intermediates such as glucosylceramide. It is important to note that the rate-limiting enzyme in the *de novo* synthesis of ceramide is SPT, which this thesis will support a role for, as a novel target in the treatment of skeletal muscle insulin resistance.

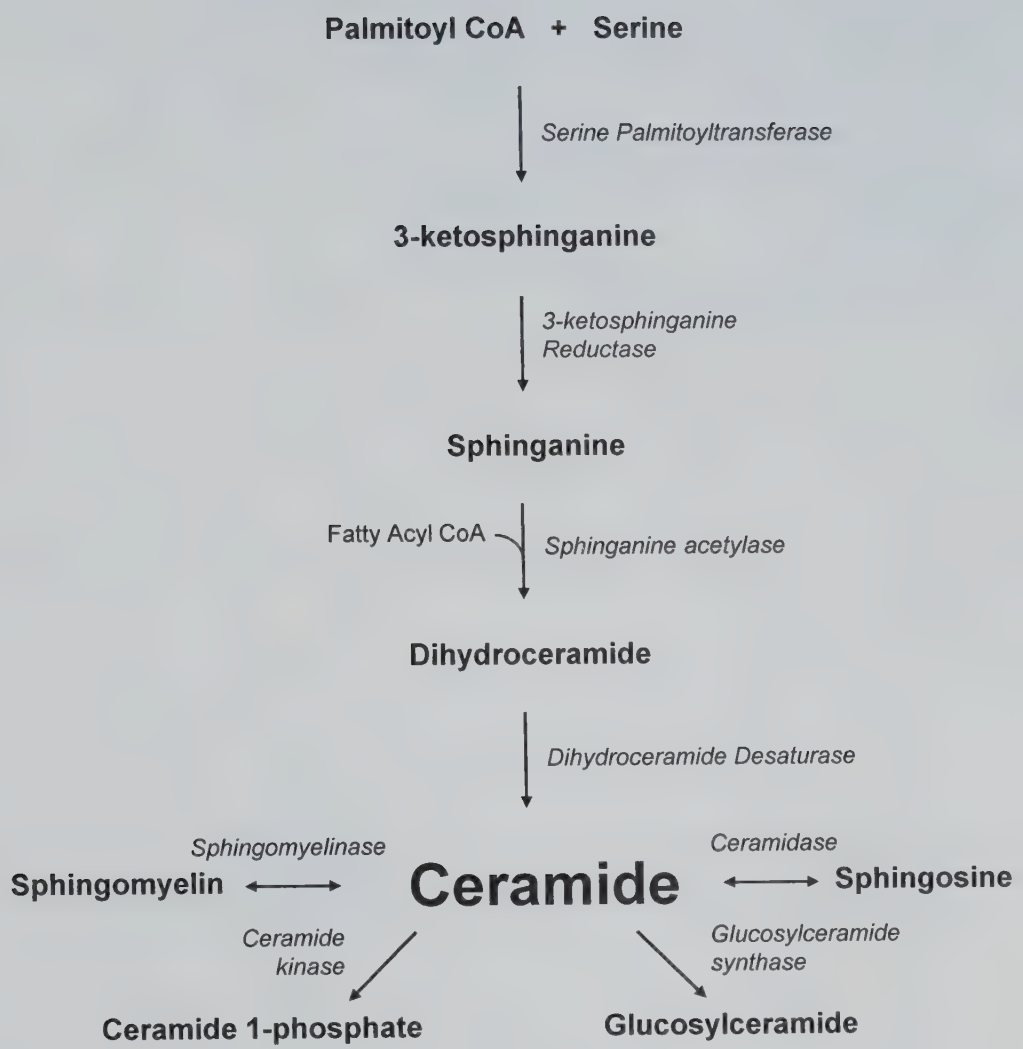
Palmitoyl CoA + Serine
Serine Palmitoyltransferase
3-ketosphinganine
3-ketosphinganine Reductase
Sphinganine
Fatty Acyl CoA
Sphinganine acetylase
Dihydroceramide
Dihydroceramide Desaturase
Sphingomyelinase
Sphingomyelin
Ceramide
Ceramidase
Sphingosine
Ceramide kinase
Glucosylceramide synthase
Ceramide 1-phosphate
Glucosylceramide

FIGURE 1-11

Figure 1-12: *Subcellular changes in metabolism during ischemia/reperfusion.* During I/R, there is a rapid activation of AMPK, which phosphorylates and inhibits ACC, resulting in an inhibition of malonyl CoA production. At the same time, sustained MCD activity contributes to the degradation of malonyl CoA, contributing to the very low levels of malonyl CoA observed in the heart during I/R. This allows fatty acids to dominate as the principle source of oxidative energy during reperfusion, and inhibits glucose oxidation via the Randle Cycle effect. However, glycolytic rates remain high, and therefore glucose oxidation is uncoupled from glycolysis, which increases H^+ production (See Figure 1-13 for a description on how increased H^+ production reduces the recovery of cardiac efficiency, and Figure 1-14 for a description on how glycolytic ATP leads to H^+ production).

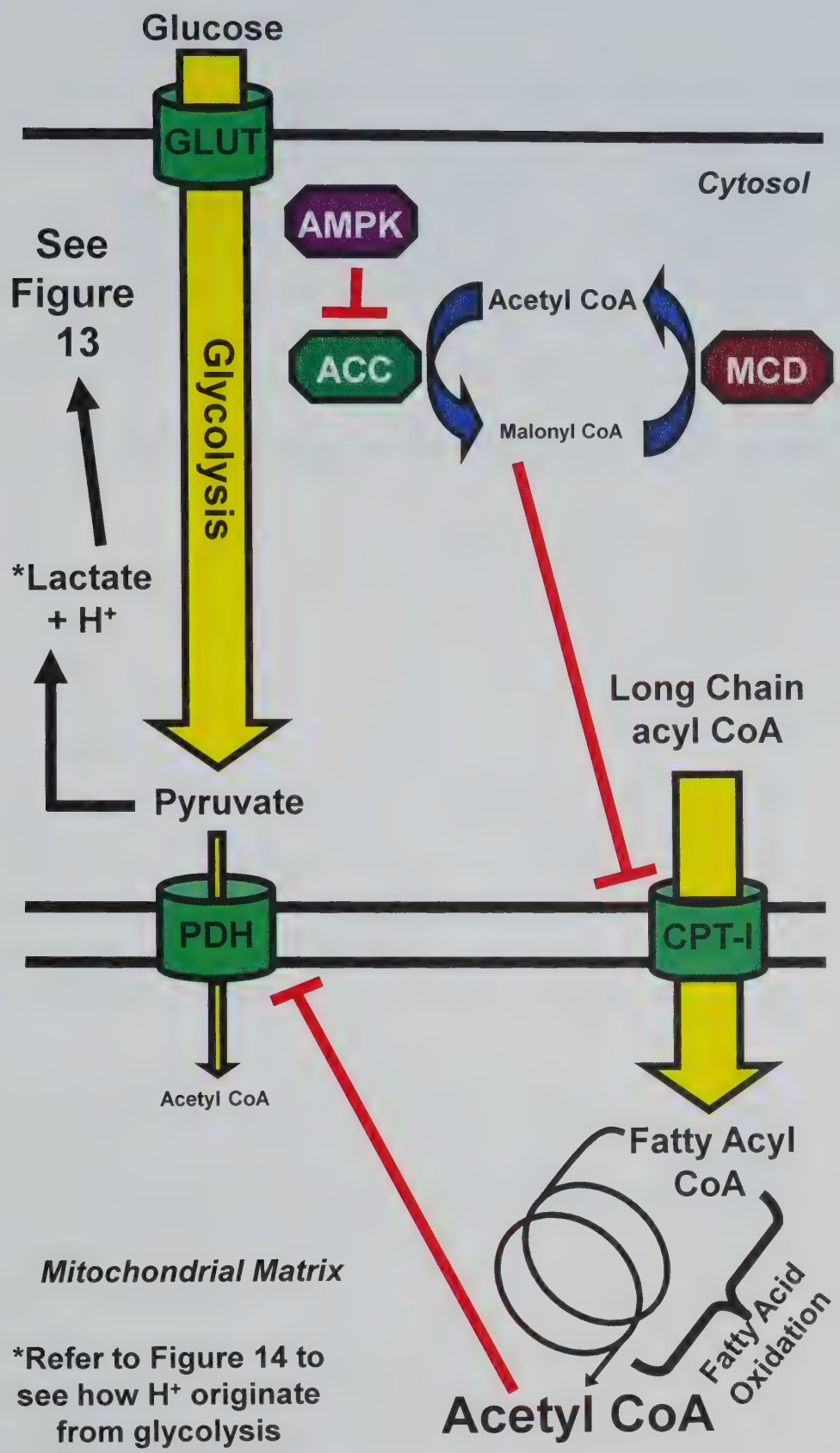
Glucose
GLUT
Cytosol
AMPK
See Figure 13
Acetyl CoA
ACC
MCD
Malonyl CoA
Glycolysis
*Lactate + H+
Long Chain acyl CoA
Pyruvate
PDH
CPT-I
Acetyl CoA
Fatty Acyl CoA
Mitochondrial Matrix
Fatty Acid Oxidation
*Refer to Figure 14 to see how H+ originate from glycolysis
Acetyl CoA

FIGURE 1-12

Figure 1-13: *Reduction in cardiac efficiency via increased H^+ production.*

The increased H^+ production described in Figure 1-12 leads to the activation of the sodium-hydrogen exchanger (NHE), which transports H^+s out of the cell in exchange for Na^+ ions. This causes the sodium-calcium exchanger (NCX) to operate in reverse mode, transporting out 1 Na^+ ion in exchange for 3 Ca^{2+} ions. As a result of this ionic imbalance, ATP is diverted away from contractile function towards the re-establishment of ionic homeostasis, which reduces cardiac efficiency and limits the recovery of cardiac function during reperfusion.

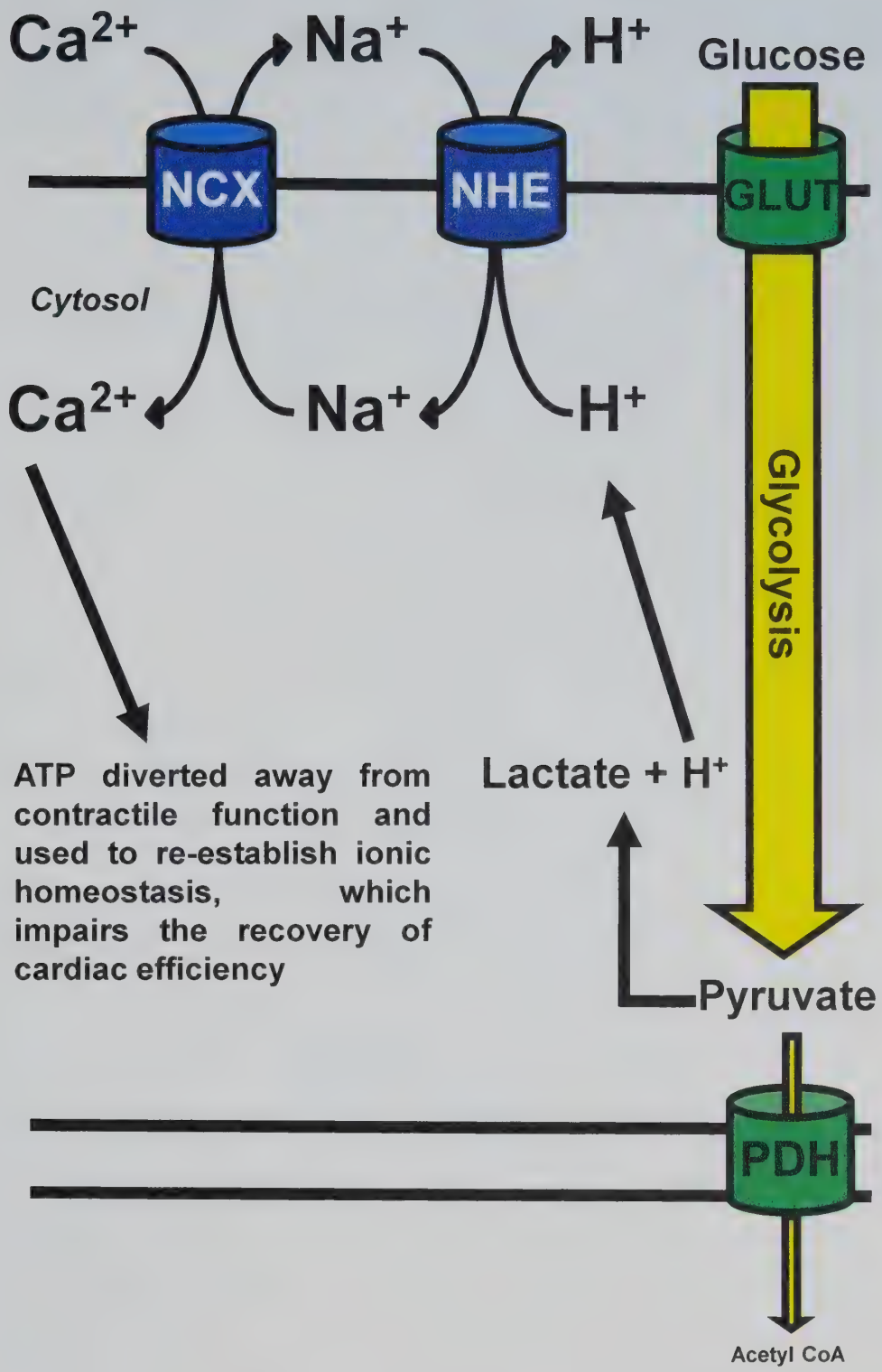
Ca2+
Na+
H+
Glucose
NCX
NHE
GLUT
Cytosol
Ca2+
Na+
H+
Glycolysis
ATP diverted away from contractile function and used to re-establish ionic homeostasis, which impairs the recovery of cardiac efficiency
Lactate + H+
Pyruvate
PDH
Acetyl CoA

FIGURE 1-13

Figure 1-14: *How does the H^+ originate from glycolysis?*

Figure depicts the origin of the H^+ from glycolytic ATP at both the **A: hexokinase** and B: PFK1 reactions of glycolysis.

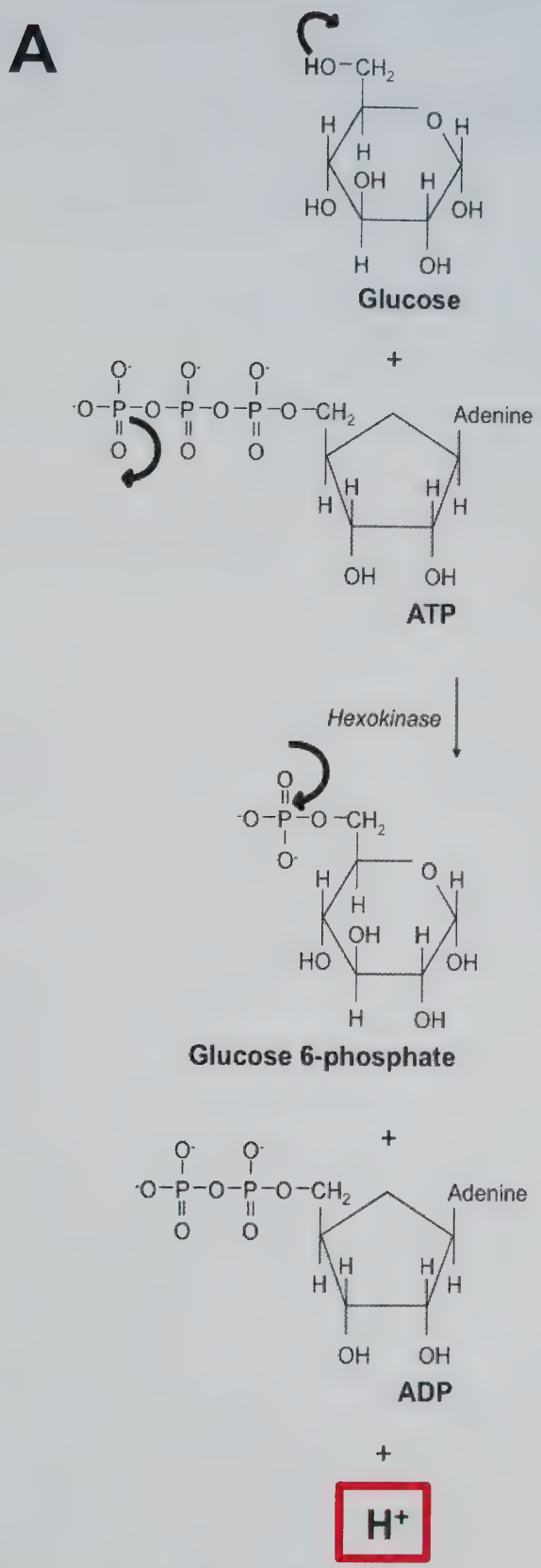
A
Glucose
+
Adenine
ATP
Hexokinase
Glucose 6-phosphate
+
Adenine
ADP
+
H+

FIGURE 1-14

Figure 1-14: *How does the H^+ originate from glycolysis?*

Figure depicts the origin of the H^+ from glycolytic ATP at both the A: hexokinase and **B: PFK1** reactions of glycolysis.

B

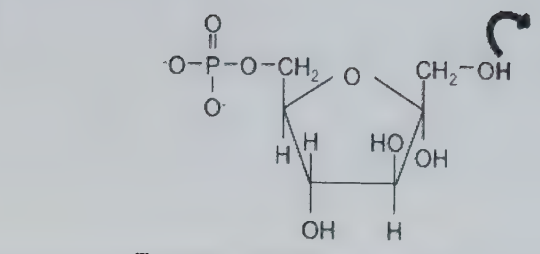

Fructose 6-phosphate

+

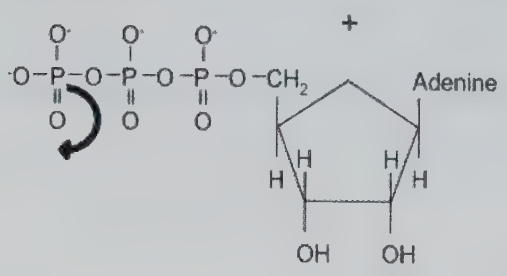

ATP

Phosphofructokinase-1

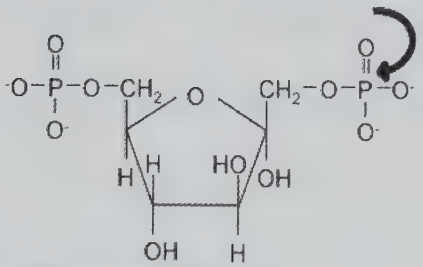

Fructose 1,6-bisphosphate

+

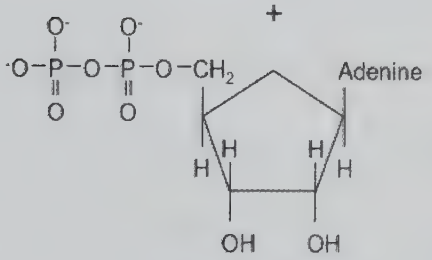

ADP

+

H^+

FIGURE 1-14

CHAPTER 2.

Materials and Methods

CHAPTER 2

Materials and Methods

Introduction

As the primary questions of this thesis involve understanding how altered fatty acid metabolism during obesity contributes to the development of metabolic diseases such as insulin resistance and ischemic heart disease, a major portion of our experimental protocols focus on measuring flux through metabolic pathways following DIO. In addition, we will utilize a number of sophisticated chromatography procedures to determine the intracellular content of a number of lipid metabolites, to better understand lipid partitioning during obesity.

We will also employ a number of *in vivo* procedures, such as glucose tolerance testing and ultrasound echocardiography, to assess insulin sensitivity and cardiac function, respectively, in our obese animals, while making use of a number of *in vitro* procedures such as Western blotting to investigate the signaling mechanisms that contribute to disease development. Overall, our studies are employing a number of state-of-the-art technologies at the whole animal, tissue, and cellular levels to understand how MCD and SPT 1 may be novel targets for the treatment of obesity-associated diseases

[U-^{14}C]glucose and D-[5-^{3}H]glucose were obtained from Amersham Canada Ltd. (Oakville, Ontario). [9,10-^{3}H]palmitic acid and [1-^{14}C]palmitic acid were obtained from NEN Research Products (Boston, Massachusetts). Bovine serum albumin (BSA fraction V, fatty acid free) was obtained from Equitech-Bio Inc. (Kerrville, Texas). Insulin (Novolin™ ge Toronto) was obtained through the University of Alberta Hospital stores from Novo Nordisk (Mississauga, Ontario). Ecolite™ Aqueous Counting Scintillation fluid was obtained from MP Biomedicals (Solon, Ohio). Hyamine hydroxide (1 M in methanol solution) was obtained from NEN Research Products (Boston, Massachusetts). FFA and TAG assay kits were obtained from Wako Pure Chemicals Industries Ltd. (Osaka, Japan). L-LDH and glutamate PDH were obtained from Roche Applied Science (Laval, Quebec). For HPLC analysis of adenine nucleotides, a Supelcosil™ LC-18-T Super Guard cartridge, 5 μm particle size, 2 x 4 mm and a Supelcosil™ LC-18-T, 5 μm particle size, 250 x 4.6 mm column were obtained from Supelco/Sigma-Aldrich (St. Louis, Missouri). For HPLC analysis of short chain CoA esters, a Nova-Pak Supelcosil™, 4 μm particle size, C18 pre-column cartridge was obtained from Waters Company (Milford, Massachusetts) and an Adsorbosphere® C18, 3μm particle size, 150 x 4.6 mm column was obtained from Altech Associates/Mandel Scientific (Guelph, Ontario). For HPLC analysis of long chain CoA esters a C18 guard cartridge, 4 x 3 mm and a Luna, 5 μm particle size, C18(2) 100 A, 250 x 2 mm column were obtained from Phenomenex

(Torrance, California). Unifilter P81 96-well filterplates were obtained from Whatman (Florham Park, New Jersey). MicroScint PS scintillant was obtained from Perkin Elmer Life and Analytical Sciences (Woodbridge, Ontario). Myriocin was obtained from Biomol (Plymouth Meeting, Pennsylvania). ECL Supelcosil™ Western blotting detection reagents were purchased from GE Healthcare (Piscataway, New Jersey) and Western Lightning® Chemiluminescence Reagents Plus were obtained from Perkin Elmer Life and Analytical Sciences (Woodbridge, Ontario). Trans-Blot® Transfer Medium (pure nitrocellulose) was obtained from BioRad (Richmond, California). FUJI Medical X-ray films were obtained from Mandel Scientific (Guelph, Ontario). Monoclonal and polyclonal primary and secondary antibodies were obtained from either Cell Signaling Technology (Danvers, Massachusetts), Santa Cruz Biotechnology (Santa Cruz, California), Calbiochem (San Diego, California), or Abgent (San Diego, California). Plasma collecting EGTA coated microfuge tubes were obtained from Sarstedt (Newton, North Carolina). Insulin kits were obtained from Alpco Diagnostics (Salem, New Hampshire). All other chemicals were purchased from Sigma-Aldrich (St. Louis, Missouri).

Methods

The University of Alberta adheres to the principles for biomedical research involving animals developed by the Council for International

Organizations of Medical Sciences and complies with Canadian Council of Animal Care Guidelines.

Generation and Breeding of Malonyl CoA Decarboxylase Deficient Mice

Chugai Pharmaceutical Co., Ltd. was responsible for the generation of this transgenic mouse strain. A mouse genomic clone corresponding to *mcd* was isolated from a bacterial artificial chromosome (BAC) using rat MCD cDNA as a probe. Mouse *mcd* gene fragments were subcloned from the BAC clone containing exon 1 (which includes both translational start sites) to a DT/A cassette plasmid vector, containing a diphtheria toxin A gene fragment as a negative selection marker. Exon 1 of the *mcd* gene was replaced with a neomycin cassette located between PvuII and EcoRV restriction sites. AB2.2-Prime mouse embryonic stem cells (Lexicon Genetics, The Woodlands, TX) were transfected via electroporation with a linearized targeting vector. Embryonic stem cells were subsequently cultured in a medium supplemented with 300 μg/mL G418 (GIBCO/BRL). The G418-resistant clones were screened by Southern blot analysis to select targeted cells. These selected stem cells were then injected into C57BL/6 (CLEA Japan, Tokyo) blastocysts to produce chimeras. To obtain *mcd*+/- (heterozygous) mutants, male chimeras were mated with C57BL/6 females.

Mcd-/- (homozygous) mutant mice (B6;129S7-*mcd*^{tm1Jish}) were produced from *mcd*+/- crosses. Heterozygous littermates were crossed to produce mice homozygous for the insert. *Mcd* mutant mice were then back-crossed for 6

generations to a C57BL/6 WT animal, in order to produce a background >99% similar to the genetic background of a C57BL/6 animal (370). Homozygous pairs allowed congenic lines of knockout and WT littermate animals to propagate. Throughout the rest of this thesis, *mcd* deficient mice will simply be referred to as "MCD-/-".

Generation and Breeding of Pyruvate Dehydrogenase Kinase 4 Deficient Mice

This transgenic mouse strain was generated in the laboratory of Dr. Robert Harris. To construct the targeting vector, a PCR-amplified 0.9 kb DNA fragment located upstream of exon 1 of the *pdhk4* gene was inserted into the SalI site of a pBluescript II/neo-TK vector (17) that contains the phosphoglycerate kinase promoter driving the neomycin-resistant gene and the herpes virus thymidine kinase gene. A 7.5 kb DNA fragment containing a part of exon 2 and extending through intron 7 of the gene was inserted at the XhoI site. The vector was linearized at NotI and used for electroporation into R1 embryonic stem cells (129SvJ origin) by the Transgenic Facility of the Duke Comprehensive Cancer Center (Durham, NC). The disrupted allele was confirmed by Southern-blot analysis with a radiolabelled PCR-amplified DNA fragment from exon 8 to exon 10. To stabilize the genetic background, heterozygous mice were backcrossed with C57BL/6J WT mice for 6 generations, in order to produce a background >99% similar to the genetic background of a C57BL/6J animal (370). Homozygous pairs allowed congenic lines of knockout and WT littermate animals

to propagate. Throughout the rest of this thesis, *pdhk4* deficient mice will simply be referred to as "PDHK4-/-".

Diet Induced Obesity Feeding Protocol

Mice were placed on either standard laboratory chow (4% kcal from lard), or a diet rich in fat (60% kcal from lard, Research Diets, D12492) to induce weight gain and eventual obesity. With our experiences, animals experience a significant increase in body weight after 1-2 wks of diet, and became glucose intolerant and insulin resistant after 8-10 wks of diet. Depending on the study involved, animals were either placed on the high fat diet for either 1, 3, 10, 12, 13, or 16 wks total duration.

Glucose/Insulin Tolerance Testing and Assessment of the Insulin Signaling Pathway

Glucose tolerance and insulin tolerance tests (GTT/ITT) were performed either 6 hr after food withdrawal or after overnight food withdrawal using glucose and insulin doses of 1 or 2 g/kg, and 0.3 or 0.7 U/kg, intraperitoneal (IP) injection, respectively. Blood glucose measurements were performed via tail bleed with the Accu Check Advantage system (Roche®) at 0, 20, 30, 60, 90, and/or 120 min post-glucose/insulin injection. To assess the status of the insulin-signaling pathway, mice were fasted for 6 hr or overnight, respectively, and injected IP with insulin doses of 0.3 U/kg or 0.7 U/kg, respectively. At 30 min post-insulin injection, animals were sacrificed and gastrocnemius muscle was isolated and

harvested in the appropriate conditions for immunoblot assessment of proteins involved in the insulin-signaling pathway (See below).

Meal Tolerance Testing

Meal tolerance tests were performed in animals fasted overnight via supplementation of a 5 g pellet of standard laboratory animal chow. Blood glucose measurements were performed via tail bleed with the Accu Check Advantage system (Roche®) at 0, 30, 60, and 90 min post-pellet consumption. Plasma was also collected at the 0, 30 and 60 min time points in EGTA coated tubes (Sarstedt).

Exercise Tolerance Testing

Exercise tolerance was performed by running animals on a calibrated, motor-driven treadmill (Columbus Instruments) at a speed of 3 m/min for 1 min, followed by increasing speeds of 4 m/min for 1 min, 5 m/min for 1 min, 6 m/min for 3 min, 8 m/min for 14 min, 9 m/min for 10 min, 10 m/min for 7 min, 12 m/min for 7 min, and 14 m/min until exhaustion. The first 6 min were used as an acclimatization period for the animals to become familiar with the treadmill and not used for data collection. Exhaustion was determined as the animal spending >5 consecutive sec on the shock grid, or the animal running off the shock grid and immediately falling back onto the shock grid 3 consecutive times.

Whole Body *In Vivo* Metabolic Assessment

In vivo metabolic assessment via indirect calorimetry was performed using the Oxymax CLAMS (Columbus Instruments). Animals were initially acclimatized in the system for a 24 hr period, the subsequent 24 hr period was utilized for data collection. The following equations were used to calculate oxygen consumption (VO_2) and carbon dioxide production (VCO_2). The oxygen consumption was calculated by taking the difference between the input oxygen flow and the output oxygen flow. Similarly, the carbon dioxide production was calculated by taking the difference between the output and input carbon dioxide flows. Standard conversion factors were included in the calculation to result with the units selected in the Software Configuration.

$VO_2 = V_i O_{2i} - V_o O_{2o}$

V_i and V_o are the input and output ventilation rates (litres per minute, LPM)
O_{2i} and O_{2o} are oxygen fractions at the input and output

$VCO_2 = V_o CO_{2o} - V_i CO_{2i}$

V_i and V_o are the input and output ventilation rates (LPM)
CO_{2i} and CO_{2o} are carbon dioxide fractions at the input and output

The respiratory exchange ratio (RER) was simply the ratio between the carbon dioxide production and the oxygen consumption. This value is a ratio and thus does not have a unit. The RER ratio was calculated before any units conversion, weight normalization, or effective mass correction.

$$RER = VCO_2/VO_2$$

To calculate heat, oxymax determines the calorific value (CV) based on the observed RER. This calorific value was then used with the observed VO_2 to calculate heat. The equations are:

$$\text{Heat} = CV \times VO_2$$

$$CV = 3.815 + 1.232 \times \text{RER}$$

Ultrasound Echocardiography

In vivo cardiac function (ejection fraction [EF], fractional shortening [FS], tei index) and M-mode ventricular wall measurements (LV wall thickness and diameters) were assessed in isoflurane anaesthetized mice with a Vevo 770 high-resolution echocardiography imaging system equipped with a 30-MHz transducer (RMV-707B; VisualSonics, Toronto, Canada) as previously described (95).

EF was calculated with the following equation;

((LV end diastolic volume [LVEDV] – LV end systolic volume [LVESV]) / LVEDV)

x 100 = % EF

FS was calculated with the following equation;

((LV end diastolic dimensions [LVEDD] – LV end systolic dimensions [LVESD]) / LVEDD) x 100 = % FS

Tei index was calculated with the following equation;

(isovolumic contraction time + isovolumic relaxation time) / ejection time

Isovolumic relaxation time and deceleration time of the early (E) filling wave were determined with pulsed-wave Tissue Doppler. Isovolumic relaxation time was calculated as the time from aortic valve closure to initiation of the E wave (in msec). The deceleration of the E wave was determined by measuring in time (msec) required for the downslope of the peak of the E wave to reach the baseline.

Isolated Working Mouse Heart

Mouse hearts were perfused in the working perfused mode as previously described (28, 216). Strain of mice and any genetic modification are described in the individual chapters. Mice were anaesthetized with sodium pentobarbital (60 mg/kg IP), and the hearts were subsequently excised and immersed in ice-cold Krebs-Henseleit bicarbonate solution (118 mM NaCl, 25 mM $NaHCO_3$, 5.9 mM KCl, 5 mM EDTA pH = 7.4, 1.2 mM $MgSO_4 \bullet 7H_2O$, 2.5 mM $CaCl_2 \bullet 2H_2O$ and 5 mM glucose). The aorta was cannulated and perfused with Krebs-Henseleit solution (37°C) initiated at a hydrostatic pressure of 60 mmHg. Hearts were trimmed of excess tissue and the opening to the left atrium was cannulated. After equilibration in the Langendorff mode, hearts were switched to the working mode by clamping off the aortic inflow line from the Langendorff reservoir and opening the left atrial inflow line. Oxygenated Krebs-Henseleit solution consisting of 0

mM (No Fat), 0.4 mM (Normal Fat) or 0.8/1.2 mM (High Fat) palmitate bound to 3% fatty acid free bovine serum albumin (BSA, palmitate was pre-bound to the albumin as described previously (28)), 5 mM glucose, in the presence or absence of 100 μU/mL insulin was delivered to the left atrium at a preload pressure of 11.5 mmHg. Perfusate was ejected from spontaneously beating hearts into a compliance chamber and into the aortic outflow line against a hydrostatic afterload pressure of 50 mmHg. The perfusate was recirculated, and pH was adjusted to 7.4 by gassing the perfusate in a glass oxygenator with a gas mixture containing 95% O_2 and 5% CO_2. At the end of perfusion, hearts were immediately frozen in liquid N_2 with Wollenberger tongs, and stored at -80°C.

Mechanical Function Measurements in Isolated Working Mouse Hearts

Heart rate and aortic pressure (mmHg) were measured with a Gould P21 pressure transducer (Harvard Apparatus) connected to the aortic outflow line. Cardiac output and aortic flow (mL/min) were measured with Transonic T206 ultrasonic flow probes in the preload and afterload lines, respectively. Coronary flow (mL/min) was calculated as the difference between cardiac output and aortic flow. Cardiac power was calculated as the product of cardiac output times LV developed pressure (aortic systolic pressure minus preload pressure). Data were collected utilizing an MP100 system from AcqKnowledge (BIOPAC Systems, Inc USA).

Measurement of Glycolysis, Glucose, and Palmitate Oxidation

Glycolysis, glucose, lactate, and palmitate oxidation were measured by perfusing hearts with [5-^{3}H/U-^{14}C]glucose, and [9,10-^{3}H]palmitate, respectively (28, 230, 233). The total myocardial $^{3}H_2O$ production and $^{14}CO_2$ production were determined at 10 min intervals during the 40 or 60 min aerobic perfusion period. To measure the rates of glycolysis and palmitate from ^{3}H substrate, $^{3}H_2O$ in perfusate samples was separated from [^{3}H]glucose and [^{3}H]palmitate utilizing a vapor transfer method as previously described (28, 230, 233). This method involves adding 500 μL of water into a 5 mL scintillation vial, then placing a lidless 1.5mL microcentrifuge tube inside the scintillation vial. A 200 μL perfusate sample was then added to the microcentrifuge tube, and the scintillation vial capped. Scintillation vials were then stored initially at 50°C for 24 hr and then at 4°C for 24 hr. Following storage, the microcentrifuge tube was removed, scintillation fluid (Ecolite, ICN) was added and the vials were counted for radioactivity in a liquid scintillation counter. Glucose oxidation rates were determined by quantitative measurement of $^{14}CO_2$ production including $^{14}CO_2$ released as a gas in the oxygenation chamber and $^{14}CO_2$ dissolved as $H^{14}CO_3^-$ in perfusate. The gaseous $^{14}CO_2$, which exits the perfusion system via an exhaust line, was trapped in hyamine hydroxide solution. The dissolved $^{14}CO_2$ as $H^{14}CO_3^-$ was released and trapped on filter paper saturated with hyamine hydroxide in the central well of 25 mL stoppered flasks after perfusate samples were acidified by the addition of 1 mL of 9*N* H_2SO_4 (28).

Calculation of Proton Production from Glucose Utilization

If glucose passes through glycolysis to lactate and the ATP formed is hydrolyzed, a net production of 2 H^+ per molecule of glucose occurs (233, 237). In contrast, if glycolysis is coupled to glucose oxidation, the net production of H^+ is zero. Therefore, subtracting the rate of glucose oxidation from the rate of glycolysis and multiplying by 2 determines the overall rate of H^+ production derived from glucose utilization. This calculation of H^+ production has been validated, whereby in a previous study in isolated working rat hearts utilizing a similar metabolic approach, the pH_i determination using ^{31}P NMR correlated well with their calculated values (233).

Calculation of Tricarboxylic Acid Cycle Activity and ATP Production

TCA cycle activity was calculated from the rates of palmitate oxidation and glucose oxidation based on the oxidation of 1 mole of glucose producing 2 moles of acetyl CoA and 1 mole of palmitate producing 8 moles of acetyl CoA. ATP production was calculated from rates of glycolysis, glucose and palmitate oxidation based on 1 mole of glucose producing 2 moles of ATP in glycolysis and 31 moles of ATP in glucose oxidation, and 1 mole of palmitate producing 104 moles of ATP.

In Vivo Ischemia/Reperfusion Injury via Ligation of the Left Anterior Descending Coronary Artery in the Mouse

12 – 16-wk-old mice were anaesthetized with an IP injection of somnotol (60 mg/kg). Once surgical anaesthesia is achieved (animal showing no signs of reflex via the toe pinch method), a left thoracotomy was performed and the ribs were spread apart to expose the left ventricle. Ischemia was induced by ligating the left anterior descending coronary artery (LAD) with a 7-0 polyprolene suture against a 2-0 silk suture (Figure 2-1). After 30 min of ischemia, the 7-0 suture was released to induce reperfusion. After 24 hr of reperfusion, animals were euthanized via IP injection of sodium pentobarbital (12 mg), and hearts were immediately excised and isolated for infarct size determination.

Infarct Size Assessment

Hearts were excised from euthanized animals and immediately hung on a Langendorff apparatus. The LAD was reoccluded and perfused retrogradely through the aorta with Evans blue dye to delineate the area at risk (AAR). The heart was frozen at -20°C for 30 min and sectioned into slices that were incubated for 10 min in 1% triphenyltetrazoliumchloride (TTC) at 37°C. Slices were left in 10% formaldehyde overnight to enhance color contrast and photographed. Dead cells lack viable mitochondria and are unable to oxidize TTC, and therefore stain white. The viable cells in the AAR stain red/pink due to lack of flow, whereas the non-ischemic viable myocardium stains an intense blue as a result of the Evans

blue. Photographs of heart slices were analyzed by planimetry with ImageJ to quantify infarct size.

Area at Risk Isolation

In another set of experiments, 12 – 16-wk-old mice underwent our *in vivo* I/R protocol, but were euthanized at 30 min of reperfusion. Hearts were immediately excised, hung on a Langendorff apparatus, and their LAD was reoccluded to determine the AAR via retrograde perfusion of the aorta with Evans Blue dye. The heart was frozen in liquid N_2 cooled isopentane for 1 min and subsequently sectioned. The AAR was isolated and dissected from the viable myocardium and both fractions stored at -80°C.

Tissue Analysis

Frozen tissue (ventricular, gastrocnemius, liver) was powdered in a mortar and pestle cooled to the temperature of liquid N_2. A portion of the powdered tissue was used to determine the dry weight to wet weight ratio. For the heart, the atrial tissue remaining on the cannula was removed, dried in an over for 24 hr at 100°C and weighed. The dried atrial weight, frozen ventricular weight and the ventricular dry to wet ratio were used to calculate the total dry weight of the heart.

Pyruvate Dehydrogenase Activity Assay

PDH activities were measured using a revised protocol based on the radiometric assay described by Constantin-Teodosiu *et al.* (76). Briefly, for

measurement of active PDH, frozen myocardial or gastrocnemius muscle tissue was homogenized in buffer containing 200 mM sucrose, 50 mM KCl, 5 mM EGTA, 50 mM Tris HCl, 50 mM NaF, 50 mM sodium pyrophosphate (NaPPi), 5 mM dichloroacetate (DCA), and 0.1% Triton X-100 (pH 7.8). For assay of "total" PDC activity (dephosphorylated), frozen tissue was homogenized in buffer containing 1 mM $CaCl_2$ but in the absence of NaF, NaPPi, and EGTA. The total PDH samples were incubated in 0.8 mM $MgCl_2$ at 37°C for 20 min. Both active and total samples were then incubated in assay buffer (150 mM Tris · HCl, 0.75 mM EDTA, 0.75 mM NADH, 1.5 mM thiamine pyrophosphate, 5 mM EGTA, 5 mM DCA, and 0.75 mM CoA), and the reaction was initiated by the addition of pyruvate. The reaction was terminated by perchloric acid. Samples were neutralized and centrifuged, and the resulting supernatant was used for determination of acetyl CoA content. Acetyl CoA was converted to [^{14}C]citrate and separated from unreacted radioactivity using Dowex resin (50WX8, 100–200 mesh). The amount of acetyl CoA was quantified by comparison of acetyl CoA standard curves run in parallel in each experiment.

5'AMP Activated Protein Kinase Activity Assay

AMPK activity was assayed by following the incorporation of [^{32}P]phosphate into a pseudo-substrate AMARA peptide (AMARAASAAALARRR) as previously described (10). The assay was performed in 25 μL of assay buffer containing 40 mM HEPES-NaOH (pH = 7.0), 80 mM NaCl, 1 mM EDTA, 0.02% (w/v) Brij-35, 1 mM DTT, 200 μM ATP, 5

mM $MgCl_2$, phosphatase inhibitors and protease inhibitors. The assay was performed at 30°C for 5 min and was terminated by the addition of H_3PO_4 (1% (v/v), final concentration). 15 μL aliquots were removed and spotted on a Unifilter P81 96-well filterplate. Each well was then washed 10x with 300 μL of 1% (v/v) H_3PO_4, and 2x with methanol. The filterplate was dried, and 50 μL of MicroScint PS scintillant was added to each well and radioactivity was subsequently counted in a Wallac MicroBeta Trilux scintillation counter.

Citrate Synthase Activity Assay

Frozen myocardial or gastrocnemius tissue (5 – 10 mg) was homogenized in buffer containing 50 mM Tris HCl (pH 8 at 4°C), 1 mM EDTA, 10% glycerol (w/v), 0.02% Brij-35 (w/v), 1 mM dithiothreitol (DTT), protease and phosphatase inhibitors (Sigma). After homogenization for 30 sec, the homogenate was left on ice for 10 min before centrifugation at 10,000 x *g* for 20 min. The resulting supernatant was brought to a final dilution of 1/50, and 2 μL of each sample was pipetted into a 96 well plate. Each well was brought to a final volume of 190 μL with 184 μL of assay buffer (100 mM Tris HCl, 1 mM EDTA, 1 mM $MgCl_2$), 2 μL of 5,5'-dithiobis-(2-nitrobenzic acid) (DNTB), and 2 μL of 30 mM acetyl CoA. The reaction was then initiated by the addition of 10 μL of 10 mM oxaloacetic acid and the reaction mixture has its absorbance followed at a 412 nM wavelength for a 2 min duration (readings taken in 30 sec intervals) with a spectrophotometer kinetic plate reader. The 96 well plate was read at a 412 nM wavelength for a 2 min duration as well before the addition of oxaloacetic acid in

order to obtain a baseline reading. The final reading was multiplied by 60 to obtain a rate per min, and citrate synthase (CS) activity in "μmol/min/g wet weight" was calculated with the following equation;

($\Delta Absorbance_{412}$/min x 0.2 mL (volume of reaction)) / (13.6 (ε for DNTB) x 0.552 (pathlength for 96 well plate) x 0.02 (mg of tissue in reaction))

β-Hydroxyacyl CoA Dehydrogenase Activity Assay

Frozen myocardial or gastrocnemius tissue (5 – 10 mg) was homogenized in buffer containing 50 mM Tris HCl (pH 8 at 4°C), 1 mM EDTA, 10% glycerol (w/v), 0.02% Brij-35 (w/v), 1 mM DTT, protease and phosphatase inhibitors (Sigma). After homogenization for 30 sec, the homogenate was left on ice for 10 min before centrifugation at 10,000 x *g* for 20 min. The resulting supernatant was brought to a final dilution of 1/20, and 10 μL of each sample was pipetted into a 96 well plate. Each well was brought to a final volume of 190 μL with 160 μL of 50 mM imidazole (pH 7.4) and 20 μL of 1.5 mM NADH. The reaction was then initiated by the addition of 10 μL of 2 mM acetoacetyl CoA and the reaction mixture has its absorbance followed at a 340 nM wavelength for a 5 min duration (readings taken in 30 sec intervals) with a spectrophotometer kinetic plate reader. The 96 well plate was read at a 340 nM wavelength for a 5 min duration as well before the addition of acetoacetyl CoA in order to obtain a baseline reading. The final reading was multiplied by 60 to obtain a rate per min, and β-hydroxyacyl

CoA Dehydrogenase (βHAD) activity in "μmol/min/g wet weight" was calculated with the following equation;

($\Delta Absorbance_{340}$/min x 0.2 mL (volume of reaction)) / (6.22 (ε for NADH disappearance) x 0.552 (pathlength for 96 well plate) x 0.4 (mg of tissue in reaction))

Metabolic Profiling

Metabolic profiling of tissues (i.e. gastrocnemius) involved quantitation by gas chromatography – mass spectrometry (GC/MS) based on dilution of stable-isotope-labeled internal standards (D3-C14:0, D3-C16:0, D3-C18:0, and 13C1-C18:1; CDN isotopes, Pointe-Claire, Quebec, and Isotec, St. Louis, MO), using a Trace Ultra GC coupled to a Trace DSQ MS (Thermo Fisher Scientific, Austin, TX). Acylcarnitine measurements were made using flow injection tandem MS of samples (~20 mg of tissue) homogenized in 20-fold volume of deionized H_2O as previously described (12). Data were acquired using a Micromass Quattro MicroTM system equipped with a model 2777 autosampler, a model 1525 high performance liquid chromatography (HPLC) solvent delivery system and a data system controlled by MassLynx 4.0 operating system (Waters, Millford, MA). The remaining lysate from the acylcarnitine preparation was subjected to 1 freeze-fracture cycle in liquid N_2, immediately thawed at room temperature and sonicated with a small pencil-tip probe at ~3 watts for 5 sec. The sonicated lysate was then centrifuged at 14,000 x *g* for 15 min at 4°C, and organic acids were

quantified from the resulting supernatant using methods previously described (176) employing Trace Ultra GC coupled to Trace DSQ MS operating under Excalibur 1.4 (Thermo Fisher Scientific, Austin, TX).

Measurement of Adenine Nucleotides and Short Chain CoA esters

Approximately 30 mg of frozen ventricular tissue was homogenized for 30 sec utilizing a Polytron® Homogenizer in 300 μL of 6% (v/v) perchloric acid and 2 mM DTT. After homogenization the samples were left on ice for 30 min and then centrifuged at 12,000 x *g* for 5 min. The resultant supernatant was split, half was ready for analysis of short chain CoA esters by HPLC (193) and the remaining supernatant required further processing for measurement of adenine nucleotides. EGTA was added until a final concentration of 0.5 mM was reached, and the samples were then titrated to a pH to 7.6 – 7.8 using 0.5 M K_2CO_3, to ensure stability of the adenine nucleotides. Samples were left on ice for 10 min and then centrifuged at 10,000 x *g* for 2 min and the resultant supernatant was left on ice for ~ 3 – 4 hr before HPLC analysis (9).

For short chain CoA ester analysis, 100 μL of each sample was run through a Nova-Pak C18 precolumn and an Adsorbosphere C18 column on a Beckman System Gold HPLC. Flow rate was set at 1 mL/min and analyte detection occurred at an absorbance of 254 nm on a Beckman System Gold model 168 diode array detector. The mobile phase consisted of a mixture of buffer A (0.2 M NaH_2PO_4, pH = 5.0) and buffer B (0.25 M NaH_2PO_4 and acetonitrile, pH 5.0). The gradient elution profile consisted of the following, 0 – 2.5 min, 97% A

3% B; 2.5 – 7.5 min, 97% A 3% B to 82% A 18% B; 7.5 – 15 min, 82% A 18% B; 15 – 18 min, 82% A 18% B to 63% A 37% B; 18 – 35 min, 63% A 37% B to 10% A 90% B; 35 – 42 min, 10% A 90% B. Peaks were integrated utilizing the Beckman System Gold software package.

For adenine nucleotide analysis, 100 μL of each sample was run through a Supelcosil™ LC-18-T guard cartridge and a Supelcosil™ LC-18-T column on a Beckman System Gold HPLC. Flow rate was set at 1.5 mL/min and analyte detection occurred at an absorbance of 260 nm on a Beckman System Gold model 168 diode array detector. The mobile phase consisted of buffer A (35 mM K_2HPO_4, 6 mM tetrabutylammoniumhydrogensulfate, pH = 6.0) and buffer B (a mixture of buffer A and acetonitrile in a ratio of 1:1 (v/v)). The gradient elution profile consisted of the following, 0 – 10 min, 98% A 2% B; 10 – 20 min, 98% A 2% B to 45% A 55% B using Beckman's curve number 3; 20 – 25 min, 45% A 55% B. Peaks were integrated utilizing the Beckman System Gold software.

Measurement of Long Chain Acyl CoA Esters

Approximately 5 mg of frozen ventricular tissue was sonicated in 200 μL of cold 100 mM KH_2PO_4 for 20 sec followed by the addition of 200 μL of cold n-propanol and further sonicated for 20 sec. 25 μL of saturated ammonium sulfate and 400 μL of acetonitrile were added successively to the homogenate, and vortexed for 5 min and centrifuged at 2,100 x *g*. The top layer was transferred to a microcentrifuge tube and evaporated under N_2 gas. The solid residue was mixed with 100 μL of 0.5 M chloroacetaldehyde reagent and then centrifuged at 21,000

x *g* for 5 min to form acyl etheno-CoA esters. The resultant supernatant was then heated at 85°C for 20 min and stored at -20°C until HPLC analysis (86).

5 to 20 μL of sample was run through a C18 Guard Cartridge and a Luna column of phenylhexyl coated silica particles maintained at 40°C on a Beckman System Gold HPLC. Flow rate was set at 0.4 mL/min and the analyte was detected utilizing a Perkin Elmer LS-5 fluorescence spectrophotometer with an excitation wavelength of 230 nm and an emission wavelength of 420 nm. The mobile phase consisted of buffer A (90% (v/v) acetonitrile, 1% (v/v) acetic acid) and buffer B (90% (v/v) acetonitrile). The gradient elution profile consisted of the following, 0 – 30 min, 80% A 20% B to 65% A 35% B; 30 – 40 min, 65% A 35% B; 40 – 42 min, 65% A 35% C to 100% B; 42 – 47 min, 100% B (217). Peaks were integrated utilizing the Beckman System Gold software.

Measurement of Triacylglycerol

To determine TAG content, ~20 mg of frozen tissue (i.e. gastrocnemius) was extracted in a 20-fold volume of 2:1 chloroform-methanol, following which 0.2 volumes of methanol was added and the following mixture vortexed for 30 sec. The mixture was then centrifuged at 3,500 revolutions per minute (RPM) for 10 min, and the supernatant was collected and volume recorded. 0.2 volumes of 0.04% $CaCl_2$ was then added to the supernatant, which was then centrifuged at 2,400 RPM for 20 min. The upper phase was removed, and the interface washed 3x with pure solvent upper phase consisting of 1.5 mL chloroform, 24.0 mL methanol, and 23.5 mL double distilled H_2O. The final wash was then removed,

and 50 μL of methanol was added to obtain one phase. The samples were finally dried under N_2 gas at 60°C and redissolved in 50 μL of 3:2 *tert*-butyl alcohol-Triton X-100. Tissue TAG was then quantified colorimetrically with a commercially available enzymatic assay kit (Wako Pure Chemical Industries).

Measurement of Ceramide

Ceramides were extracted as previously described (38). In brief, tissue was extracted with 1 mL of a 1:1:1 chloroform-methanol-1 *N* HCl in the presence of 0.3 mL saline solution. The resulting organic phase was separated and dried under N_2 gas. 0.5 mL of 1 M KOH in 90% (v/v) methanol is added and samples were heated at 90°C for 1 hr to deacylate ceramide into sphingosine. Samples were then extracted with 1 M HCl in methanol, chloroform, and 1 M aqueous NaCl. The resulting organic phase was dried under N_2 gas, redissolved in methanol, and derivatized to *o*-Phthalaldehyde to generate a fluorescent compound that was separated by HPLC and quantified by fluorescence spectrometry.

Measurement of Diacylglycerol

To determine DAG content, ~5 mg of frozen tissue (i.e. gastrocnemius) was homogenized in 0.8 mL of 1 mM NaCl. The homogenate was then transferred over to a 13 x 100 mm test tube and extracted with 3.0 mL of 1:2 chloroform-methanol and mixed. 1 mL of 1 mM NaCl and chloroform was then added to break phases and the resulting sample was centrifuged briefly at 5,000 x

g to separate the organic and aqueous phases. The chloroform phase was then collected and evaporated under N_2 gas. The lipids were then solubilized with a 7.5% octyl-β-D-glucoside/5mM cardiolipin/1mM DETAPAC solution and incubated at room temperature for 5 – 15 min. The sample was then brought to 100 μL volume with 50 μL of 2x reaction buffer, 20 μL 10 mM DTT and 10 μL DAG kinase (0.5 mg/mL). The reaction was initiated by the addition of 10 μL of 10 mM ATP (mixed with [γ-^{32}P]ATP) and incubated for 30 min at 25°C. 3 mL chloroform/methanol (1:2) and 0.7 mL 1% $HClO_4$ was then added to each tube and mixed before the addition of 1 mL chloroform and 1 mL 1% $HClO_4$. The phases were then separated via centrifugation at 2,000 x *g* at 4°C for 5 min. The aqueous phase was discarded and the chloroform phase washed twice with 2 mL of 1% $HClO_4$. The sample was then evaporated under N_2 gas and dissolved in 100 μL of 5% methanol in chloroform. 20 μL of each sample was spotted onto a thin layer chromatography (TLC) plate and activated by acetone (develop with chloroform/methanol/acetic acid (65:15:5)). After TLC plate has ran, the plate was exposed to X-ray film and developed for ~48 hr. Finally, the silicon was scraped off the plate into 5 mL scintillation vials with 4 mL of scintillation solution (Ecolite, ICN) and ^{32}P counted in a liquid scintillation counter.

Plasma Insulin Determination

Plasma insulin concentrations were determined via use of a commercially available enzyme-linked immunosorbent assay kit (Alpco Diagnostics). 5 μL of each sample was added to each well with 75 μL of a provided enzyme conjugate,

and the 96 well plate was then incubated for 2 hr at room temperature on an orbital microplate shaker at ~700-900 RPM. After incubation, the plate was washed 6x with a provided working strength wash buffer, and then 100 μL of a provided substrate was added to each well to start the reaction, which was terminated after 30 min via addition of 100 μL of stop solution. Any air bubbles were removed and plasma insulin levels "ng/mL" were determined via reading the absorbance of the plate at a wavelength of 450 nm.

Whole Cell Homogenate Preparation and Immunoblot Analysis

Frozen myocardial or gastrocnemius tissue (25-30 mg) was homogenized in buffer containing 50 mM Tris HCl (pH 8 at 4°C), 1 mM EDTA, 10% glycerol (w/v), 0.02% Brij-35 (w/v), 1 mM DTT, protease and phosphatase inhibitors (Sigma). After homogenization for 30 sec, the homogenate was left on ice for 10 min before centrifugation at 10,000 x *g* for 20 min. The resulting supernatant was processed for immunoblotting. Protein concentration of homogenates was determined via Bradford protein assay kit (Bio-Rad). Samples (20 μg protein each) were resolved via 8% sodium dodecyl sulfate polyacrylamide gel electrophoresis (SDS-PAGE) and transferred onto a 0.45 μm nitrocellulose membrane. Membranes were blocked with 10% fat free milk for 2 hr and probed with either anti-AMPK (Cell Signaling Technologies, 1/1000 dilution), anti-phosphoThreonine-172 AMPK (Cell Signaling Technologies, 1/500 dilution), anti-Akt (Cell Signaling Technologies, 1/1000 dilution), anti-phosphoSerine-473 Akt (Cell Signaling Technologies, 1/500 dilution), anti-GSK3β (Cell Signaling

Technologies, 1/1000 dilution), anti-phosphoSerine-9 GSK3β (Cell Signaling Technologies, 1/500 dilution), anti-p38 mitogen activated protein kinase (MAPK) (Cell Signaling Technologies, 1/1000 dilution), anti-phosphoThreonine-180 p38 MAPK (Cell Signaling Technologies, 1/500 dilution), anti-Jun-N terminal kinase (JNK) (Cell Signaling Technologies, 1/1000 dilution), anti-phosphoThreonine-180 JNK (Cell Signaling Technologies, 1/500 dilution), anti-PDH (Cell Signaling Technologies, 1/500 dilution), anti-phosphoSerine-293 PDH (Calbiochem, 1/1000 dilution), anti-PDHK4 (Abgent, 1/200 dilution), anti-peroxisome proliferator-activated receptor-γ coactivator 1α (PGC1α) (Santa Cruz Biotechnology, 1/200 dilution), or anti-actin (Santa Cruz Biotechnology, 1/200 dilution, 1/1000 dilution) antibodies in 5% fatty acid free BSA. Membranes were then washed with 1x phosphate buffered saline and subsequently probed with goat anti-rabbit (Santa Cruz Biotechnology, 1/2000 dilution) secondary antibody in 1% fat-free milk. Immunoblots were visualized with the enhanced chemiluminescence Western blot detection kit (Perkin Elmer) and quantified with Quantity One (4.4.0) Software (Bio-Rad Laboratories).

Statistical Analysis

All values are presented as mean ± standard error (SE) (*n* observations). The significance of differences was determined by the use of an unpaired, two-tailed Student's *t*-test, two-way analysis of variance (ANOVA), or a one-way ANOVA followed by a Bonferroni post-hoc analysis where appropriate. Differences were considered significant when $P < 0.05$.

Figure 2-1: *In vivo model of ischemia/reperfusion.*

A: Image depicts the exposure of the left ventricle following left thoracotomy and spreading of the ribs. The arrow head depicts the LAD located beneath the left atrial appendage. B: A 7-0 polyprolene suture is threaded beneath the LAD, and C: Tied against a 2-0 silk suture to induce ischemia, which is clearly indicated by the appearance of a pale/pink color in the left ventricle.

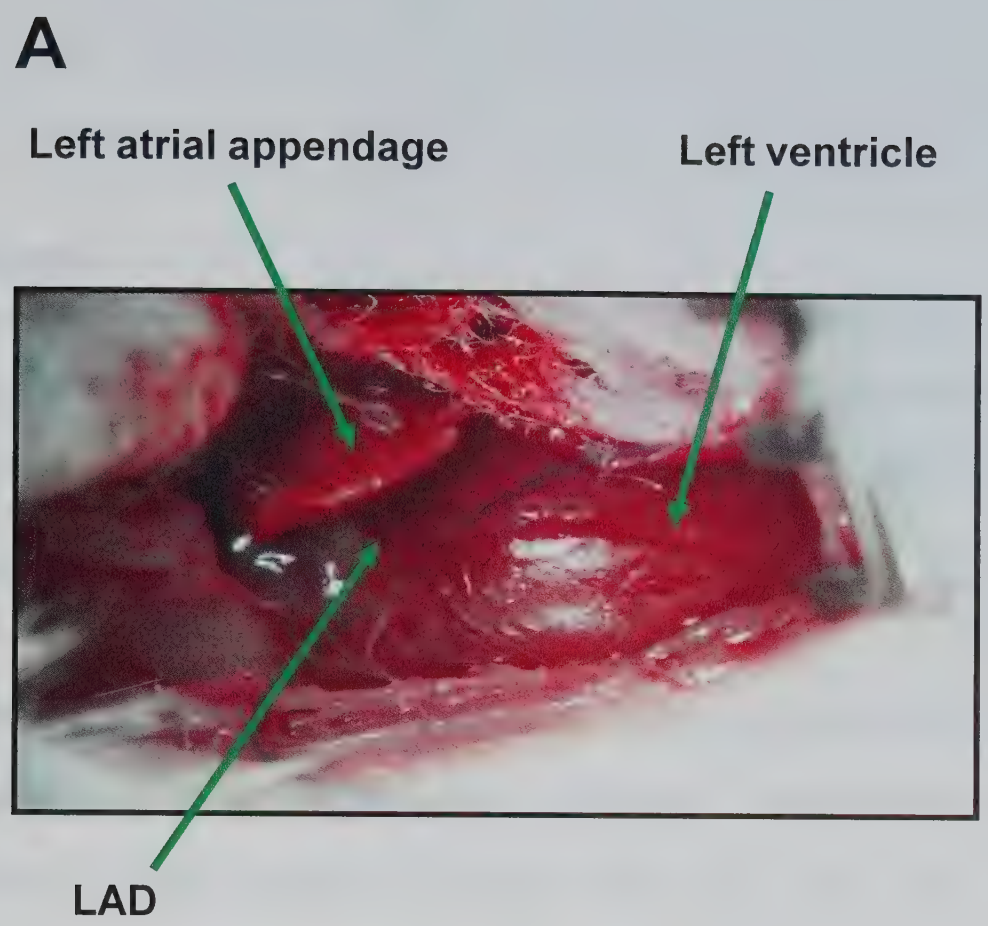

FIGURE 2-1

CHAPTER 3.

Evidence for the Randle Cycle in skeletal muscle: Short term high fat feeding and fasting lead to an impairment in muscle pyruvate dehydrogenase activity

---

My role in this work involved performing all experiments (except those noted below), as well as the writing of the manuscript. Panakkezhum Thomas performed the HPLC analysis of the long chain acyl CoA, Liyan Zhang performed the gastrocnemius PDH activity measurements, and Wendy Keung determined the intramyocellular DAG and ceramide content.

Manuscript Status: This manuscript is currently in preparation to be submitted to the *Journal of Biological Chemistry* for publication as an original article.

CHAPTER 3.

Evidence for the Randle Cycle in skeletal muscle: Short term high fat feeding and fasting lead to an impairment in muscle pyruvate dehydrogenase activity

Abstract

Objective – Increasing fatty acid oxidation results in a reciprocal decrease in glucose oxidation, a phenomenon coined the "Randle Cycle". It has been postulated that the Randle Cycle does not operate in skeletal muscle, thus accelerating fatty acid oxidation can ameliorate insulin resistance by decreasing the accumulation of lipid metabolites, such as ceramide, without any negative consequences on glucose metabolism. Our aim was to determine if the Randle Cycle is operative or not in muscle.

Materials and Methods – C57BL/6 mice were fed a low/high fat diet for 1 or 3 wks, or fasted for 6 hr before sacrifice. Insulin resistance was assessed via insulin tolerance testing, while pyruvate dehydrogenase (PDH) activity and lipid metabolites were assessed in gastrocnemius muscles.

Results – Both 1 and 3 wks of high fat feeding, as well as fasting, result in an inhibition of PDH activity. This inhibition of PDH activity was not accompanied by an accumulation of intramyocellular lipid metabolites at 1 wk of high fat feeding, but an increase in long chain acyl CoA (0.56 ± 0.07 vs. 1.21 ± 0.20 nmol/g wet weight) and ceramide (40.7 ± 3.2 vs. 67.5 ± 5.2 nmol/g wet weight) at

3 wks of high fat feeding. Despite this inhibition of PDH activity, short term high fat feeding did not cause insulin resistance.

Conclusions – Our data reveal that both short-term high fat feeding and fasting of mice inhibits muscle PDH activity, an important component of the Randle Cycle, suggesting that the Randle Cycle does operate in skeletal muscle.

Previous studies have postulated that an impairment in skeletal muscle fatty acid oxidation leads to the cytosolic accumulation of intramyocellular fatty acid metabolites, such as TAG, long chain acyl CoA, DAG, or ceramide, which impede insulin signaling and directly contribute towards the development of skeletal muscle insulin resistance (188, 303, 305, 367, 447). As such, it has been proposed that an acceleration of skeletal muscle fatty acid oxidation would prevent the accumulation of these fatty acid metabolites in the cytosol, restoring skeletal muscle insulin signaling and reversing insulin resistance (68, 69, 305, 447).

This hypothesis is in direct contrast to historical work performed by Randle and colleagues in the 1960s (315), whereby increases in fatty acid oxidation inhibition glucose oxidation via an increase in fatty acid byproducts (acetyl CoA, NADH) that inhibit the rate-limiting enzyme of glucose oxidation, PDH (314). The acceleration of fatty acid oxidation also leads to an accumulation of citrate, which inhibits the rate-limiting enzyme of glycolysis, PFK1. Inhibition of PFK1 would lead to an accumulation of gluose-6-phosphate, which subsequently inhibits hexokinase and reduces glucose uptake. This phenomenon has been termed the "Randle Cycle", and based on its discovery it was proposed that an accelerated rates of fatty acid oxidation would decrease glucose metabolism, causing skeletal muscle insulin resistance and eventually, diabetes.

However, recent studies utilizing ^{31}P-MRS by Shulman and colleagues have suggested that the Randle Cycle does not operate in skeletal muscle, (303, 305, 326). It is important to note that these conclusions are based off results showing that levels of glucose-6-phosphate do not accumulate in skeletal muscle exposed to high levels of fatty acids. While this observation could be explained by the suggestion that glycolysis is not inhibited by fatty acids, it could just as easily be explained by a decrease in glucose uptake in muscle exposed to high levels of fatty acids, which would limit the amount of glucose available to form sugar phosphates. Measurement of glucose-6-phosphate via ^{31}P-MRS would also not account for any effects of fatty acids on mitochondrial glucose oxidation, an important aspect of the Randle Cycle.

Indeed, work in the heart suggests that fatty acid inhibition of glucose metabolism is much more potent at the level of PDH and glucose oxidation, as opposed to PFK1 and glycolysis (46, 343). These findings may explain the results of Shulman and colleagues, as they were only investigating one component of the Randle Cycle. Furthermore, recent studies in MCD and PDHK4 deficient mice, both models of reduced fatty acid oxidation and enhanced glucose oxidation, have improved skeletal muscle insulin sensitivity and are protected from obesity-induced insulin resistance (177, 202). Such genetic models support the classic proposal of Randle and colleagues and suggest that the Randle Cycle does operate in skeletal muscle. Downregulation of MCD via siRNA in human skeletal muscle myotubes also shifted metabolism in favor of glucose oxidation independently of the insulin signaling pathway (41). In addition, previous work

in our lab employing the partial fatty acid oxidation inhibitor, ranolazine, resulted in a dramatic switch in substrate oxidation from fatty acids to glucose in perfused isolated epitrochlearis muscle (255).

Our objective was to show that the Randle Cycle at the level of PDH does exist in skeletal muscle. We accomplished this by feeding C57BL/6 mice either a low (4% kcal from lard) or a high fat diet (60% kcal from lard) for 1 or 3 wks before sacrifice and assessment of gastrocnemius PDH activity.

Animal Studies

All animals received care according to the Canadian Council on Animal Care and the University of Alberta Health Sciences Animal Welfare Committee. 12-wk-old C57BL/6 mice were placed on a standard chow/low fat diet (4% kcal from lard) or high fat diet (60% kcal from lard, Research Diets; D12492) for a 1 or 3 wk period. At the end of the diet protocol, animals were sacrificed via IP injection of sodium pentobarbital (12 mg) in the fed state, or after a 6 hr fast, in the middle of the dark cycle. Tissues were excised and immediately frozen in liquid N_2 for biochemical analyses. Protocols for assessment of PDH activity, intramyocellular lipid metabolite accumulation, ITTs, indirect calorimetry, immunoblotting, and statistical analysis are described in **Chapter 2** of this thesis.

Fasting and short-term high fat feeding lead to a reduction in gastrocnemius muscle PDH activity

Fasting mice for a 6 hr period results in a significant increase in gastrocnemius PDHK4 expression (Figure 3-1A), which is associated with a dramatic increase in PDH phosphorylation at the PDHK site, indicative of PDHK4-induced inactivation of PDH activity (Figure 3-1B). Actual measurement of PDH activity also confirms that fasting of mice results in a dramatic inhibition of gastrocnemius PDH activity (Figure 3-1C). In another set of experiments, mice were fed a high fat diet for 1 or 3 wks, and gastrocnemius PDH status was assessed. Our results show that while 1 wk of high fat feeding elevates gastrocnemius PDHK4 expression, 3 wks of high fat feeding does not, though this was likely due to the high variability observed in the 3 wk high fat diet group (Figure 3-1D/G). However, both the 1 and 3 wk high fat diet fed groups show a dramatic increase in gastrocnemius PDH phosphorylation at the PDHK site (Figure 3-1E/H), and actual activity measurements show that high fat feeding impairs gastrocnemius PDH activity (Figure 3-1F/I).

Short-term high fat feeding does not impair insulin sensitivity despite a dramatic shift in substrate preference

Our results show that 3 wks of high fat feeding does not impair whole body insulin sensitivity despite a significant increase in body weight (Table 3-1)

as assessed via insulin tolerance testing (Figure 3-2). However, at 1 wk of high fat feeding we report a shift in whole body substrate utilization as indirect calorimetry revealed a dramatic drop in RER (Figure 3-3A/B), indicating that these animals are relying primarily on fatty acids as an energy substrate. Furthermore, 1 wk of high fat feeding is sufficient to impair metabolic flexibility, as indicated by the lack of a substrate shift in the RER between the dark and light cycle, which is readily apparent in mice fed a low fat diet for 1 wk (Figure 3-3B). Our previous findings have shown that insulin resistance induced by chronic high fat feeding for 12 wks causes an impairment in whole body oxygen consumption rates (unpublished data). In contrast, we report that 1 wk of high fat feeding has no adverse effects on whole body oxygen consumption rates, as well as heat production and animal activity (Figure 3-3C-E).

Short-term high fat feeding or fasting do not impair the insulin signaling pathway at the level of Akt or GSK3

Both 1 and 3 wks of high fat feeding, and fasting for a 6 hr period are insufficient to impair insulin signaling at the level of Akt or GSK3 phosphorylation in gastrocnemius muscle (Figure 3-4A/B). Phosphorylation of AMPK, another protein proposed to be involved in insulin sensitivity in muscle (120, 121), is also unaltered in gastrocnemius muscle of mice fed a high fat diet or subjected to fasting (Figure 3-4C).

Intramyocellular lipid metabolite accumulation in response to short-term high fat feeding or fasting

Our results show that 1 wk of high fat feeding does not result in the accumulation of either TAG, long chain acyl CoA, DAG, or ceramide in mouse gastrocnemius muscle (Figure 4-5A-D). On the other hand, 3 wks of high fat feeding results in the accumulation of gastrocnemius long chain acyl CoA and ceramide, but not TAG or DAG (Figure 4-5E-F). Interestingly, mice subjected to a 6 hr fast experienced an increase in gastrocnemius palmitoyl CoA levels, but no other lipid metabolite (Figure 4-5B/F). Furthermore, mice fed a high fat diet for 1 or 3 wks before the 6 hr fast had a significant accumulation of TAG versus mice that were fed a low fat diet before the fast (Figure 4-5A/E). Last, both DAG and ceramide are decreased in high fat diet fed mice subjected to a 6 hr fast versus their non-fasted counterparts (Figure 4-5D/G/H).

Table 3-1: *Body weight in mice subjected to a short-term high fat diet.*

	1 Wk Low Fat Diet (n=5)	1 Wk High Fat Diet (n=6)	3 Wks Low Fat Diet (n=5)	3 Wks High Fat Diet (n=5)
Body Weight (g)	24.37 ± 0.50	27.08 ± 0.91*	25.49 ± 0.44	34.30 ± 0.53*
Liver Weight (g)	0.88 ± 0.06	1.08 ± 0.04*	0.96 ± 0.04	1.09 ± 0.03*
Epididymal Fat (g)	0.24 ± 0.04	0.64 ± 0.05*	0.29 ± 0.05	1.95 ± 0.07*

Body weight gain and tissue weight in mice following 1 and 3 wks of high fat feeding. Values represent means ± SE. Differences were determined using a two-tailed Student's *t*-test. *$P<0.05$, significantly different from low fat diet counterpart.

Figure 3-1: *Fasting and short-term high fat feeding inhibit gastrocnemius PDH activity.*

A: PDHK4 expression in gastrocnemius muscle of fed and fasted mice. B: PDH phosphorylation at serine 293 in gastrocnemius muscle of fed and fasted mice. C: PDH activity (% active/total) in gastrocnemius muscle of fed and fasted mice. D: PDHK4 expression in gastrocnemius muscle of mice fed a low or high fat diet for 1 wk. E: PDH phosphorylation at serine 293 in gastrocnemius muscle of mice fed a low or high fat diet for 1 wk. F: PDH activity (% active/total) in gastrocnemius muscle of mice fed a low or high fat diet for 1 wk. G: PDHK4 expression in gastrocnemius muscle of mice fed a low or high fat diet for 3 wks. H: PDH phosphorylation at serine 293 in gastrocnemius muscle of mice fed a low or high fat diet for 3 wks. I: PDH activity (% active/total) in gastrocnemius muscle of mice fed a low or high fat diet for 3 wks. Values represent mean ± SE (n = 5-7). Differences were determined using a two-tailed Student's *t*-test. $*P<0.05$, significantly different from low fat fed group.

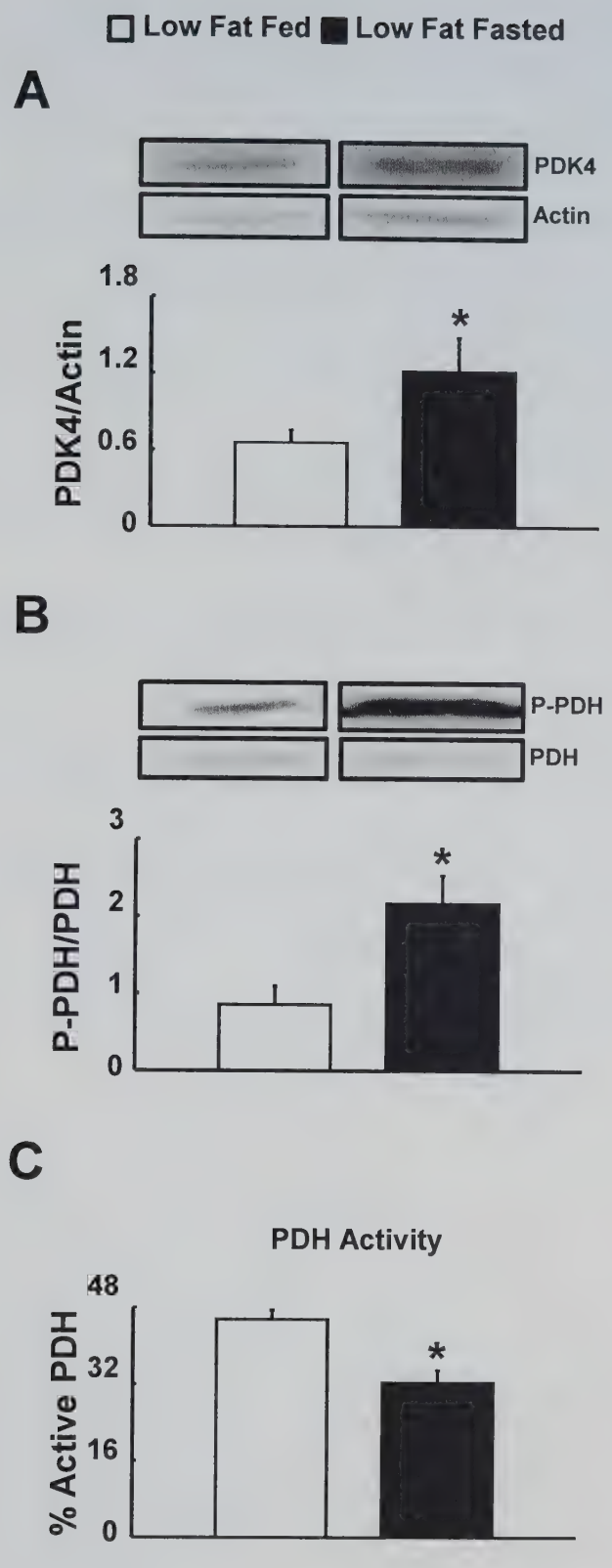
Low Fat Fed
Low Fat Fasted
A
PDK4
Actin
PDK4/Actin
1.8
1.2
0.6
0
*
B
P-PDH
PDH
P-PDH/PDH
3
2
1
0
*
C
PDH Activity
% Active PDH
48
32
16
0
*

FIGURE 3-1

Figure 3-1: *Fasting and short-term high fat feeding inhibit gastrocnemius PDH activity.*

A: PDHK4 expression in gastrocnemius muscle of fed and fasted mice. B: PDH phosphorylation at serine 293 in gastrocnemius muscle of fed and fasted mice. C: PDH activity (% active/total) in gastrocnemius muscle of fed and fasted mice. **D: PDHK4 expression in gastrocnemius muscle of mice fed a low or high fat diet for 1 wk. E: PDH phosphorylation at serine 293 in gastrocnemius muscle of mice fed a low or high fat diet for 1 wk. F: PDH activity (% active/total) in gastrocnemius muscle of mice fed a low or high fat diet for 1 wk.** G: PDHK4 expression in gastrocnemius muscle of mice fed a low or high fat diet for 3 wks. H: PDH phosphorylation at serine 293 in gastrocnemius muscle of mice fed a low or high fat diet for 3 wks. I: PDH activity (% active/total) in gastrocnemius muscle of mice fed a low or high fat diet for 3 wks. Values represent mean ± SE (n = 5-7). Differences were determined using a two-tailed Student's *t*-test. $*P<0.05$, significantly different from low fat fed group.

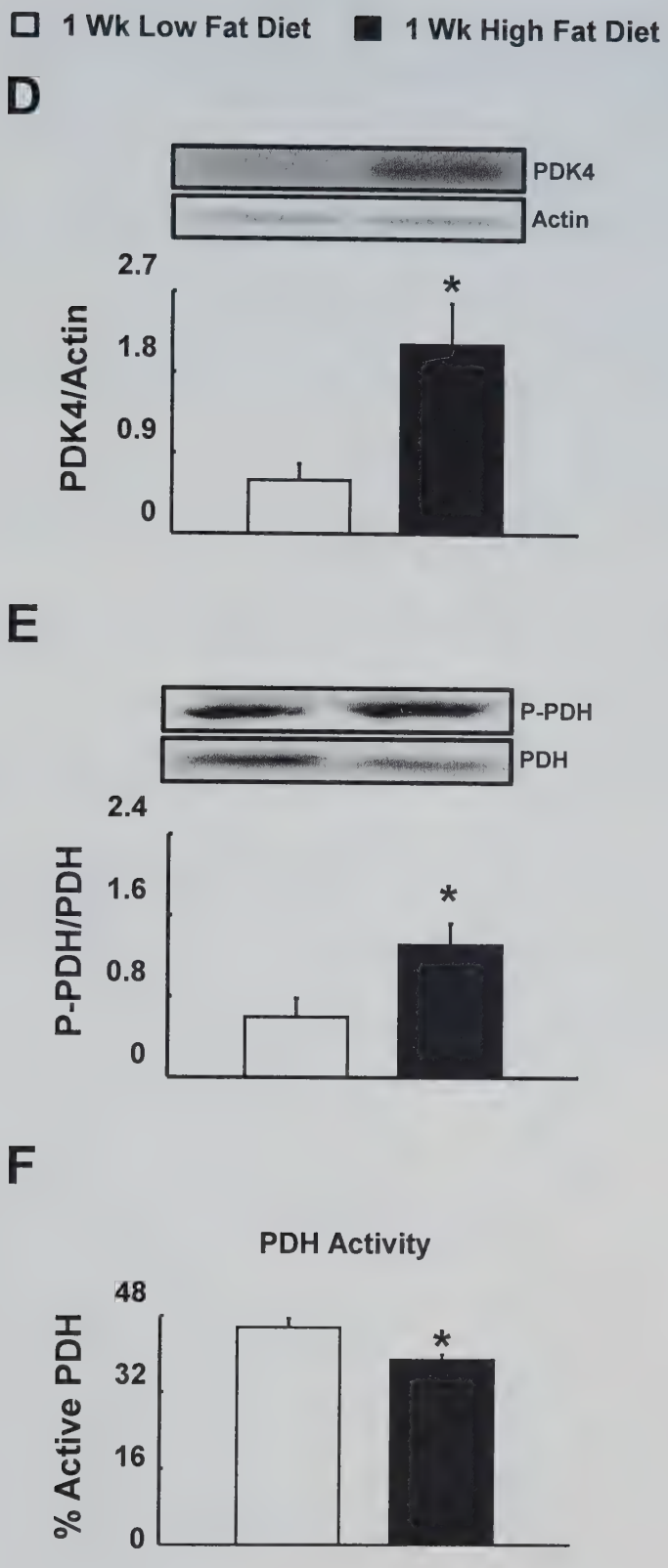
1 Wk Low Fat Diet
1 Wk High Fat Diet
D
PDK4
Actin
2.7
1.8
0.9
0
PDK4/Actin
*
E
P-PDH
PDH
2.4
1.6
0.8
0
P-PDH/PDH
*
F
PDH Activity
48
32
16
0
% Active PDH
*

FIGURE 3-1

Figure 3-1: *Fasting and short-term high fat feeding inhibit gastrocnemius PDH activity.*

A: PDHK4 expression in gastrocnemius muscle of fed and fasted mice. B: PDH phosphorylation at serine 293 in gastrocnemius muscle of fed and fasted mice. C: PDH activity (% active/total) in gastrocnemius muscle of fed and fasted mice. D: PDHK4 expression in gastrocnemius muscle of mice fed a low or high fat diet for 1 wk. E: PDH phosphorylation at serine 293 in gastrocnemius muscle of mice fed a low or high fat diet for 1 wk. F: PDH activity (% active/total) in gastrocnemius muscle of mice fed a low or high fat diet for 1 wk. **G: PDHK4 expression in gastrocnemius muscle of mice fed a low or high fat diet for 3 wks. H: PDH phosphorylation at serine 293 in gastrocnemius muscle of mice fed a low or high fat diet for 3 wks. I: PDH activity (% active/total) in gastrocnemius muscle of mice fed a low or high fat diet for 3 wks.** Values represent mean ± SE (n = 5-7). Differences were determined using a two-tailed Student's *t*-test. **P*<0.05, significantly different from low fat fed group.

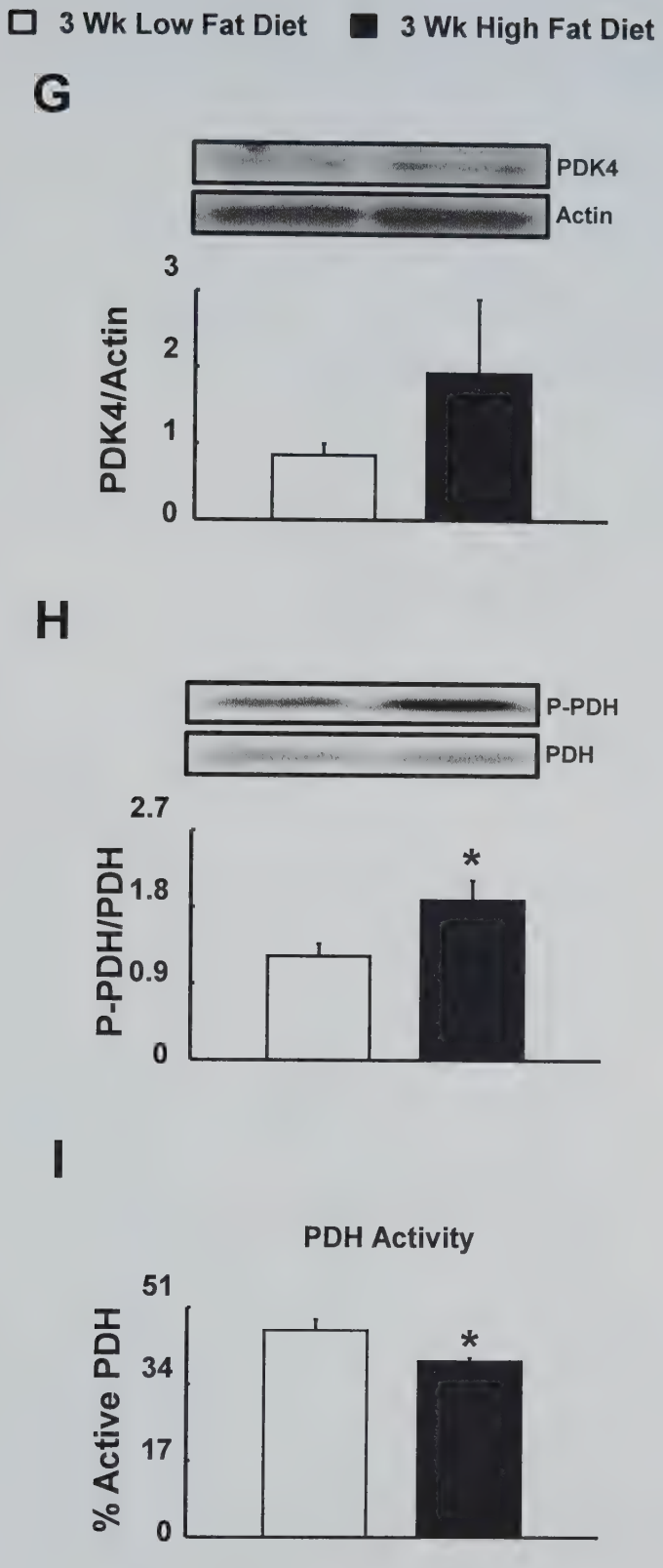
3 Wk Low Fat Diet
3 Wk High Fat Diet
G
PDK4
Actin
PDK4/Actin
3
2
1
0
H
P-PDH
PDH
P-PDH/PDH
2.7
1.8
0.9
0
*
I
PDH Activity
% Active PDH
51
34
17
0
*

FIGURE 3-1

Figure 3-2: *Short-term high fat feeding does not cause insulin resistance in mice.* A: Insulin tolerance test (ITT) in mice fed a low or high fat diet for 3 wks. B: % Change in blood glucose levels during the ITT. Values represent mean ± SE (n = 5).

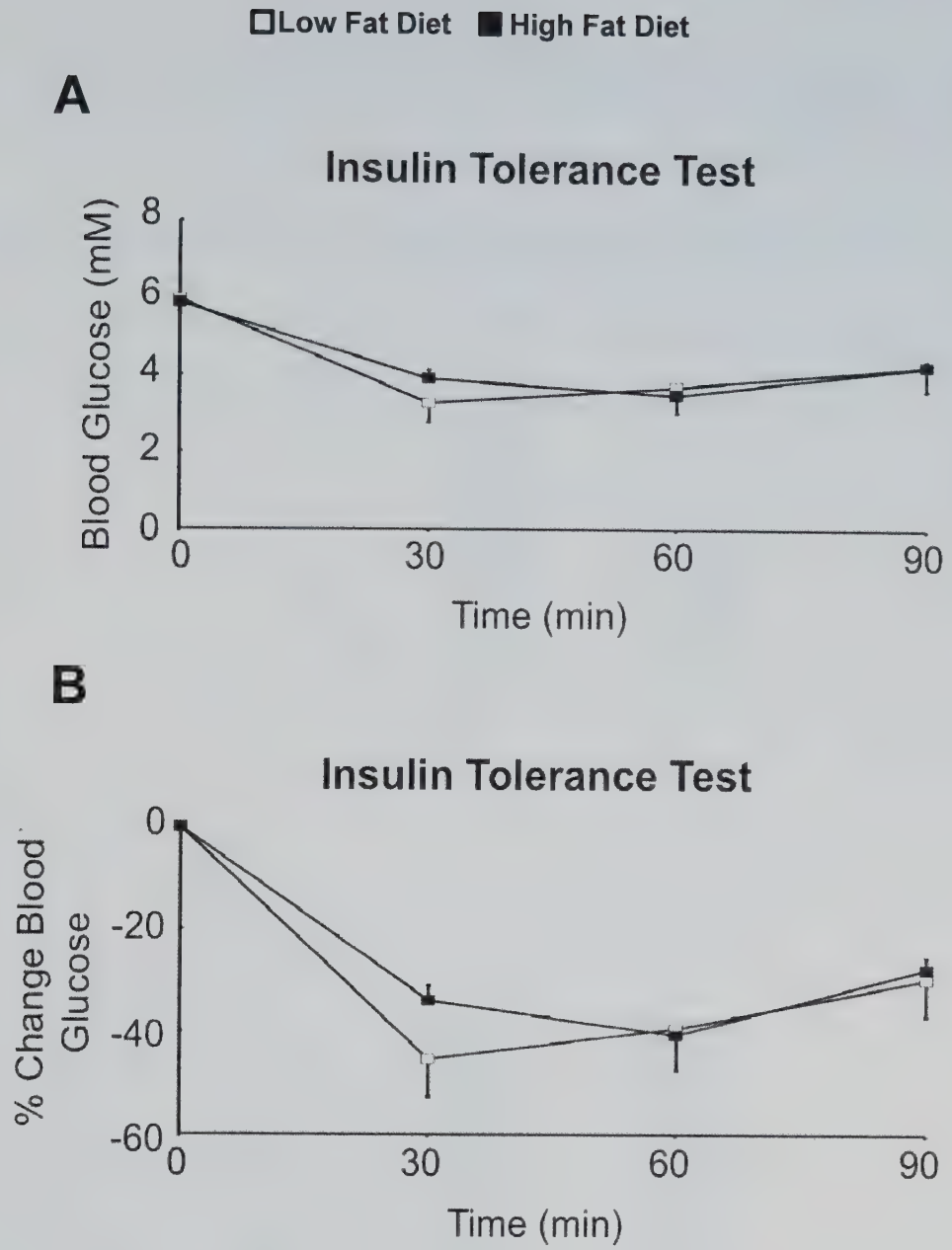
Low Fat Diet
High Fat Diet
A
Insulin Tolerance Test
Blood Glucose (mM)
8
6
4
2
0
0
30
60
90
Time (min)
B
Insulin Tolerance Test
% Change Blood Glucose
0
-20
-40
-60
0
30
60
90
Time (min)

FIGURE 3-2

Figure 3-3: *In vivo metabolic profile in mice subjected to a short-term high fat diet.*

A: Dark and light cycle respiratory exchange ratio (RER), B: average oxygen consumption, C: average heat production, and D: ambulatory activity, in mice fed a low or high diet for 1 wk. Values represent mean ± SE (n = 5). Differences were determined using a two-way ANOVA followed by a Bonferroni post-hoc analysis. $^{*}P<0.05$, significantly different from low fat counterpart. $^{\dagger}P<0.05$, significantly different from the light cycle.

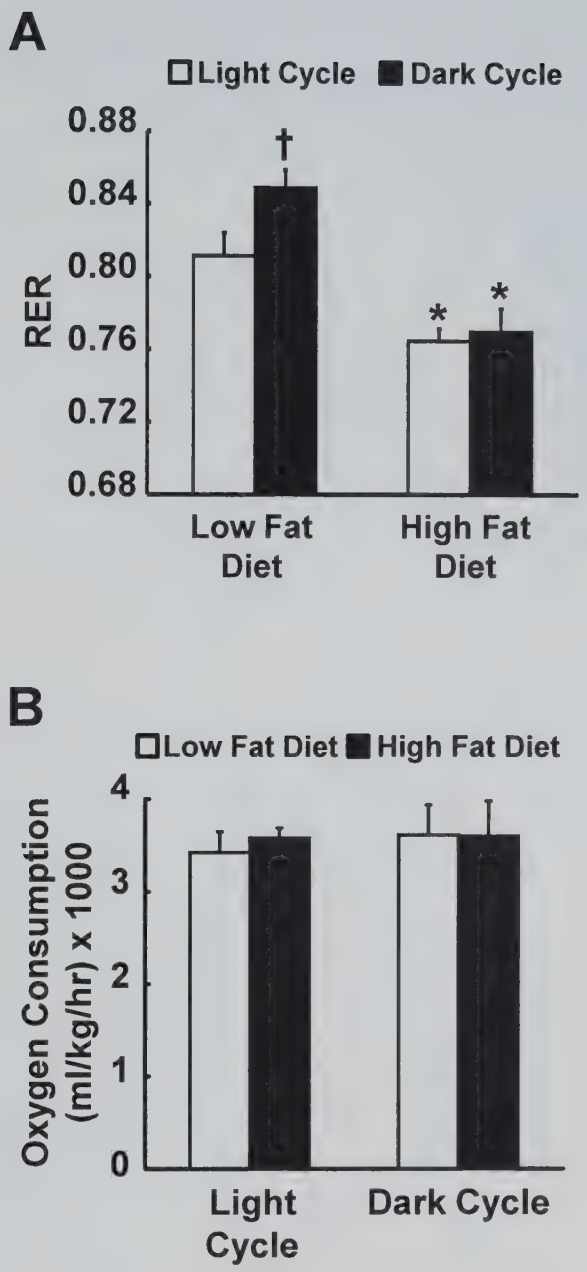
A
Light Cycle
Dark Cycle
0.88
0.84
0.80
0.76
0.72
0.68
RER
†
*
*
Low Fat Diet
High Fat Diet
B
Low Fat Diet
High Fat Diet
Oxygen Consumption (ml/kg/hr) x 1000
4
3
2
1
0
Light Cycle
Dark Cycle

FIGURE 3-3

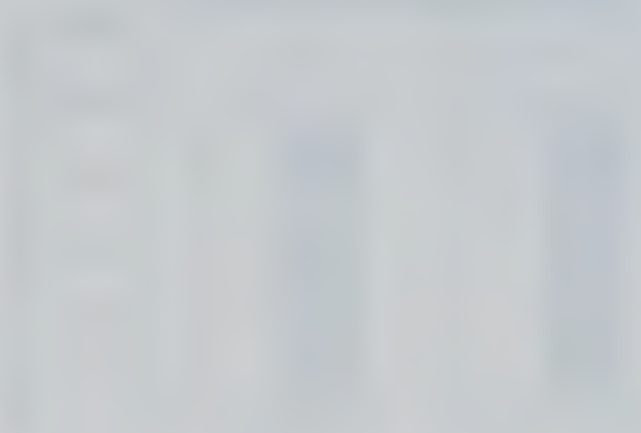

Figure 3-3: *In vivo metabolic profile in mice subjected to a short-term high fat diet.*

A: Dark and light cycle respiratory exchange ratio, B: average oxygen consumption, **C: average heat production, and D: ambulatory activity, in mice fed a low or high diet for 1 wk.** Values represent mean ± SE (n = 5).

C

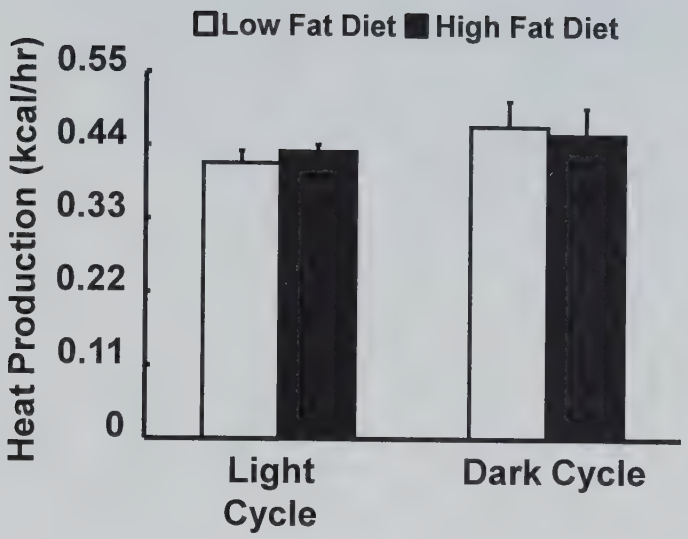
Low Fat Diet
High Fat Diet
Heat Production (kcal/hr)
0.55
0.44
0.33
0.22
0.11
0
Light Cycle
Dark Cycle

D

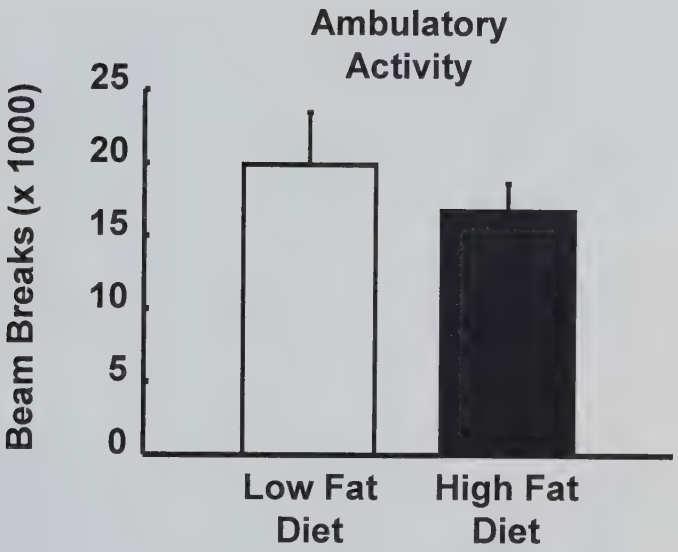
Ambulatory Activity
Beam Breaks (x 1000)
25
20
15
10
5
0
Low Fat Diet
High Fat Diet

FIGURE 3-3

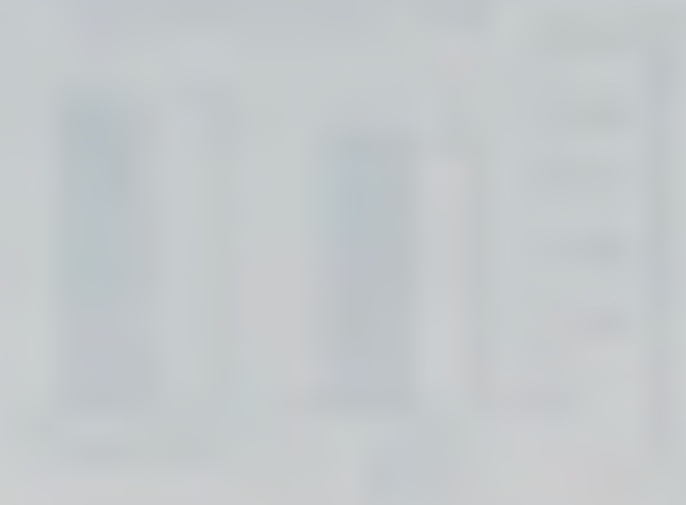

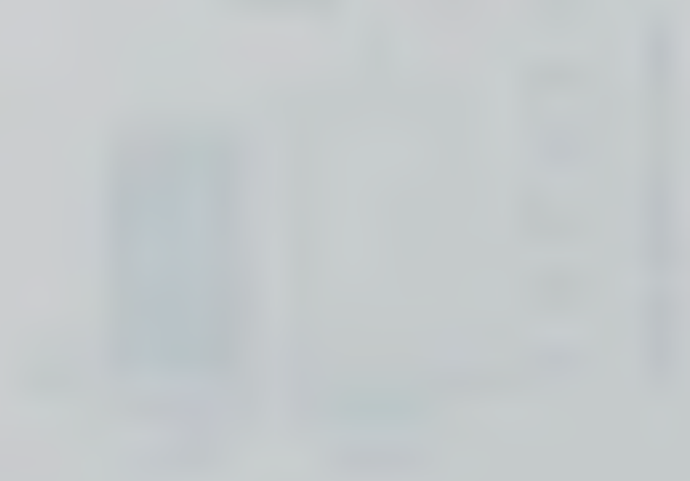

Figure 3-4: *Fasting and short-term high fat feeding has no effect on Akt and AMPK signaling.*

A: Akt phosphorylation at serine 473, B: GSK3β phosphorylation at serine 9, and C: AMPK phosphorylation at threonine 172 are unaltered in gastrocnemius muscle of fasted mice, or mice fed a high fat diet for 1 or 3 wks. Values represent mean ± SE (n = 5).

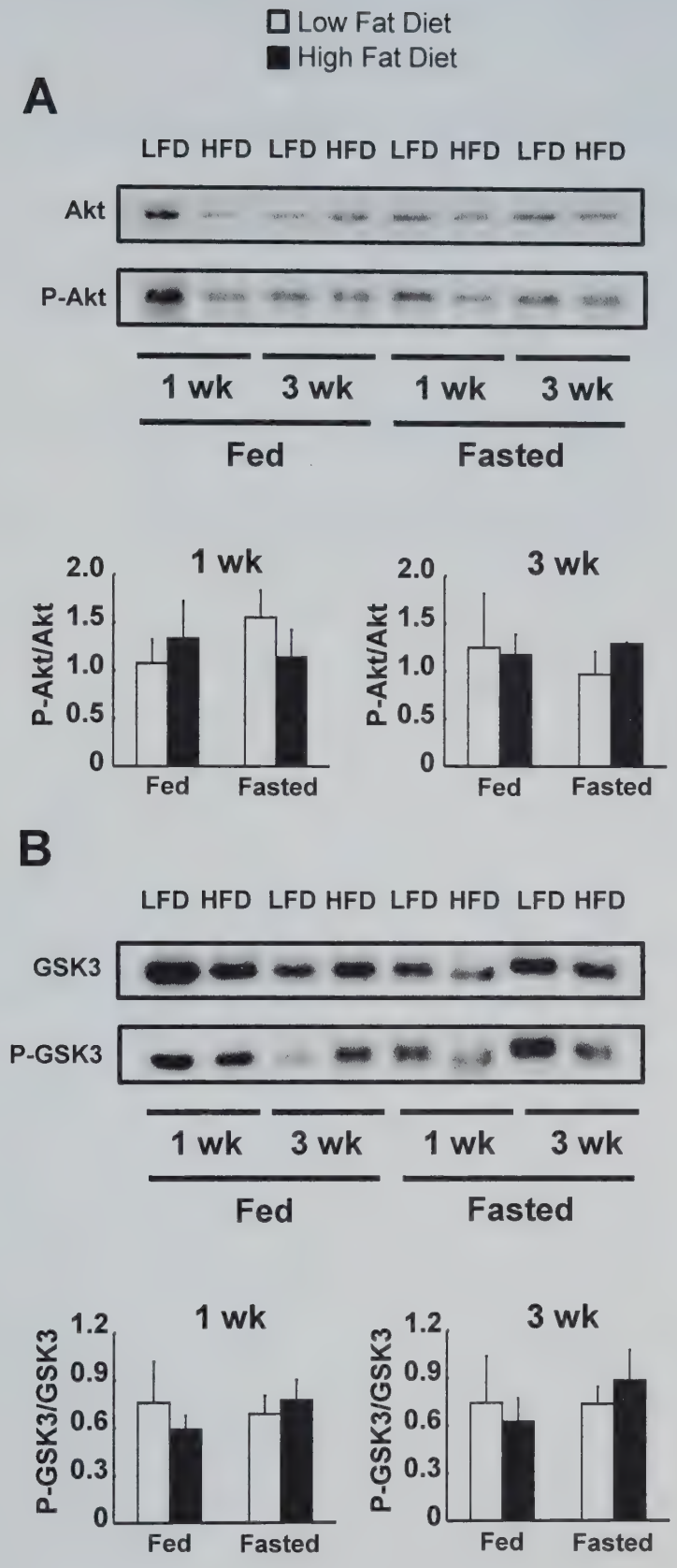
Low Fat Diet
High Fat Diet
A
LFD HFD LFD HFD LFD HFD LFD HFD
Akt
P-Akt
1 wk 3 wk 1 wk 3 wk
Fed
Fasted
1 wk
3 wk
P-Akt/Akt
2.0
1.5
1.0
0.5
0
Fed
Fasted
B
LFD HFD LFD HFD LFD HFD LFD HFD
GSK3
P-GSK3
1 wk 3 wk 1 wk 3 wk
Fed
Fasted
1 wk
3 wk
P-GSK3/GSK3
1.2
0.9
0.6
0.3
0
Fed
Fasted

FIGURE 3-4

Figure 3-4: *Fasting and short-term high fat feeding has no effect on Akt and AMPK signaling.*

A: Akt phosphorylation at serine 473, B: GSK3β phosphorylation at serine 9, and **C: AMPK phosphorylation at threonine 172** are unaltered in gastrocnemius muscle of fasted mice, or mice fed a high fat diet for 1 or 3 wks. Values represent mean ± SE (n = 5).

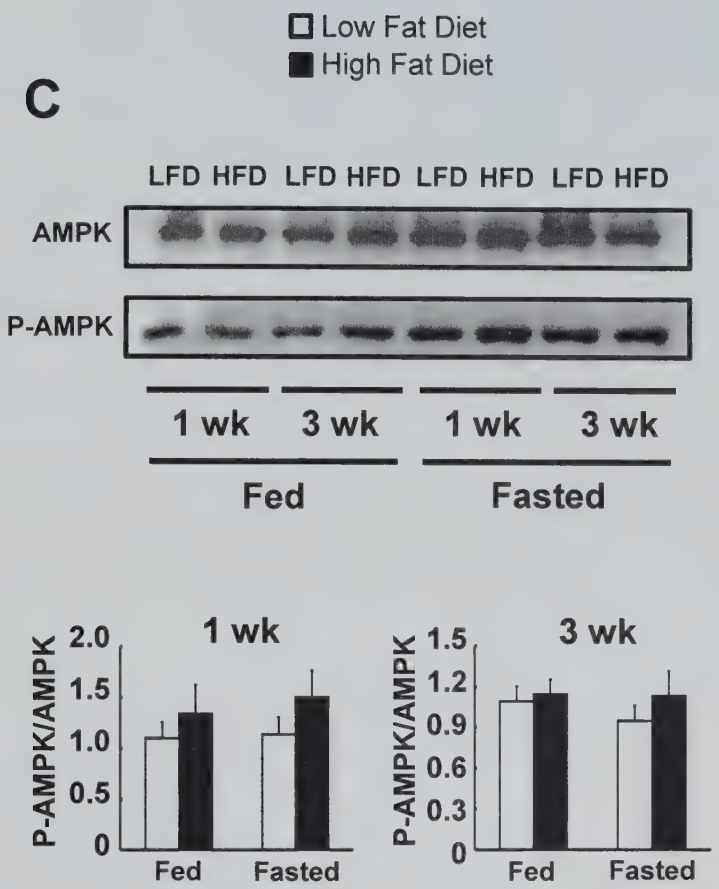
Low Fat Diet
High Fat Diet
C
LFD HFD LFD HFD LFD HFD LFD HFD
AMPK
P-AMPK
1 wk
3 wk
1 wk
3 wk
Fed
Fasted
1 wk
P-AMPK/AMPK
2.0
1.5
1.0
0.5
0
Fed
Fasted
3 wk
P-AMPK/AMPK
1.5
1.2
0.9
0.6
0.3
0
Fed
Fasted

FIGURE 3-4

Figure 3-5: *Ceramide and long chain acyl CoA accumulate in gastrocnemius muscle of mice following 3 wks of high fat feeding, but not after 1 wk.*

A: Triacylglycerol (TAG), B: long chain acyl CoA, C: diacylglycerol (DAG), and D: ceramide levels in gastrocnemius muscle of mice fed a low or high fat diet for 1 wk, or after a 6 hr fast. E: TAG, F: long chain acyl CoA, G: DAG, and H: ceramide levels in gastrocnemius muscle of mice fed a low or high fat diet for 3 wks, or after a 6 hr fast. Values represent mean ± SE (n = 5). Differences were determined using a two-way ANOVA followed by a Bonferroni post-hoc analysis. $^{*}P<0.05$, significantly different from fed counterpart. $^{\dagger}P<0.05$, significantly different from low fat fed counterpart.

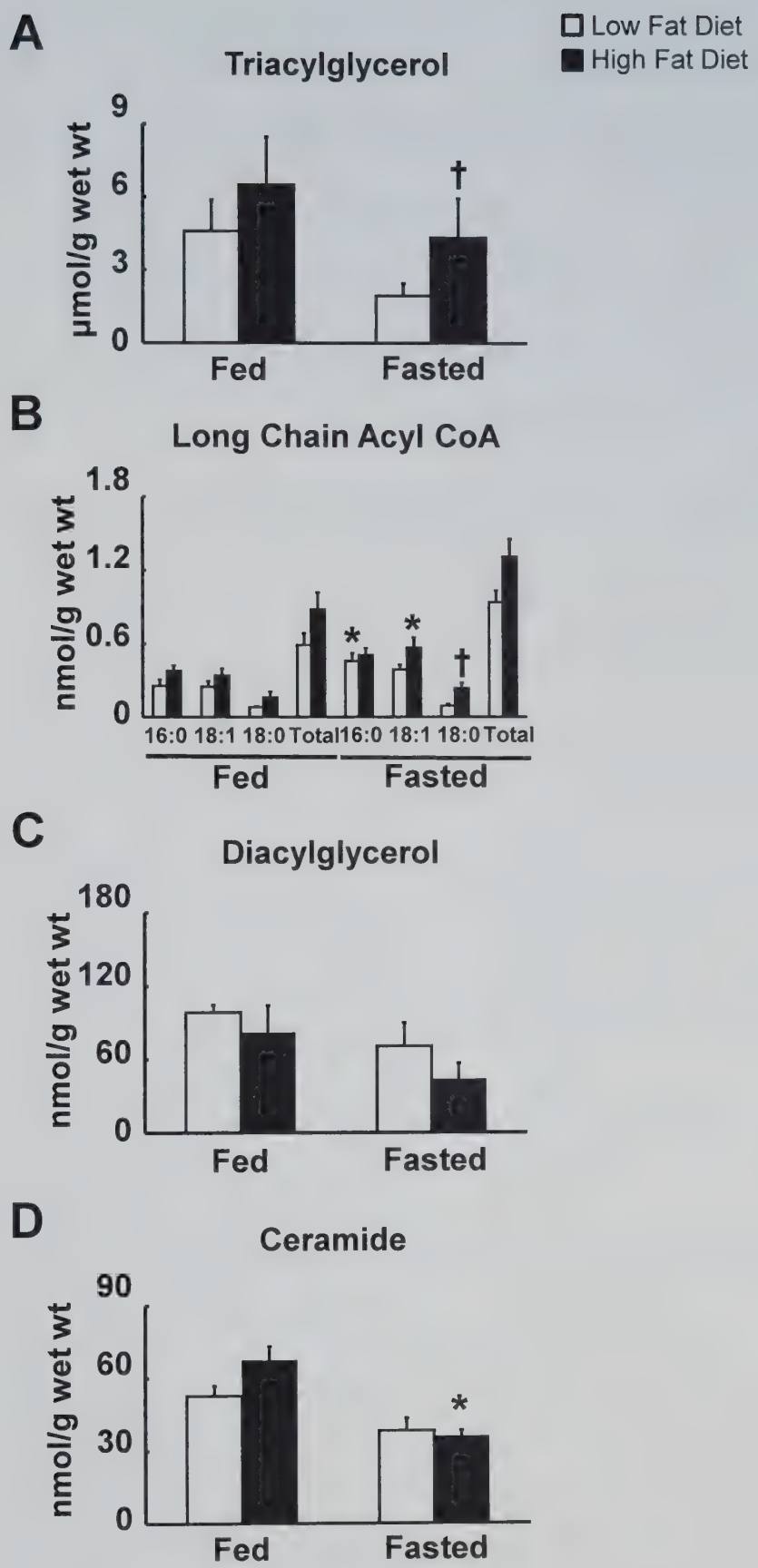
A
Triacylglycerol
Low Fat Diet
High Fat Diet
µmol/g wet wt
9
6
3
0
†
Fed
Fasted
B
Long Chain Acyl CoA
nmol/g wet wt
1.8
1.2
0.6
0
*
*
†
16:0 18:1 18:0 Total 16:0 18:1 18:0 Total
Fed
Fasted
C
Diacylglycerol
nmol/g wet wt
180
120
60
0
Fed
Fasted
D
Ceramide
nmol/g wet wt
90
60
30
0
*
Fed
Fasted

FIGURE 3-5

Figure 3-5: *Ceramide and long chain acyl CoA accumulate in gastrocnemius muscle of mice following 3 wks of high fat feeding, but not after 1 wk.*

A: Triacylglycerol (TAG), B: long chain acyl CoA, C: diacylglycerol (DAG), and D: ceramide levels in gastrocnemius muscle of mice fed a low or high fat diet for 1 wk, or after a 6 hr fast. **E: TAG, F: long chain acyl CoA, G: DAG, and H: ceramide levels in gastrocnemius muscle of mice fed a low or high fat diet for 3 wks, or after a 6 hr fast.** Values represent mean ± SE (n = 5). Differences were determined using a two-way ANOVA followed by a Bonferroni post-hoc analysis. $^{*}P<0.05$, significantly different from fed counterpart. $^{\dagger}P<0.05$, significantly different from low fat fed counterpart.

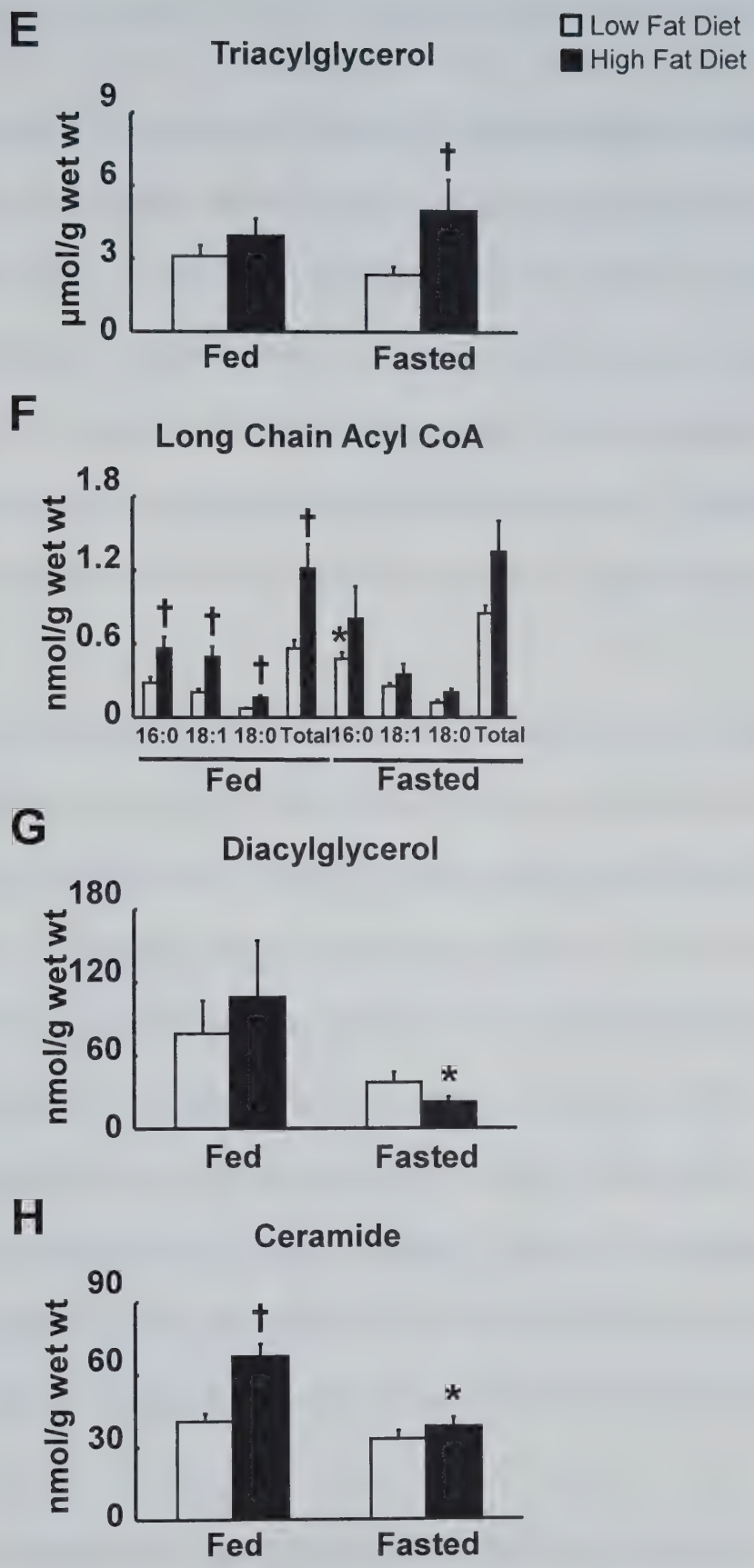
E
Triacylglycerol
Low Fat Diet
High Fat Diet
µmol/g wet wt
9
6
3
0
†
Fed
Fasted
F
Long Chain Acyl CoA
nmol/g wet wt
1.8
1.2
0.6
0
†
*
16:0 18:1 18:0 Total 16:0 18:1 18:0 Total
Fed
Fasted
G
Diacylglycerol
nmol/g wet wt
180
120
60
0
*
Fed
Fasted
H
Ceramide
nmol/g wet wt
90
60
30
0
†
*
Fed
Fasted

FIGURE 3-5

In this study, we demonstrate that both short-term high fat feeding and fasting of mice are associated with an inhibition of skeletal muscle PDH activity. This inhibition likely results from phosphorylation of PDH via increased expression of PDHK4. Although both 1 and 3 wks of high fat feeding inhibited skeletal muscle PDH activity, this was not associated with impairments in the insulin signaling cascade, or the development of insulin resistance. Such findings suggest, that at least at the level of PDH, the Randle Cycle is operative in skeletal muscle.

Classic studies performed by Randle and colleagues in the 1960s (315) demonstrated that increases in fatty acid oxidation lead to the direct inhibition of glucose oxidation via an increase in fatty acid byproducts (acetyl CoA, NADH) that inhibit the rate-limiting enzyme of glucose oxidation, PDH (314). The acceleration of fatty acid oxidation also leads to an accumulation of citrate, which inhibits the rate-limiting enzyme of glycolysis, PFK1. Inhibition of PFK1 would lead to an accumulation of gluose-6-phosphate, which subsequently inhibits hexokinase and reduces glucose uptake. Therefore, based on this Randle Cycle effect, it was proposed that an acceleration of fatty acid oxidation would decrease glucose metabolism, causing skeletal muscle insulin resistance and eventually, diabetes.

However, these studies were performed in cardiac and diaphragm muscle (315), and studies utilizing ^{31}P-MRS by Shulman and colleagues have suggested

that the Randle Cycle may not operate in skeletal muscle, based off results showing that levels of glucose-6-phosphate do not accumulate in skeletal muscle exposed to high levels of fatty acids (303, 305, 326). While this observation could be explained by the suggestion that increased fatty acid exposure does not inhibit glycolysis, it could also be explained by a decrease in skeletal muscle glucose uptake, which would limit the amount of glucose available to form sugar phosphates. It is also important to note that measurement of glucose-6-phosphate via ^{31}P-MRS would also not account for any effects of fatty acids on mitochondrial glucose oxidation, an important component of the Randle Cycle. Our results address this important issue, as we clearly show in two different models of elevated fatty acid exposure to muscle, short term high fat feeding and fasting, that skeletal muscle PDH activity is inhibited. Although we did not directly measure skeletal muscle glucose oxidation, because PDH is the rate-limiting enzyme of glucose oxidation, it is highly suggestive of reduced glucose oxidation rates in muscle from high fat fed or fasted mice, and consistent with an operating Randle Cycle in muscle.

Mitochondrial dysfunction in the form of an impaired ability to oxidize fatty acids in skeletal muscle has been suggested to play a key role in the cytosolic accumulation of lipid metabolites, such as TAG, DAG, and ceramide, which interfere with the insulin response and contribute to the development of insulin resistance (68, 69, 303, 305, 353, 413, 447). On the contrary, a large number of recent studies have actually shown that skeletal muscle fatty acid oxidation is accelerated during obesity-induced insulin resistance (140, 202, 396),

and that the observed mitochondrial dysfunction in obese and type 2 diabetic patients is either due to the sedentary nature of the individuals, or a consequence of the disease itself (37, 200, 202). Our results agree with the latter, as short-term high fat feeding resulted in an increased PDK4 expression in gastrocnemius muscle. PDHK4 is a well-characterized target gene of peroxisome proliferator activated receptor alpha (PPARα), a transcription factor whose activity is associated with an upregulation of fatty acid oxidation rates (108, 113, 246). It is plausible in our study that increased fatty acid delivery to the skeletal muscle provided a surplus of fatty acid ligand, which activated PPARα and increased PPARα-target gene expression, such as PDHK4, to enhance fatty acid oxidation rates and subsequently inhibit glucose oxidation rates. Once again, these results are consistent with an operating Randle Cycle in skeletal muscle.

In addition, the RER data observed in this study is also consistent with an operating Randle Cycle in skeletal muscle. With mice fed a low fat diet, we observed metabolic flexibility in terms of a substrate switch from carbohydrates to fatty acids for oxidative energy metabolism, as seen by the significant drop in the RER during the transition from the dark to the light cycle. As mice are either asleep or significantly less active during the light cycle, it mimics a state of fasting, increases the delivery of fatty acid substrate for oxidation to the muscle, and manifests itself in the form of a lower RER. With mice fed a high fat diet for 1 wk, we observed a dramatic drop in the RER, as values approached 0.7, indicating that these animals are relying almost solely on fatty acids, such as palmitate, for oxidative energy metabolism. Thus, the contribution of

carbohydrates to oxidative energy metabolism was significantly reduced, supportive of a substrate switch and operating Randle Cycle in skeletal muscle.

Thus, the findings of our study would argue against the proposal that accelerating skeletal muscle fatty acid oxidation can ameliorate obesity-induced insulin resistance, as this would likely enhance the inhibition of PDH activity, and decrease glucose oxidation rates even further. Moreover, despite an ~16% decrease in PDH activity following 1 and 3 wks of high fat feeding, these animals did not display any form of insulin resistance using insulin tolerance testing and Akt signaling as our markers. It is possible that skeletal muscle insulin resistance does not completely manifest until a more severe reduction in PDH activity is observed, and suggests that stimulation of PDH activity may be a novel target for the treatment of this disease.

Interestingly, we have shown that mice deficient for MCD (MCD-/-) are protected from high fat diet-induced insulin resistance (202). MCD catalyzes the degradation of malonyl CoA, a potent endogenous inhibitor of CPT 1, the rate-limiting enzyme of mitochondrial fatty acid uptake and subsequent oxidation (257, 262, 382, 404). Thus, deficiency of MCD is associated with increased levels of malonyl CoA in skeletal muscle, and an inhibition of mitochondrial fatty acid uptake and subsequent oxidation. Despite this impairment in skeletal muscle fatty acid oxidation, these animals display improved glucose and insulin tolerance, and a higher RER, indicative of elevated whole body carbohydrate oxidation and supportive of a Randle Cycle effect (202). Furthermore, the gastrocnemius muscle of MCD-/- mice subjected to a high fat diet displays greater

PDH activity versus their WT counterparts (unpublished data). Recent data in human muscle myotubes supports our data, as siRNA knockdown of MCD reduced fatty acid oxidation rates, which was associated with a subsequent increase in glucose uptake and glucose oxidation rates (41). Although PDH activity was not measured in these myotubes, it is highly likely that PDH activity would be higher in the myotubes with MCD knocked down. Finally, PDHK4 deficient mice, which also display increased skeletal muscle PDH activity, glucose oxidation rates, and decreased fatty acid oxidation rates, are also protected from high fat diet-induced insulin resistance (177).

A particularly surprising finding in this study was that although we did not observe any form of insulin resistance development following 3 wks of high fat feeding, we did observe an accumulation of ceramide and long chain acyl CoA in the gastrocnemius muscle. These observations suggest a number of possibilities. For example, long chain acyl CoA and ceramide may not play as large a role as initially anticipated towards the development of insulin resistance (68, 188, 385). In addition, insulin resistance may not develop until either an accumulation of either TAG or DAG occurs (68, 69, 188, 231). However, there are now a large number of studies that have reported that insulin resistance can be significantly improved, despite an elevation of skeletal muscle TAG and DAG content (153, 231, 310, 312). It may also be possible that the insulin resistance does not develop until the lipid overload in the mitochondria finally results in mitochondrial dysfunction (202, 280, 385), oxidative stress impairs mitochondrial function (37), or until a severe inflammation develops in the cell (362, 385).

The finding that the accumulation of ceramide following 3 wks of high fat feeding does not cause insulin resistance is in contrast to previous findings from our laboratory showing that inhibition of *de novo* ceramide synthesis results in a dramatic reversal of insulin resistance induced by chronic high fat feeding (unpublished data). This discrepancy between the 2 studies can be explained by the possibility that the initial build up of ceramide itself is not a primary cause of insulin resistance, but that its chronic downstream effects, such as mitochondrial dysfunction (126, 134, 385), impaired insulin signaling (312, 357, 385), or inflammation (338, 385), need to occur before ceramide accumulation manifests as a full blown insulin resistance. In support of this, we did not observe any impairment in whole body oxygen consumption in animals fed a short-term high fat diet, indicative of normal mitochondrial function. Akt and GSK3 signaling were not impaired in skeletal muscle of mice fed a short-term high fat diet, indicative of normal insulin signaling, p38 MAPK phosphorylation, a key marker of inflammation, was not increased in mice fed a short term high fat diet (*data not shown*), indicative of the absence of severe inflammation. It may also be possible that ceramide metabolites, such as glucosylceramide, are more important than ceramide itself towards the development of insulin resistance (7). Thus, it is possible that while ceramide accumulated in skeletal muscle following a short-term high fat diet, ceramide metabolites did not, explaining the lack of insulin resistance in our animals.

Although our findings challenge the proposal that the Randle Cycle does not operate in skeletal muscle, it does not mean that the ^{31}P-MRS data showing

that glucose-6-phosphate does not accumulate in skeletal muscle exposed to high levels of fatty acids is incorrect. As we have already mentioned, there are two major components of the Randle Cycle, and our findings have dealt with the second component, supporting that increasing rates of fatty acid oxidation results in a subsequent inhibition of PDH and glucose oxidation (292, 315, 343). The other component deals with a citrate inhibition of PFK1, that increases glucose-6-phosphate levels to feedback inhibit hexokinase and reduce glucose uptake in skeletal muscle (305, 314, 315). Thus, the ^{31}P-MRS data suggests that possibly this component of the Randle Cycle is not prominent in skeletal muscle, which is consistent with findings demonstrating that the TCA mitochondrial transporter, which exports citrate outside of the mitochondria, is not abundant in cardiac and skeletal muscle tissue (379).

In summary, our findings suggest that the Randle Cycle is operative in skeletal muscle, at least at the level of PDH and glucose oxidation. Such findings argue against the notion that enhancing skeletal muscle fatty acid oxidation can ameliorate obesity-induced insulin resistance, as such strategies may exacerbate the inhibition of glucose oxidation and lead to a further impairment of glucose utilization.

CHAPTER 4.

Malonyl CoA decarboxylase deficient mice are protected against obesity-induced skeletal muscle insulin resistance

---

Some of the data in this chapter has been published. Koves TR, **Ussher JR,** Noland RC, Slentz D, Mosedale M, Ilkayeva O, Bain J, Stevens R, Dyck JR, Newgard CB, Lopaschuk, GD, Muoio DM. Mitochondrial overload and incomplete fatty acid oxidation contribute to skeletal muscle insulin resistance. *Cell Metabolism.* 2008. Jan;7(1):45-56.

My role in this work involved performing all experiments (except those noted below), as well as the writing of the manuscript. Panakkezhum Thomas performed the HPLC analysis of CoA esters and ATP levels, Liyan Zhang performed the gastrocnemius PDH activity measurements, and Tim Koves (Duke University) performed the GC/MS metabolic profiling.

CHAPTER 4.

Malonyl CoA decarboxylase deficient mice are protected against obesity-induced skeletal muscle insulin resistance

Abstract

Previous studies have postulated that insulin resistance develops secondary to diminished skeletal muscle fatty acid oxidation, which results in the intramyocellular accumulation of cytosolic lipid metabolites that impede insulin signaling. In contrast to this hypothesis, the present study employed a genetic model of fatty acid oxidation deficiency that afforded protection against obesity-induced insulin resistance, the malonyl CoA decarboxylase deficient (MCD-/-) mouse. MCD-/- mice have increased levels of malonyl CoA, a potent endogenous inhibitor of carnitine palmitoyl transferase 1, the rate-limiting enzyme of mitochondrial fatty acid uptake and subsequent oxidation. In this study we showed that the protection against obesity-induced insulin resistance in MCD-/- mice is associated with increased gastrocnemius pyruvate dehydrogenase activity (0.21 ± 0.04 vs. 0.05 ± 0.01 μmol/g wet weight/min), indicative of increased carbohydrate oxidation, which was observed in isolated soleus muscle experiments (0.41 ± 0.04 vs. 0.31 ± 0.01 μmol/g wet weight/hr). Further evidence for elevated carbohydrate oxidation rates in obese MCD-/- mice was observed during indirect calorimetry studies, whereby MCD-/- mice yielded higher RER values versus their wild type (WT) littermates (0.742 ± 0.008 vs. 0.719 ± 0.005).

Despite this protection against obesity-induced insulin resistance, MCD-/- mice accumulated significant amounts of intramyocellular lipid, comparable to that observed in the WT littermates. However, we observed that the MCD-/- mice accumulated significantly less incomplete fatty acid oxidation by-products in muscle via gas chromatography/mass spectrometry metabolic profiling. These findings challenge current dogma in regards to skeletal muscle fatty acid oxidation rates, the accumulation of lipid metabolites, and insulin sensitivity, and illustrate a paradigm shift for novel therapies in the treatment of obesity-related diseases such as insulin resistance and type 2 diabetes.

Obesity and type 2 diabetes frequently occur hand in hand, and are characterized by a hyperlipidemia, which is believed to be a major precipitating event in the development of skeletal muscle insulin resistance (182, 281).

The present investigation sought to advance our understandings of lipid-induced insulin resistance in skeletal muscle, the major site of insulin-stimulated glucose disposal. Numerous studies *in vivo* and *in vitro* have provided overwhelming evidence that lipid surplus leads to an accumulation of intramyocellular lipid-derived metabolites, which coincide with the development of insulin resistance (353, 367). Previous studies have postulated that this accumulation of lipid-derived metabolites results from an impaired mitochondrial fatty acid oxidative capacity (69, 383, 413, 447). Thus, esterified fatty acids in the form of long chain acyl CoA are diverted away from CPT 1, the rate limiting enzyme in mitochondrial uptake and oxidation of fatty acids, towards TAG and other lipid metabolites such as ceramide and DAG. These metabolites are believed to activate classical PKC isoforms that phosphorylate and inactivate IRS proteins, impeding the insulin signaling cascade (353, 367). It has been postulated that enhancing the ability of the muscle to oxidize fat can protect against insulin resistance, by preventing the accumulation of these lipid metabolites and removing inhibition of insulin signaling (47, 69, 203, 353, 413).

Recent studies have challenged this theory by demonstrating that genetic manipulations that increase tissue levels of these lipid metabolites do not

necessarily result in the development of insulin resistance (12, 108, 270). Moreover, emerging studies are providing strong support that obesity-induced insulin resistance might be due to metabolic overload of skeletal muscle mitochondria, whereby rates of fatty acid oxidation are too high for the TCA cycle to keep up with, resulting in incomplete oxidation of fatty acids (108, 200, 202, 280). In fact, a number of recent studies have now provided substantial evidence supporting a role for excessive fatty acid oxidation rates during obesity-induced insulin resistance (140, 396), and suggest that the accumulation of these lipid metabolites is simply due to excessive fatty acid supply to the tissue.

Our goal in this study was to characterize incomplete fatty acid oxidation as a marker for obesity-induced insulin resistance in WT and MCD-/- mice. MCD-/- mice have elevated levels of malonyl CoA, and thus should have reduced CPT 1 activity and subsequent mitochondrial fatty acid uptake and oxidation. We hypothesized that MCD-/- mice subjected to DIO would be protected against the development of insulin resistance due to less mitochondrial lipid overload, which would manifest as a reduction in incomplete fatty acid oxidation by-products. We also anticipated that a Randle Cycle effect would contribute to the improved insulin sensitivity in MCD-/- mice, whereby reducing mitochondrial fatty acid oxidation rates in MCD-/- mice would result in a compensatory increase in carbohydrate oxidation rates.

Animal Studies

All animals received care according to the Canadian Council on Animal Care and the University of Alberta Health Sciences Animal Welfare Committee. 10 – 12-wk-old MCD-/- mice and their WT littermates were placed on a standard chow/low fat diet (4% kcal from lard) or high fat diet (60% kcal from lard, Research Diets; D12492) for a 12 wk period. At the end of wk 12, animals were sacrificed via IP injection of sodium pentobarbital (12 mg) in the fed state in the middle of the dark cycle. Tissues were excised and immediately frozen in liquid N_2. Protocols for assessment of intramyocellular lipid metabolite accumulation, GC/MS metabolic profiling, GTTs, ITTs, indirect calorimetry, isolated soleus muscle metabolism experiments, PDH activity, exercise capacity, ATP levels, immunoblotting, and statistical analysis are described in **Chapter 2** of this thesis.

MCD-/- mice gain similar amounts of body weight during DIO but display improved glucose and insulin tolerance

As expected, WT mice placed on a high fat diet for 12 wks gain significant amounts of body weight (Table 4-1), and become both glucose and insulin intolerant (*data not shown*). On the other hand, MCD-/- mice gain similar amounts of body weight after 12 wks of a high fat diet (Table 4-1), but display a significant improvement in both glucose and insulin tolerance (Figure 4-1A-D) that is very similar to the profiles observed in their lean counterparts. In addition, fasting plasma glucose levels show a trend towards a reduction in MCD-/- mice subjected to a high fat diet (Table 4-1).

The protection against obesity-induced insulin resistance observed in MCD-/- mice is associated with increased glucose oxidation rates in isolated muscle and increased PDH activity

We hypothesize that the improvements in glucose and insulin tolerance in MCD-/- mice subjected to DIO are partly due to improvements in overall carbohydrate utilization, as a result of a Randle Cycle effect. Indeed, we show that glucose oxidation rates in isolated soleus muscle of DIO MCD-/- mice are significantly greater than their DIO WT littermates, while insulin-stimulated glucose oxidation rates are increased in the extensor digitorum longus (EDL) muscle of DIO MCD-/- mice (Figure 4-2A). Interestingly, lactate production is

similar in the soleus and EDL muscle of DIO WT and MCD-/- mice, (Figure 4-2B), suggesting that glycolytic rates may also be greater in skeletal muscle of DIO MCD-/- mice. These improvements in glucose metabolism in the DIO MCD-/- mice are associated with an increase in the active portion of skeletal muscle PDH activity (Figure 4-2C-E). In addition, placement of DIO MCD-/- mice in our CLAMS apparatus for indirect calorimetry assessment reveals an increased reliance on carbohydrates for energy metabolism during the dark cycle, as indicated by their higher RER values (Figure 4-3A/B).

***In vivo* metabolic profiles and exercise capacity in WT and MCD-/- mice subjected to DIO**

Despite the greater reliance on carbohydrates for energy metabolism found in DIO MCD-/- mice, we observed no differences in whole body oxygen consumption rates, or heat production between DIO WT and MCD-/- mice (Figure 4-3C/D). In addition, we observed no differences in ambulatory activity or 24 hr food intake in DIO WT and MCD-/- mice (Figure 4-3E/F). Interestingly, however, exercise distance and time are greater in DIO MCD-/- mice (Figure 4-4A/B), which may be due to the improved energetic status of DIO MCD-/- mice, indicated by their trend to higher gastrocnemius muscle ATP levels (Figure 4-4C). Since AMPK is a cellular fuel gauge that is inactivated during states of high energy (i.e. high ATP levels), we observed a reduction in the phosphorylation of AMPK at threonine 172 (necessary for AMPK activation (97, 140, 396)) in DIO

MCD-/- mice (Figure 4-4D), supporting the notion of their improved energetic status.

Intramyocellular lipid metabolite accumulation in lean and DIO WT and MCD-/- mice

As predicted, MCD-/- mice have elevated levels of skeletal muscle malonyl CoA (Table 4-2), which would suggest reduced CPT 1 activity and rates of mitochondrial fatty acid uptake and subsequent oxidation (260, 405). This reduction in skeletal muscle mitochondrial fatty acid oxidation rates likely contributes to the increased levels of oleoyl CoA observed in the gastrocnemius muscle of lean MCD-/- mice (Figure 4-5A). In line with the findings of others (188, 353), DIO results in the significant accumulation of a number of long chain acyl CoA species in the gastrocnemius muscle of WT mice, which is also apparent in DIO MCD-/- mice (Figure 4-5A). Unexpectedly, however, we did not observe an increase in gastrocnemius muscle TAG levels in both DIO WT and MCD-/- mice (Figure 4-5B).

GC/MS metabolic profiling reveals dramatic changes in TCA cycle intermediates and long chain acylcarnitine levels in DIO mice that are consistent with the incomplete oxidation of fatty acids

Previous studies have now suggested rather than a general impairment in skeletal muscle fatty acid oxidation, that obesity-induced insulin resistance is accompanied via accelerated rates of incomplete fatty acid oxidation (200, 202,

280). A recent study in humans has also shown that obese patients have increased levels of incomplete fatty acid oxidation by-products (31). Because obese patients are generally sedentary (141), there is low metabolic demand on the TCA cycle, whereby it is unable to upregulate its intermediates to deal with the increased supply of acetyl CoA arising from increased rates of fatty acid oxidation in the mitochondria (202, 280, 393). Since the increased mitochondrial long chain acyl CoA species' are not being completely oxidized, they re-esterify to carnitine. Thus, by monitoring TCA cycle intermediates and long chain acylcarnitine profiles, we are able to gauge the range of incomplete fatty acid oxidation taking place in the skeletal muscle

Utilizing GC/MS metabolic profiling, we provide evidence of skeletal muscle incomplete fatty acid oxidation, as TCA cycle intermediates are decreased in gastrocnemius muscle of DIO WT mice versus their lean counterparts, and long chain acylcarnitine species increased (Figure 4-6A-C). Interestingly, a number of major long chain acylcarnitine species do not accumulate in gastrocnemius muscle of DIO MCD-/- mice, while a number of TCA cycle intermediates are significantly greater than that observed in DIO WT mice (Figure 4-6A-C). Confirming phenotype in the MCD-/- mice, we also found a dramatic increase in their malonylcarnitine (C3-DC) levels in gastrocnemius muscle (Figure 4-6A), likely arising from their greater malonyl CoA content (Table 4-2). Overall, these observations suggest that the protection against obesity-induced insulin resistance in DIO MCD-/- mice is associated with a reduction in skeletal muscle incomplete fatty acid oxidation by-products.

Table 4-1: *Body weight gain in WT and MCD-/- mice following DIO.*

	WT (LF) (n=6)	MCD-/- (LF) (n=6)	WT (DIO) (n=6)	MCD-/- (DIO) (n=12)
Body Weight (g)	26.33 ± 0.99	28.44 ± 1.78	41.33 ± 0.54*	39.68 ± 1.86*
Fed Glucose (mM)	ND	ND	8.56 ± 0.45	8.69 ± 0.58
Fasted Glucose (mM)	ND	ND	8.13 ± 0.37	7.27 ± 0.25†

Both WT and MCD-/- mice gained similar amounts of body weight following 12 wks of DIO, while fasted plasma glucose levels showed a trend towards a reduction in MCD-/- (DIO) mice. Values represent means ± SE. Differences were determined using either a two-tailed Student's *t*-test or a two-way ANOVA followed by a Bonferroni post-hoc analysis. $^{*}P<0.05$, indicates a significant difference from LF counterpart. $^{\dagger}P=0.07$, indicates a significant difference from WT (DIO). LF = low fat, DIO = diet induced obesity, ND = not determined.

Table 4-2: *Gastrocnemius malonyl CoA levels (nmol/g wet weight) in DIO WT and MCD-/- mice.*

Study Group	WT (DIO) (n=4)	MCD-/- (DIO) (n=6)
Malonyl CoA	0.49 ± 0.09	1.80 ± 0.47*

Gastrocnemius malonyl CoA content was measured in WT and MCD-/- mice following 12 wks of DIO (n = 4-6). Values represent means ± SE. Differences were determined using a two-tailed Student's *t*-test $^{*}P<0.05$, indicates a significant difference from WT (DIO). DIO = diet induced obesity.

Figure 4-1: *MCD-/- mice are protected against DIO-associated insulin resistance.*

A: Glucose tolerance in low fat diet WT and MCD-/- mice. B: Glucose tolerance in WT and MCD-/- mice subjected to 12 wks of DIO. C: Insulin tolerance in low fat diet WT and MCD-/- mice, and D: Insulin tolerance in WT and MCD-/- mice subjected to 12 wks of DIO. Values represent mean ± SE (n = 6-8). Differences were determined using a two-way ANOVA followed by a Bonferroni post-hoc analysis. $*P<0.05$, significantly different from WT mice.

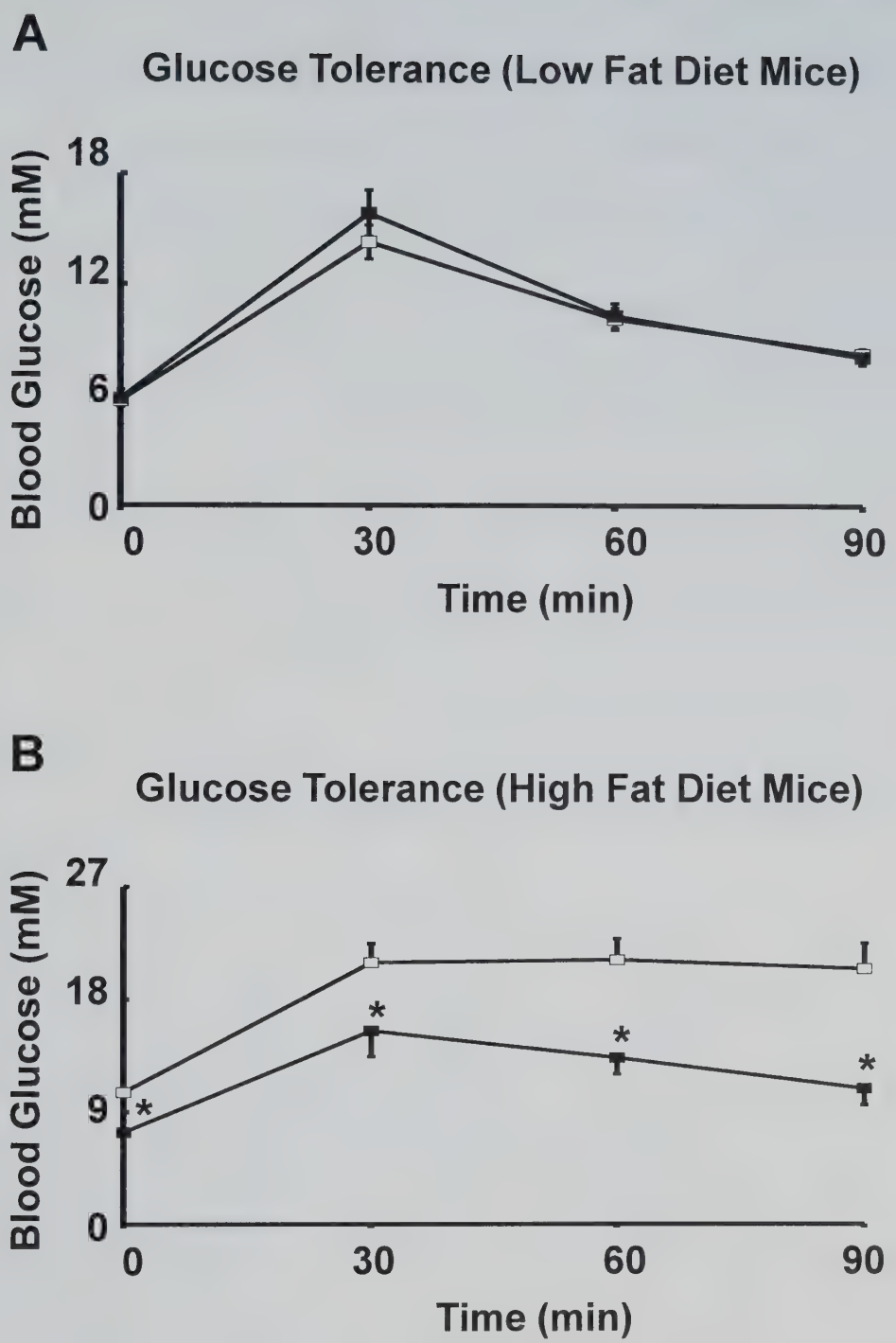
A
Glucose Tolerance (Low Fat Diet Mice)
Blood Glucose (mM)
18
12
6
0
0
30
60
90
Time (min)
B
Glucose Tolerance (High Fat Diet Mice)
Blood Glucose (mM)
27
18
9
0
*
*
*
*
0
30
60
90
Time (min)

FIGURE 4-1

Figure 4-1: *MCD-/- mice are protected against DIO-associated insulin resistance.*

A: Glucose tolerance in low fat diet WT and MCD-/- mice. B: Glucose tolerance in WT and MCD-/- mice subjected to 12 wks of DIO. **C: Insulin tolerance in low fat diet WT and MCD-/- mice, and D: Insulin tolerance in WT and MCD-/- mice subjected to 12 wks of DIO.** Values represent mean ± SE (n = 6-8). Differences were determined using a two-way ANOVA followed by a Bonferroni post-hoc analysis. $*P<0.05$, significantly different from WT mice.

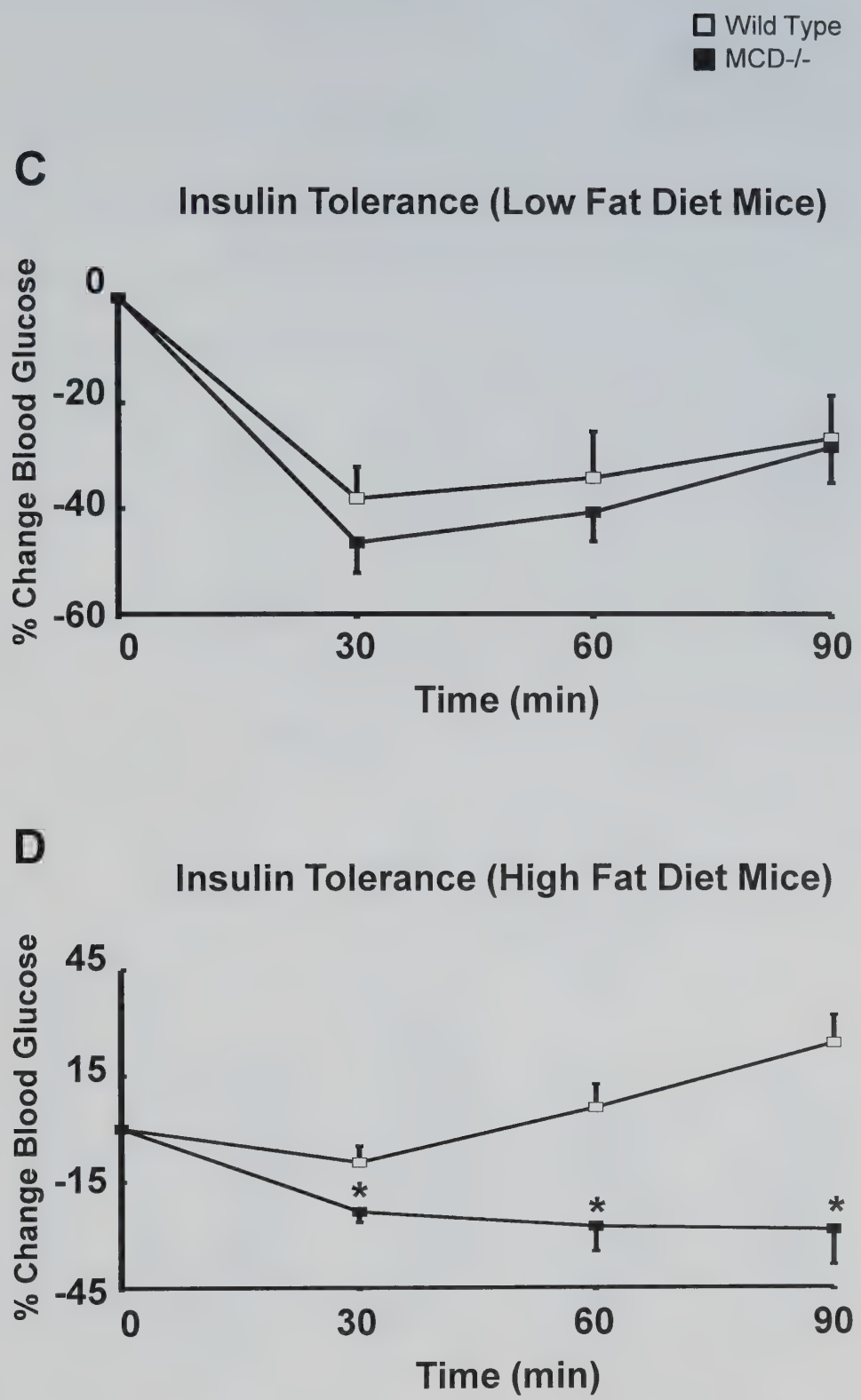
Wild Type
MCD-/-
C
Insulin Tolerance (Low Fat Diet Mice)
% Change Blood Glucose
0
-20
-40
-60
0
30
60
90
Time (min)
D
Insulin Tolerance (High Fat Diet Mice)
% Change Blood Glucose
45
15
-15
-45
*
*
*
0
30
60
90
Time (min)

FIGURE 4-1

Figure 4-2: *Increased skeletal muscle glucose oxidation rates and PDH activity in MCD-/- mice subjected to DIO.*

A: Glucose oxidation rates and, B: lactate production in isolated soleus and EDL muscle of WT and MCD-/- mice following 10 wks of DIO. C: Total PDH activity, D: Active PDH activity, and E: % active PDH in gastrocnemius muscle of WT and MCD-/- mice following 10 wks of DIO. Values represent mean ± SE (n = 5-6). Differences were determined using a two-way ANOVA followed by a Bonferroni post-hoc analysis. $*P<0.05$, significantly different from WT mice.

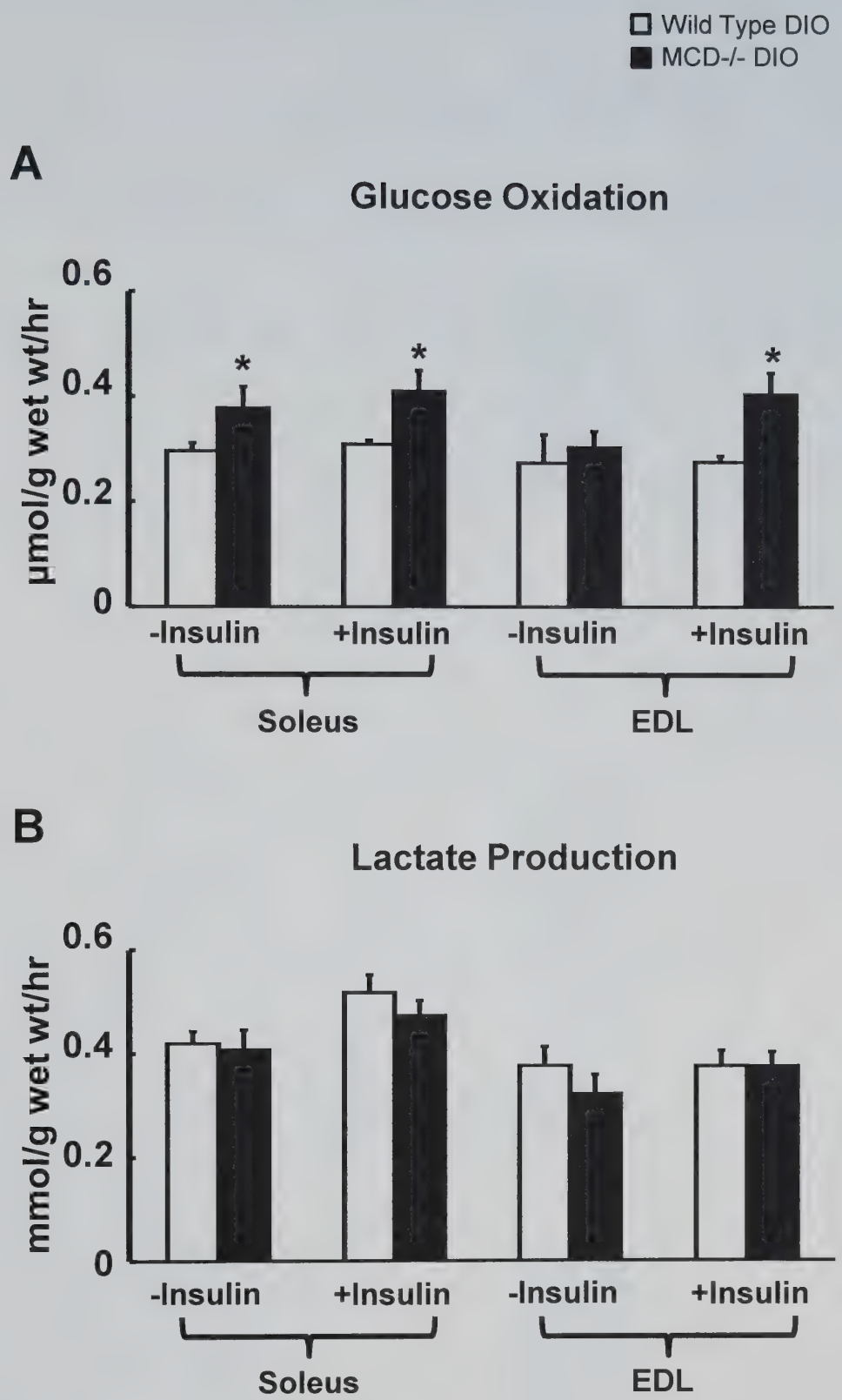
Wild Type DIO
MCD-/- DIO
A
Glucose Oxidation
µmol/g wet wt/hr
0.6
0.4
0.2
0
*
*
*
-Insulin
+Insulin
-Insulin
+Insulin
Soleus
EDL
B
Lactate Production
mmol/g wet wt/hr
0.6
0.4
0.2
0
-Insulin
+Insulin
-Insulin
+Insulin
Soleus
EDL

FIGURE 4-2

Figure 4-2: *Increased skeletal muscle glucose oxidation rates and PDH activity in MCD-/- mice subjected to DIO.*

A: Glucose oxidation rates and, B: lactate production in isolated soleus and EDL muscle of WT and MCD-/- mice following 10 wks of DIO. **C: Total PDH activity, D: active PDH activity, and E: % active PDH in gastrocnemius muscle of WT and MCD-/- mice following 10 wks of DIO.** Values represent mean ± SE (n = 5-6). Differences were determined using a two-tailed Student's *t*-test. $*P<0.05$, significantly different from WT mice.

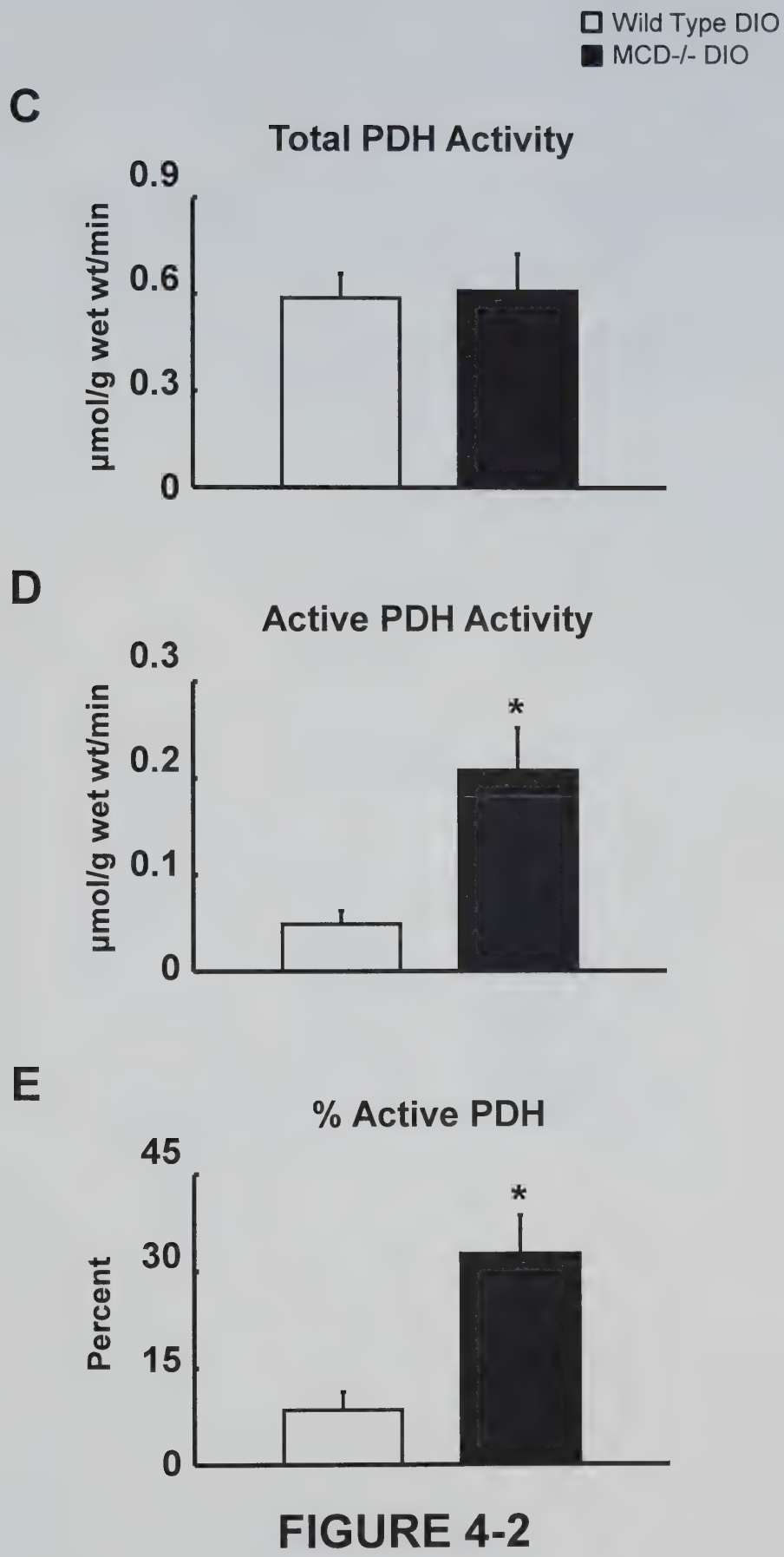
Wild Type DIO
MCD-/- DIO
C
Total PDH Activity
µmol/g wet wt/min
0.9
0.6
0.3
0
D
Active PDH Activity
µmol/g wet wt/min
0.3
0.2
0.1
0
*
E
% Active PDH
Percent
45
30
15
0
*

FIGURE 4-2

Figure 4-3: *In vivo metabolic parameters in DIO WT and MCD-/- mice.*

A: 24 hr respiratory exchange ratio (RER), B: peak dark cycle RER, C: average oxygen consumption, D: average heat production, E: 24 hr ambulatory activity, and F: 24 hr food intake in WT and MCD-/- mice following 8 wks of DIO. Values represent mean ± SE (n = 6-9). Differences were determined using a two-tailed Student's *t*-test. $*P<0.05$, significantly different from WT mice.

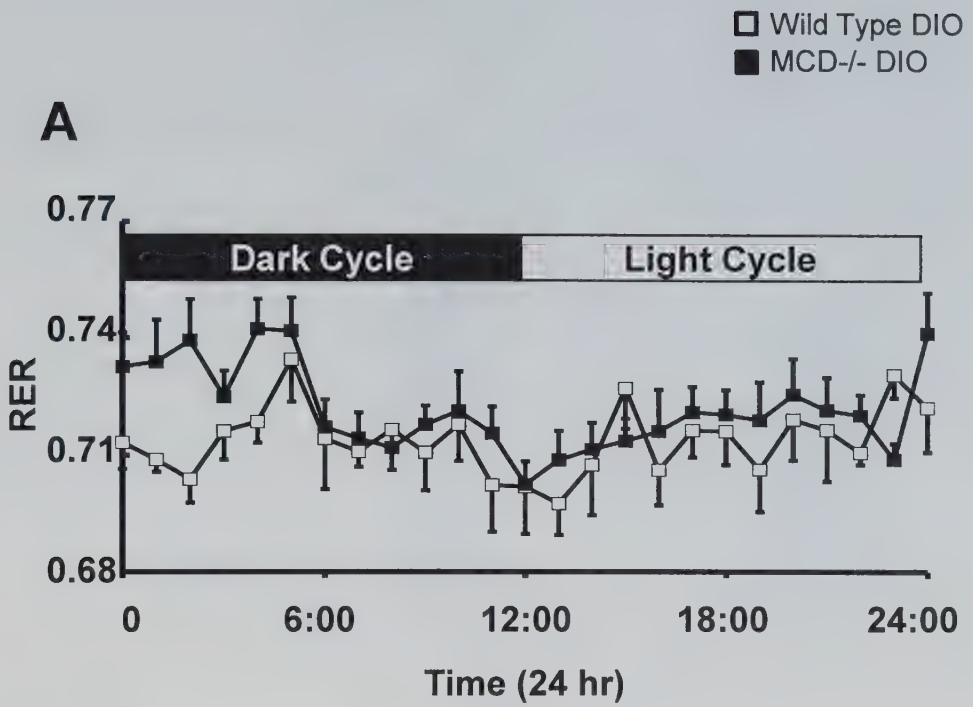
Wild Type DIO
MCD-/- DIO
A
0.77
0.74
0.71
0.68
RER
Dark Cycle
Light Cycle
0
6:00
12:00
18:00
24:00
Time (24 hr)

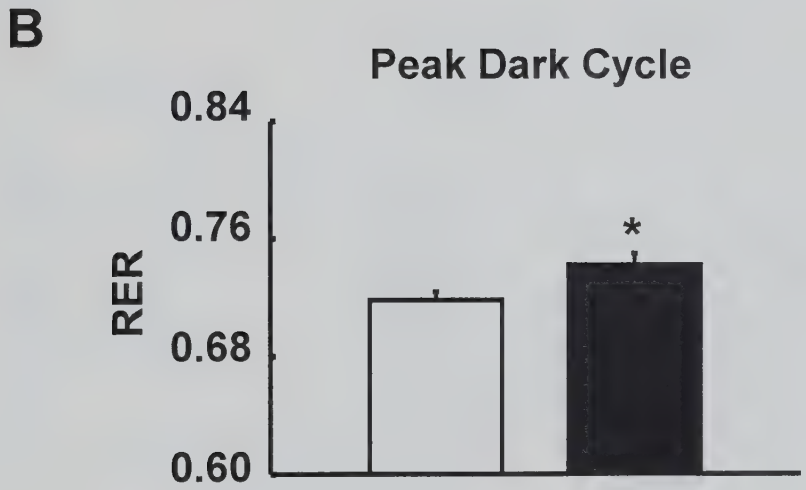
B
Peak Dark Cycle
0.84
0.76
0.68
0.60
RER
*

FIGURE 4-3

Figure 4-3: *In vivo metabolic parameters in DIO WT and MCD-/- mice.*

A: 24 hr respiratory exchange ratio (RER), B: peak dark cycle RER, **C: average oxygen consumption, D: average heat production,** E: 24 hr ambulatory activity, and F: 24 hr food intake in WT and MCD-/- mice following 8 wks of DIO. Values represent mean ± SE (n = 6-9).

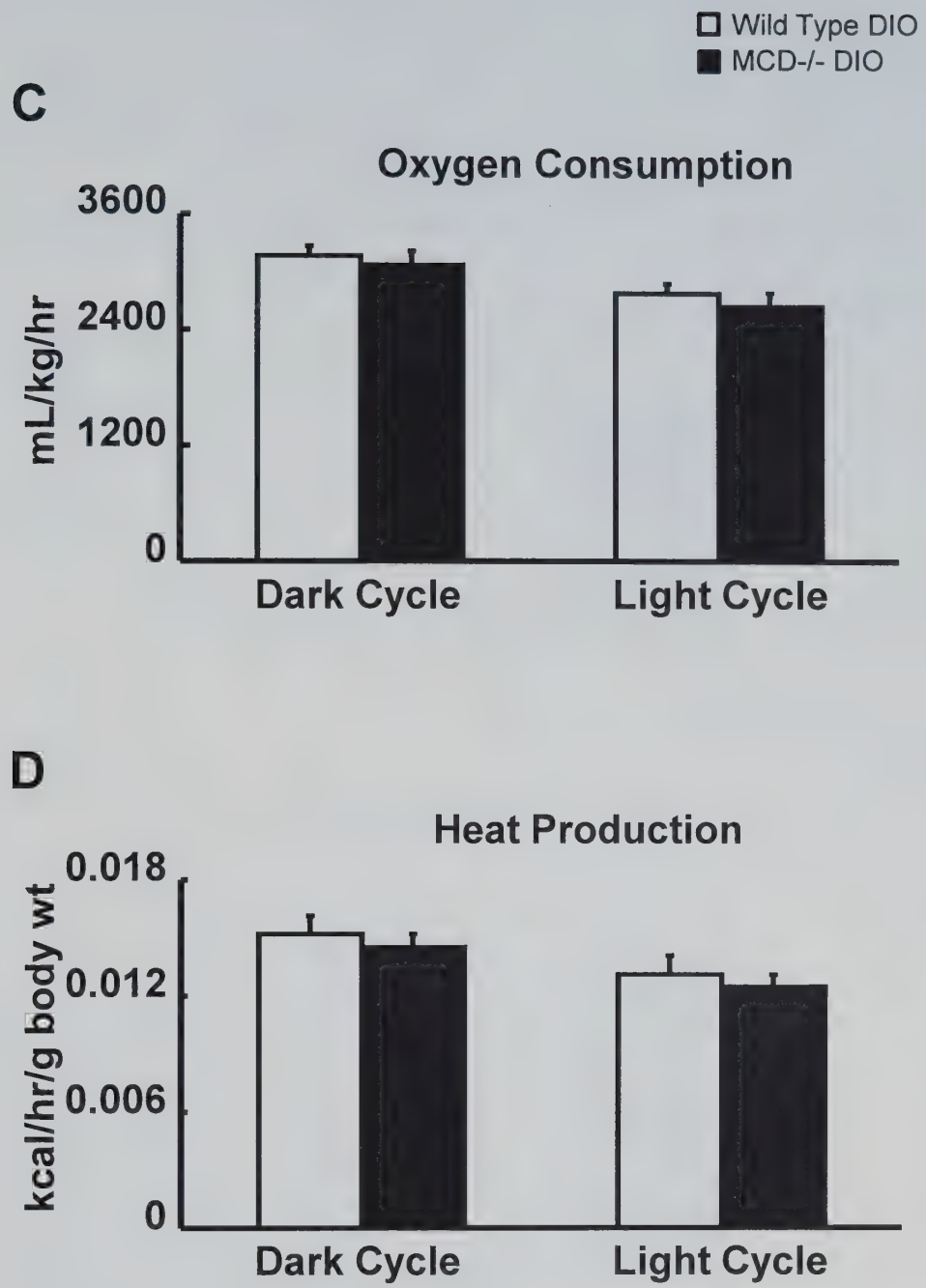
Wild Type DIO
MCD-/- DIO
C
Oxygen Consumption
3600
2400
1200
0
mL/kg/hr
Dark Cycle
Light Cycle
D
Heat Production
0.018
0.012
0.006
0
kcal/hr/g body wt
Dark Cycle
Light Cycle

FIGURE 4-3

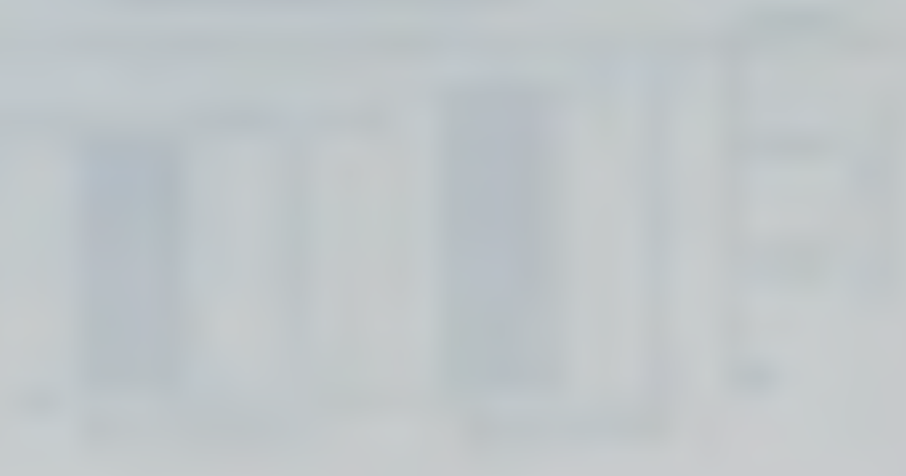

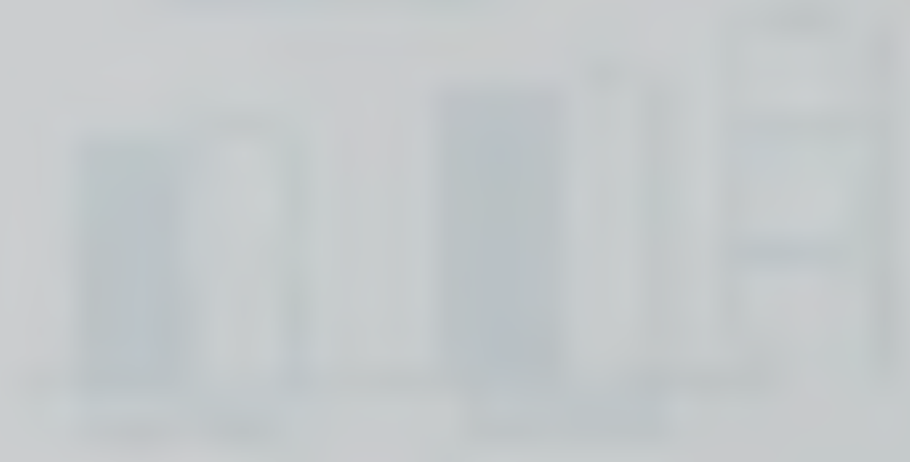

Figure 4-3: *In vivo metabolic parameters in DIO WT and MCD-/- mice.*

A: 24 hr respiratory exchange ratio (RER), B: Peak dark cycle RER, C: Average oxygen consumption, D: Average heat production, **E: 24 hr ambulatory activity, and F: 24 hr food intake in WT and MCD-/- mice following 8 wks of DIO.** Values represent mean ± SE (n = 6-9).

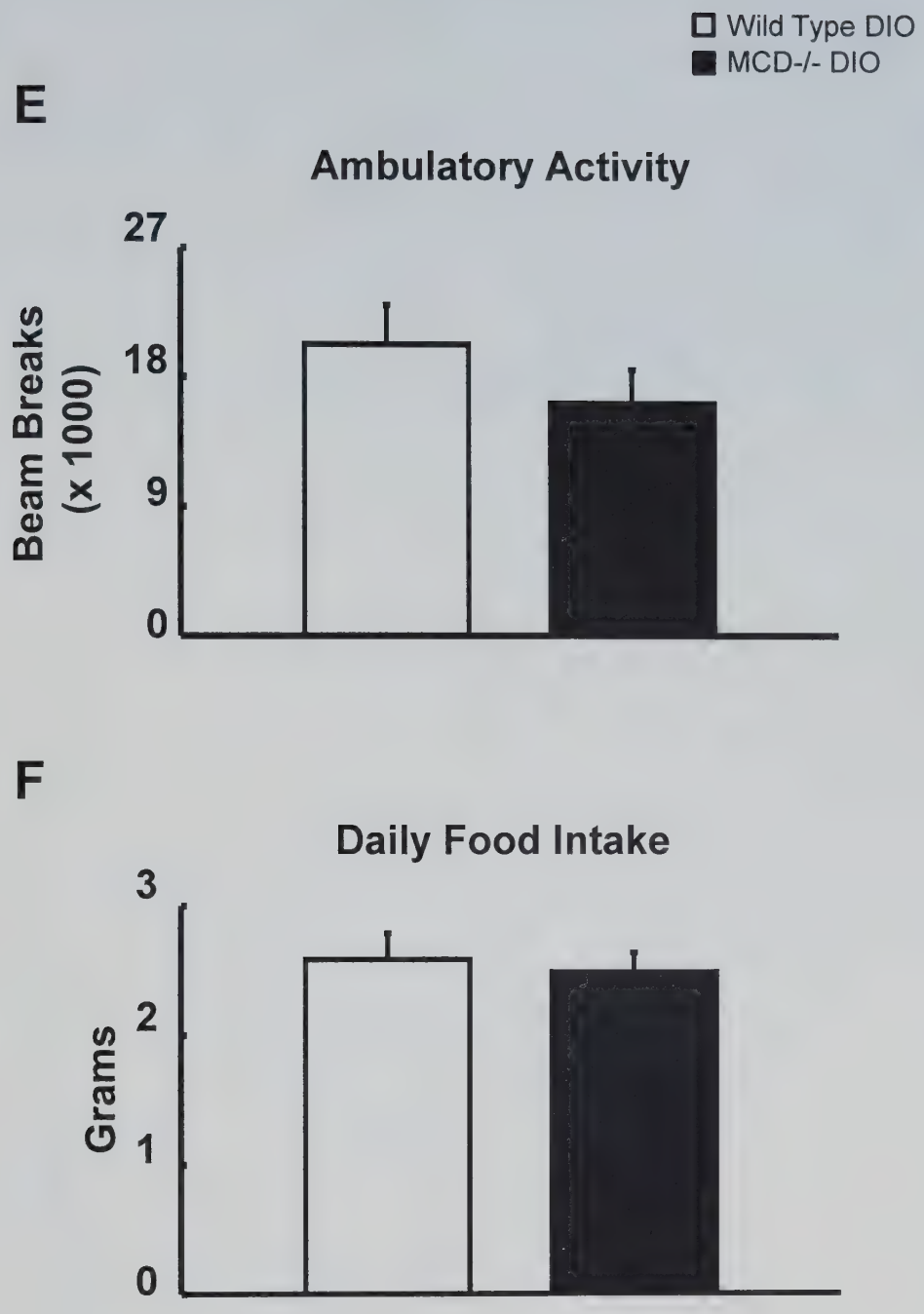
Wild Type DIO
MCD-/- DIO
E
Ambulatory Activity
Beam Breaks (x 1000)
27
18
9
0
F
Daily Food Intake
Grams
3
2
1
0

FIGURE 4-3

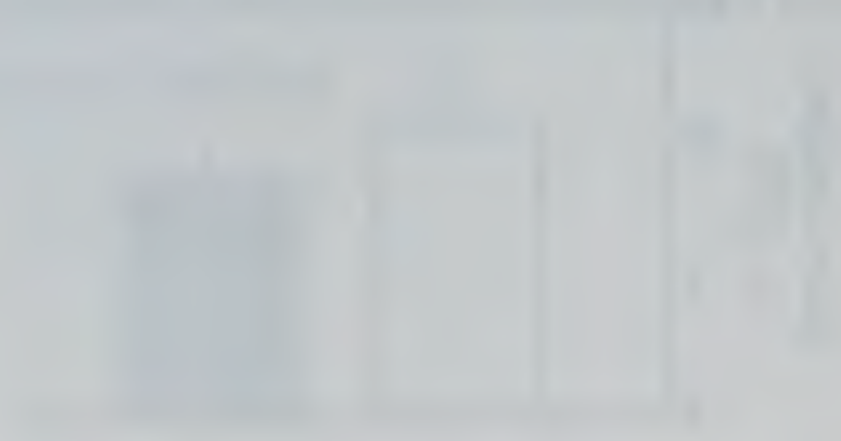

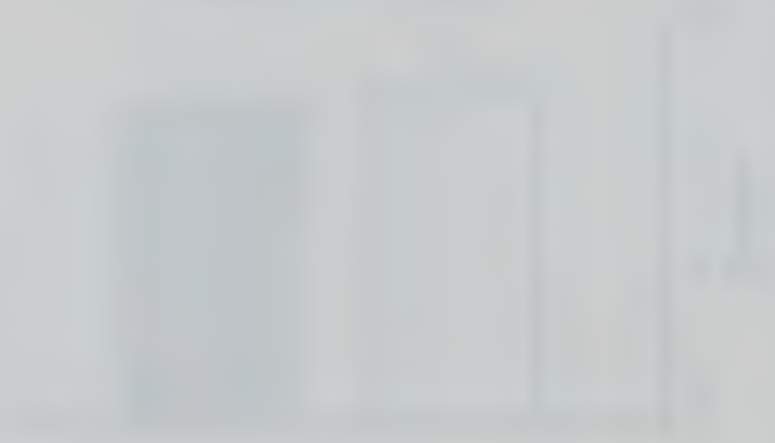

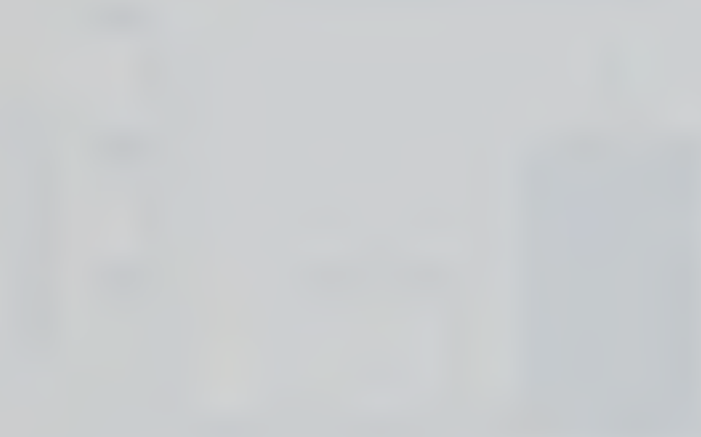

Figure 4-4: *Improved exercise capacity in MCD-/- mice subjected to DIO.*

A: Exercise time, and B: distance on a running treadmill are improved in DIO MCD-/- mice versus their WT littermates. C: Gastrocnemius ATP levels, and D: AMPK phosphorylation in WT and MCD-/- mice following 10 wks of DIO. Values represent mean ± SE (n = 6-9). Differences were determined using a two-tailed Student's *t*-test. $*P<0.05$, significantly different from WT mice.

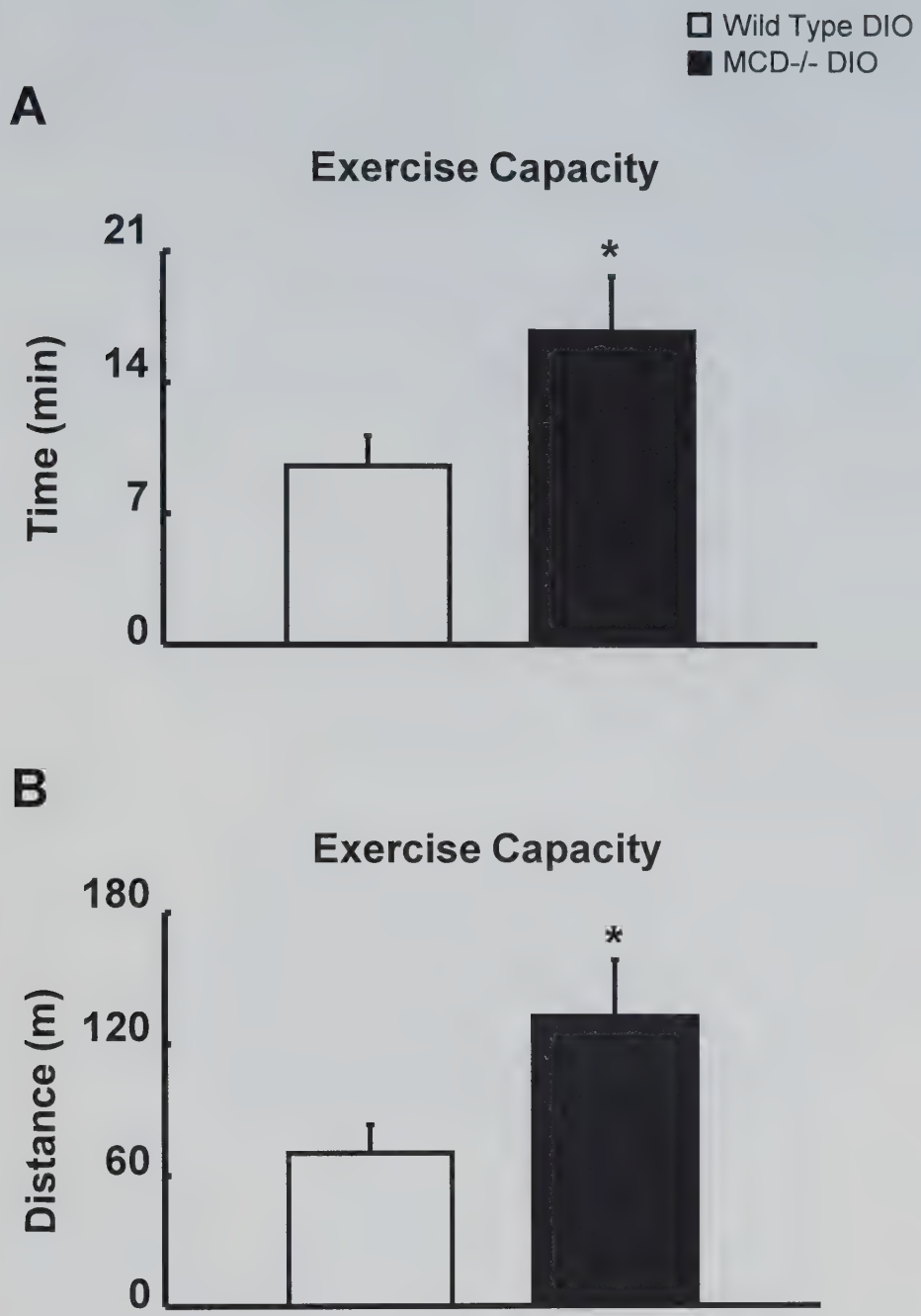
Wild Type DIO
MCD-/- DIO
A
Exercise Capacity
Time (min)
21
14
7
0
*
B
Exercise Capacity
Distance (m)
180
120
60
0
*

FIGURE 4-4

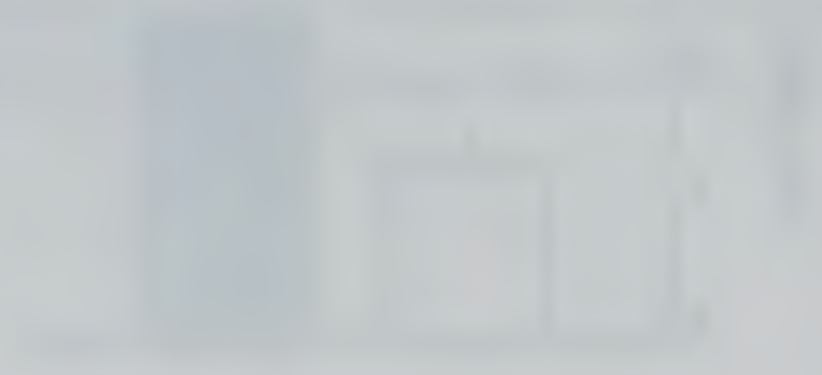

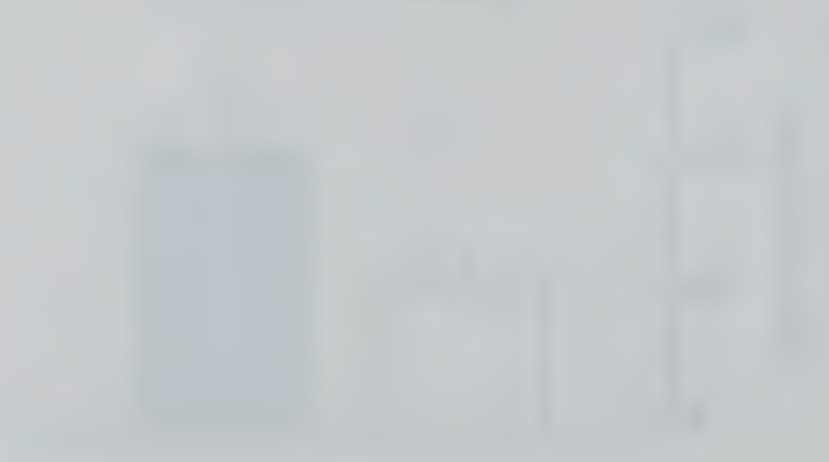

Figure 4-4: *Improved exercise capacity in MCD-/- mice subjected to DIO.*

A: Exercise time, and B: distance on a running treadmill are improved in DIO MCD-/- mice versus their WT littermates. **C: Gastrocnemius ATP levels, and D: AMPK phosphorylation in WT and MCD-/- mice following 10 wks of DIO.** Values represent mean ± SE (n = 6-9). Differences were determined using a two-tailed Student's *t*-test. $*P<0.05$, significantly different from WT mice.

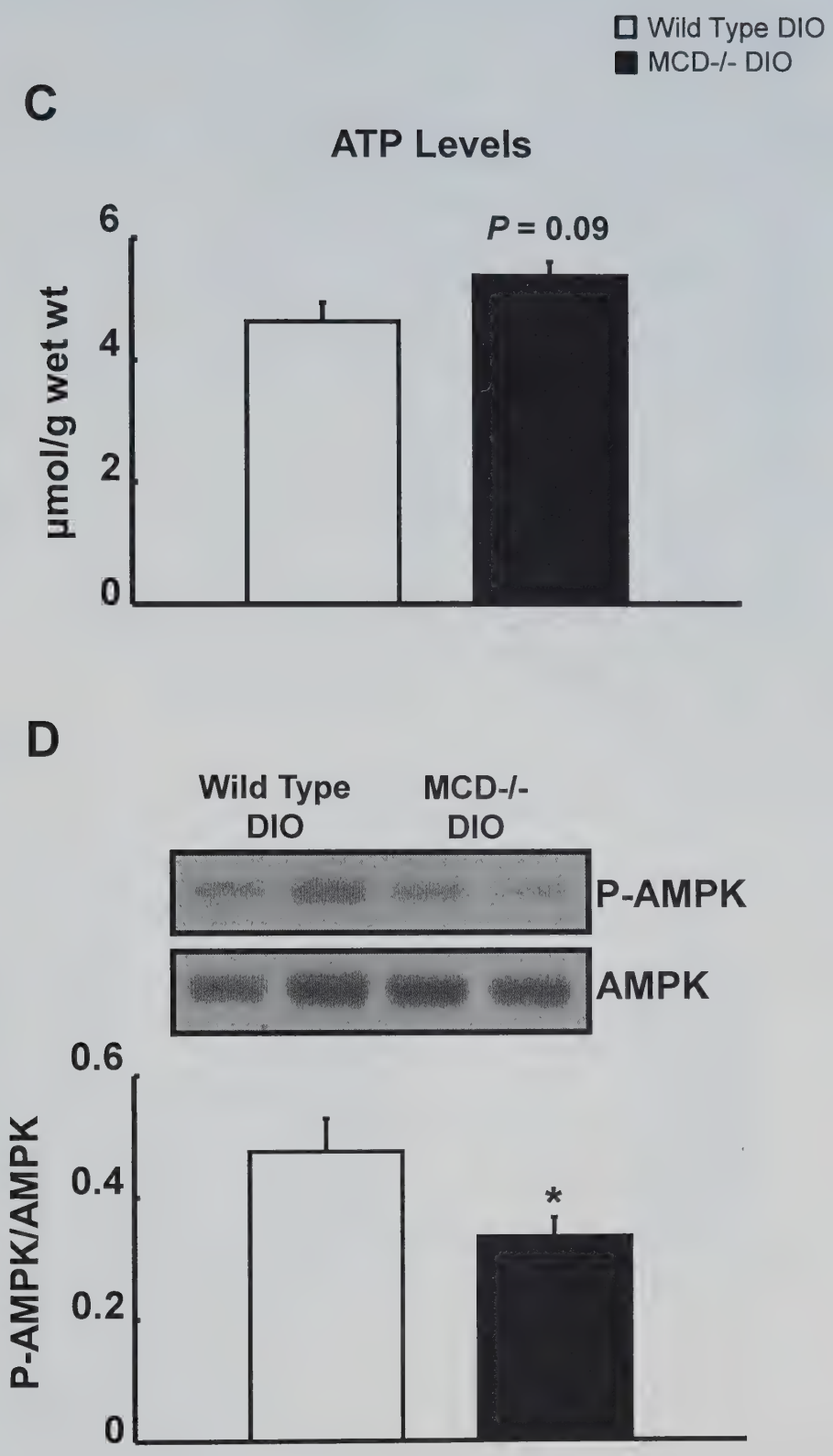
Wild Type DIO
MCD-/- DIO
C
ATP Levels
P = 0.09
µmol/g wet wt
6
4
2
0
D
Wild Type DIO
MCD-/- DIO
P-AMPK
AMPK
P-AMPK/AMPK
0.6
0.4
0.2
0
*

FIGURE 4-4

Figure 4-5: *Skeletal muscle lipid metabolite content in WT and MCD-/- subjected to DIO.*

A: Long chain acyl CoA and B: triacylglycerol content in gastrocnemius muscle of WT and MCD-/- mice fed a low or high fat diet for 12 wks. Values represent mean ± SE (n = 5 in each group except the low fat fed MCD-/- mice, where n = 11). Differences were determined using a two-way ANOVA followed by Bonferroni post-hoc analysis. $^{*}P<0.05$, significantly different from low fat diet counterpart. $^{\dagger}P<0.05$, significantly different from diet-matched WT counterpart.

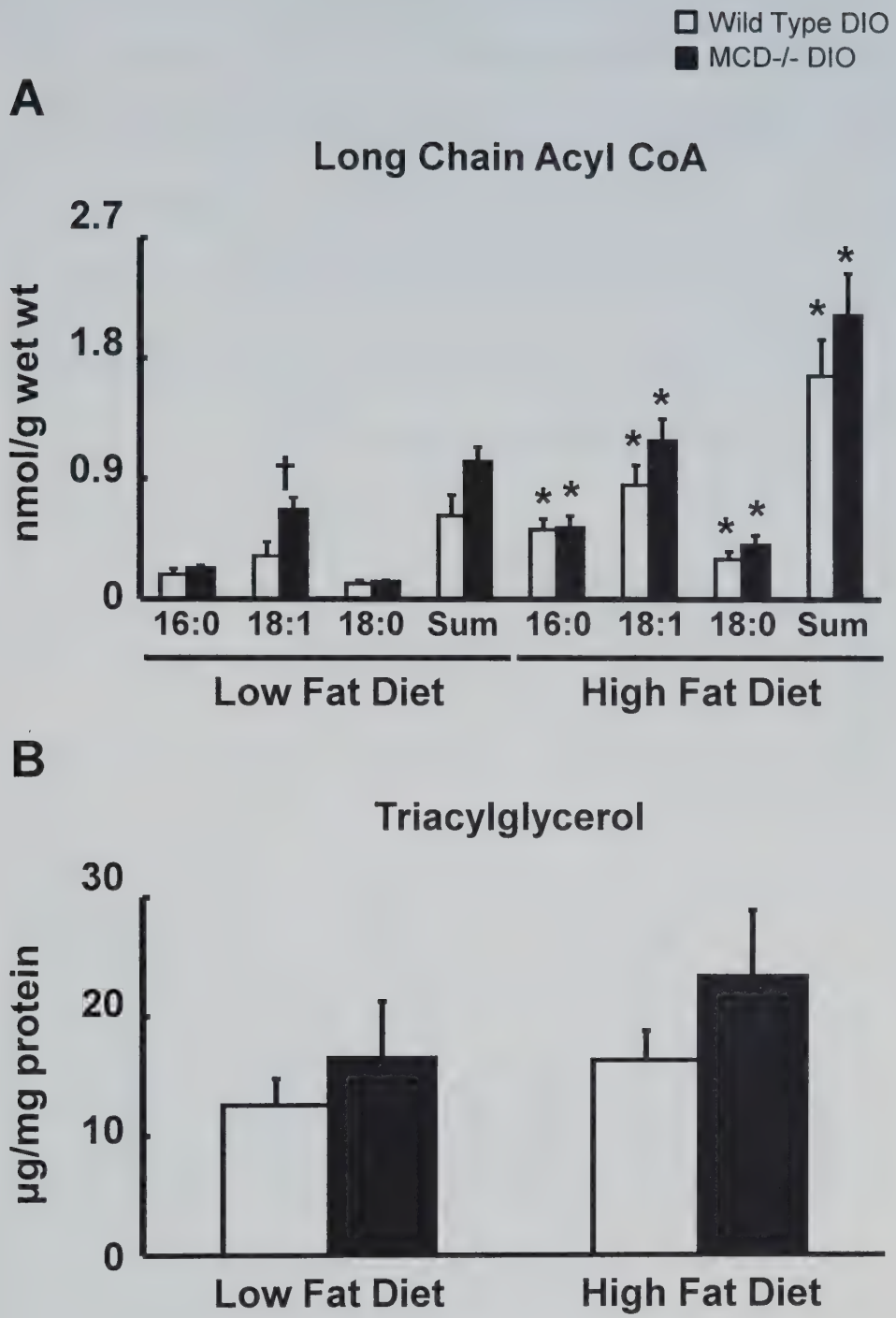
Wild Type DIO
MCD-/- DIO
A
Long Chain Acyl CoA
nmol/g wet wt
2.7
1.8
0.9
0
16:0
18:1
18:0
Sum
16:0
18:1
18:0
Sum
Low Fat Diet
High Fat Diet
B
Triacylglycerol
µg/mg protein
30
20
10
0
Low Fat Diet
High Fat Diet

FIGURE 4-5

Figure 4-6: *Metabolic profiling reveals a reduction in incomplete fatty acid oxidation by-products in skeletal muscle of MCD-/- mice subjected to DIO.*

A: Malonylcarnitine, B: acylcarnitine (short and long chain), and C: organic acid (lactate, pyruvate, and tricarboxylic acid cycle intermediates) content in gastrocnemius muscle of WT and MCD-/- mice following 12 wks of DIO. Values represent mean ± SE (n = 5). Differences were determined using a two-tailed Student's *t*-test. $*P<0.05$, significantly different from WT mice.

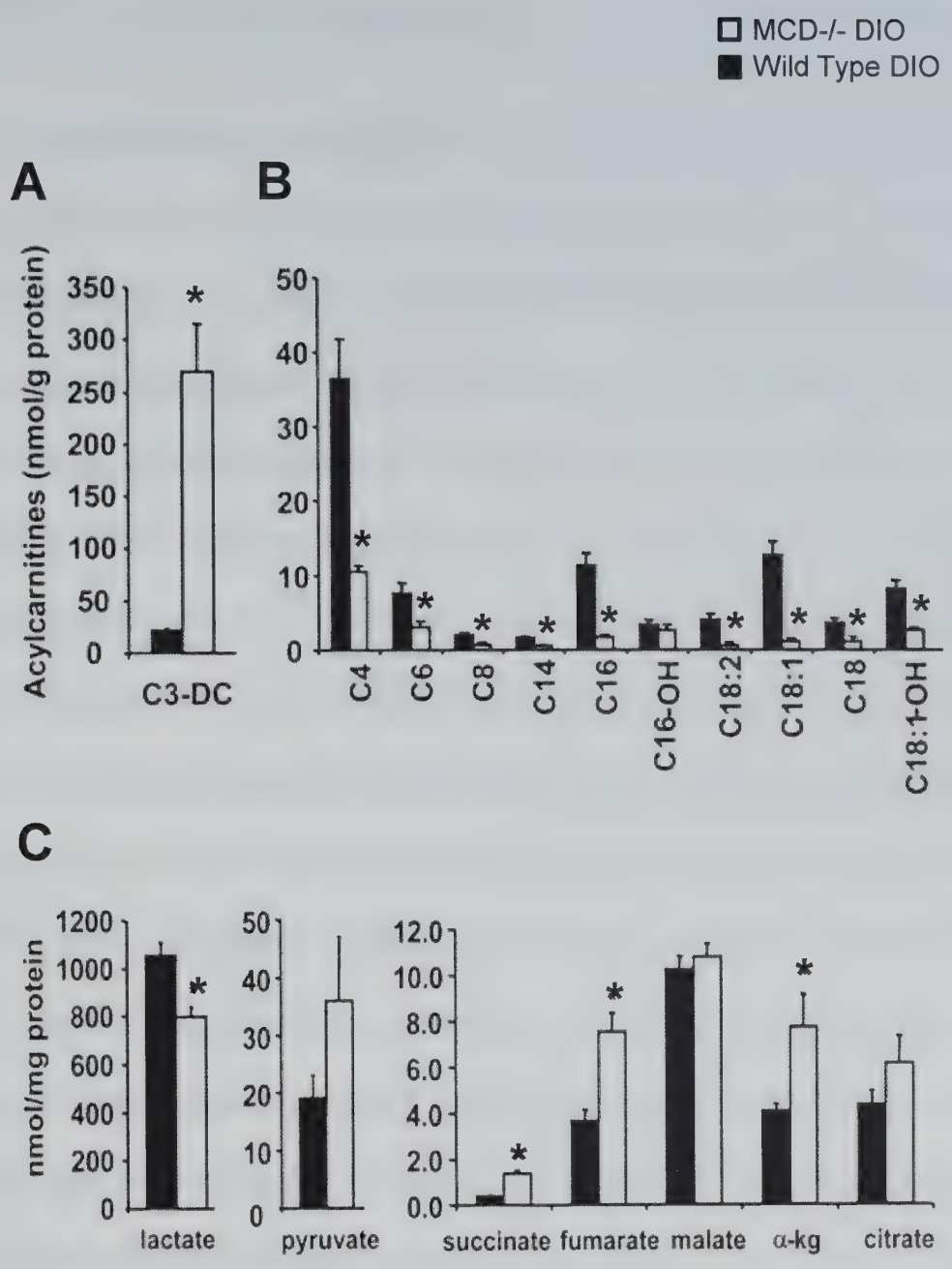
MCD-/- DIO
Wild Type DIO
A
B
Acylcarnitines (nmol/g protein)
350
300
250
200
150
100
50
0
C3-DC
50
40
30
20
10
0
C4
C6
C8
C14
C16
C16-OH
C18:2
C18:1
C18
C18:1-OH
C
nmol/mg protein
1200
1000
800
600
400
200
0
lactate
50
40
30
20
10
0
pyruvate
12.0
10.0
8.0
6.0
4.0
2.0
0.0
succinate
fumarate
malate
α-kg
citrate

FIGURE 4-6

In summary, our findings demonstrate and support a recent paradigm shift with regards to fatty acid metabolism in the skeletal muscle and the development of insulin resistance as a result of obesity (140, 200, 280, 311). Popular belief is that a general impairment in skeletal muscle oxidative capacity is a major contributor to the accumulation of intramyocellular lipid metabolites, such as TAG, long chain acyl CoA, ceramide, and DAG, that interfere with the insulin response (68, 69, 305, 353, 385, 413). However, our MCD-/- mouse model is a model of reduced fatty acid oxidation, as seen by their higher levels of malonyl CoA in a number of tissues (i.e. skeletal muscle and heart), that would inhibit the rate-limiting enzyme of mitochondrial fatty acid uptake and oxidation, CPT 1 (257, 262, 405). Therefore, our findings showing that MCD-/- mice are protected against obesity-induced insulin resistance (as indicated by glucose and insulin tolerance testing) contradicts current dogma, and suggests that strategies aimed at reducing fatty acid oxidation in muscle may actually be protective against the development of insulin resistance, as initially proposed by Randle and colleagues in the 1960s (316, 317).

Indeed, evidence for CPT 1 inhibition in MCD-/- mice is apparent in the acylcarnitine profile, as the vast majority of acylcarnitine species were decreased in MCD-/- mice, except for malonylcarnitine, which arises from the greater malonyl CoA levels in these mice. The lower levels of long chain acylcarnitine species in DIO MCD-/- mice, in conjunction with greater levels of TCA cycle

intermediates, illustrates that skeletal muscle incomplete fatty acid oxidation rates are significantly lower (280). During obesity-induced insulin resistance, the TCA cycle cannot accommodate the increased delivery of long chain acyl CoA species' being oxidized in the mitochondria, resulting in the re-esterification of long chain acyl CoA into long chain acylcarnitine (280, 393). Treatments that improve insulin sensitivity in muscle of obese rodents, such as exercise, reduce the accumulation of long chain acylcarnitines (200, 393). This is because exercise increases the demand on the TCA cycle, allowing mitochondrial fatty acids to be completely oxidized (200, 280, 393). It is important to note though, that the acylcarnitines per se are probably not directly inducing insulin resistance. We propose that rather than being direct mediators, the accumulation of long chain acylcarnitine species' serves as a marker for mitochondrial overload or some form of mitochondrial stress, such as increased mitochondrial oxidative stress and H_2O_2 production (14, 37). Nonetheless, our findings have profound implications for the design of novel therapies against obesity-associated skeletal muscle insulin resistance, and suggest that strategies aimed at simply increasing mitochondrial fatty acid oxidation, without an actual increase in work and energy demand of the muscle may provide no benefit.

This proposed reduction in skeletal muscle mitochondrial fatty acid oxidation rates contributing to the development of insulin resistance has resulted in the proposal that directly stimulating fatty acid oxidation can benefit insulin resistant muscle, which is in contrast to the historical work performed by Randle and colleagues in the 1960s (316, 317). However, more recent studies by the

Shulman laboratory involving ^{31}P-MRS in human patients have suggested that the Randle Cycle may not operate in skeletal muscle (304, 305, 353), explaining why accelerating fatty acid oxidation in muscle would not result in a compensatory decrease in carbohydrate oxidation and metabolism. However, recent work in our laboratory has shown that short term high fat feeding of rats or fasting, both of which would increase fatty acid delivery to the muscle, result in a significant inhibition of gastrocnemius muscle PDH activity, supporting an operating Randle Cycle in muscle (unpublished data). The results in this study also support the concept that the Randle Cycle is operative in skeletal muscle, as PDH activity and glucose oxidation rates were increased in the skeletal muscle of DIO MCD-/- mice. In addition, the higher RER values during the dark cycle in DIO MCD-/- mice also supports an operating Randle Cycle in muscle, indicating that these animals have an increased preference for carbohydrates as an oxidative fuel.

Interestingly, we also observe an increase in exercise capacity in DIO MCD-/- mice, which seems somewhat unexpected, as one might postulate that an impaired ability to oxidize fatty acids would starve the muscle of needed energy to sustain the elevated work demand required for exercise. Nonetheless, the capacity for muscle to consume oxygen during exercise versus its resting capacity is anywhere from 30-50 fold greater in muscle of obese individuals, and can be even as high as 100 fold greater in healthy individuals (140). Furthermore, exercise induces changes in CPT 1, although not understood, that render it more resistant to inhibition via malonyl CoA (48, 201). We propose that because the muscle of DIO MCD-/- mice is not undergoing the mitochondrial overload that

the muscle of DIO WT mice is subjected to, as determined via the acylcarnitine and organic acid profiling, it has an improved energetic status that allows the animal to exercise longer. In support of this statement, we observed a trend to increased ATP levels in the gastrocnemius muscle of DIO MCD-/- mice, as well a reduction in AMPK phosphorylation. AMPK is a fuel sensor that is activated in times of low energy status via phosphorylation by a number of upstream kinases (56, 97, 195). Therefore, the lower phosphorylation of AMPK observed in DIO MCD-/- mice suggests that overall energetic status (i.e. ATP levels) is greater in these animals, allowing them to exercise over a longer time period.

Last, the results of this study show a disassociation between the intramyocellular accumulation of lipid metabolites and the development of skeletal muscle insulin resistance. Previous studies have provided strong evidence that the accumulation of long chain acyl CoA and other lipid metabolites, such as DAG, are powerful contributors to the development of obesity-induced insulin resistance (64, 188, 318, 353). However, our findings in DIO MCD-/- mice show that a number of long chain acyl CoA species' accumulate to a similar extent to that observed in DIO WT mice, yet they show a profound protection against obesity-induced insulin resistance. Moreover, we actually do not observe a DIO-associated increase in intramyocellular TAG, though there is a trend to a higher gastrocnemius muscle TAG content in DIO MCD-/- mice. It is important to note though, that the sometimes observed dramatic increase in skeletal muscle TAG content can be confounded by the

presence of surrounding adipocytes, which may be accidentally extracted during tissue extraction and skew potential measurements (118, 356, 418).

Regardless, our findings that demonstrate a disassociation between intramyocellular lipid and insulin resistance is not unwarranted, as there have been a significant amount of recent studies that support our findings. For example, overexpression of DAG acyl transferase 1 (DGAT1) increases intramyocellular TAG content, but also provides significant protection against DIO-associated insulin resistance (231). Furthermore, contractile stimulation of hind limb muscle from obese Zucker rats improves insulin-stimulated glucose metabolism, but is associated with a dramatic elevation of intramyocellular long chain acyl CoA content (393). Similar findings are observed in humans, as the exercise paradox shows that aerobic exercise training of obese patients significantly improves their insulin sensitivity, but induces the accumulation of intramyocellular TAG (90, 129). Unfortunately, we did not measure intramyocellular DAG and ceramide content in the muscle of DIO MCD-/- mice, and such studies will be important to perform in the future, as these lipid metabolites may be more important towards the development of skeletal muscle insulin resistance (64, 68, 153, 353, 385).

Overall, our findings show that MCD-/- mice are protected against the insulin resistance associated with DIO, which is accompanied by a reduction of incomplete fatty acid oxidation by-products in muscle, and enhanced glucose oxidation rates and PDH activity. We also found that MCD-/- mice subjected to DIO have a greater exercise capacity than their WT littermates, which may result

from an improved energetic status. Because these experiments were part of a prevention study, it will be important in future studies to determine whether MCD inhibition/deficiency can also reverse the insulin resistance associated with DIO. Nonetheless, our observations do suggest that MCD is an exciting novel therapeutic target for the treatment of obesity-induced insulin resistance, and challenge current dogma regarding skeletal muscle fatty acid metabolism, lipid metabolite accumulation, and insulin sensitivity.

CHAPTER 5.

Inhibition of 3-ketoacyl CoA thiolase is unable to reverse diet-induced insulin resistance, but does prevent diet-induced cardiac dysfunction and hypertrophy

---

My role in this work involved performing all experiments (except those noted below), as well as the writing of the manuscript. Panakkezhum Thomas performed the HPLC analysis of the long chain acyl CoA, Wendy Keung determined the intramyocellular DAG and ceramide content, and Donna Beker performed the ultrasound echocardiography.

Manuscript Status: This manuscript is currently in preparation to be submitted to *Diabetes* for publication as a brief report.

CHAPTER 5.

Inhibition of 3-ketoacyl CoA thiolase is unable to reverse diet-induced insulin resistance, but does prevent diet-induced cardiac dysfunction and hypertrophy

Abstract

Objective – It has been postulated that insulin resistance results from an impairment in skeletal muscle fatty acid oxidation, causing an accumulation of cytosolic lipid metabolites that impede insulin signaling. On the contrary, our recent work shows that inhibition of fatty acid oxidation secondary to the inhibition of its mitochondrial uptake prevents diet-induced insulin resistance. Our aim was to determine if direct inhibition of fatty acid oxidation could reverse diet-induced insulin resistance.

Research Design And Methods – C57BL/6 mice were fed a high fat diet for 10 wks before receiving daily treatment with trimetazidine (15mg/kg) or saline for a 3 wk period. Insulin resistance was assessed via glucose tolerance and insulin tolerance testing, while lipid metabolite accumulation was assessed in gastrocnemius muscles. Cardiac function was assessed via ultrasound echocardiography.

Results – Although inhibition of fatty acid oxidation with trimetazidine led to a further increase in plasma triacylglycerol (298 ± 16 vs. 241 ± 13 mg/dL) and long chain acyl CoA (1.16 ± 0.14 vs. 0.73 ± 0.09 nmol/g wet weight) than high fat

feeding alone, this did not exacerbate the insulin resistant state (25 ± 7 vs. 21 ± 5 % decrease in blood glucose concentration 30 min post insulin injection). Finally, diet-induced cardiac hypertrophy and contractile dysfunction were prevented via trimetazidine treatment.

Conclusions – Our data reveal that direct inhibition of fatty acid oxidation is insufficient to reverse diet-induced insulin resistance, but does have beneficial effects on cardiac function, possibly explaining trimetazidine's beneficial effects on patients with dilated cardiomyopathy.

Obesity and type 2 diabetes commonly occur together, and are thought of as diseases of the Western World due to lifestyles characterized by the excessive consumption of food and physical inactivity. This causes hyperlipidemia, which is believed to be a major precipitating event in the development of skeletal muscle insulin resistance (182, 281).

The current investigation aimed to advance our understandings of lipid-induced insulin resistance in skeletal muscle, the major site of insulin-stimulated glucose disposal. Numerous studies *in vivo* and *in vitro* have provided strong evidence that lipid surplus leads to an accumulation of intramyocellular lipid-derived metabolites, which coincide with the development of insulin resistance (353, 367). Previous studies have postulated that this accumulation of lipid-derived metabolites results from an impaired mitochondrial fatty acid oxidative capacity (69, 383, 413, 447). Thus, esterified fatty acids in the form of long chain acyl CoA are diverted away from CPT 1, the rate limiting enzyme in mitochondrial uptake and oxidation of fatty acids, towards TAG and other lipid metabolites such as ceramide and DAG. These metabolites are believed to activate classical PKC isoforms that phosphorylate and inactivate IRS proteins, preventing the insulin response (353, 367). It has been postulated that enhancing the ability of the muscle to oxidize fat can protect against insulin resistance, by preventing the accumulation of these lipid metabolites and removing inhibition of the insulin signaling cascade (47, 69, 203, 353, 413).

This theory has come under fire of recent, due to a number of studies showing clear dissociation between intramyocellular lipid metabolite accumulation and insulin sensitivity (12, 231, 310, 393). Our most recent work reveals that insulin resistance is actually characterized by elevated rates of incomplete fatty acid oxidation in muscle, rather than a reduction in fatty acid oxidation (200, 202). Mice with a genetic deficiency for MCD, the enzyme responsible for degrading malonyl CoA, a potent endogenous inhibitor of CPT 1, experience reduced mitochondrial fatty acid uptake and rates of incomplete fatty acid oxidation, but are protected from the development of insulin resistance (202). In support of this, PPARα overexpressing mice have increased rates of fatty acid oxidation and are insulin resistant, however, treatment with oxfenicine, a CPT 1 inhibitor, restores insulin sensitivity in these animals (108).

A common feature of these 2 studies is that insulin resistance was prevented by treatments that inhibited mitochondrial fatty acid uptake and oxidation. Thus, the important question arises of whether it is, 1) the inhibition of mitochondrial fatty acid uptake, or 2) the inhibition of mitochondrial fatty acid oxidation, that is responsible for preventing/reversing insulin resistance. This investigation addresses this important issue in further detail. Our objective was to determine if direct inhibition of fatty acid oxidation via treatment with trimetazidine would be sufficient to reverse diet-induced insulin resistance. Trimetazidine is a long chain 3-ketoacyl thiolase (3-KAT) inhibitor (236), the last enzyme involved in mitochondrial fatty acid oxidation. Therefore, fatty acids would still have free access into the mitochondria through CPT 1.

Animal Studies

All animals received care according to the Canadian Council on Animal Care and the University of Alberta Health Sciences Animal Welfare Committee. 24 – 26-wk-old C57BL/6 mice were placed on a standard chow/low fat diet (4% kcal from lard) or high fat diet (60% kcal from lard, Research Diets; D12492) for a 10 wk period. At the end of wk 10, animals were IP injected daily with trimetazidine hydrochloride (15mg/kg) dissolved in saline or vehicle control for a 3 wk period. At the end of the 3 wk treatment protocol, animals were sacrificed via IP injection of sodium pentobarbital (12 mg) in the fed state in the middle of the dark cycle. Tissues were excised and immediately frozen in liquid N_2. Protocols for assessment of intramyocellular lipid metabolite accumulation, GC/MS metabolic profiling, GTTs, ITTs, indirect calorimetry, exercise capacity, *in vivo* cardiac function, immunoblotting, and statistical analysis are described in **Chapter 2** of this thesis.

Treatment with trimetazidine has no effect on body weight or glucose tolerance of mice subjected to diet-induced insulin resistance

As expected, mice fed a high fat diet for 10 wks experienced a significant increase in weight gain (Figure 5-1A) and became glucose intolerant (Figure 5-2A). Starting at wk 11, animals received daily IP injections of either trimetazidine (15 mg/kg) or vehicle control (saline). Following 1 wk of treatment with trimetazidine, we observed no effect on the body weight of DIO mice (Figure 5-1B/C), but plasma TAG levels were elevated with no change in plasma FFA levels (Figure 5-1D/E). In addition, GTT (Figure 5-2B) and ITT (Figure 5-2C/D) studies after 1 wk of treatment revealed that inhibiting fatty acid oxidation with trimetazidine had no beneficial effects against diet-induced insulin resistance.

Treatment with trimetazidine increases the reliance on carbohydrate oxidation as a fuel source in diet-induced insulin resistant mice

Diet-induced insulin resistant mice were placed in Oxymax metabolic cages after 2 wks of treatment with trimetazidine or vehicle control for whole body metabolic assessment. Our results demonstrated that treatment of insulin-resistant mice with trimetazidine had no effect on whole body oxygen consumption, heat production, ambulatory activity, or 24 hr food intake, but significantly increased the RER during the light cycle (Figure 5-3A-F). This

latter observation is consistent with a "Randle Cycle" effect, whereby inhibition of fatty acid oxidation results in a compensatory increase in glucose oxidation rates (315). Moreover, treatment with trimetazidine had no effect on overall aerobic exercise capacity as determined via treadmill running (*data not shown*).

Intramyocellular lipid metabolite accumulation in diet-induced insulin resistant mice treated with trimetazidine

Numerous studies from our laboratory and others (188, 202, 367, 413) have shown that high fat diet-induced insulin resistance leads to an accumulation of intramyocellular lipid metabolites, which include TAG, long chain acyl CoA, DAG, and ceramide. Inhibition of fatty acid oxidation with trimetazidine resulted in a trend to an increase in gastrocnemius TAG content, which was accompanied via significant increase in gastrocnemius long chain acyl CoA content (Figure 5-4A/B). However, these animals experienced no changes in the accumulation of gastrocnemius DAG and ceramide content (Figure 5-4C/D). GC/MS metabolic profiling of gastrocnemius muscle from control and trimetazidine treated insulin resistant mice demonstrated no change in any of the intermediates from the TCA cycle (Figure 5-4E). Although the majority of long chain acylcarnitine species such as palmitoyl and steroylcarnitine did not experience a further accumulation in gastrocnemius muscle of insulin resistant mice treated with trimetazidine (75 ± 23 vs. 41 ± 5 and 55 ± 22 vs. 30 ± 6 nmol/g protein, respectively), there was a trend to a further increase in other long chain acylcarnitine species (Figure 5-4F/G).

Treatment with trimetazidine prevents diet-induced cardiac hypertrophy and contractile dysfunction

While trimetazidine did not have beneficial effects on diet-induced insulin resistance, numerous studies have shown that trimetazidine has protective effects against cardiac I/R injury, and trimetazidine is actually used clinically in many European countries as a therapy for stable angina (71, 171, 236, 402). Hence, we measured *in vivo* cardiac function via 2D M mode ultrasound echocardiography, and observed that trimetazidine prevented the diet-induced increase in LV posterior wall and intraventricular septal wall thickness during diastole (Table 5-1). Furthermore, trimetazidine treatment prevented the diet-induced decline in EF (Table 5-1). Finally, assessment of diastolic function via tissue Doppler echocardiography revealed that chronic high fat feeding causes a decline in the mitral E'/A' ratio, while increasing the mitral E/E' ratios, both of which are suggestive early signs of diastolic dysfunction development (Table 5-1). Interestingly, trimetazidine treatment prevented the development of diastolic dysfunction in diet-induced insulin resistant mice (Table 5-1).

Table 5-1: *In vivo assessment of cardiac function and LV wall dimensions in DIO mice treated with trimetazidine.*

	Pre-Control	Post-Control	%Change (n=6)	Pre-Tri-metazidine	Post-Tri-metazidine	%Change (n=6)
EF (%)	63.8±2.3	58.1 ± 2.2	-8.5 ± 3.7	59.7 ± 1.6	61.4 ± 1.2	3.2 ± 2.9*
FS (%)	34.4 ± 1.7	30.3 ± 1.5	-11.2 ± 5.0	31.4 ± 1.1	32.5 ± 0.8	4.1 ± 3.9*
LV Mass (mg)	101.4 ± 6.8	118.9 ± 7.0	18.6 ± 7.8	93.4 ± 3.1	96.5 ± 6.1	3.8 ± 6.8
IVS:d (mm)	0.81 ± 0.03	0.97 ± 0.03	20.9 ± 5.6	0.79 ± 0.02	0.82 ± 0.04	2.8 ± 3.9*
LVID:d (mm)	4.11 ± 0.10	3.99 ± 0.09	-2.7 ± 1.8	4.05 ± 0.10	4.00 ± 0.09	-1.0 ± 3.1
LVPW:d (mm)	0.80 ± 0.03	0.93 ± 0.04	16.2 ± 4.8	0.77 ± 0.02	0.81 ± 0.02	5.0 ± 1.8*
IVS:s (mm)	1.20 ± 0.01	1.29 ± 0.03	7.6 ± 3.7	1.17 ± 0.03	1.26 ± 0.05	7.2 ± 3.2
LVID:s (mm)	2.70 ± 0.11	2.79 ± 0.06	3.8 ± 4.0	2.78 ± 0.07	2.70 ± 0.08	-2.6 ± 3.8
LVPW:s (mm)	1.22 ± 0.02	1.23 ± 0.04	1.2 ± 4.0	1.13 ± 0.03	1.21 ± 0.04	7.5 ± 2.2
E'/A'	1.13 ± 0.05	0.92 ± 0.04	-17.5 ± 3.4	1.18 ± 0.08	1.13 ± 0.07	-1.7 ± 3.9*

In vivo cardiac function and ventricular wall measurements were assessed via ultrasound echocardiography in isoflurane anesthetized obese mice treated with vehicle control or trimetazidine. Values represent means ± SE. Differences were determined using a two-tailed Student's *t*-test. $^{*}P<0.05$, indicates a significant difference from control treated mice. d = diastole, EF = Ejection fraction, FS = Fractional shortening, IVS = intraventricular septum, LV = Left ventricular, LVID = LV internal diameter, LVPW = LV posterior wall, s = systole.

Figure 5-1: *Trimetazidine treatment has no effect on body weight gain, but significantly increases plasma triacylglycerol levels in diet-induced insulin resistant mice.*

A: 10 wks of high fat feeding resulted in a significant increase in body weight. B: Treatment with trimetazidine had no effect on daily body weight gain, or C: Overall body weight 1 wk post-treatment. D: Plasma triacylglycerol levels were increased in the fed state of diet-induced insulin resistant mice treated with trimetazidine, E: while no changes were observed with regards to plasma free fatty acid levels. Values represent mean ± SE (n = 5-6). Differences were determined using a two-tailed Student's *t*-test. $*P<0.05$, significantly different from pre-high fat diet (HFD) counterpart.

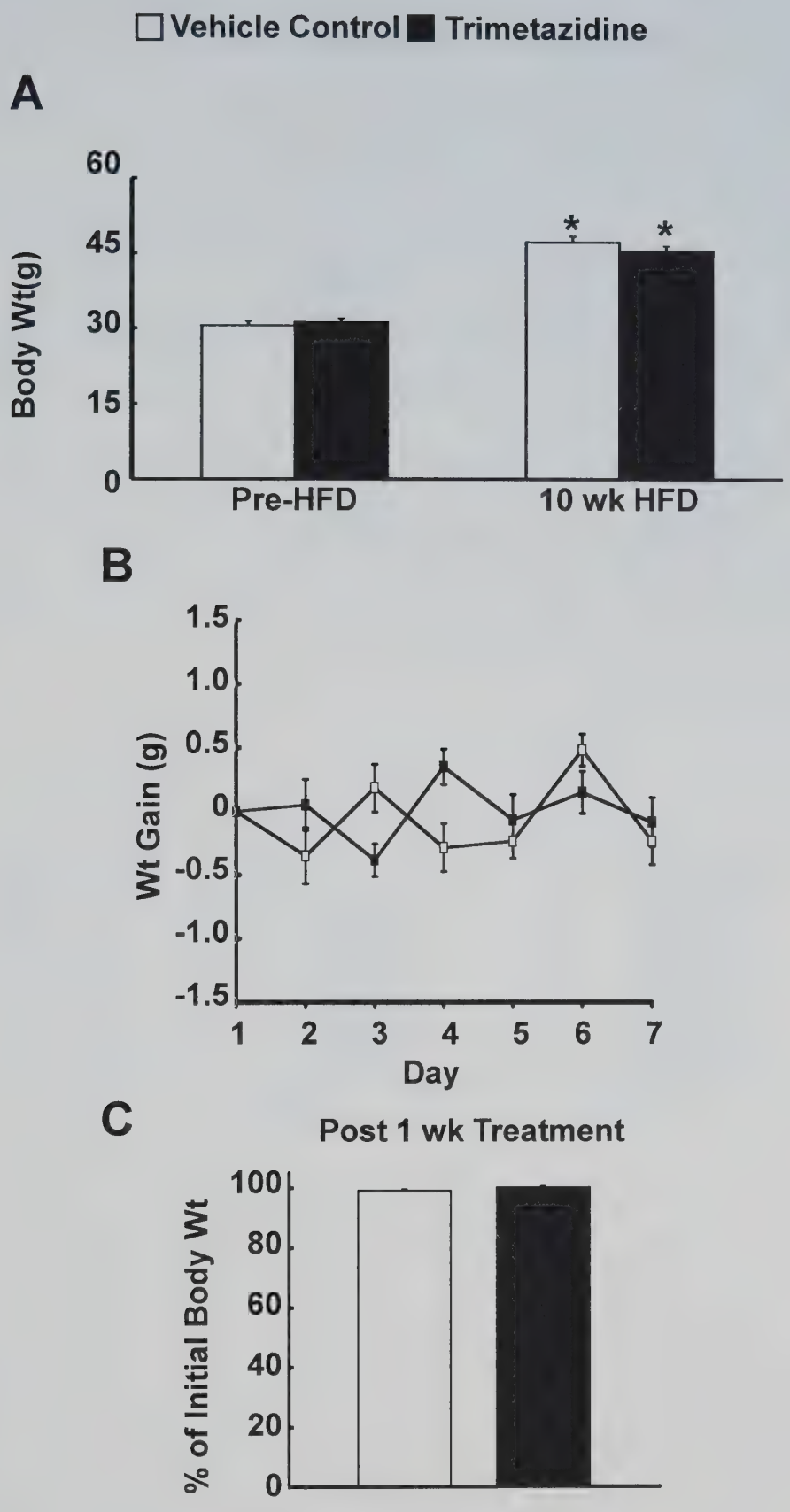
Vehicle Control
Trimetazidine
A
Body Wt(g)
60
45
30
15
0
*
*
Pre-HFD
10 wk HFD
B
Wt Gain (g)
1.5
1.0
0.5
0
-0.5
-1.0
-1.5
1
2
3
4
5
6
7
Day
C
Post 1 wk Treatment
% of Initial Body Wt
100
80
60
40
20
0

FIGURE 5-1

Figure 5-1: *Trimetazidine treatment has no effect on body weight gain, but significantly increases plasma triacylglycerol levels in diet-induced insulin resistant mice.*

A: 10 wks of high fat feeding resulted in a significant increase in body weight. B: Treatment with trimetazidine had no effect on daily body weight gain, or C: Overall body weight 1 wk post-treatment. **D: Plasma triacylglycerol levels were increased in the fed state of diet-induced insulin resistant mice treated with trimetazidine, E: While no changes were observed with regards to plasma free fatty acid levels.** Values represent mean ± SE (n = 5-6). Differences were determined using a two-tailed Student's *t*-test. $^{\dagger}P<0.05$, significantly different from vehicle control mice.

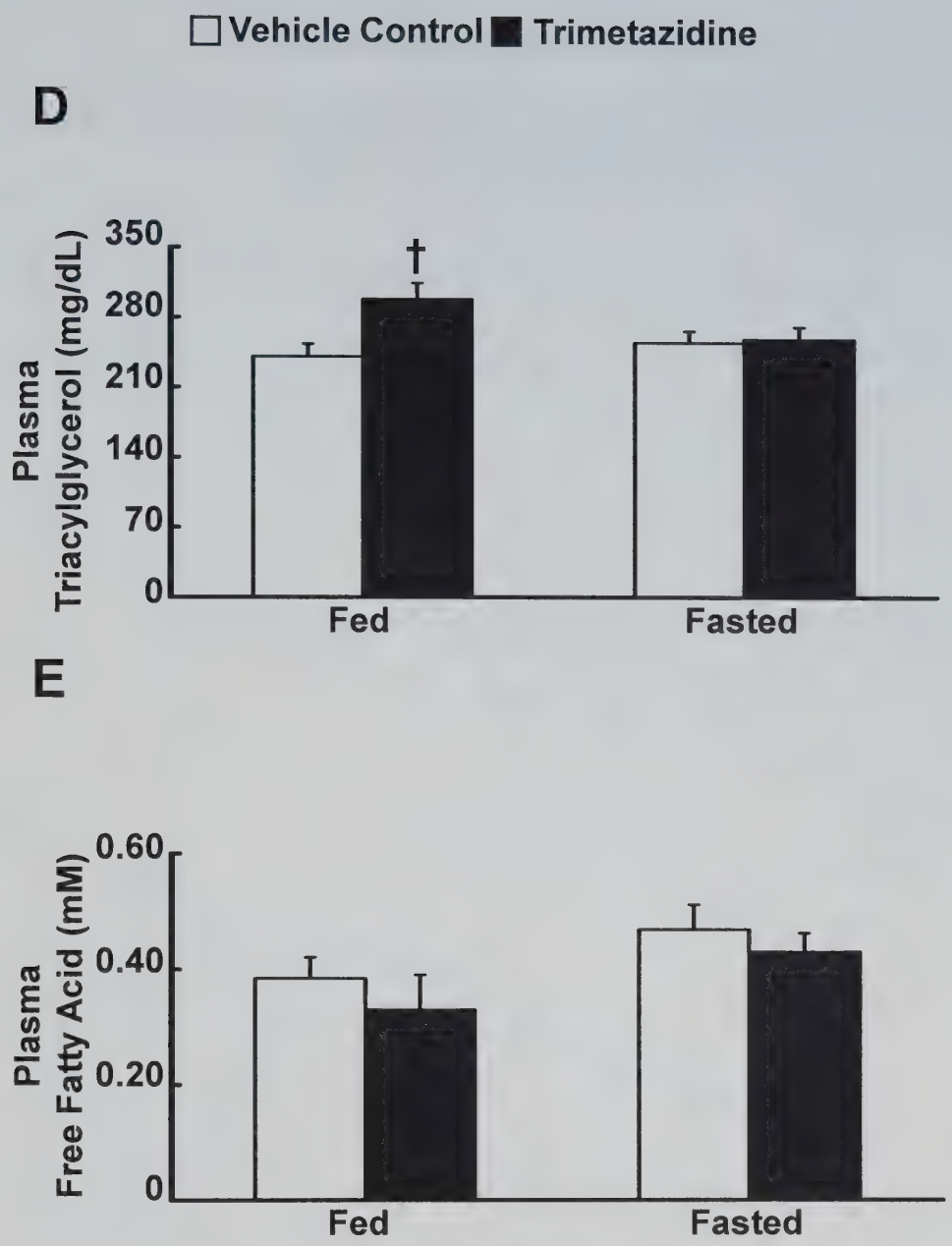
Vehicle Control
Trimetazidine
D
Plasma Triacylglycerol (mg/dL)
350
280
210
140
70
0
†
Fed
Fasted
E
Plasma Free Fatty Acid (mM)
0.60
0.40
0.20
0
Fed
Fasted

FIGURE 5-1

Figure 5-2: *Trimetazidine treatment has no effect on glucose intolerance and insulin sensitivity in diet-induced insulin resistant mice.*

A: Pre-treatment glucose tolerance test (GTT) in diet-induced insulin resistant mice. B: 1 wk post-trimetazidine treatment GTT. C: 1 wk post-trimetazidine treatment insulin tolerance test (ITT) blood glucose levels, and D: % change in blood glucose levels during the ITT. Values represent mean ± SE (n = 6).

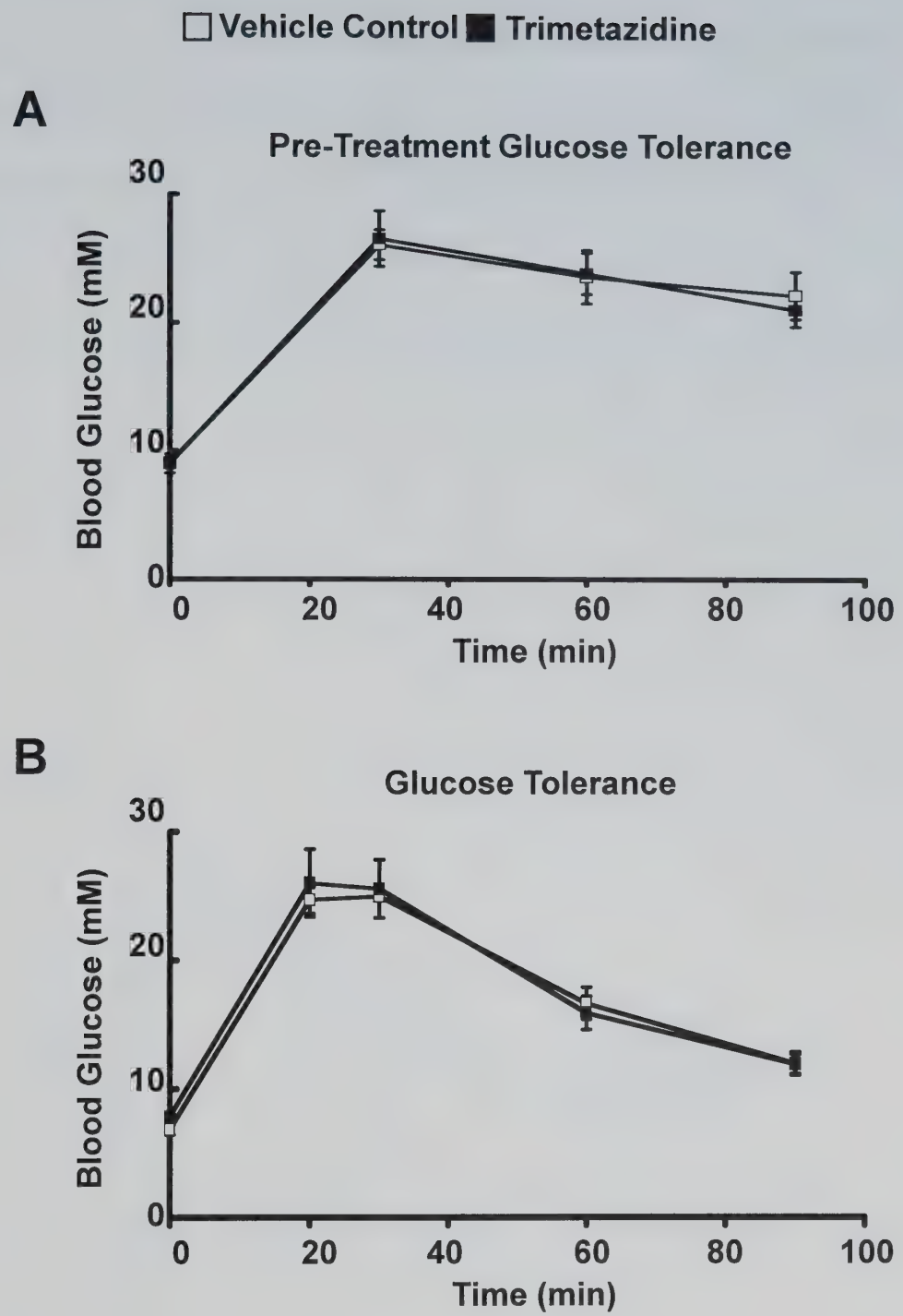
Vehicle Control
Trimetazidine
A
Pre-Treatment Glucose Tolerance
Blood Glucose (mM)
30
20
10
0
0
20
40
60
80
100
Time (min)
B
Glucose Tolerance
Blood Glucose (mM)
30
20
10
0
0
20
40
60
80
100
Time (min)

FIGURE 5-2

Figure 5-2: *Trimetazidine treatment has no effect on glucose intolerance and insulin sensitivity in diet-induced insulin resistant mice.*

A: Pre-treatment glucose tolerance test (GTT) in diet-induced insulin resistant mice. B: 1 wk post-trimetazidine treatment GTT. **C: 1 wk post-trimetazidine treatment insulin tolerance test (ITT) blood glucose levels, and D: % change in blood glucose levels during the ITT.** Values represent mean ± SE (n = 6).

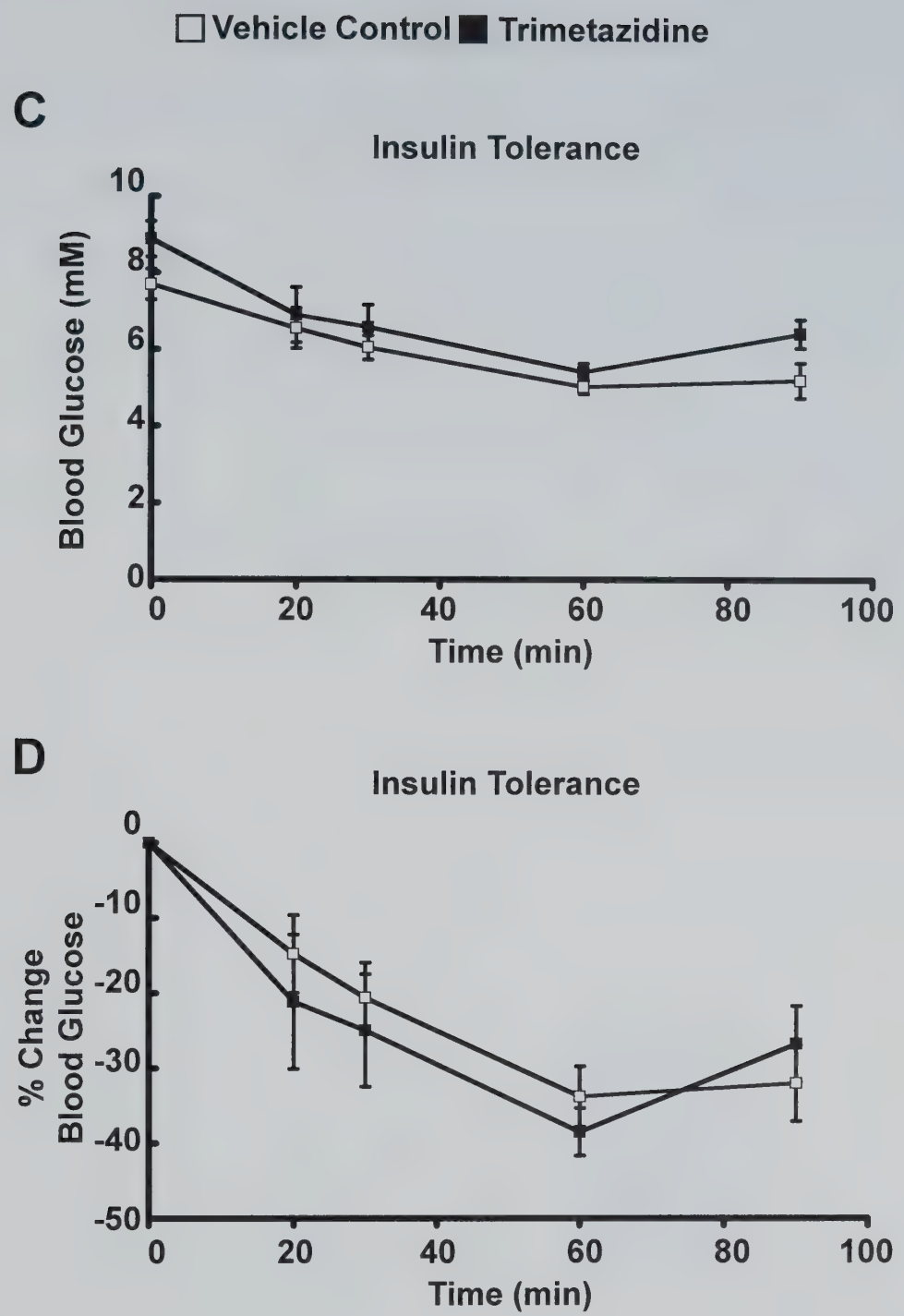
Vehicle Control
Trimetazidine
C
Insulin Tolerance
Blood Glucose (mM)
10
8
6
4
2
0
0
20
40
60
80
100
Time (min)
D
Insulin Tolerance
% Change Blood Glucose
0
-10
-20
-30
-40
-50
0
20
40
60
80
100
Time (min)

FIGURE 5-2

Figure 5-3: *Assessment of in vivo metabolic parameters in vehicle control and trimetazidine treated diet-induced insulin resistant mice.*

A: 24 hr respiratory exchange ratio (RER), B: average light cycle RER, C: 24 hr whole body oxygen consumption, D: 24 hr heat production, E: 24 hr ambulatory activity, and F: 24 hr food intake in vehicle control and trimetazidine treated diet-induced insulin resistant mice. Values represent mean ± SE (n = 6). Differences were determined using either a two-tailed Student's *t*-test, or a two-way ANOVA followed by a Bonferroni post-hoc analysis. $*P<0.05$, significantly different from vehicle control mice.

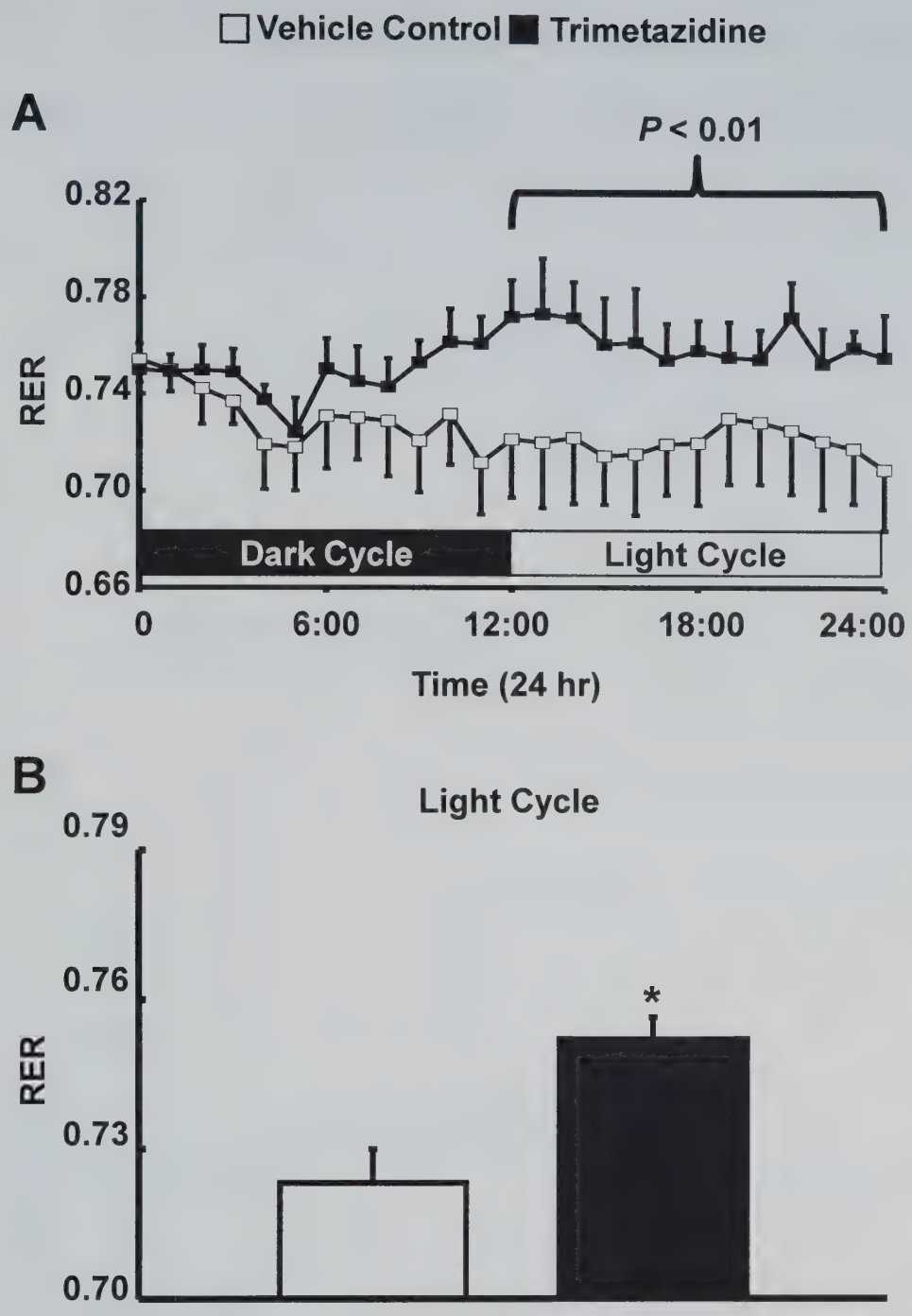
Vehicle Control
Trimetazidine
A
P < 0.01
0.82
0.78
0.74
0.70
0.66
RER
Dark Cycle
Light Cycle
0
6:00
12:00
18:00
24:00
Time (24 hr)
B
Light Cycle
0.79
0.76
0.73
0.70
RER
*

FIGURE 5-3

Figure 5-3: *Assessment of in vivo metabolic parameters in vehicle control and trimetazidine treated diet-induced insulin resistant mice.*

A: 24 hr respiratory exchange ratio (RER), B: average light cycle RER, **C: 24 hr whole body oxygen consumption, D: 24 hr heat production,** E: 24 hr ambulatory activity, and F: 24 hr food intake in vehicle control and trimetazidine treated diet-induced insulin resistant mice. Values represent mean ± SE (n = 6).

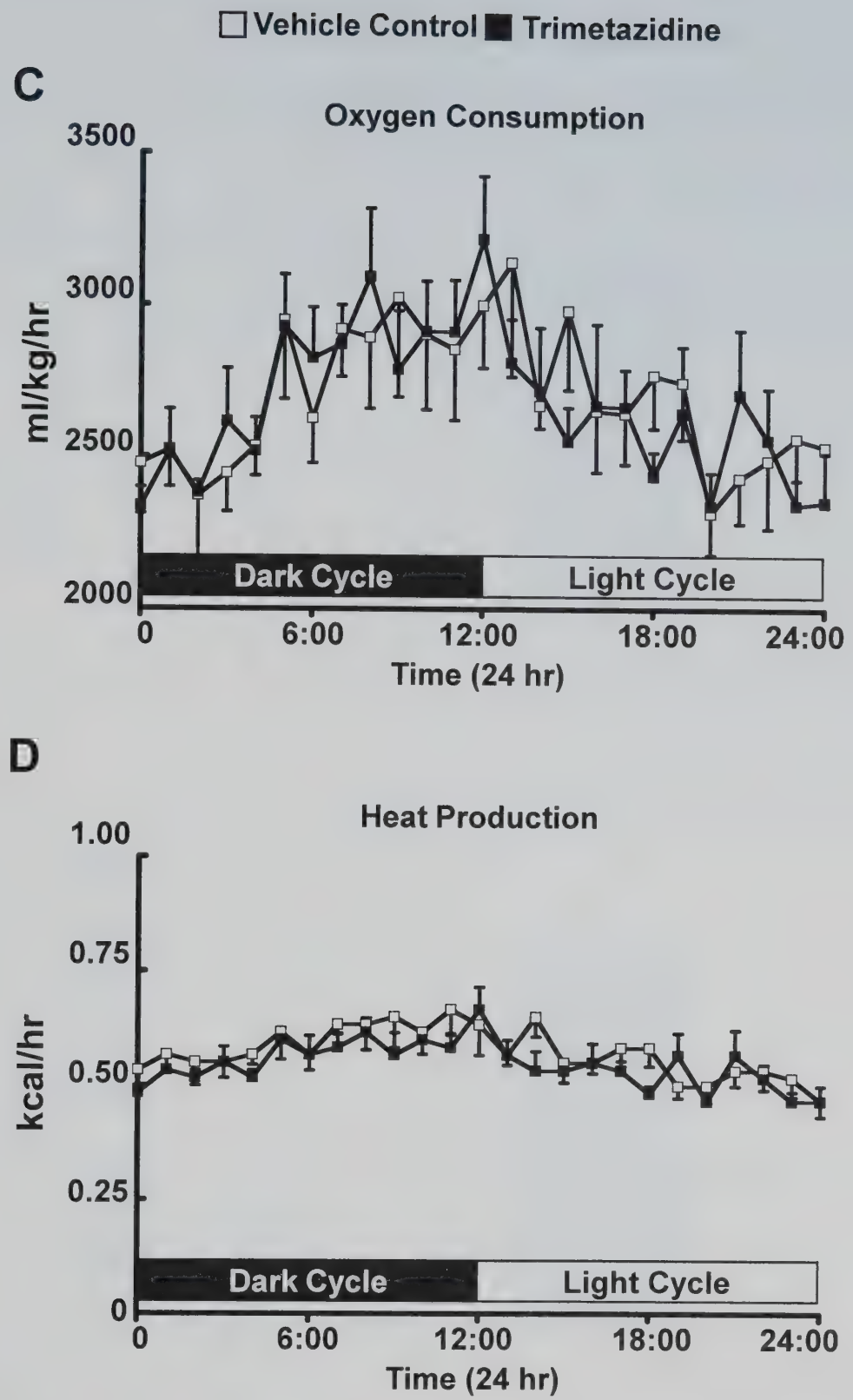
Vehicle Control
Trimetazidine
C
Oxygen Consumption
3500
3000
2500
2000
ml/kg/hr
Dark Cycle
Light Cycle
0
6:00
12:00
18:00
24:00
Time (24 hr)
D
Heat Production
1.00
0.75
0.50
0.25
0
kcal/hr
Dark Cycle
Light Cycle
0
6:00
12:00
18:00
24:00
Time (24 hr)

FIGURE 5-3

Figure 5-3: *Assessment of in vivo metabolic parameters in vehicle control and trimetazidine treated diet-induced insulin resistant mice.*

A: 24 hr respiratory exchange ratio (RER), B: average light cycle RER, C: 24 hr whole body oxygen consumption, D: 24 hr heat production, **E: 24 hr ambulatory activity, and F: 24 hr food intake in vehicle control and trimetazidine treated diet-induced insulin resistant mice.** Values represent mean ± SE (n = 6).

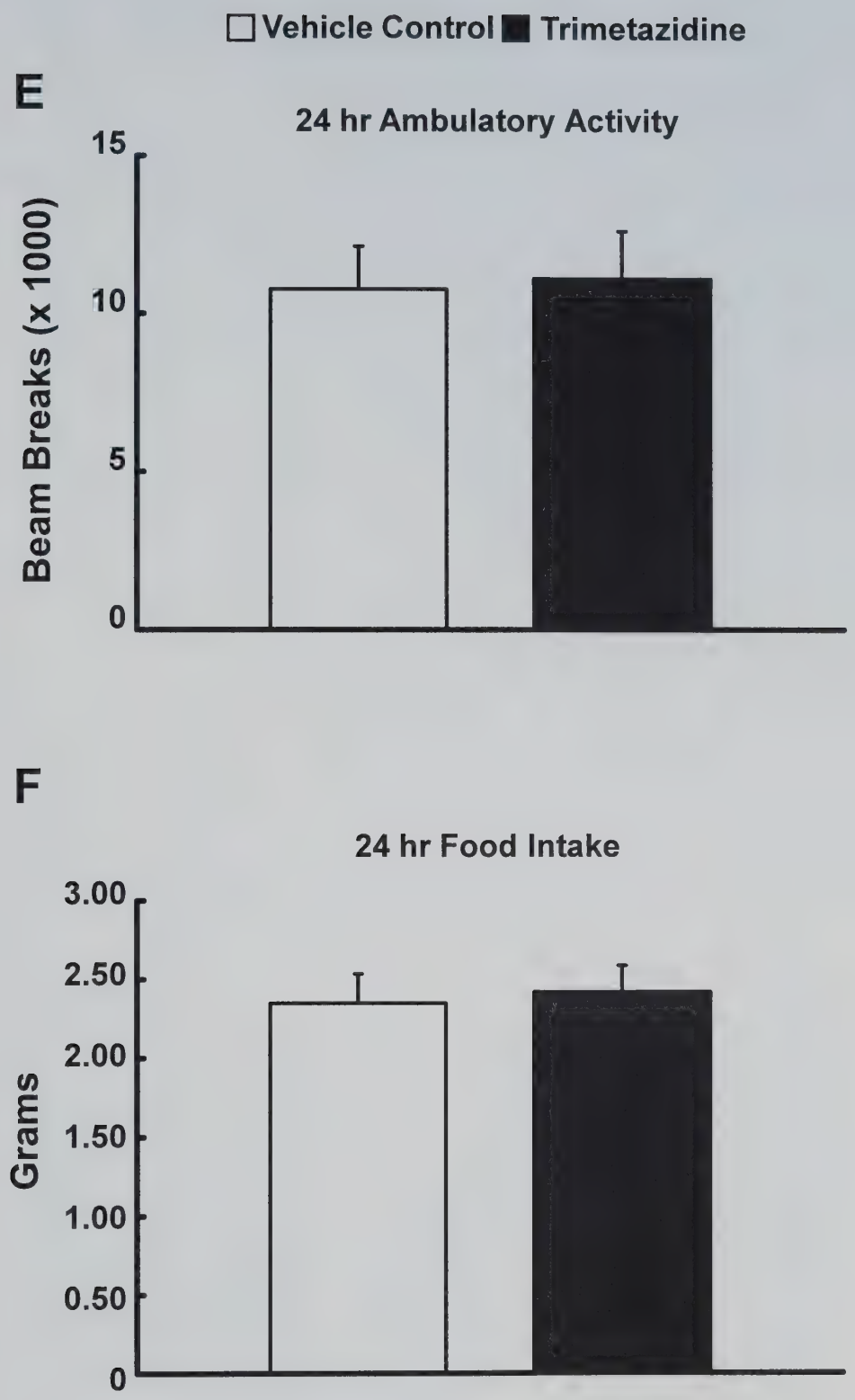
Vehicle Control
Trimetazidine
E
24 hr Ambulatory Activity
Beam Breaks (x 1000)
15
10
5
0
F
24 hr Food Intake
Grams
3.00
2.50
2.00
1.50
1.00
0.50
0

FIGURE 5-3

Figure 5-4: *Intramyocellular lipid metabolite accumulation and levels of tricarboxylic acid cycle intermediates in vehicle control and trimetazidine treated diet-induced insulin resistant mice.*

A: Gastrocnemius triacylglycerol content, B: long chain acyl CoA content, C: diacylglycerol content, D: ceramide content, E: tricarboxylic acid cycle intermediate levels, F: medium chain acylcarnitine content, and G: long chain acylcarnitine content in vehicle control and trimetazidine treated diet-induced insulin resistant mice. Values represent mean ± SE (n = 6). Differences were determined using a two-tailed Student's *t*-test. $*P<0.05$, significantly different from vehicle control mice.

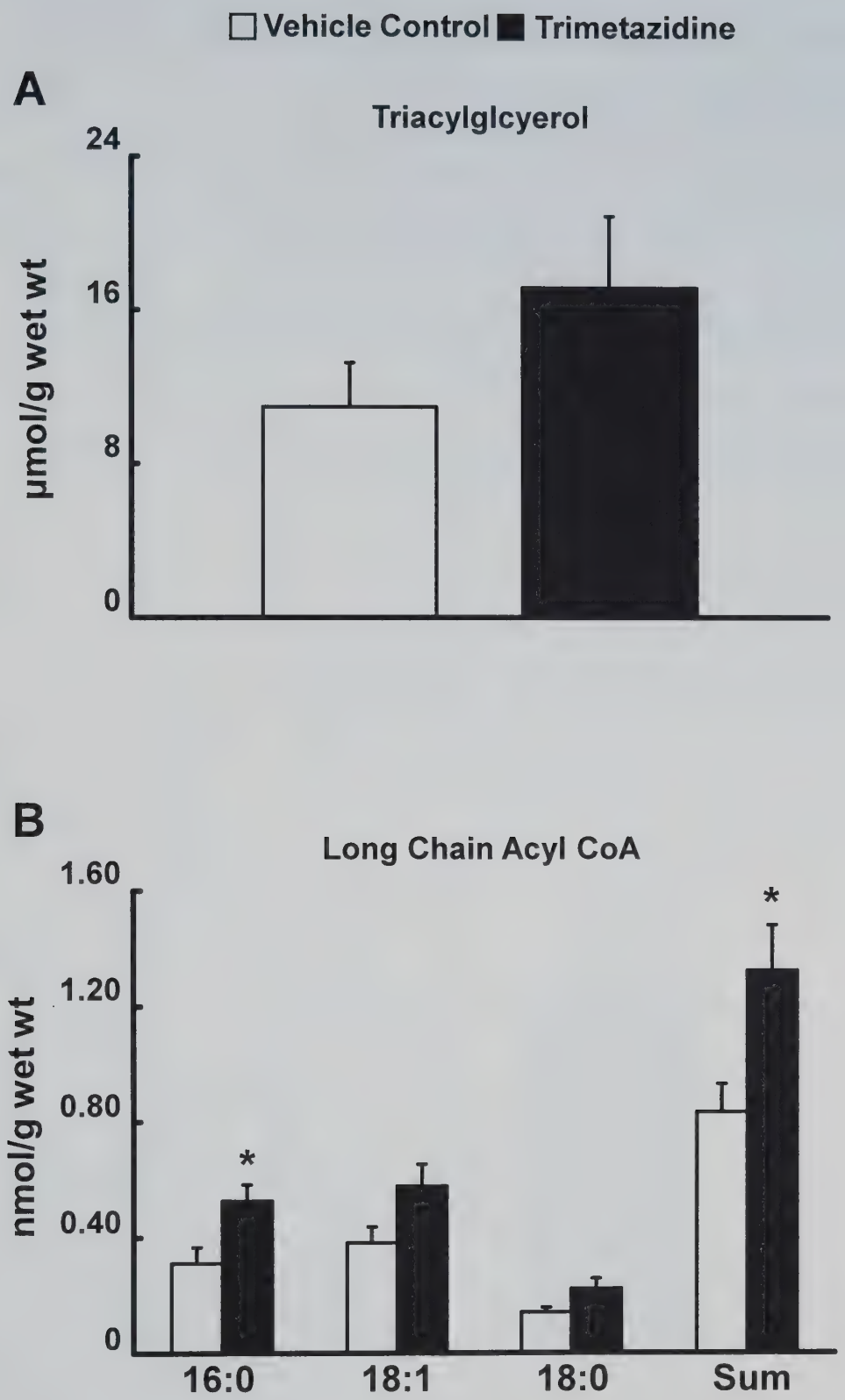
Vehicle Control
Trimetazidine
A
Triacylglcyerol
µmol/g wet wt
24
16
8
0
B
Long Chain Acyl CoA
nmol/g wet wt
1.60
1.20
0.80
0.40
0
*
*
16:0
18:1
18:0
Sum

FIGURE 5-4

Figure 5-4: *Intramyocellular lipid metabolite accumulation and levels of tricarboxylic acid cycle intermediates in vehicle control and trimetazidine treated diet-induced insulin resistant mice.*

A: Gastrocnemius triacylglycerol content, B: long chain acyl CoA content, **C: diacylglycerol content, D: ceramide content,** E: tricarboxylic acid cycle intermediate levels, F: medium chain acylcarnitine content, and G: long chain acylcarnitine content in vehicle control and trimetazidine treated diet-induced insulin resistant mice. Values represent mean ± SE (n = 6).

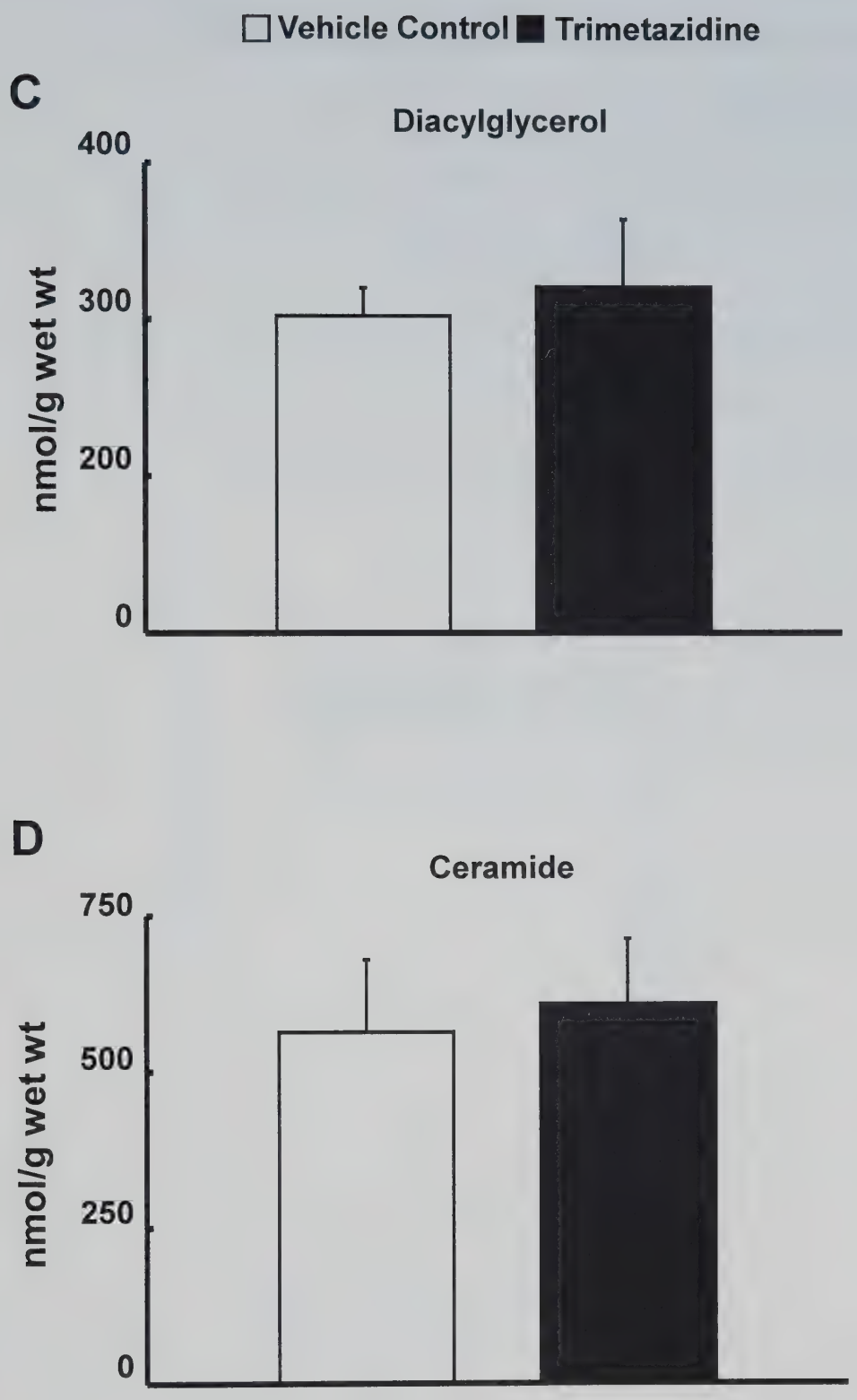
Vehicle Control
Trimetazidine
C
Diacylglycerol
400
300
200
0
nmol/g wet wt
D
Ceramide
750
500
250
0
nmol/g wet wt

FIGURE 5-4

Figure 5-4: *Intramyocellular lipid metabolite accumulation and levels of tricarboxylic acid cycle intermediates in vehicle control and trimetazidine treated diet-induced insulin resistant mice.*

A: Gastrocnemius triacylglycerol content, B: long chain acyl CoA content, C: diacylglycerol content, D: ceramide content, **E: tricarboxylic acid (TCA) cycle intermediate levels,** F: medium chain acylcarnitine content, and G: long chain acylcarnitine content in vehicle control and trimetazidine treated diet-induced insulin resistant mice. Values represent mean ± SE (n = 6).

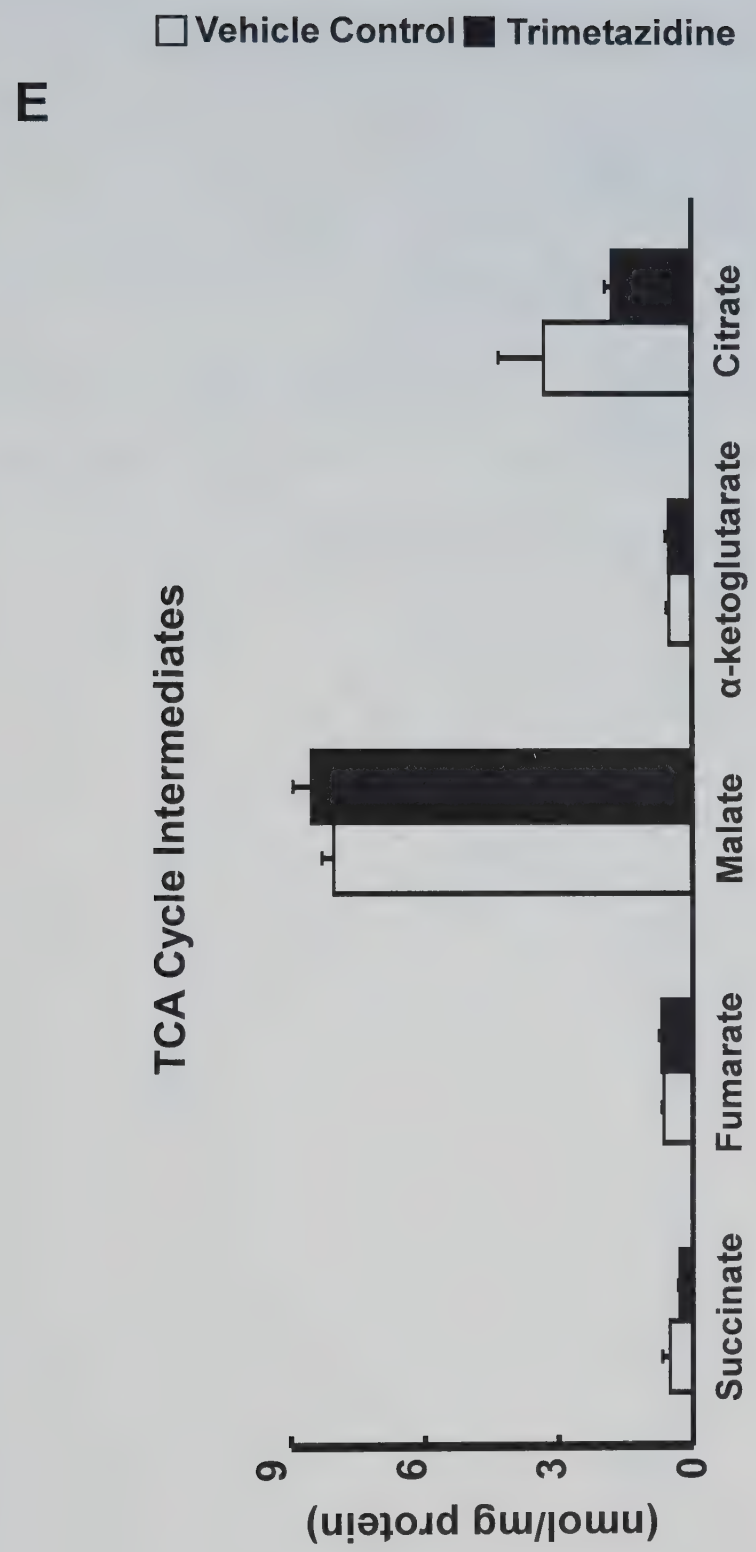
Vehicle Control
Trimetazidine
E
TCA Cycle Intermediates
(nmol/mg protein)
0
3
6
9
Succinate
Fumarate
Malate
α-ketoglutarate
Citrate

FIGURE 5-4

Figure 5-4: *Intramyocellular lipid metabolite accumulation and levels of tricarboxylic acid cycle intermediates in vehicle control and trimetazidine treated diet-induced insulin resistant mice.*

A: Gastrocnemius triacylglycerol content, B: long chain acyl CoA content, C: diacylglycerol content, D: ceramide content, E: tricarboxylic acid cycle intermediate levels, **F: medium chain acylcarnitine content,** and G: long chain acylcarnitine content in vehicle control and trimetazidine treated diet-induced insulin resistant mice. Values represent mean ± SE (n = 6).

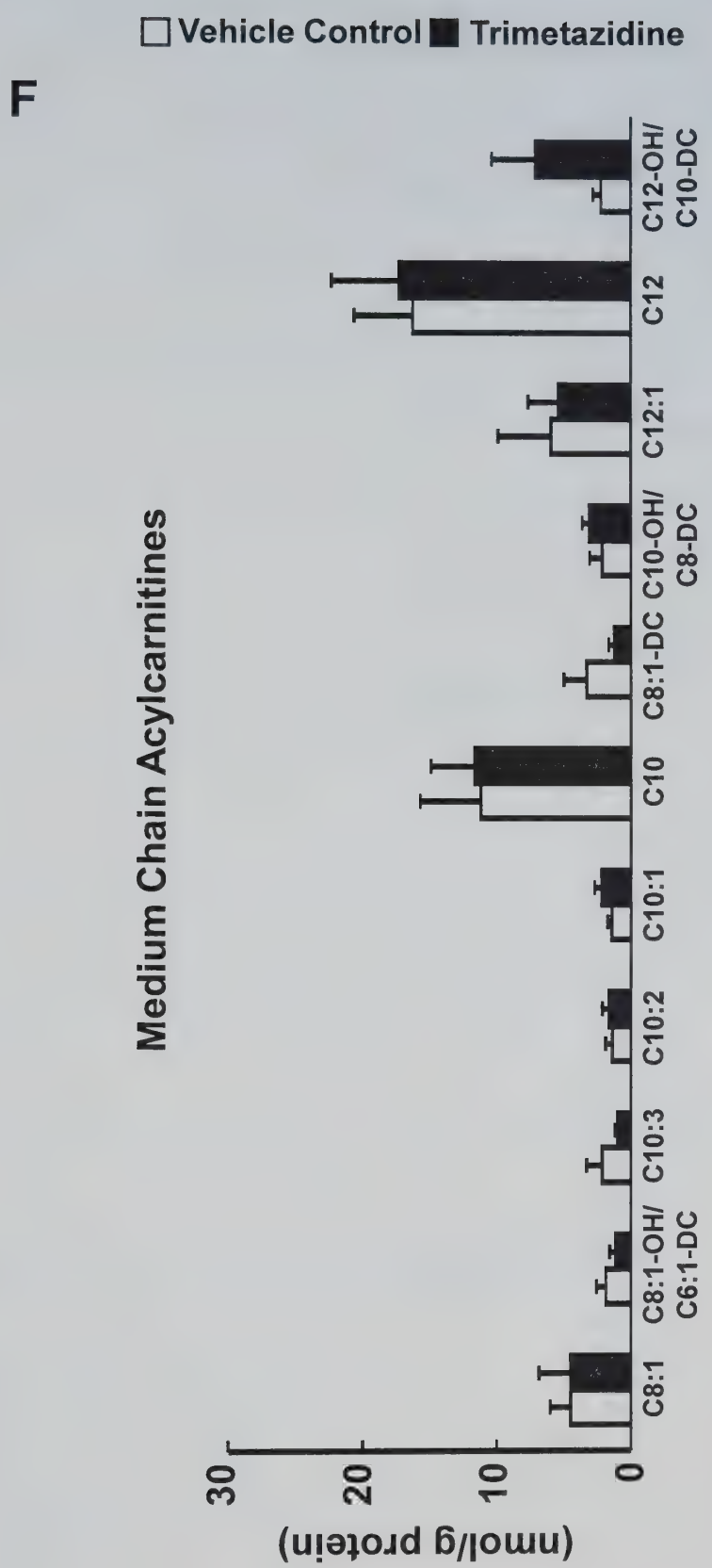
F
Vehicle Control
Trimetazidine
Medium Chain Acylcarnitines
(nmol/g protein)
0
10
20
30
C8:1
C8:1-OH/ C6:1-DC
C10:3
C10:2
C10:1
C10
C8:1-DC
C10-OH/ C8-DC
C12:1
C12
C12-OH/ C10-DC

FIGURE 5-4

Figure 5-4: *Intramyocellular lipid metabolite accumulation and levels of tricarboxylic acid cycle intermediates in vehicle control and trimetazidine treated diet-induced insulin resistant mice.*

A: Gastrocnemius triacylglycerol content, B: long chain acyl CoA content, C: diacylglycerol content, D: ceramide content, E: tricarboxylic acid cycle intermediate levels, F: medium chain acylcarnitine content, and **G: long chain acylcarnitine content in vehicle control and trimetazidine treated diet-induced insulin resistant mice.** Values represent mean ± SE (n = 6). Differences were determined using a two-tailed Student's t-test. $^{\dagger}P<0.1$, significantly different from vehicle control mice.

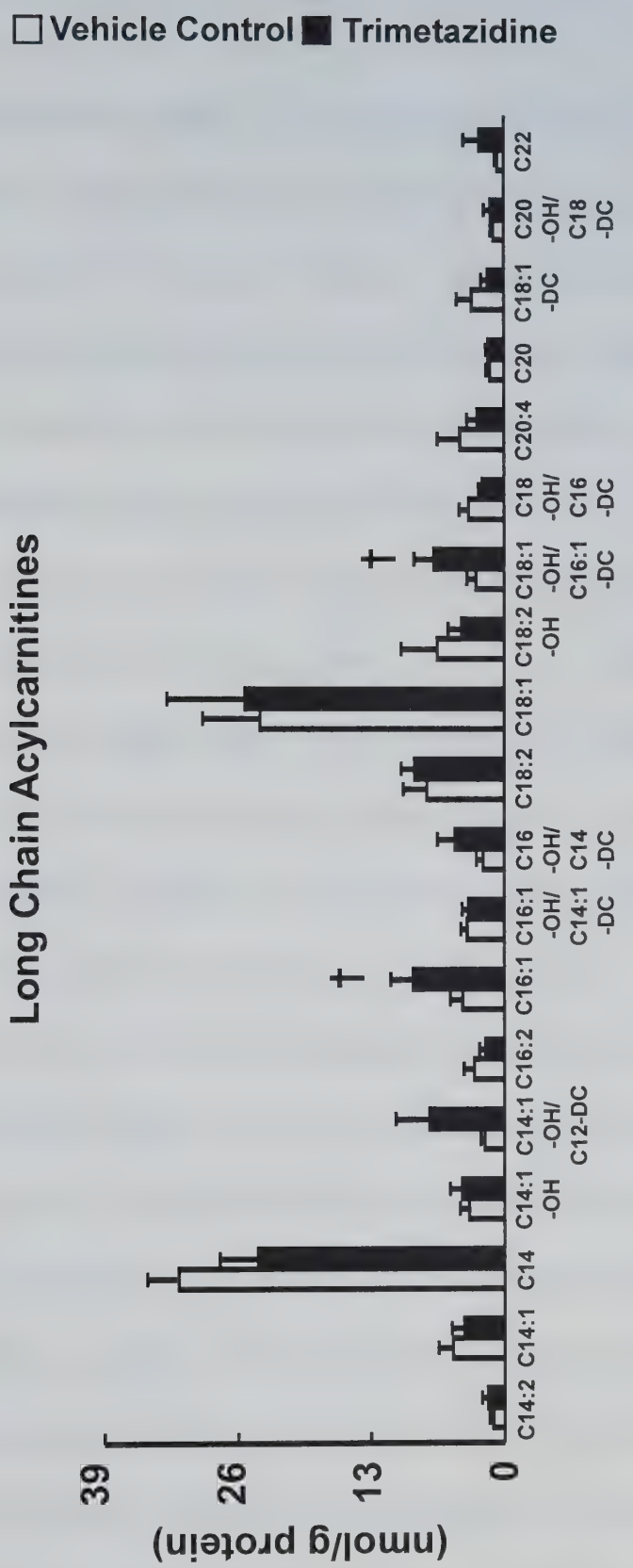
Vehicle Control
Trimetazidine
G
Long Chain Acylcarnitines
(nmol/g protein)
39
26
13
0
†
†
C14:2
C14:1
C14
C14:1 -OH
C14:1 -OH/ C12-DC
C16:2
C16:1
C16:1 -OH/ C14:1 -DC
C16 -OH/ C14 -DC
C18:2
C18:1
C18:2 -OH
C18:1 -OH/ C16:1 -DC
C18 -OH/ C16 -DC
C20:4
C20
C18:1 -DC
C20 -OH/ C18 -DC
C22

FIGURE 5-4

Contrary to previous findings, our data demonstrate that direct inhibition of mitochondrial fatty acid oxidation does not exacerbate diet-induced insulin resistance as determined by glucose tolerance and insulin tolerance testing. Interestingly, direct inhibition of fatty acid oxidation does improve the overall oxidation of carbohydrates, as indicated by an increase in light cycle RER. In addition, we demonstrate that trimetazidine treatment has no effect on body weight gain or food intake. As expected, treatment with trimetazidine leads to a further increase in intramyocellular long chain acyl CoA. A trend is also seen towards an increase in intramyocellular TAG, while intramyocellular DAG and ceramide content do not accumulate any further than that seen with high fat feeding alone. Moreover, treatment of diet-induced insulin resistant mice with trimetazidine results in a further increase in plasma TAG levels.

Although previous findings have suggested that impairments in skeletal muscle fatty acid oxidation can cause insulin resistance and type 2 diabetes (69, 353, 367, 383, 413, 447), our recent work and others has shown that insulin resistance is actually accompanied by excessive rates of skeletal muscle fatty acid oxidation (108, 396) and a shift towards incomplete oxidation of fatty acids (200, 202). Moreover, these studies showed that inhibition of fatty acid oxidation could prevent either diet- or genetic-induced insulin resistance (108, 202). However, a common feature of these studies was that inhibition of fatty acid oxidation was achieved secondary to an inhibition of mitochondrial fatty acid uptake.

Thus, this study aimed to address whether it is the inhibition of mitochondrial fatty acid uptake, or the inhibition of mitochondrial fatty acid oxidation that is important in protecting against the development of insulin resistance. As trimetazidine is a 3-KAT inhibitor, the last enzyme involved in the mitochondrial oxidation of fatty acids, it acts as a direct inhibitor of fatty acid oxidation, and fatty acids should still have an unimpeded entry into the mitochondria through CPT 1. This is evinced by similar levels of long chain acylcarnitines in gastrocnemius muscle from both vehicle control and trimetazidine treated animals, while particular long chain acylcarnitine species (i.e. palmitoleoylcarnitine) actually revealed a trend to an increase. Furthermore, long chain acyl CoA accumulation increased further in muscle from trimetazidine treated animals, while intramyocellular DAG and ceramide content are similar. These findings support a surge of recent studies showing clear dissociation between long chain acyl CoA and TAG being the mediator of skeletal muscle insulin resistance (12, 202, 231, 310, 393), and support recent notions that it is actually a mitochondrial lipid-derived as opposed to a cytosolic lipid-derived stress that is potentially mediating the insulin resistant phenotype (14, 202). In support of this, recent work in our lab has also shown that inhibition of mitochondrial fatty acid uptake through CPT 1 via oxfenicine treatment can reverse high fat diet-induced insulin resistance (unpublished data).

Previous studies have postulated that accelerating skeletal muscle fatty acid oxidation can protect against the development of insulin resistance, by preventing the accumulation of intramyocellular lipid metabolites observed with

obesity, and removing inhibition of the insulin signaling cascade (47, 69, 203, 353, 413). This proposal is in direct contrast to the original work of Sir Philip Randle and colleagues, who described in the 1960s an inverse carbohydrate-fatty acid cycle, whereby increasing the oxidation of fatty acids as a fuel source results in a reduction of carbohydrate oxidation as a fuel source (315, 317). These authors suggested that this "Randle Cycle" effect was responsible for the metabolic disturbances associated with diabetes. Based on the work of Randle and colleagues, it would seem counterintuitive to increase skeletal muscle fatty acid oxidation as an approach to treat insulin resistance, as that should result in a reciprocal depression of glucose oxidation. However, recent studies by Shulman and colleagues utilizing ^{31}P-MRS to measure glucose-6-phosphate accumulation have suggested that the Randle Cycle is non-existent in muscle (303, 304, 306, 353). On the contrary, our data suggest that the Randle Cycle is operative in skeletal muscle, as the RER values are higher in obese, insulin resistant mice treated with trimetazidine, indicative of increased reliance on carbohydrate oxidation as a fuel source. The fact that trimetazidine treatment does not reverse diet-induced insulin resistance though, suggests that simply increasing carbohydrate oxidation is insufficient to improve insulin-stimulated glucose metabolism. It is possible that via the Randle Cycle effect, trimetazidine simply only increases the oxidation of glucose molecules that are already being taken up by the muscle. Because mitochondrial lipid would still accumulate, the insulin response would remain inhibited, and glucose homeostasis impaired.

Although inhibition of skeletal muscle fatty acid oxidation may not be detrimental in our study, it is important to note that the inhibition of fatty acid oxidation in liver may have detrimental effects, potentially exacerbating the development of hepatic insulin resistance and steatosis (179, 180, 447). Nonetheless, we do not observe any further increase in hepatic TAG, long chain acyl CoA, and ceramide accumulation from trimetazidine treated animals (*data not shown*). The lack of an increase in liver TAG accumulation in these animals may arise from increases in liver TAG secretion, possibly explaining the observed increase in plasma TAG levels.

It is interesting to note that although trimetazidine treatment does not have beneficial effects against diet-induced insulin resistance, it does prevent the development of diet-induced cardiac hypertrophy and contractile dysfunction. Furthermore, early signs of diastolic dysfunction in terms of a decreased E'/A' ratio are observed in control treated obese mice, while this respective decrease does not occur in animals treated with trimetazidine. These results are consistent with a recent clinical trial carried out by Tuunanen *et al.* (397), whereby treatment of idiopathic dilated cardiomyopathy (IDCM) patients with trimetazidine caused a modest 10% decrease in myocardial fatty acid oxidation rates, but significantly improved LV EF. In contrast to the findings of our study, these IDCM patients appeared to be more insulin sensitive, though this was determined only by means of a homeostasis model assessment (HOMA) index. Further in-depth studies are required before true conclusions can be made with regards to the effect of trimetazidine on insulin resistance in human patients.

In conclusion, our results reveal important insights with regards to conflicting theories on the contribution of fatty acid oxidation to skeletal muscle insulin resistance. On one side, it has been postulated that impairments in skeletal muscle fatty acid oxidation cause insulin resistance. Thus, treatment with trimetazidine in obese mice would be expected to exacerbate the development of skeletal muscle insulin resistance, findings which we do not observe. On the other hand, recent studies have suggested that inhibiting mitochondrial fatty acid uptake and subsequent oxidation can protect against and/or reverse skeletal muscle insulin resistance. Our findings demonstrate that direct inhibition of mitochondrial fatty acid oxidation cannot reverse insulin resistance, suggesting that mitochondrial lipid stress likely plays a major role in mediating insulin resistance and subsequent type 2 diabetes. Future studies should be aimed at investigating how mitochondrial lipid accumulation results in skeletal muscle insulin resistance.

CHAPTER 6.

Inhibition of *de novo* ceramide synthesis reverses diet-induced insulin resistance and restores whole body oxygen consumption

---

My role in this work involved performing all experiments (except those noted below), as well as the writing of the manuscript. Panakkezhum Thomas performed the HPLC analysis of long chain acyl CoA and ceramide, and Wendy Keung determined the intramyocellular DAG content.

Manuscript Status: This manuscript is currently under review at *Diabetes* for publication as an original article.

CHAPTER 6.

Inhibition of *de novo* ceramide synthesis reverses diet-induced insulin resistance and restores whole body oxygen consumption

Abstract

Objective – It has been proposed that skeletal muscle insulin resistance arises from the accumulation of intramyocellular lipid metabolites that impede insulin signaling, including diacylglycerol and ceramide. We determined the role of *de novo* ceramide synthesis in mediating muscle insulin resistance.

Research Design and Methods – C57BL/6 mice were subjected to 12 wks of diet-induced obesity (DIO) and then treated for 4 wks with myriocin, an inhibitor of serine palmitoyl transferase 1 (SPT 1), the rate-limiting enzyme of *de novo* ceramide synthesis.

Results – Following 12 wks of DIO, C57BL/6 mice demonstrated a doubling in gastrocnemius ceramide levels, which was completely reversed (141.5 ± 15.8 vs. 94.6 ± 10.2 nmol/g dry wt) via treatment with myriocin. Interestingly, myriocin treatment did not alter the DIO-associated increase in gastrocnemius diacylglycerol content, and the only correlation observed between lipid metabolite accumulation and glucose intolerance occurred with ceramide (R = 0.61). DIO mice treated with myriocin showed a complete reversal of insulin resistance, which was associated with enhanced insulin-stimulated Akt phosphorylation. Furthermore, myriocin treatment also decreased intramyocellular ceramide

content and prevented insulin resistance development in *db/db* mice. Finally, DIO mice displayed impairments in oxygen consumption (30,347 ± 985 vs. 25,094 ± 1087 area under the curve) that were reversed via myriocin treatment.

Conclusions – Our results demonstrate that the intramyocellular accumulation of ceramide correlates strongly with the development of insulin resistance, and suggests that inhibition of SPT 1 is a potentially promising target for the treatment of insulin resistance.

Obesity and type 2 diabetes frequently occur hand in hand, and are thought of as diseases of Western society, due to lifestyles characterized by over nutrition and physical inactivity. This over nutrition manifests itself as a hyperlipidemia, which is believed to be a major precipitating event in the development of skeletal muscle insulin resistance (182, 281).

Numerous studies *in vivo* and *in vitro* have provided strong evidence that lipid excess leads to an accumulation of intramyocellular lipid-derived metabolites, which coincide with an impaired insulin response (353, 367). Previous studies have postulated that this accumulation of lipid-derived metabolites results from an impaired ability of the mitochondria to oxidize fatty acids (69, 383, 413, 447). Thus, esterified fatty acids in the form of long-chain acyl CoA are diverted away from CPT 1, towards TAG and other lipid metabolites, such as ceramide and DAG. These metabolites are believed to activate classical/novel PKC isoforms that phosphorylate and inactivate IRS proteins, preventing the insulin response at the level of Akt and GLUT4 translocation (353, 367).

This theory has been challenged recently, due to a number of studies showing clear dissociation between intramyocellular lipid metabolite accumulation and insulin sensitivity (12, 231, 310, 393). In addition, our most recent work suggests that insulin resistance is actually characterized by excessive rates of incomplete fatty acid oxidation in muscle, rather than an impairment in

fatty acid oxidation (200, 202). Furthermore, many other studies have also reported elevated rates of fatty acid oxidation, or upregulated expression of proteins involved in fatty acid oxidation, in various models of obesity and type 2 diabetes (108, 140, 396).

Thus, it is still up for debate whether the intramyocellular lipid metabolite accumulation observed in obesity and type 2 diabetes arises from either excessive, or impaired rates of fatty acid oxidation. However, it is generally agreed that intramyocellular lipid metabolites do accumulate during obesity and type 2 diabetes, and likely play a key role in the disease's progression (154, 281, 353, 367, 385).

Of the aforementioned lipid metabolites, ceramide is an attractive candidate to be a primary culprit involved in mediating the skeletal muscle insulin resistance seen with obesity and type 2 diabetes, as it is elevated by both inflammation and lipid overload, and hence links two popular models of insulin resistance development (385). Numerous studies in both culture and animal models demonstrate that increasing ceramide levels inhibits insulin signaling and causes insulin resistance (153, 231, 310, 312). Moreover, Holland and colleagues have shown that inhibiting *de novo* synthesis of ceramide by pharmacological inhibition of SPT 1 can prevent insulin resistance caused by corticosteroids, saturated fats, and genetic models of obesity (153). Pharmacological inhibition of SPT 1 in human muscle cells has also been shown to prevent the inhibition of insulin stimulated glycogen synthesis induced by palmitic acid (310). Finally, improvements in insulin sensitivity brought about by exercise training in obese

individuals is associated with significant reductions in skeletal muscle ceramide levels, whereas TAG and DAG levels were either unchanged or only showed a trend towards a reduction (48, 90).

Our objective in this investigation was to determine if inhibition of *de novo* ceramide synthesis could reverse the insulin resistance induced by chronic high fat feeding of mice, and to gain a further understanding of how ceramides affect insulin sensitivity in muscle.

Animal Studies

All animals received care according to the Canadian Council on Animal Care and the University of Alberta Health Sciences Animal Welfare Committee. 12-wk-old C57BL/6 mice were placed on a standard chow/low fat diet (4% kcal from lard) or high fat diet (60% kcal from lard, Research Diets; D12492) for a 12-wk period. At the end of wk 12, animals were injected IP every other day with the SPT 1 inhibitors, myriocin (0.5 mg/kg) suspended in 1x PBS, L-cycloserine (25 mg/kg) suspended in 1x PBS, or vehicle control for a 4 wk period. At the end of the 4 wk treatment protocol, animals were sacrificed via IP injection of sodium pentobarbital (12 mg) in the fed state in the middle of the dark cycle. Tissues were excised and immediately frozen in liquid N_2. In another study, 6-wk-old *db/db* mice and their heterozygous controls (*db/+*) (Jackson Laboratories) were placed on an identical 4 wk treatment regimen. Protocols for assessment of intramyocellular lipid metabolite accumulation, GTTs, ITTs, indirect calorimetry, exercise capacity, immunoblotting, and statistical analysis are described in **Chapter 2** of this thesis.

Chronic high fat feeding results in dramatic weight gain, whole body insulin resistance, and altered substrate preference

As expected, mice fed a high fat diet for 12 wks became obese as indicated by a significant increase in weight gain, (Figure 6-1A) and became insulin resistant (Figure 6-1B-D). Diet-induced insulin resistant and lean mice were placed in a CLAMS apparatus for a whole body metabolic assessment, which demonstrated a high fat diet-induced shift in fuel preference towards fatty acids as an oxidative energy source, indicated by the large drop in the RER (Figure 6-2A/B). Further support for an increase in fatty acid oxidation in obese mice was seen with the increase in gastrocnemius βHAD activity (Table 6-1). Contrary to previous findings (226, 363), we also found that obesity induced by chronic high fat feeding impaired whole body oxygen consumption rates (Figure 6-2C/D)

Inhibition of *de novo* ceramide synthesis via pharmacological inhibition of SPT 1 reverses diet-induced insulin resistance

After 12 wks of a low or high fat diet, mice were treated with either myriocin (0.5 mg/kg every other day) or vehicle control. After 2 wks of treatment, we demonstrated that inhibition of SPT 1 with myriocin reversed diet-induced insulin resistance, as determined by glucose tolerance and insulin tolerance testing (Figure 6-3A-D). To determine if these protective effects took place at the skeletal muscle level, a group of animals were sacrificed at 30 min

post-insulin injection during the insulin tolerance test, and muscles were excised and harvested for immunoblot analysis of the insulin-signaling pathway. We demonstrated that insulin stimulation of both Akt and GSK3β phosphorylation was significantly improved in the gastrocnemius muscle of obese mice treated with myriocin (Figure 6-3E/F). Myriocin treatment was without affect on food intake, body weight, and plasma insulin levels, but did reduce both postprandial and fasted plasma glucose levels in obese, insulin resistant mice (Table 6-2). Interestingly, indirect calorimetry revealed that the improved insulin sensitivity in DIO mice treated with myriocin was not associated with a decrease in fatty acid oxidation and an increase in carbohydrate oxidation, as similar RER values were observed between the DIO control and myriocin treated animals (Figure 6-4).

In a parallel series of experiments, after 12 wks of high fat feeding, mice were treated with either the SPT 1 inhibitor, L-cycloserine (25 mg/kg every other day), or vehicle control. Although not as dramatic as the results observed with myriocin, after 2 wks of L-cycloserine treatment, we found improvements in glucose and insulin tolerance (Figure 6-5).

Inhibition of *de novo* ceramide synthesis via pharmacological inhibition of SPT 1 reverses diet-induced impairments on exercise capacity, which coincide with a restoration of whole body oxygen consumption rates

Obese, insulin resistant mice were run on an exercise treadmill to determine exercise capacity, and as expected, obese mice showed a dramatic reduction in both their treadmill time and distance when compared to their lean

counterparts (Figure 6-6A/B). Interestingly, treatment of obese mice for 2 wks with myriocin reversed this reduction in exercise capacity (Figure 6-6A/B). This improvement in exercise capacity observed in obese mice treated with myriocin can be explained by a restoration of the DIO-associated impairment in whole body oxygen consumption rates (Figure 6-7A-C). In addition, we observed greater CS activity in gastrocnemius muscle of obese mice treated with myriocin (Figure 6-7D). These observations illustrated improvements in mitochondrial function, possibly explaining why exercise capacity and whole body oxygen consumption rates were not reduced in this group.

Inhibition of *de novo* ceramide synthesis via pharmacological inhibition of SPT 1 reverses diet-induced impairments on heat production with no effect on animal activity

After 3 wks of treatment with myriocin, *in vivo* heat production and ambulatory activity were assessed in our CLAMS apparatus. Paralleling our observations with regards to whole body oxygen consumption rates, obesity caused a decline in whole body heat production that was reversed by myriocin treatment (Figure 6-8A/B). Moreover, obesity-induced insulin resistance was associated with reductions in physical activity that were also not altered by myriocin treatment (Figure 6-8C/D).

Inhibition of *de novo* ceramide synthesis via pharmacological inhibition of SPT 1 has no effect on the obesity-associated increase of long chain acyl CoA and DAG accumulation in muscle, but significantly elevates TAG levels

Investigation of the lipid metabolite profile in gastrocnemius muscle demonstrated that chronic high fat feeding increased long chain acyl CoA, ceramide, and DAG content, but only a trend to an increase in TAG content was observed (Figure 6-9A-D). Treatment with myriocin in obese mice increased gastrocnemius TAG content in comparison to their low fat counterparts, but did not change the DIO-associated rise in long chain acyl CoA and DAG content, and as expected, resulted in a dramatic reduction in ceramide content (Figure 6-9A-D). These results suggest a key role for ceramide in mediating skeletal muscle insulin resistance, and indicate that the other lipid metabolites may possibly not be as important in the insulin resistance process. Further support for this statement was seen with the positive correlation between ceramide content and the area under the curve during the glucose tolerance test, whereas no correlation was observed with any of the other lipid metabolites (Figure 6-9E-H). Interestingly, in a previous study we showed that mice deficient for MCD (MCD-/-) were protected from obesity-induced glucose intolerance and insulin resistance, which was associated with a reduction in incomplete fatty acid oxidation rates (202). In this study we showed that these same MCD-/- mice did not accumulate ceramide in their gastrocnemius muscle following 12 wks of high fat feeding (Figure 6-10), although they did accumulate other lipid metabolites such as long chain acyl CoA (202).

Inhibition of *de novo* ceramide synthesis via pharmacological inhibition of SPT 1 has no effect on inflammatory protein expression or phosphorylation in muscle of diet-induced insulin resistant mice

Interestingly, inflammatory proteins that have been proposed to negatively impact the insulin signaling cascade, such as p38 MAPK and JNK, were not altered in muscle of vehicle control or myriocin treated obese insulin-resistant mice (Figure 6-11A/B). However, PGC1α, a transcriptional coactivator that plays a key role in regulating a number of genes involved in energy metabolism and inflammation (141), showed a trend towards a reduction in control treated DIO mice (P = 0.077) that was not apparent in myriocin treated DIO mice (Supplementary Figure 6-11C).

Inhibition of *de novo* ceramide synthesis via pharmacological inhibition of SPT 1 prevents the development of insulin resistance in leptin receptor deficient type 2 diabetic *db/db* mice

To determine if ceramides may also be involved in genetic forms of insulin resistance and type 2 diabetes, we treated leptin receptor deficient (*db/db*) mice with myriocin to see if we could prevent the progression of insulin resistance in these animals. We split *db/db* mice at 6 wks of age into 2 groups and ensured that there were no differences in glucose tolerance before initiating treatment with myriocin (Figure 6-12A). Both the *db/db* control and myriocin treated groups experienced similar body weight increases following 2 wks of treatment (*data not shown*), however, while the *db/db* control group became

glucose intolerant, the *db/db* group treated with myriocin did not (Figure 6-12B/C). Fasting blood glucose levels were also significantly lower in the *db/db* mice treated with myriocin, and although their response to insulin was delayed, myriocin treated *db/db* mice demonstrated lower blood glucose levels at nearly all time points during an insulin tolerance test (Figure 6-12D/E). Placing these animals in the CLAMS apparatus yielded a profile similar to that of the obesity-induced insulin resistant mice. The *db/db* controls had a lower RER in the dark cycle than *db/+* lean mice, had a lower whole body oxygen consumption and ambulatory activity, but no change in overall heat production; interestingly, myriocin treatment of *db/db* mice did not restore any of these altered parameters in *db/db* controls, except for a restoration of whole body oxygen consumption rates during the light cycle (Figure 6-13A-D). Examination of the lipid metabolite profile revealed that TAG and long chain acyl CoA levels were elevated in gastrocnemius muscle of *db/db* controls versus *db/+* lean mice, while unexpectedly, DAG and ceramide levels were similar between the two groups (Figure 6-13E-H). Myriocin treatment of *db/db* mice had no effect on TAG, long chain acyl CoA, or DAG levels in gastrocnemius versus *db/db* control mice, but did lead to a dramatic reduction in ceramide levels (Figure 6-13E-H). Insulin-stimulated Akt and GSK3β phosphorylation were also depressed in *db/db* control versus *db/+* lean mice, but showed an improvement in *db/db* mice treated with myriocin (Figure 6-13I/J).

Table 6-1: *βHAD activity in gastrocnemius muscle of lean and obese mice treated with vehicle control or myriocin.*

	LF Control (n=5)	LF Myriocin (n=5)	HF Control (n=5)	HF Myriocin (n=5)
βHAD Activity	3.05 ± 0.29	3.19 ± 0.52	4.28 ± 0.31*	4.98 ± 0.60*

Values reported are μmol/g wet weight/min and represent the mean ± SE. Differences were determined using a two-way ANOVA followed by a Bonferroni post-hoc analysis. *Significantly different from the LF counterpart. LF = low fat diet, HF = high fat diet, βHAD = β-hydroxyacyl CoA dehydrogenase.

Table 6-2: *Effect of myriocin on body and tissue weight, and plasma glucose and insulin levels in lean and obese mice.*

	LF Control (n=6-8)	LF Myriocin (n=6-8)	HF Control (n=9-11)	HF Myriocin (n=10-12)
Body Weight (g)	29.80 ± 0.20	28.26 ± 0.77	43.73 ± 0.98*	41.77 ± 0.94*
Fed Blood Glucose (mM)	8.35 ± 0.39	7.74 ± 0.41	12.39 ± 1.86*	8.65 ± 0.55
Fasted Blood Glucose (mM)	6.24 ± 0.26	6.29 ± 0.22	7.44 ± 0.49*	6.26 ± 0.22†
Fasted Plasma Insulin (ng/mL)	0.32 ± 0.02	0.42 ± 0.02	3.95 ± 0.30*	4.73 ± 0.83*
Liver Weight (g)	1.41 ± 0.04	1.23 ± 0.04	1.63 ± 0.10	1.32 ± 0.06†
Abdominal Fat Weight (g)	0.43 ± 0.06	0.71 ± 0.28	1.53 ± 0.17*	1.51 ± 0.10*

Values represent the mean ± SE. Differences were determined using a two-way ANOVA followed by a Bonferroni post-hoc analysis. *Significantly different from the LF counterpart, †Significantly different from HF control. LF = low fat diet, HF = high fat diet.

Figure 6-1: *The effect of chronic high fat feeding on body weight and insulin sensitivity.*

A: Body weight in mice following 12 wks of high fat feeding. B: Development of glucose intolerance, and C: insulin resistance following 11 wks of high fat feeding. D: Respective % change in blood glucose levels during the insulin tolerance test. Values represent mean ± SE (n = 15). Differences were determined using a two-way ANOVA followed by a Bonferroni post-hoc analysis. $*P<0.05$, significantly different from low fat diet mice.

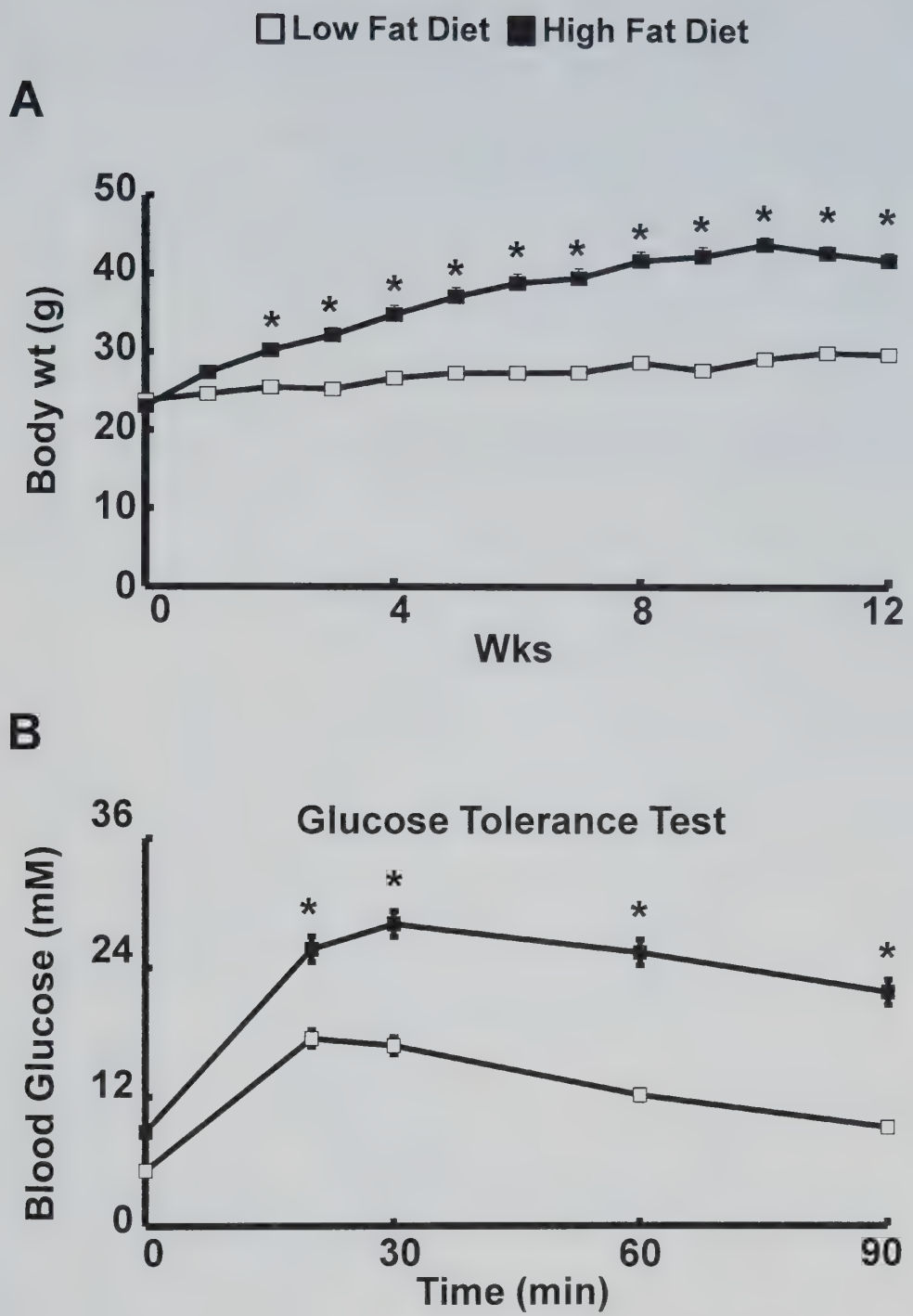
Low Fat Diet
High Fat Diet
A
Body wt (g)
50
40
30
20
10
0
0
4
8
12
Wks
B
Glucose Tolerance Test
Blood Glucose (mM)
36
24
12
0
0
30
60
90
Time (min)

FIGURE 6-1

Figure 6-1: *The effect of chronic high fat feeding on body weight and insulin sensitivity.*

A: Body weight in mice following 12 wks of high fat feeding. B: Development of glucose intolerance, and **C: insulin resistance following 11 wks of high fat feeding. D: Respective % change in blood glucose levels during the insulin tolerance test.** Values represent mean ± SE (n = 15). Differences were determined using a two-way ANOVA followed by a Bonferroni post-hoc analysis. *$P<0.05$, significantly different from low fat diet mice.

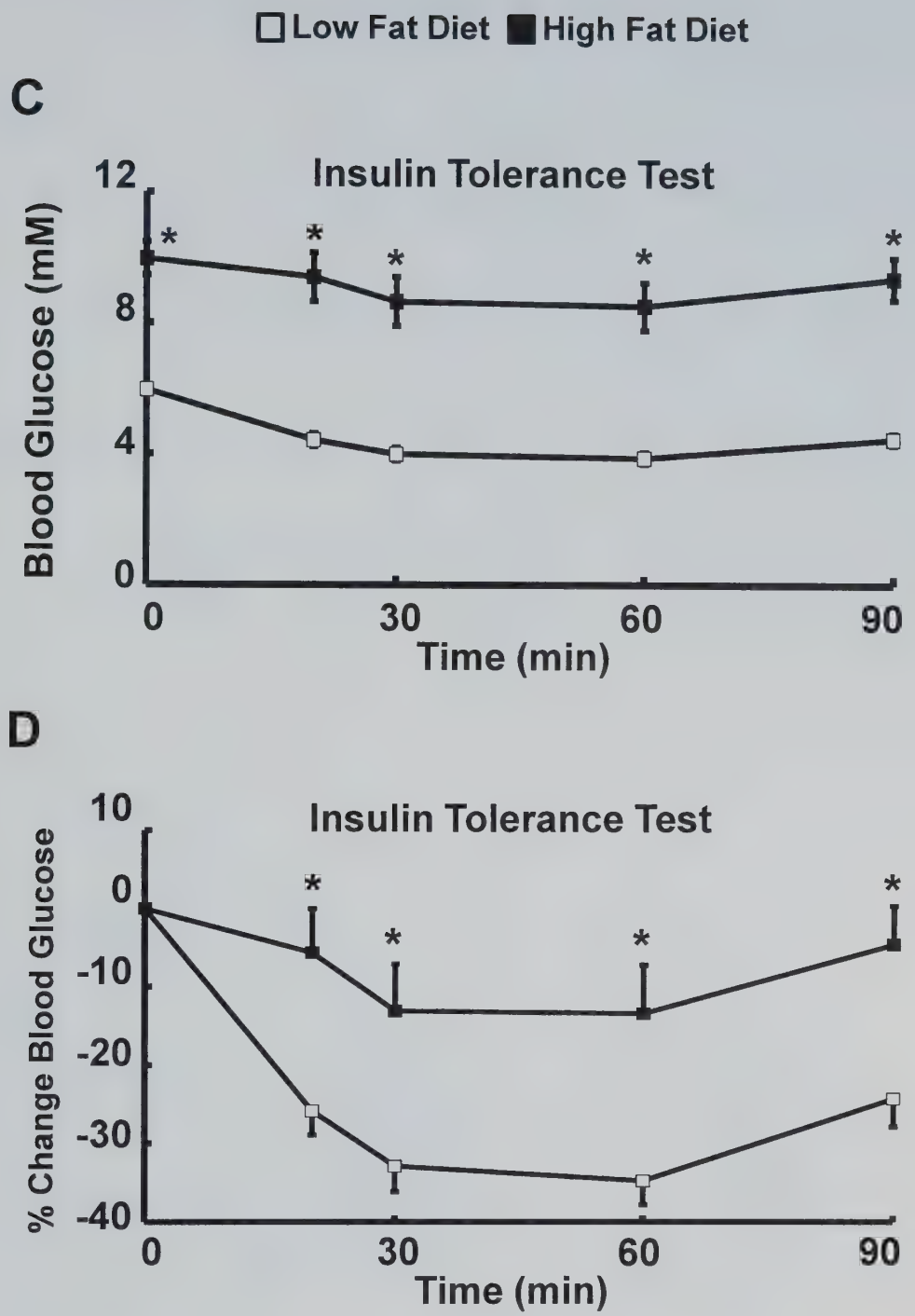
Low Fat Diet
High Fat Diet
C
Insulin Tolerance Test
Blood Glucose (mM)
12
8
4
0
0
30
60
90
Time (min)
D
Insulin Tolerance Test
% Change Blood Glucose
10
0
-10
-20
-30
-40
0
30
60
90
Time (min)

FIGURE 6-1

Figure 6-2: *High fat diet-induced insulin resistance is associated with a dramatic shift in substrate preference and an impairment of whole body oxygen consumption rates.*

Following 11 wks of high fat feeding, A: 24 hr respiratory exchange ratio (RER), B: dark and light cycle RER, C: 24 hr whole body oxygen consumption, and D: dark and light cycle whole body oxygen consumption were assessed. Values represent mean ± SE (n = 6). Differences were determined using a two-way ANOVA followed by a Bonferroni post-hoc analysis. $^{*}P<0.05$, significantly different from the low fat diet counterpart. $^{\dagger}P<0.05$, significantly different from the dark cycle counterpart.

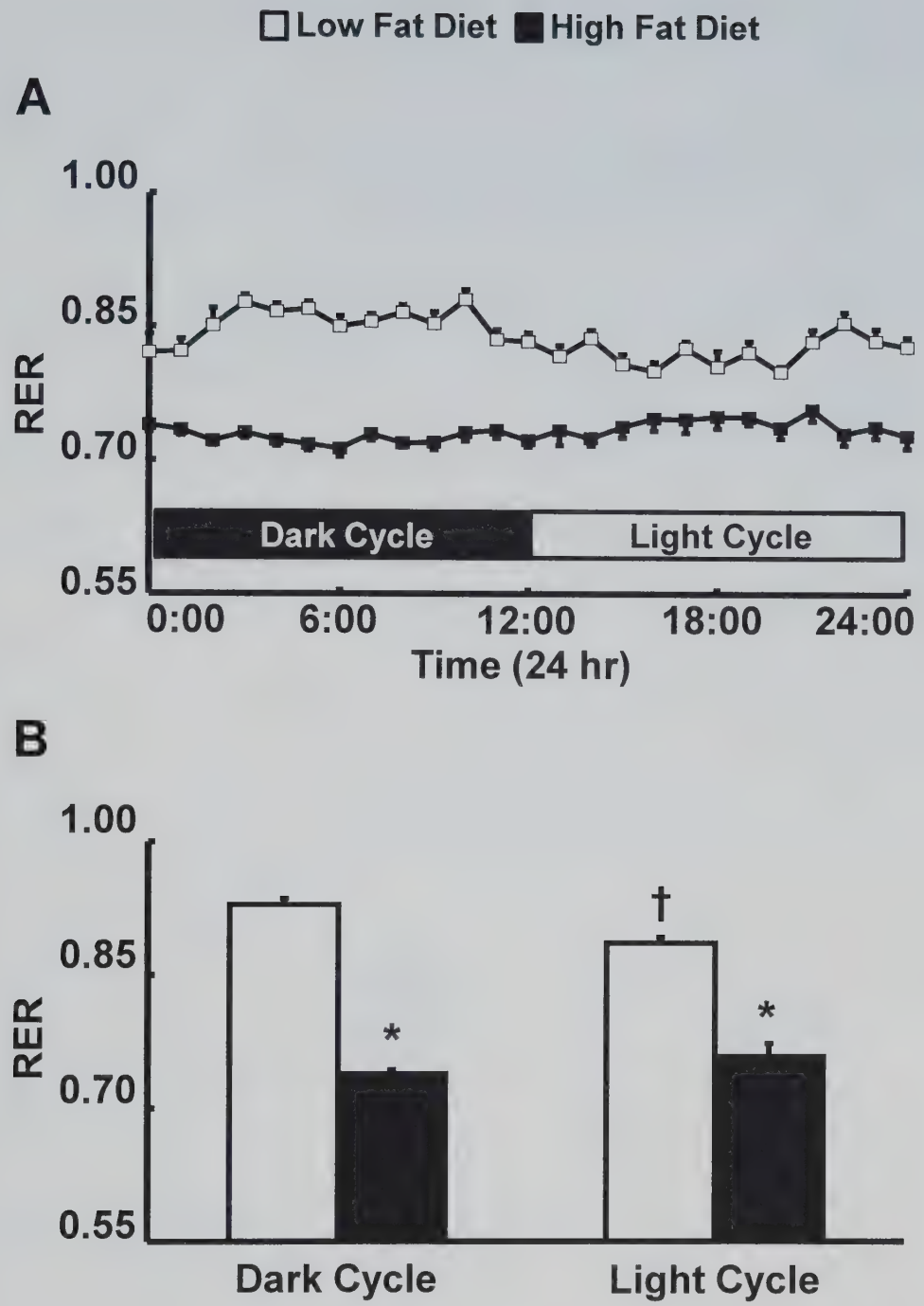
Low Fat Diet
High Fat Diet
A
1.00
0.85
0.70
0.55
RER
Dark Cycle
Light Cycle
0:00
6:00
12:00
18:00
24:00
Time (24 hr)
B
1.00
0.85
0.70
0.55
RER
*
†
*
Dark Cycle
Light Cycle

FIGURE 6-2

Figure 6-2: *High fat diet-induced insulin resistance is associated with a dramatic shift in substrate preference and an impairment of whole body oxygen consumption rates.*

Following 11 wks of high fat feeding, A: 24 hr respiratory exchange ratio (RER), B: dark and light cycle RER, **C: 24 hr whole body oxygen consumption, and D: dark and light cycle whole body oxygen consumption were assessed.** Values represent mean ± SE (n = 6). Differences were determined using a two-way ANOVA followed by a Bonferroni post-hoc analysis. $^{*}P<0.05$, significantly different from the low fat diet counterpart. $^{\dagger}P<0.05$, significantly different from the dark cycle counterpart.

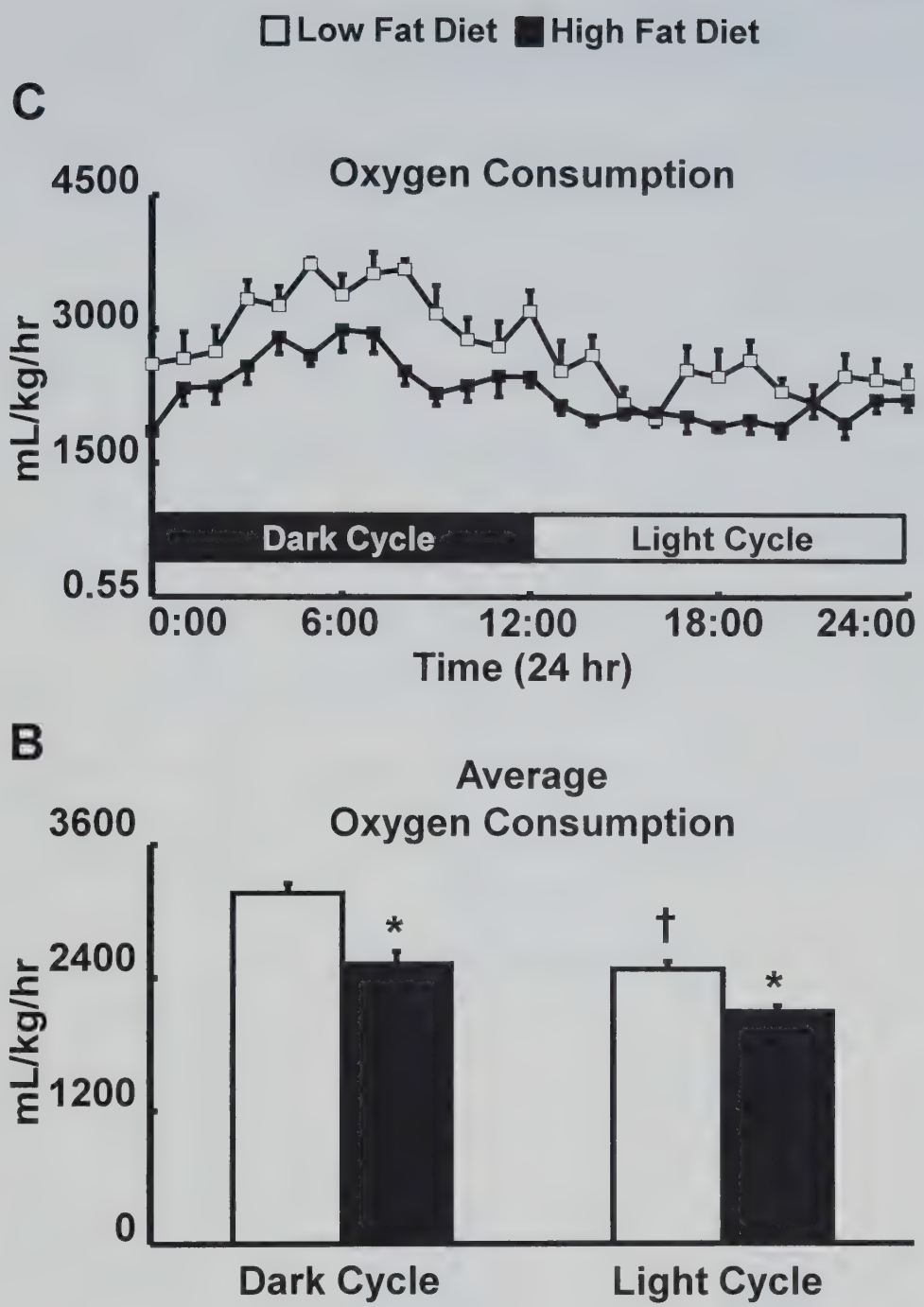
Low Fat Diet
High Fat Diet
C
Oxygen Consumption
4500
3000
1500
0.55
mL/kg/hr
Dark Cycle
Light Cycle
0:00
6:00
12:00
18:00
24:00
Time (24 hr)
B
Average
Oxygen Consumption
3600
2400
1200
0
mL/kg/hr
*
†
*
Dark Cycle
Light Cycle

FIGURE 6-2

Figure 6-3: *Inhibition of SPT 1 reverses high fat diet-induced insulin resistance and improves insulin signaling.*

A: Glucose tolerance test (GTT) in low fat diet and obese-insulin resistant mice treated with either vehicle control or myriocin. B: Area under the curve (AUC) during the GTT. C: Insulin tolerance test (ITT) in low fat diet and obese-insulin resistant mice treated with either vehicle control or myriocin. D: % Change in blood glucose levels during the ITT. E: Insulin stimulated Akt phosphorylation at serine 473, and F: GSK3β phosphorylation at serine 9 in gastrocnemius muscle of obese-insulin resistant mice treated with either vehicle control or myriocin. Values represent mean ± SE (n = 8-12 for A-D, n = 4 for E/F). Differences were determined using a two-way ANOVA followed by a Bonferroni post-hoc analysis. $^{*}P<0.05$, significantly different from all other groups. $^{\dagger}P<0.05$, significantly different from the high fat diet control mice.

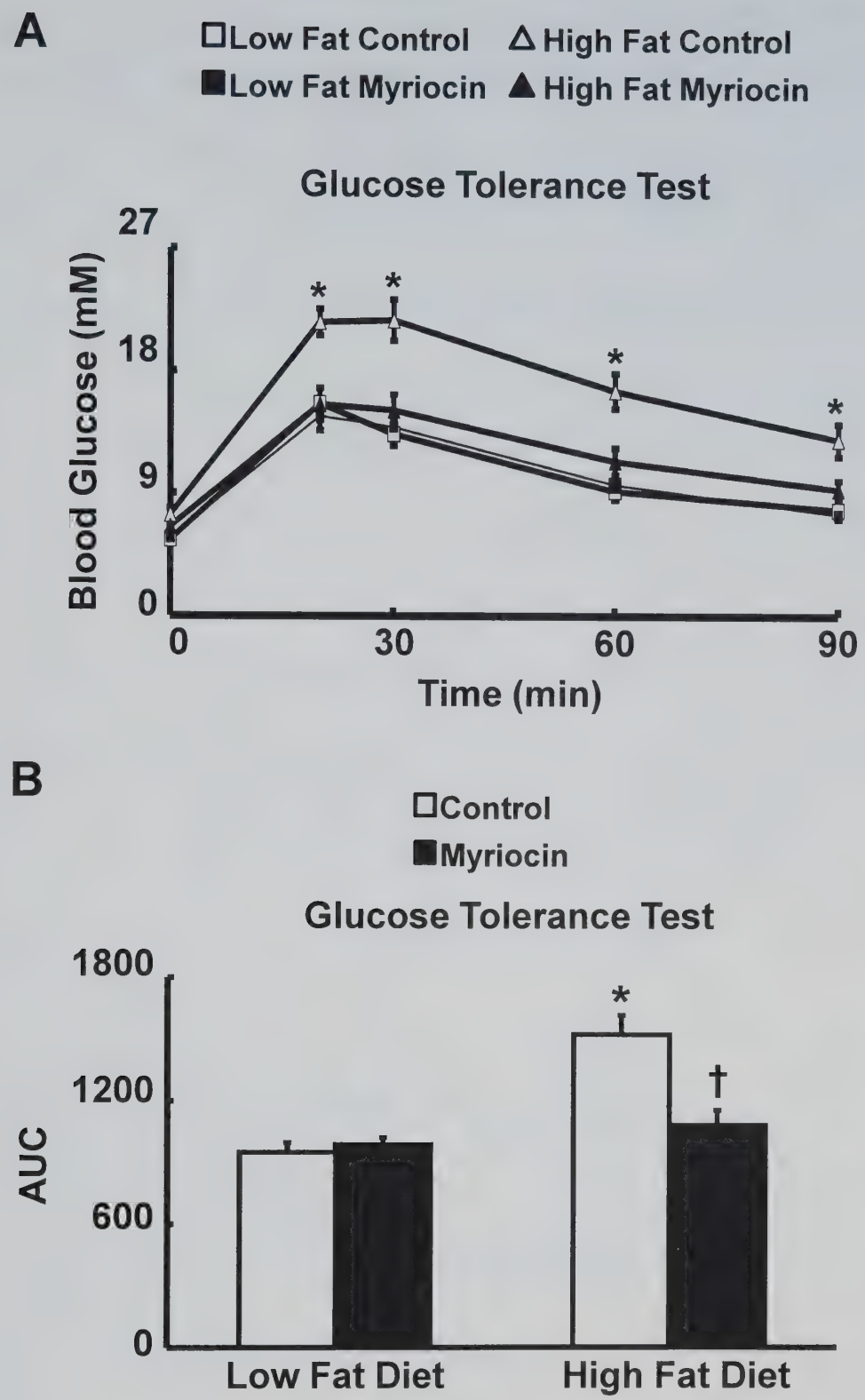
A
Low Fat Control
High Fat Control
Low Fat Myriocin
High Fat Myriocin
Glucose Tolerance Test
Blood Glucose (mM)
27
18
9
0
0
30
60
90
Time (min)
*
B
Control
Myriocin
Glucose Tolerance Test
AUC
1800
1200
600
0
*
†
Low Fat Diet
High Fat Diet

FIGURE 6-3

Figure 6-3: *Inhibition of SPT 1 reverses high fat diet-induced insulin resistance and improves insulin signaling.*

A: Glucose tolerance test (GTT) in low fat diet and obese-insulin resistant mice treated with either vehicle control or myriocin. B: Area under the curve (AUC) during the GTT. **C: Insulin tolerance test (ITT) in low fat diet and obese-insulin resistant mice treated with either vehicle control or myriocin. D: % Change in blood glucose levels during the ITT.** E: Insulin stimulated Akt phosphorylation at serine 473, and F: GSK3β phosphorylation at serine 9 in gastrocnemius muscle of obese-insulin resistant mice treated with either vehicle control or myriocin. Values represent mean ± SE (n = 8-12 for A-D, n = 4 for E/F). Differences were determined using a two-way ANOVA followed by a Bonferroni post-hoc analysis. $*P<0.05$, significantly different from all other groups.

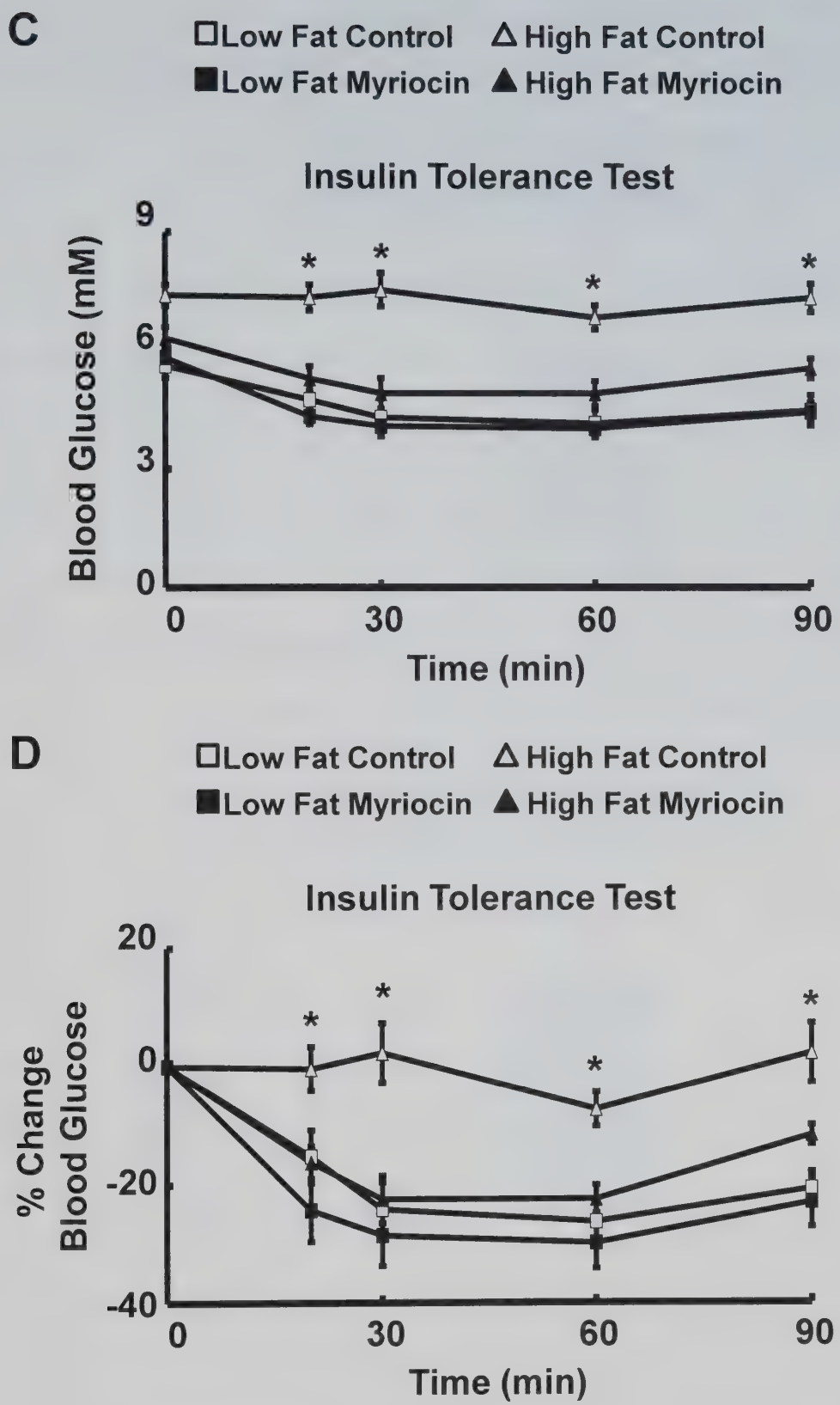
C
Low Fat Control
High Fat Control
Low Fat Myriocin
High Fat Myriocin
Insulin Tolerance Test
Blood Glucose (mM)
9
6
3
0
0
30
60
90
Time (min)
*
D
Low Fat Control
High Fat Control
Low Fat Myriocin
High Fat Myriocin
Insulin Tolerance Test
% Change Blood Glucose
20
0
-20
-40
0
30
60
90
Time (min)
*

FIGURE 6-3

Figure 6-3: *Inhibition of SPT 1 reverses high fat diet-induced insulin resistance and improves insulin signaling.*

A: Glucose tolerance test (GTT) in low fat diet and obese-insulin resistant mice treated with either vehicle control or myriocin. B: Area under the curve (AUC) during the GTT. C: Insulin tolerance test (ITT) in low fat diet and obese-insulin resistant mice treated with either vehicle control or myriocin. D: % Change in blood glucose levels during the ITT. **E: Insulin stimulated Akt phosphorylation at serine 473, and F: GSK3β phosphorylation at serine 9 in gastrocnemius muscle of obese-insulin resistant mice treated with either vehicle control or myriocin.** Values represent mean ± SE (n = 8-12 for A-D, n = 4 for E/F). Differences were determined using a two-tailed Student's *t*-test. $^{\dagger}P<0.05$, significantly different from the high fat diet control mice.

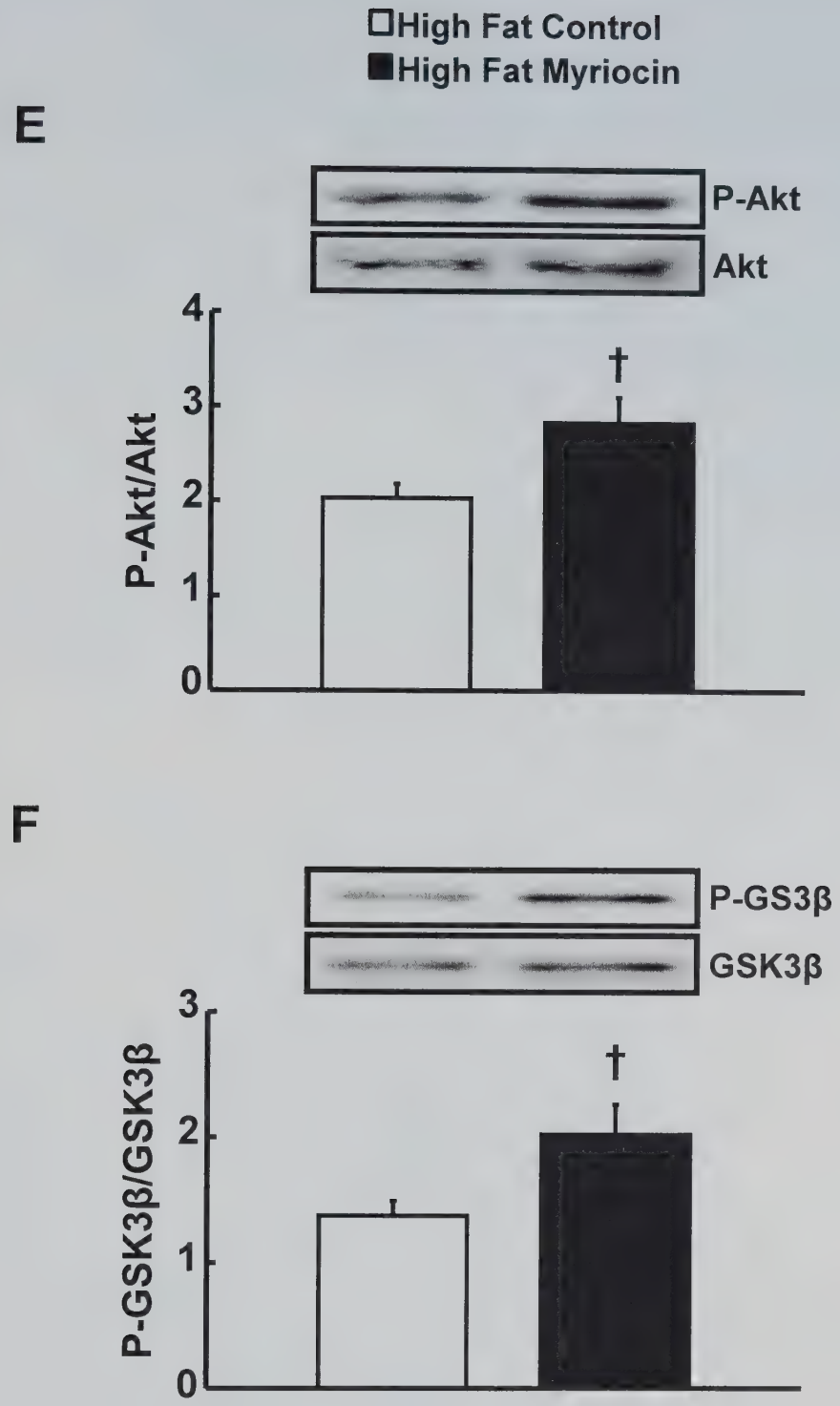
High Fat Control
High Fat Myriocin
E
P-Akt
Akt
P-Akt/Akt
4
3
2
1
0
†
F
P-GS3β
GSK3β
P-GSK3β/GSK3β
3
2
1
0
†

FIGURE 6-3

Figure 6-4: *Substrate preference in lean and obese mice treated with myriocin.* A: 24 hr, B: dark cycle, and C: light cycle respiratory exchange ratio (RER) in low fat diet and obese-insulin resistant mice treated with either vehicle control or myriocin. Values represent mean ± SE (n = 8-12). Differences were determined using a two-way ANOVA followed by a Bonferroni post-hoc analysis. $*P<0.05$, significantly different from the low fat diet counterpart.

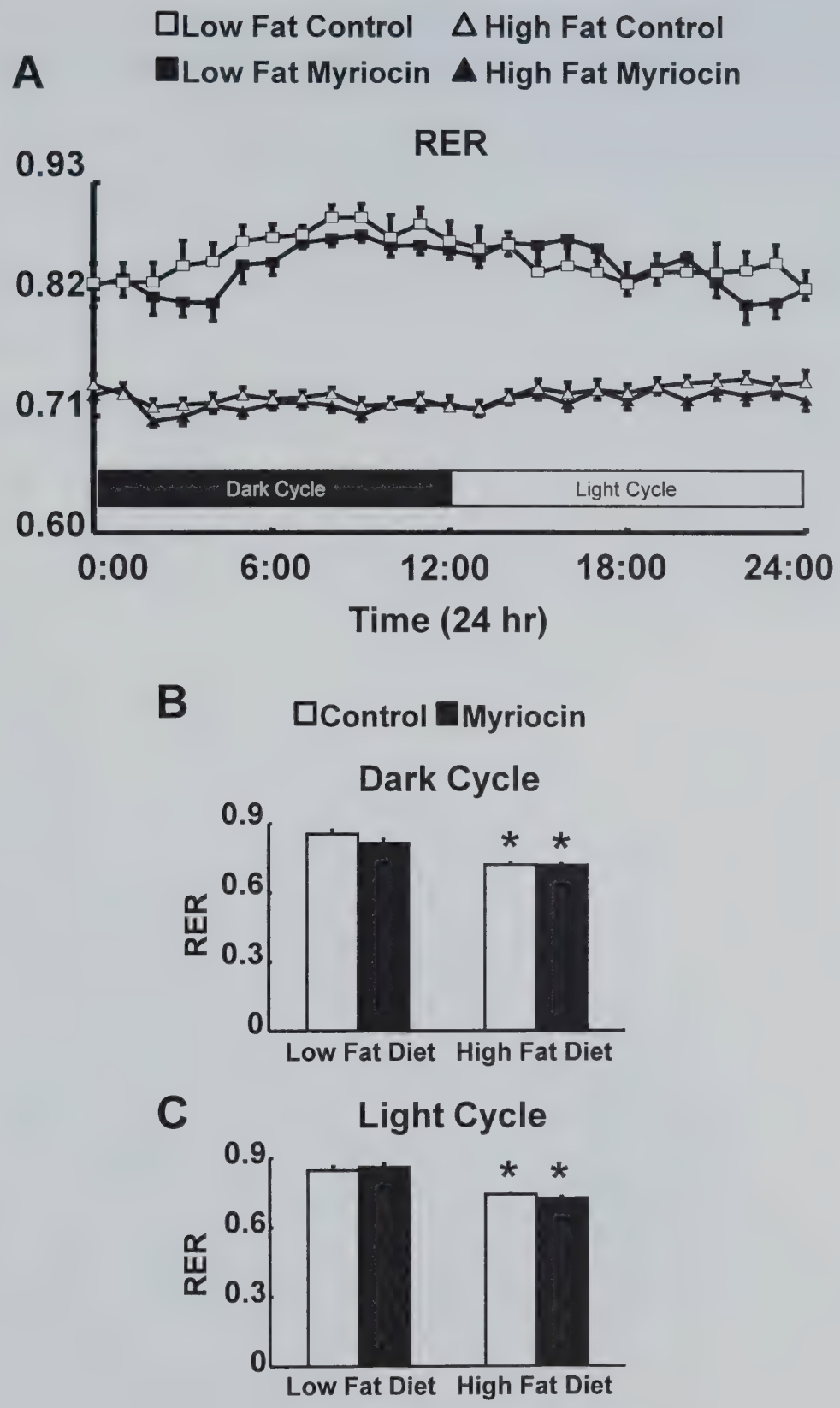
A
Low Fat Control
High Fat Control
Low Fat Myriocin
High Fat Myriocin
RER
0.93
0.82
0.71
0.60
Dark Cycle
Light Cycle
0:00
6:00
12:00
18:00
24:00
Time (24 hr)
B
Control
Myriocin
Dark Cycle
RER
0.9
0.6
0.3
0
*
*
Low Fat Diet
High Fat Diet
C
Light Cycle
RER
0.9
0.6
0.3
0
*
*
Low Fat Diet
High Fat Diet

FIGURE 6-4

Figure 6-5: *L-cycloserine treatment reverses high-fat diet induced insulin resistance.*

A: Blood glucose levels during a glucose tolerance test (GTT) in obese-insulin resistant mice treated with either vehicle control or L-cycloserine. B: Area under the curve (AUC) during the GTT. C: Blood glucose levels during an insulin tolerance test (ITT) in obese-insulin resistant mice treated with either vehicle control or L-cycloserine. D: % Change in blood glucose levels during the ITT. Values represent mean ± SE (n = 5-7). Differences were determined using a two-way ANOVA followed by a Bonferroni post-hoc analysis. $*P<0.05$, significantly different from the high fat diet control mice.

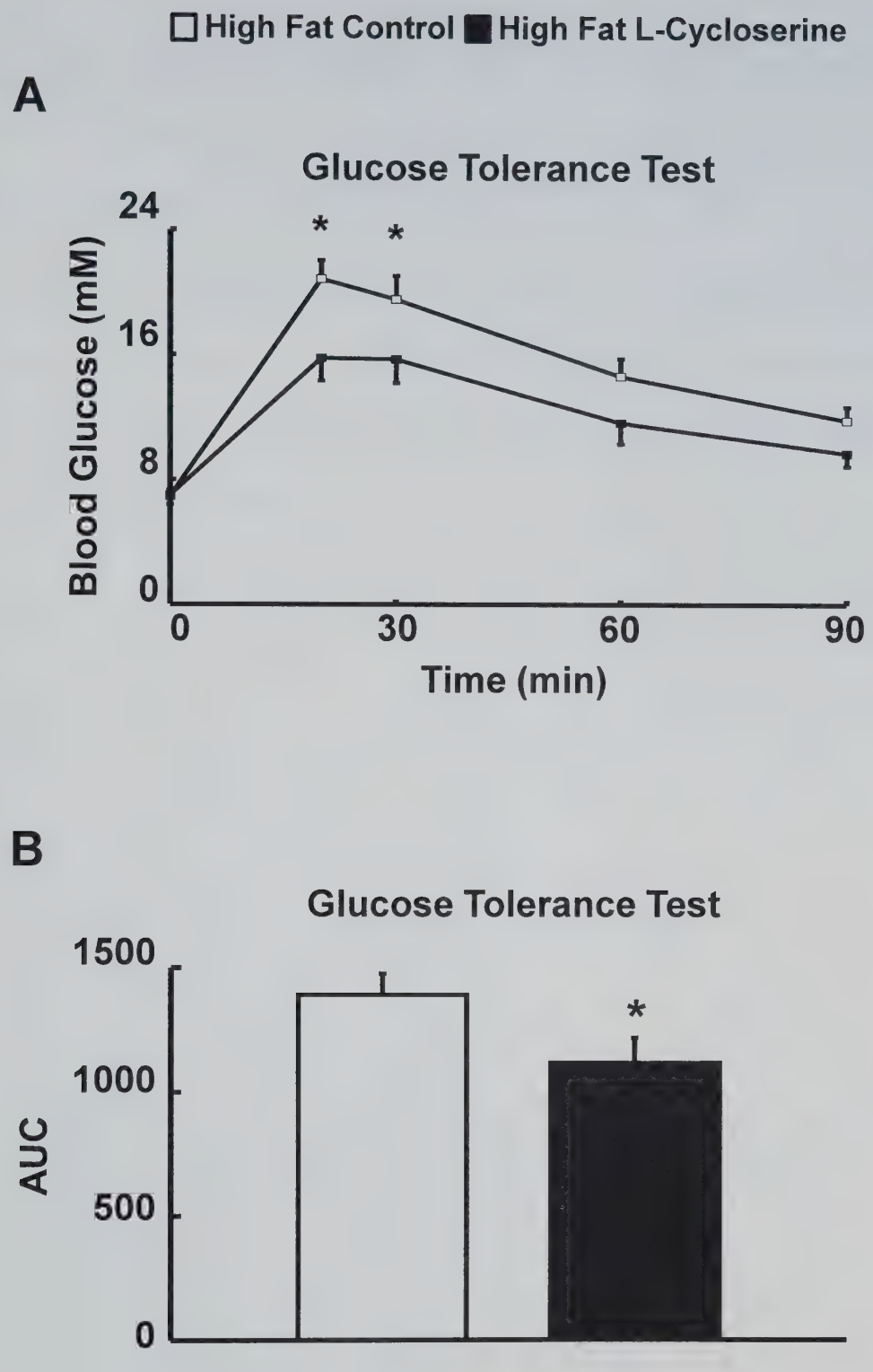
High Fat Control
High Fat L-Cycloserine
A
Glucose Tolerance Test
Blood Glucose (mM)
24
16
8
0
*
*
0
30
60
90
Time (min)
B
Glucose Tolerance Test
AUC
1500
1000
500
0
*

FIGURE 6-5

Figure 6-5: *L-cycloserine treatment reverses high-fat diet induced insulin resistance.*

A: Blood glucose levels during a glucose tolerance test (GTT) in obese-insulin resistant mice treated with either vehicle control or L-cycloserine. B: Area under the curve (AUC) during the GTT. **C: Blood glucose levels during an insulin tolerance test (ITT) in obese-insulin resistant mice treated with either vehicle control or L-cycloserine. D: % Change in blood glucose levels during the ITT.** Values represent mean ± SE (n = 5-7). Differences were determined using a two-way ANOVA followed by a Bonferroni post-hoc analysis. $*P<0.05$, significantly different from the high fat diet control mice.

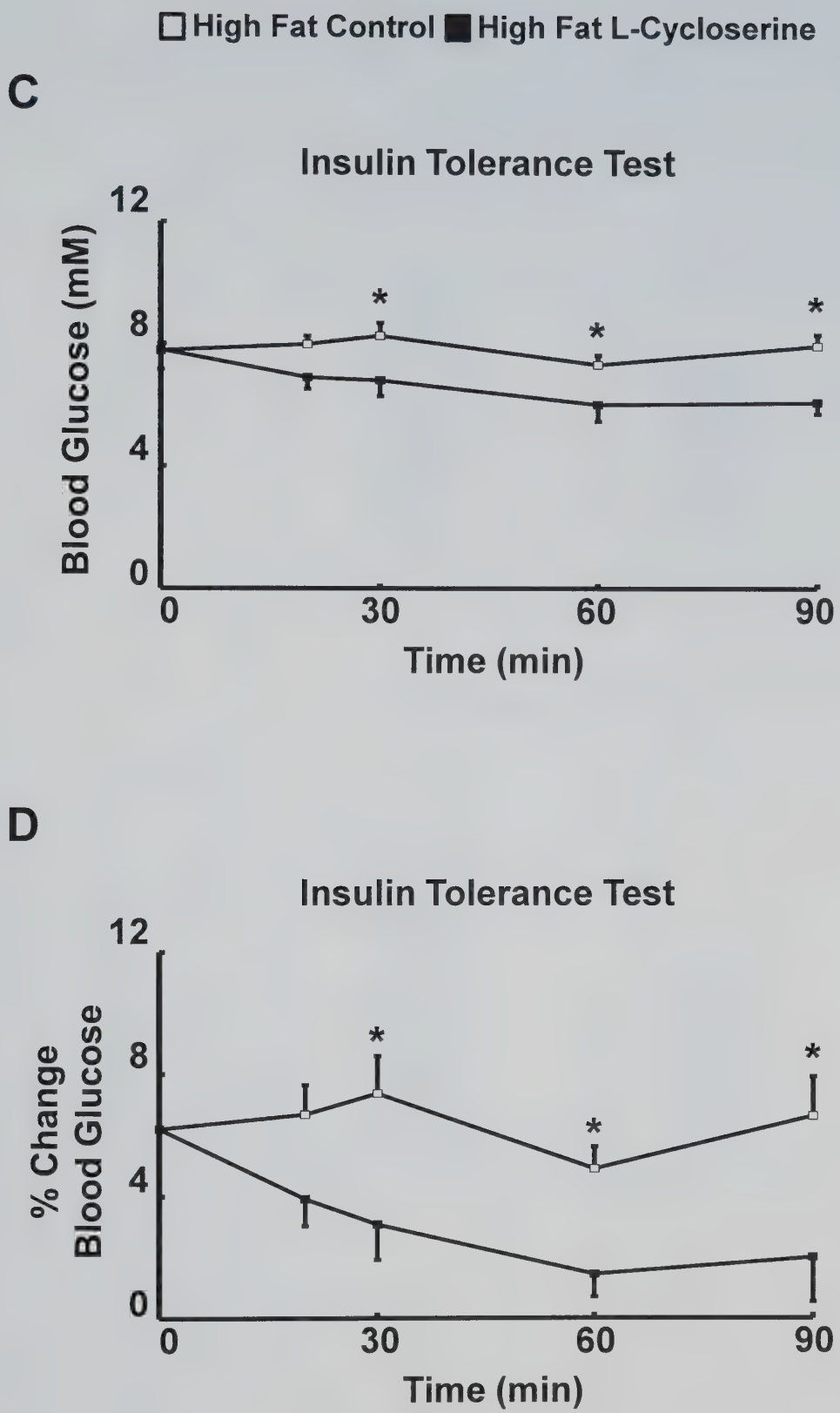
High Fat Control
High Fat L-Cycloserine
C
Insulin Tolerance Test
Blood Glucose (mM)
12
8
4
0
0
30
60
90
Time (min)
*
*
*
D
Insulin Tolerance Test
% Change Blood Glucose
12
8
4
0
0
30
60
90
Time (min)
*
*
*

FIGURE 6-5

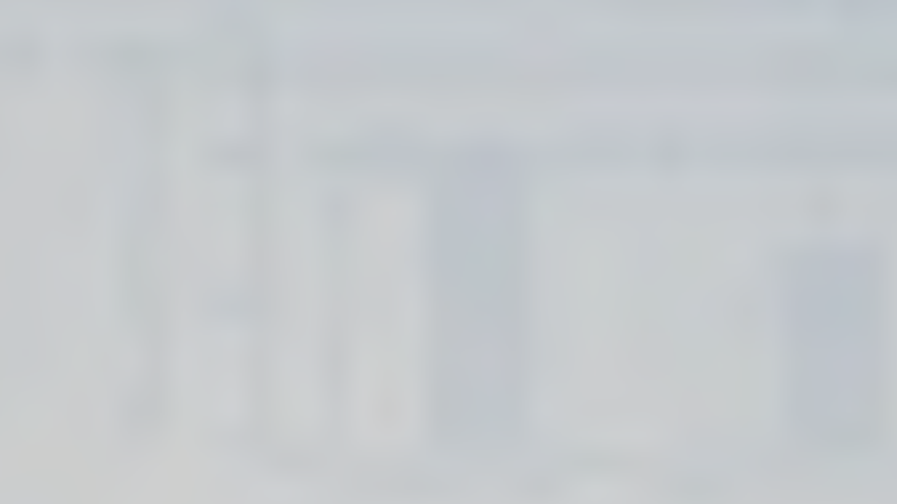

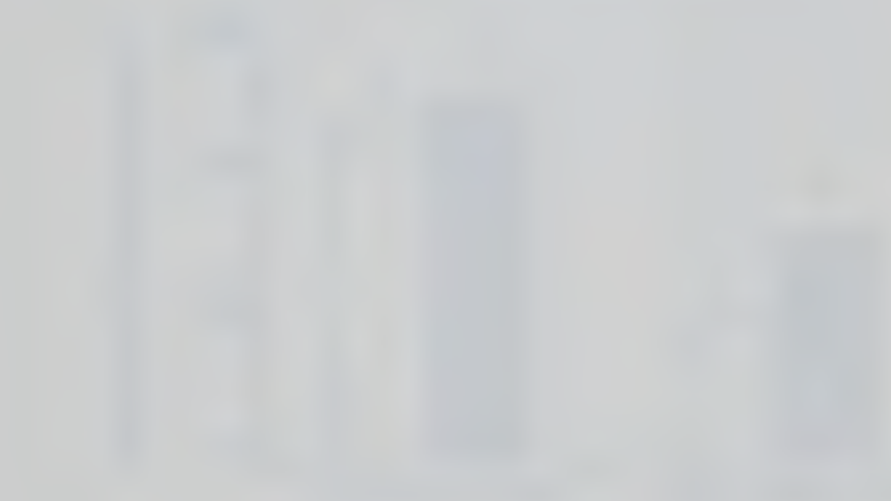

Figure 6-6: *Myriocin treatment reverses the impairment in aerobic exercise capacity caused by DIO.*

A: Time and B: distance during an exercise capacity challenge on a running treadmill. Values represent mean ± SE (n = 8-12). Differences were determined using a two-way ANOVA followed by a Bonferroni post-hoc analysis. $*P<0.05$, significantly different from the low fat diet counterpart.

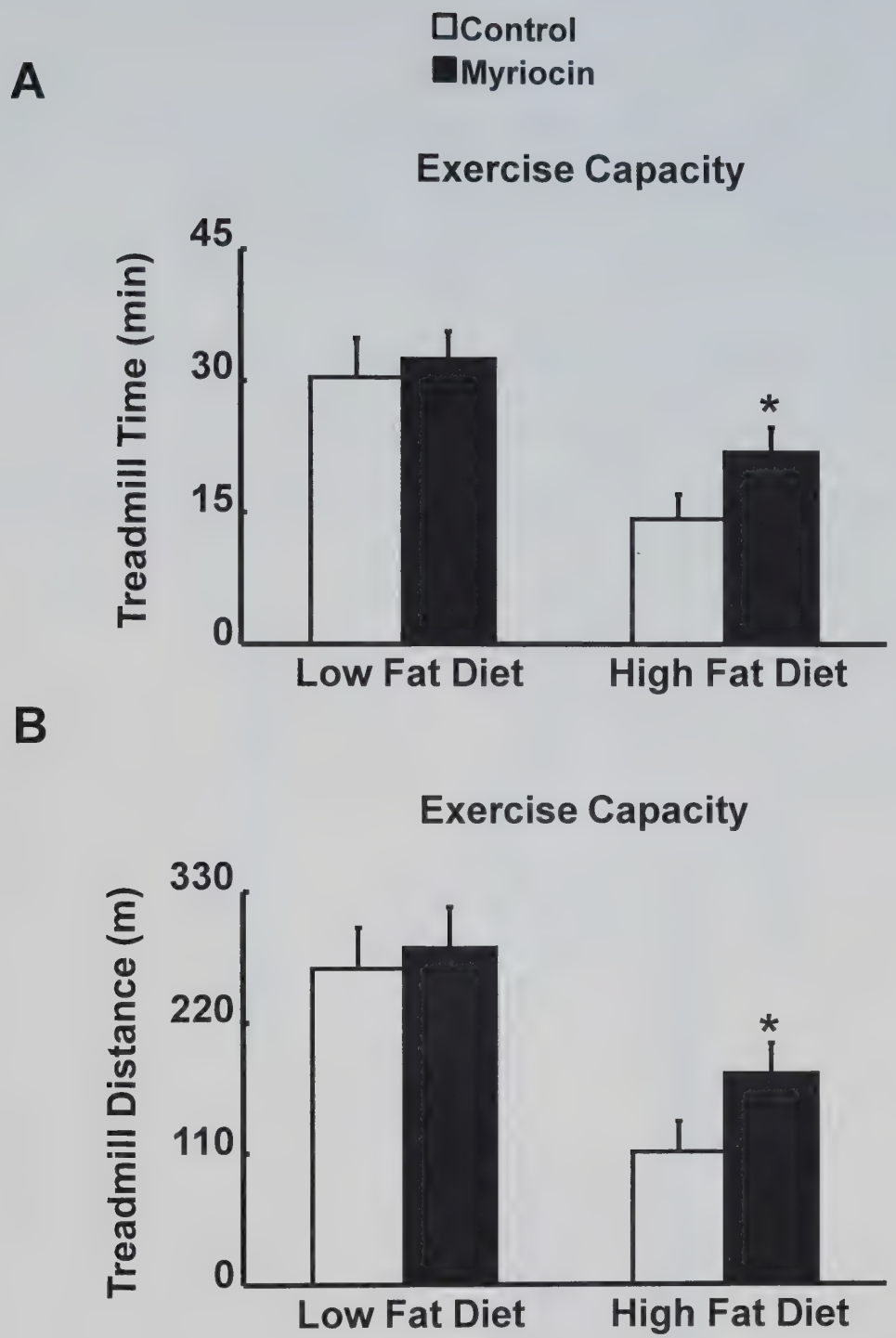
A
Control
Myriocin
Exercise Capacity
Treadmill Time (min)
45
30
15
0
*
Low Fat Diet
High Fat Diet
B
Exercise Capacity
Treadmill Distance (m)
330
220
110
0
*
Low Fat Diet
High Fat Diet

FIGURE 6-6

Figure 6-7: *Myriocin treatment reverses the impairment in whole body oxygen consumption rates caused by DIO.*

A: 24 hr, B: dark cycle, and C: light cycle **whole body oxygen consumption assessment in low fat diet and obese-insulin resistant mice treated with either vehicle control or myriocin.** D: Gastrocnemius muscle citrate synthase activity in vehicle control and myriocin treated DIO mice. Values represent mean ± SE (n = 8-12). Differences were determined using a two-way ANOVA followed by a Bonferroni post-hoc analysis. $^{\dagger}P<0.05$, significantly different from the high fat diet control mice.

A

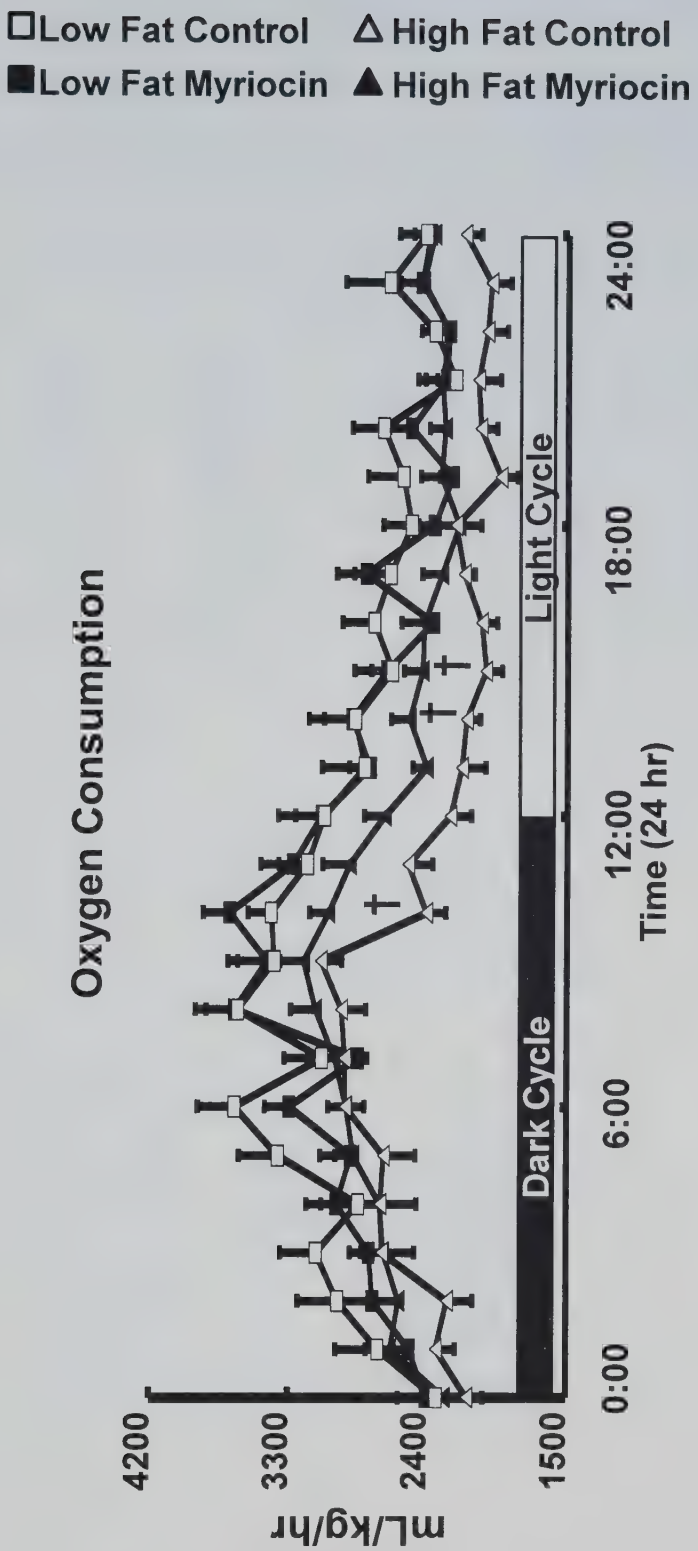
Low Fat Control
High Fat Control
Low Fat Myriocin
High Fat Myriocin
Oxygen Consumption
mL/kg/hr
4200
3300
2400
1500
Dark Cycle
Light Cycle
0:00
6:00
12:00
18:00
24:00
Time (24 hr)

FIGURE 6-7

Figure 6-7: *Myriocin treatment reverses the impairment in whole body oxygen consumption rates caused by DIO.*

A: 24 hr, **B: dark cycle, and C: light cycle whole body oxygen consumption assessment in low fat diet and obese-insulin resistant mice treated with either vehicle control or myriocin. D: Gastrocnemius muscle citrate synthase activity in vehicle control and myriocin treated DIO mice.** Values represent mean ± SE (n = 8-12). Differences were determined using a two-tailed Student's *t*-test or a two-way ANOVA followed by a Bonferroni post-hoc analysis. $^{*}P<0.05$, significantly different from the low fat diet counterpart. $^{\dagger}P<0.05$, significantly different from the high fat diet control mice.

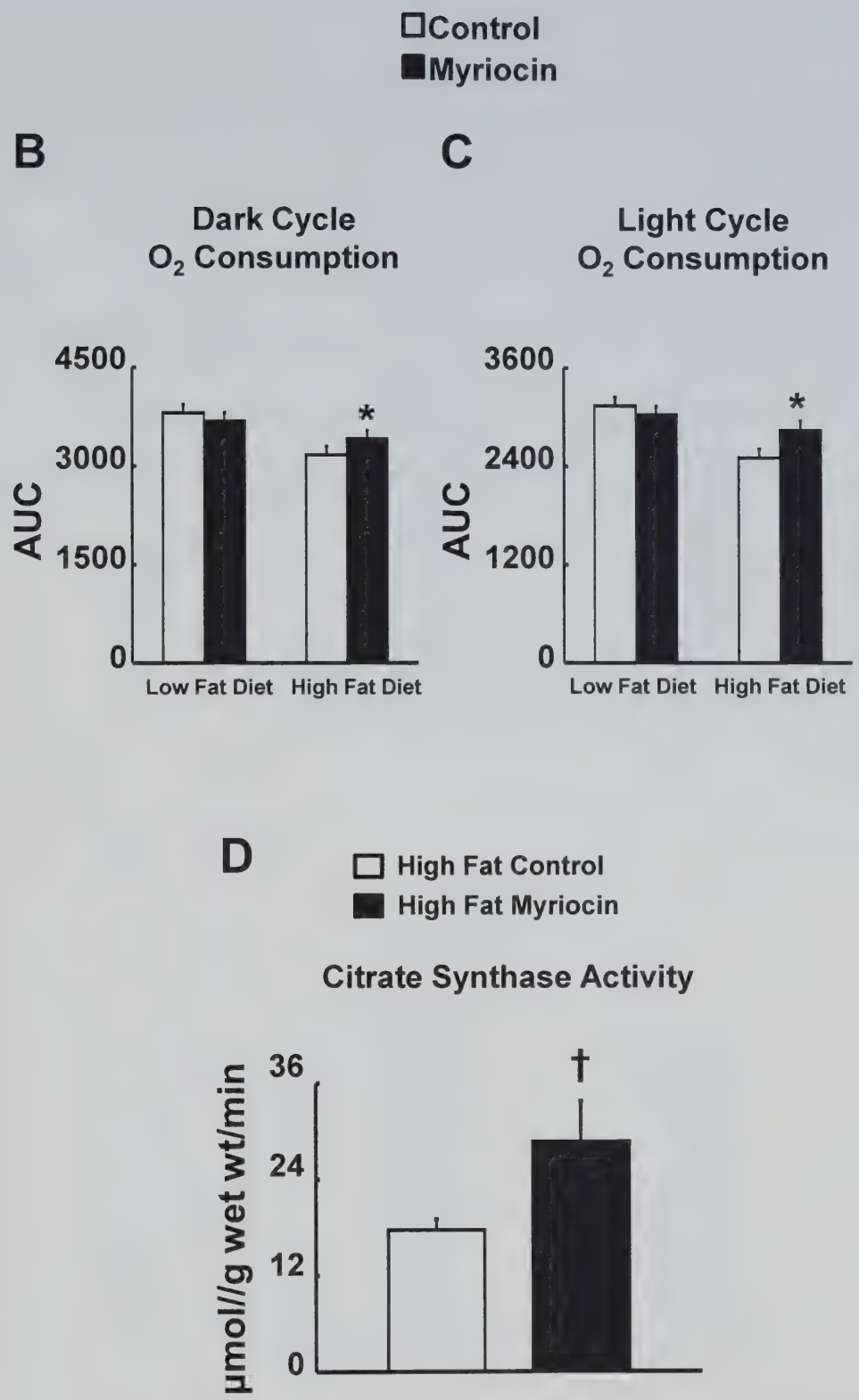
Control
Myriocin
B
Dark Cycle
O2 Consumption
AUC
4500
3000
1500
0
*
Low Fat Diet
High Fat Diet
C
Light Cycle
O2 Consumption
AUC
3600
2400
1200
0
*
Low Fat Diet
High Fat Diet
D
High Fat Control
High Fat Myriocin
Citrate Synthase Activity
µmol//g wet wt/min
36
24
12
0
†

FIGURE 6-7

Figure 6-8: *Heat production and activity in lean and DIO mice treated with myriocin.*

A: Dark cycle and B: light cycle heat production in low fat diet and obese-insulin resistant mice treated with either vehicle control or myriocin. C: Dark cycle and D: light cycle ambulatory activity in low fat diet and obese-insulin resistant mice treated with either vehicle control or myriocin. Values represent mean ± SE (n = 8-12). Differences were determined using a two-way ANOVA followed by a Bonferroni post-hoc analysis. $*P<0.05$, significantly different from the low fat diet counterpart.

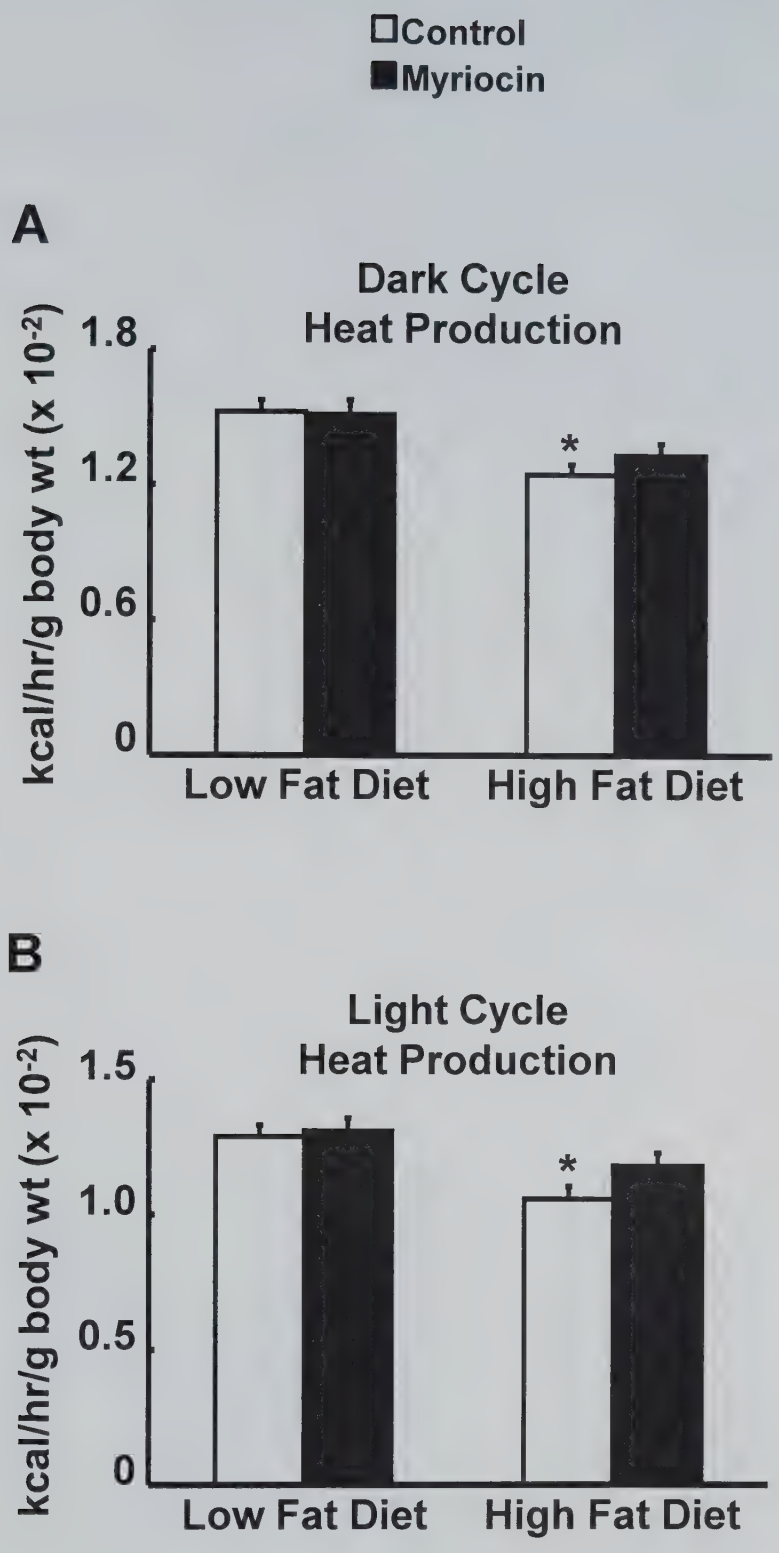
Control
Myriocin
A
Dark Cycle
Heat Production
kcal/hr/g body wt (x 10-2)
1.8
1.2
0.6
0
*
Low Fat Diet
High Fat Diet
B
Light Cycle
Heat Production
kcal/hr/g body wt (x 10-2)
1.5
1.0
0.5
0
*
Low Fat Diet
High Fat Diet

FIGURE 6-8

Figure 6-8: *Heat production and activity in lean and DIO mice treated with myriocin.*

A: Dark cycle and B: light cycle heat production in low fat diet and obese-insulin resistant mice treated with either vehicle control or myriocin. **C: Dark cycle and D: light cycle ambulatory activity in low fat diet and obese-insulin resistant mice treated with either vehicle control or myriocin.** Values represent mean ± SE (n = 8-12). Differences were determined using a two-way ANOVA followed by a Bonferroni post-hoc analysis. $*P<0.05$, significantly different from the low fat diet counterpart.

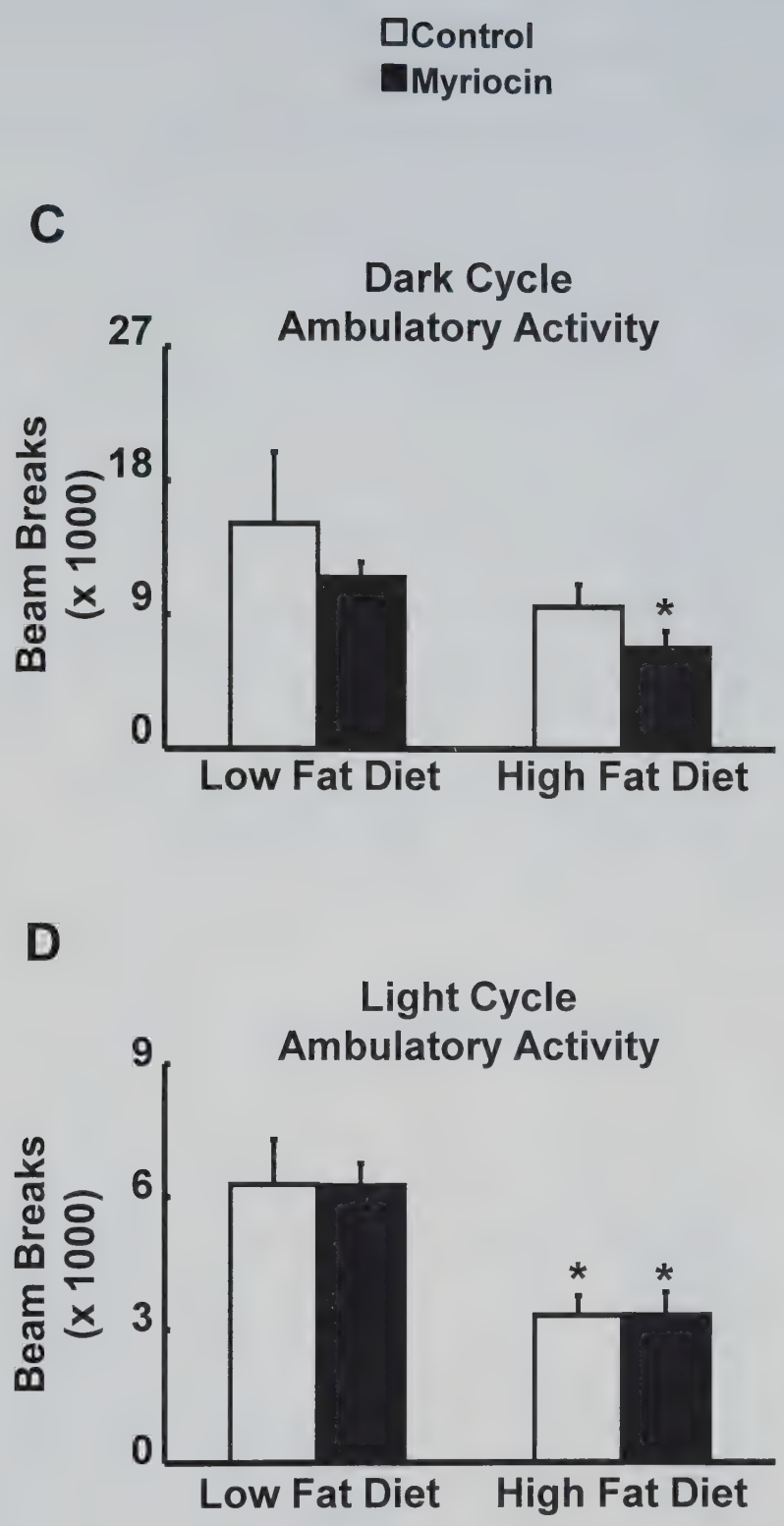
Control
Myriocin
C
Dark Cycle
Ambulatory Activity
27
18
9
0
Beam Breaks
(x 1000)
*
Low Fat Diet
High Fat Diet
D
Light Cycle
Ambulatory Activity
9
6
3
0
Beam Breaks
(x 1000)
*
*
Low Fat Diet
High Fat Diet

FIGURE 6-8

Figure 6-9: *Inhibition of SPT 1 reduces skeletal muscle ceramide levels without any effect on other lipid metabolites.*

A: Gastrocnemius triacylglycerol (TAG), B: long chain acyl CoA, C: ceramide, and D: diacylglycerol (DAG) levels in low fat fed and obese-insulin resistant mice treated with either vehicle control or myriocin. Values represent mean ± SE (n = 4-8). Differences were determined using a two-way ANOVA followed by a Bonferroni post-hoc analysis. $*P<0.05$, significantly different from the low fat diet counterpart. E: Correlation between the respective area under the curve during the glucose tolerance test and Ceramide, F: TAG G: long chain acyl CoA, and H: DAG, of (n = 14-18) samples.

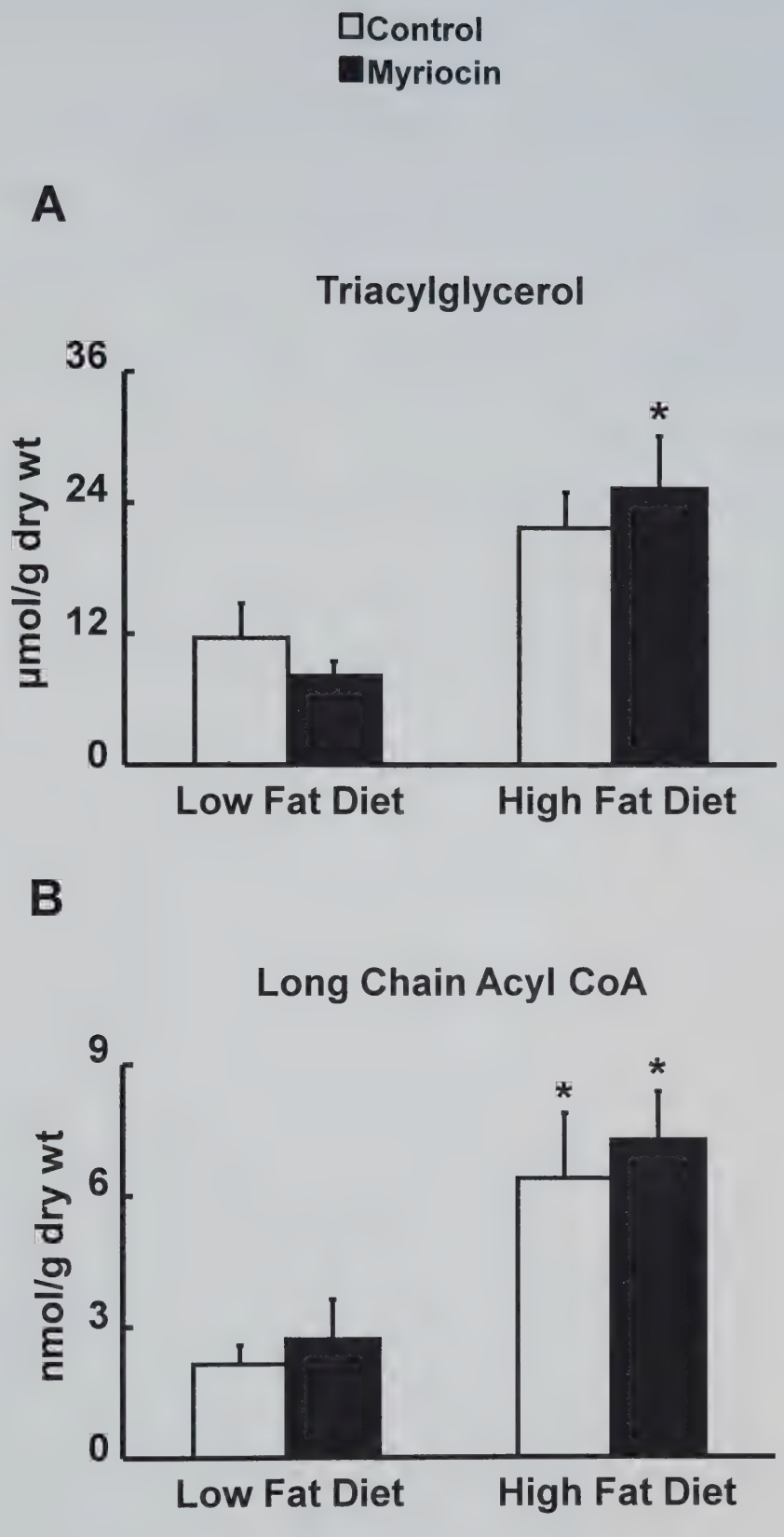
Control
Myriocin
A
Triacylglycerol
µmol/g dry wt
36
24
12
0
*
Low Fat Diet
High Fat Diet
B
Long Chain Acyl CoA
nmol/g dry wt
9
6
3
0
*
*
Low Fat Diet
High Fat Diet

FIGURE 6-9

Figure 6-9: *Inhibition of SPT 1 reduces skeletal muscle ceramide levels without any effect on other lipid metabolites.*

A: Gastrocnemius triacylglycerol (TAG), B: long chain acyl CoA**, C: ceramide, and D: diacylglycerol (DAG) levels in low fat fed and obese-insulin resistant mice treated with either vehicle control or myriocin.** Values represent mean ± SE (n = 4-8). Differences were determined using a two-way ANOVA followed by a Bonferroni post-hoc analysis. $^{*}P<0.05$, significantly different from the low fat diet counterpart. $^{\dagger}P<0.05$, significantly different from the high fat diet control mice. E: Correlation between the respective area under the curve during the glucose tolerance test and Ceramide, F: TAG G: long chain acyl CoA, and H: DAG, of (n = 14-18) samples.

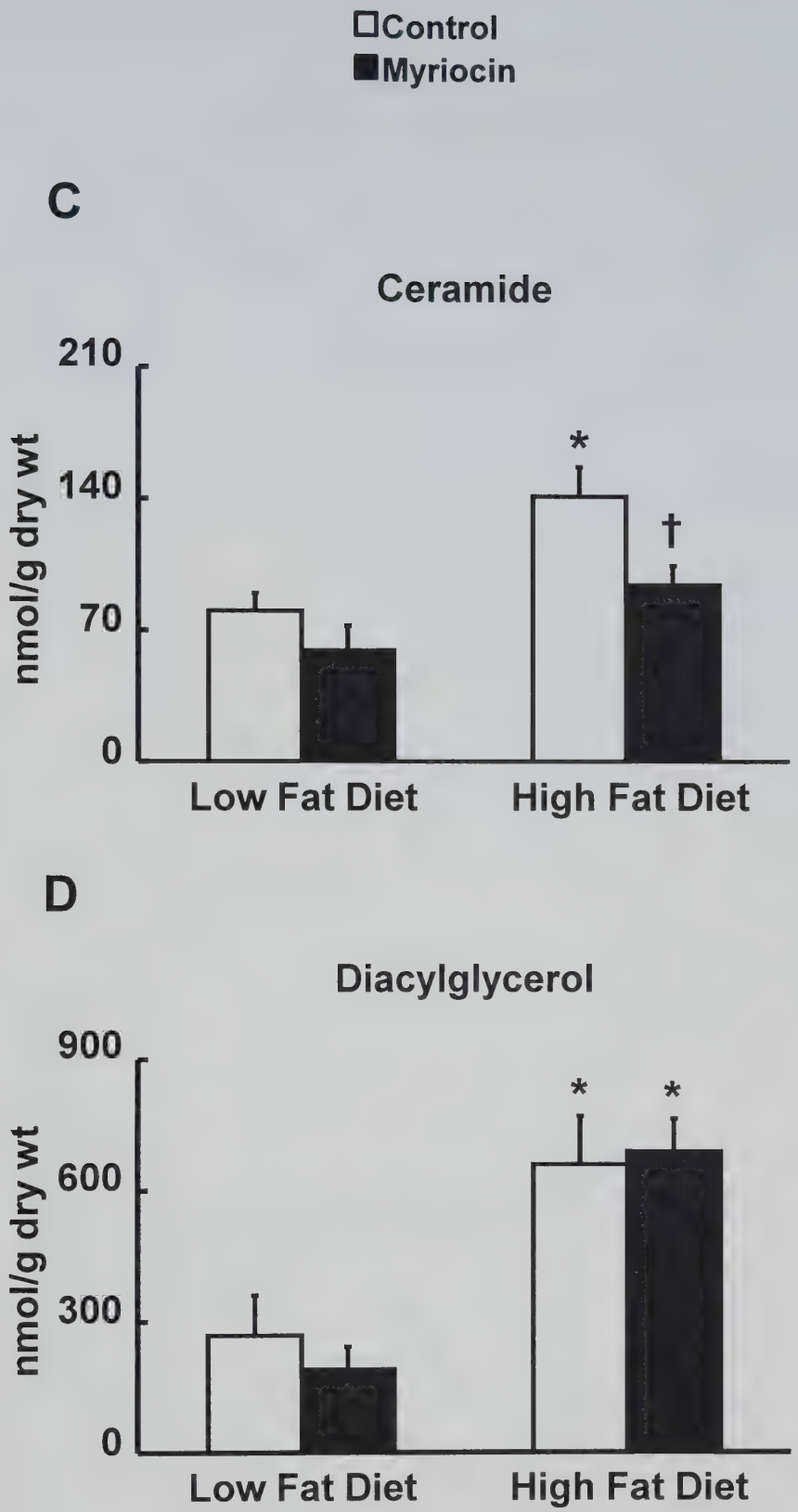
Control
Myriocin
C
Ceramide
210
140
70
0
nmol/g dry wt
*
†
Low Fat Diet
High Fat Diet
D
Diacylglycerol
900
600
300
0
nmol/g dry wt
*
*
Low Fat Diet
High Fat Diet

FIGURE 6-9

Figure 6-9: *Inhibition of SPT 1 reduces skeletal muscle ceramide levels without any effect on other lipid metabolites.*

A: Gastrocnemius triacylglycerol (TAG), B: long chain acyl CoA, C: ceramide, and D: diacylglycerol (DAG) levels in low fat fed and obese-insulin resistant mice treated with either vehicle control or myriocin. Values represent mean ± SE (n = 4-8). **E: Correlation between the respective area under the curve (AUC) during the glucose tolerance test and Ceramide, F: TAG** G: long chain acyl CoA, and H: DAG, of (n = 14-18) samples. Correlation was determined via Pearson correlation test.

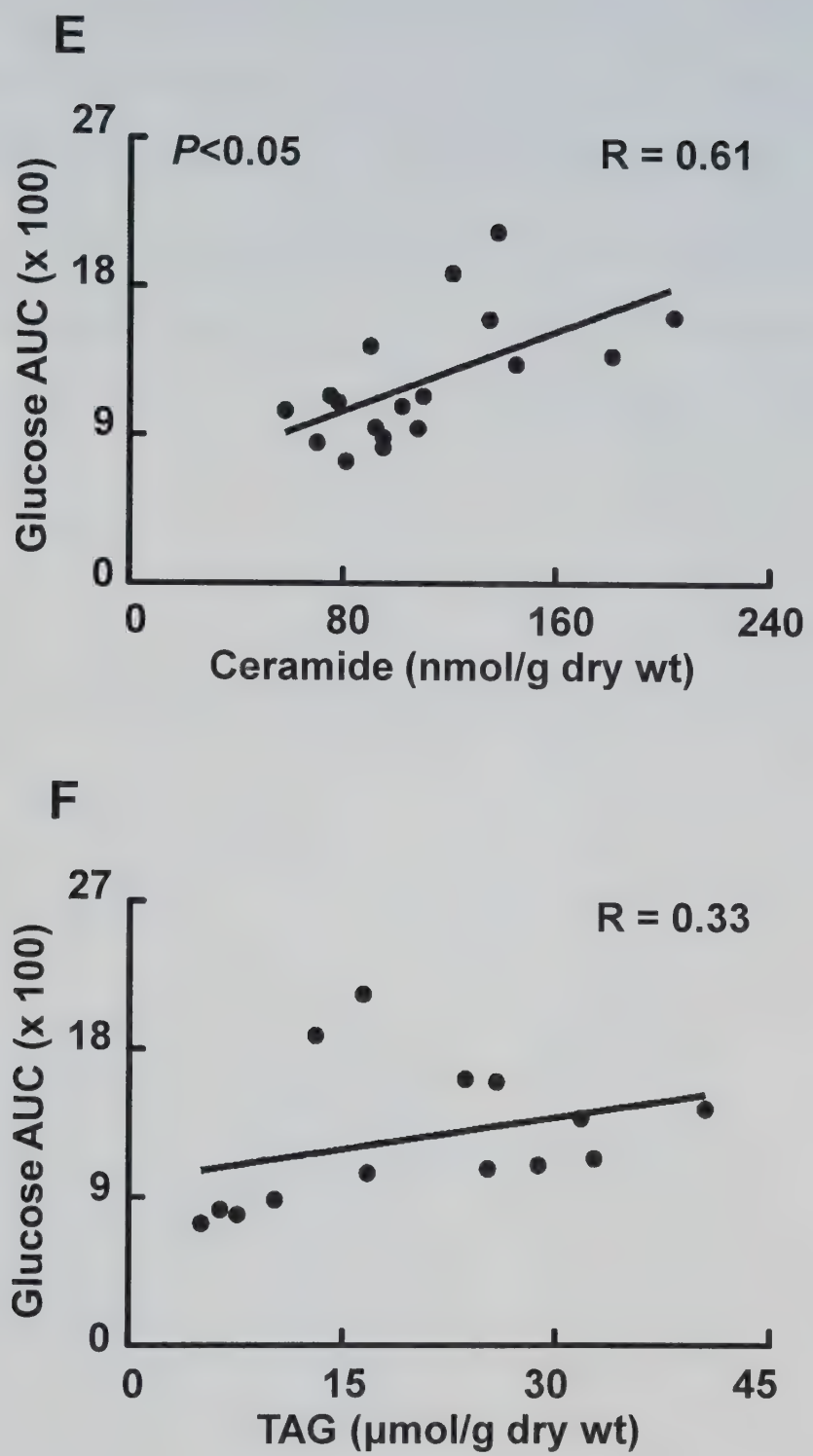
E
27
18
9
0
P<0.05
R = 0.61
Glucose AUC (x 100)
0
80
160
240
Ceramide (nmol/g dry wt)
F
27
18
9
0
R = 0.33
Glucose AUC (x 100)
0
15
30
45
TAG (µmol/g dry wt)

FIGURE 6-9

Figure 6-9: *Inhibition of SPT 1 reduces skeletal muscle ceramide levels without any effect on other lipid metabolites.*

A: Gastrocnemius triacylglycerol (TAG), B: long chain acyl CoA, C: ceramide, and D: diacylglycerol (DAG) levels in low fat fed and obese-insulin resistant mice treated with either vehicle control or myriocin. Values represent mean ± SE (n = 4-8). E: Correlation between the respective area under the curve (AUC) during the glucose tolerance test and Ceramide, F: TAG **G: long chain acyl CoA, and H: DAG, of (n = 14-18) samples.**

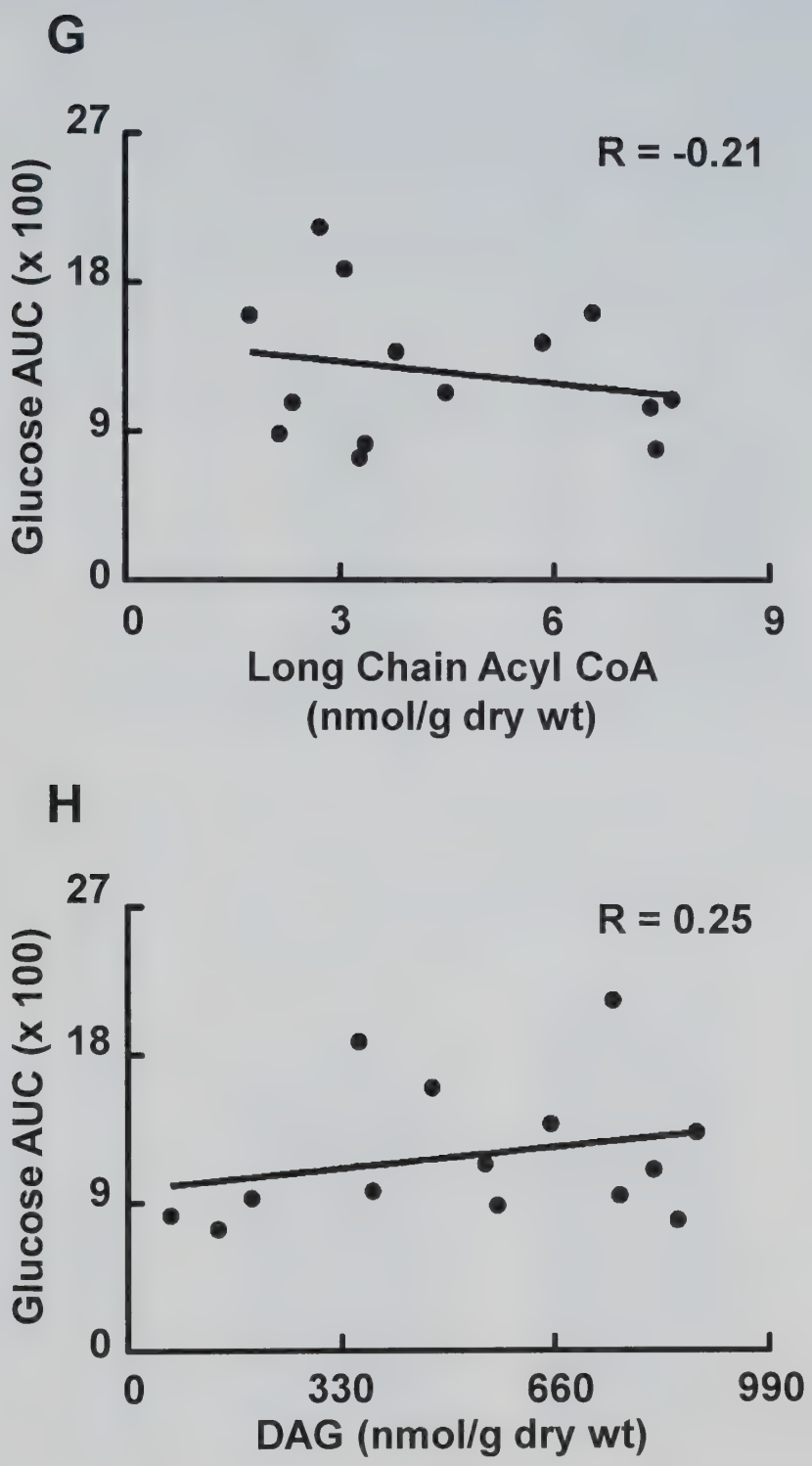
G
27
18
9
0
Glucose AUC (x 100)
R = -0.21
0
3
6
9
Long Chain Acyl CoA
(nmol/g dry wt)
H
27
18
9
0
Glucose AUC (x 100)
R = 0.25
0
330
660
990
DAG (nmol/g dry wt)

FIGURE 6-9

Figure 6-10: *MCD-/- mice do not accumulate ceramide in their skeletal muscle following 12 wks of high fat feeding.*

A: Area under the curve (AUC) during a glucose tolerance test following 12 wks of high fat feeding in WT and MCD-/- mice. B: Corresponding gastrocnemius ceramide levels in MCD-/- mice following 12 wks of high fat feeding. Values represent mean ± SE (n = 5-8). Differences were determined using a two-way ANOVA followed by a Bonferroni post-hoc analysis. $^{*}P<0.05$, significantly different from low fat diet counterpart. $^{\dagger}P<0.05$, significantly different from the high fat diet WT mice.

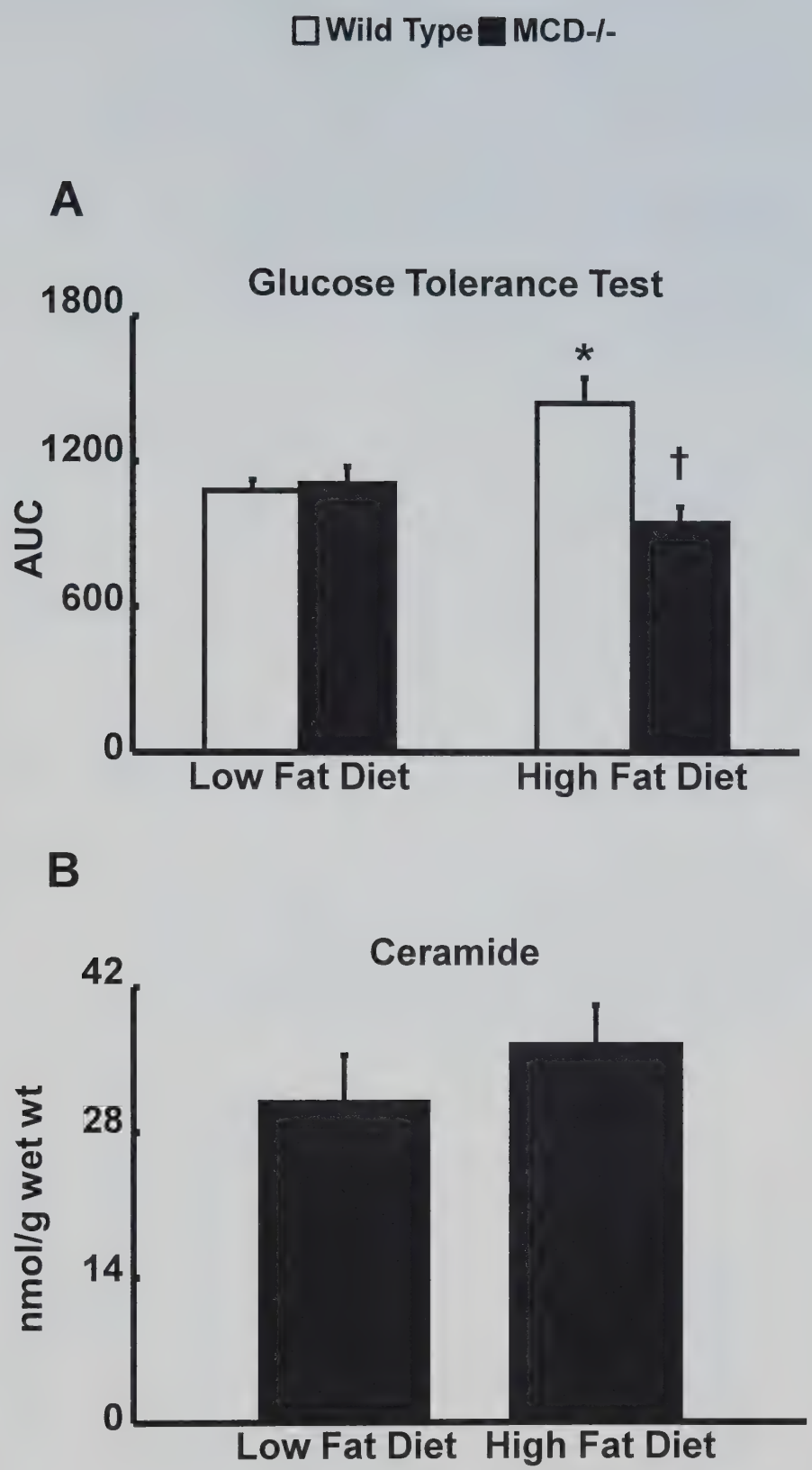
Wild Type
MCD-/-
A
Glucose Tolerance Test
1800
1200
600
0
AUC
*
†
Low Fat Diet
High Fat Diet
B
Ceramide
42
28
14
0
nmol/g wet wt
Low Fat Diet
High Fat Diet

FIGURE 6-10

Figure 6-11: *Expression and phosphorylation status of proteins involved in inflammation in skeletal muscle.*

A: Gastrocnemius JNK phosphorylation at threonine 183, B: p38 MAPK phosphorylation at threonine 180, and C: PGC1α expression in low fat diet and obese-insulin resistant mice treated with either vehicle control or myriocin. Values represent mean ± SE (n = 5-7).

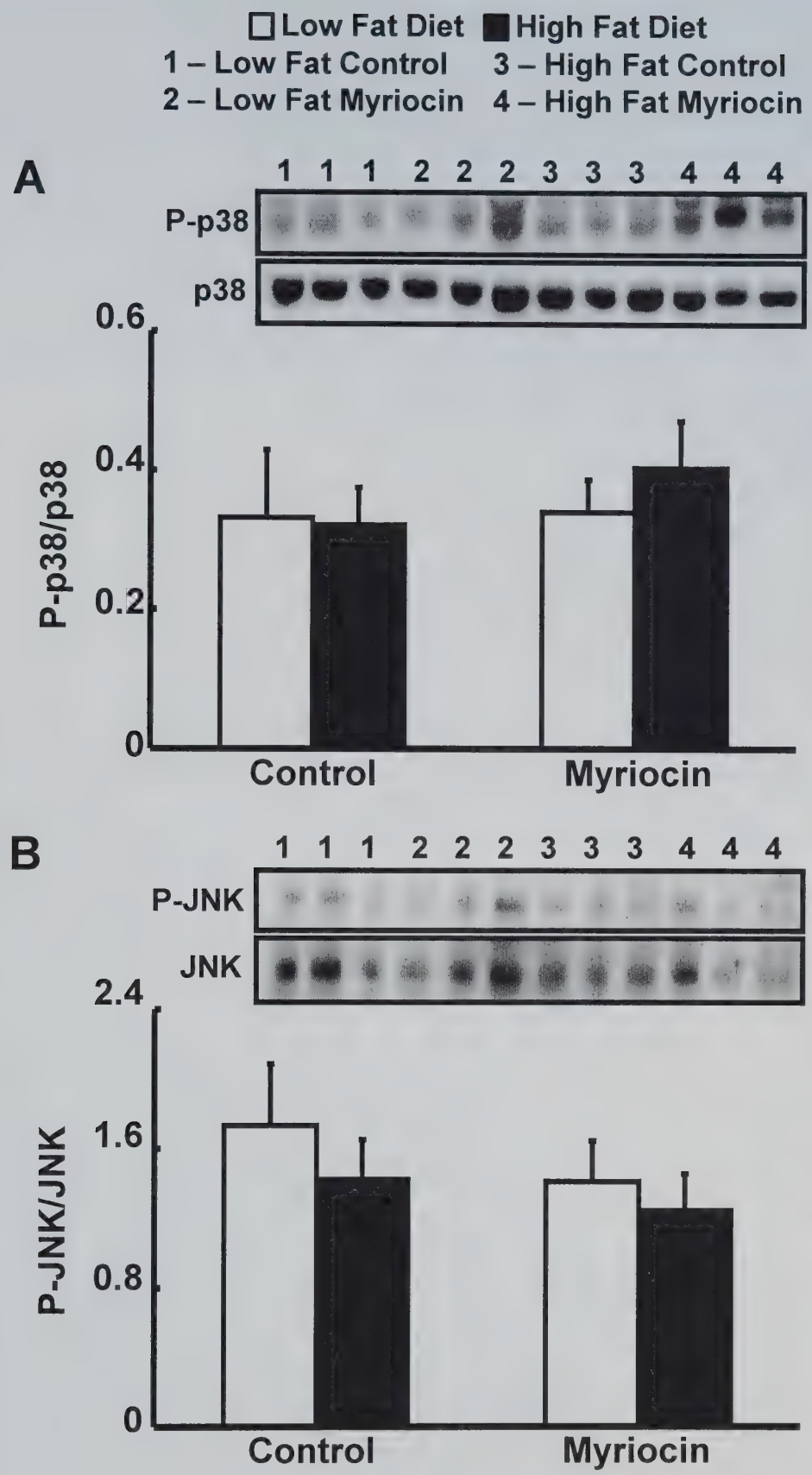
Low Fat Diet
High Fat Diet
1 – Low Fat Control
3 – High Fat Control
2 – Low Fat Myriocin
4 – High Fat Myriocin
A
1 1 1 2 2 2 3 3 3 4 4 4
P-p38
p38
0.6
0.4
0.2
0
P-p38/p38
Control
Myriocin
B
1 1 1 2 2 2 3 3 3 4 4 4
P-JNK
JNK
2.4
1.6
0.8
0
P-JNK/JNK
Control
Myriocin

FIGURE 6-11

Figure 6-11: *Expression and phosphorylation status of proteins involved in inflammation in skeletal muscle.*

A: Gastrocnemius JNK phosphorylation at threonine 183, B: p38 MAPK phosphorylation at threonine 180, and **C: PGC1α expression in low fat diet and obese-insulin resistant mice treated with either vehicle control or myriocin.** Values represent mean ± SE (n = 5-7). *P = 0.077, versus the low fat diet counterpart.

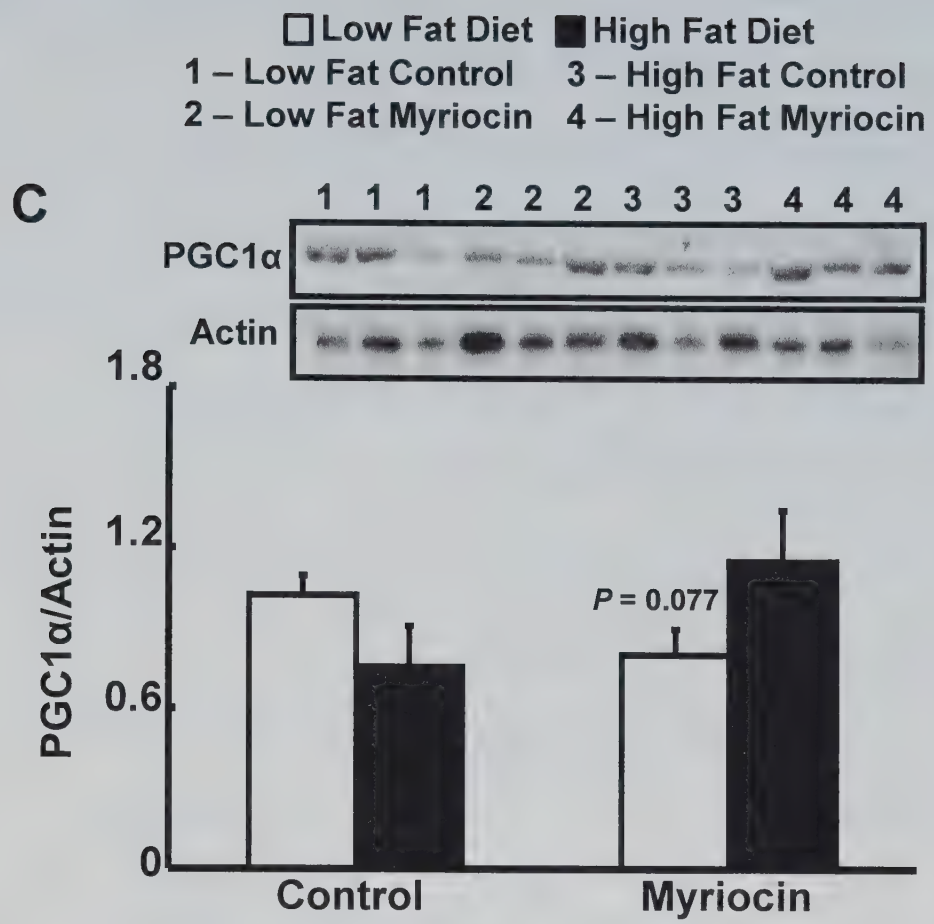
Low Fat Diet
High Fat Diet
1 – Low Fat Control
3 – High Fat Control
2 – Low Fat Myriocin
4 – High Fat Myriocin
C
1 1 1 2 2 2 3 3 3 4 4 4
PGC1α
Actin
1.8
1.2
0.6
0
PGC1α/Actin
P = 0.077
Control
Myriocin

FIGURE 6-11

Figure 6-12: *Prevention of insulin resistance in db/db mice via myriocin treatment.*

A: Pre-treatment glucose tolerance test (GTT) in *db/db* mice at 6 wks of age. B: GTT in *db/db* mice treated with vehicle control or myriocin. C: Respective area under the curve (AUC) for the post-treatment GTT in *db/db* mice. D: Insulin tolerance test in *db/db* mice treated with vehicle control or myriocin. E: Fed and fasted plasma glucose levels in *db/db* mice treated with vehicle control or myriocin. Values represent mean ± SE (n = 5-6). Differences were determined using either a two-tailed Student's *t*-test, or a two-way ANOVA followed by a Bonferroni post-hoc analysis. $*P<0.05$, significantly different from the *db/db* control mice.

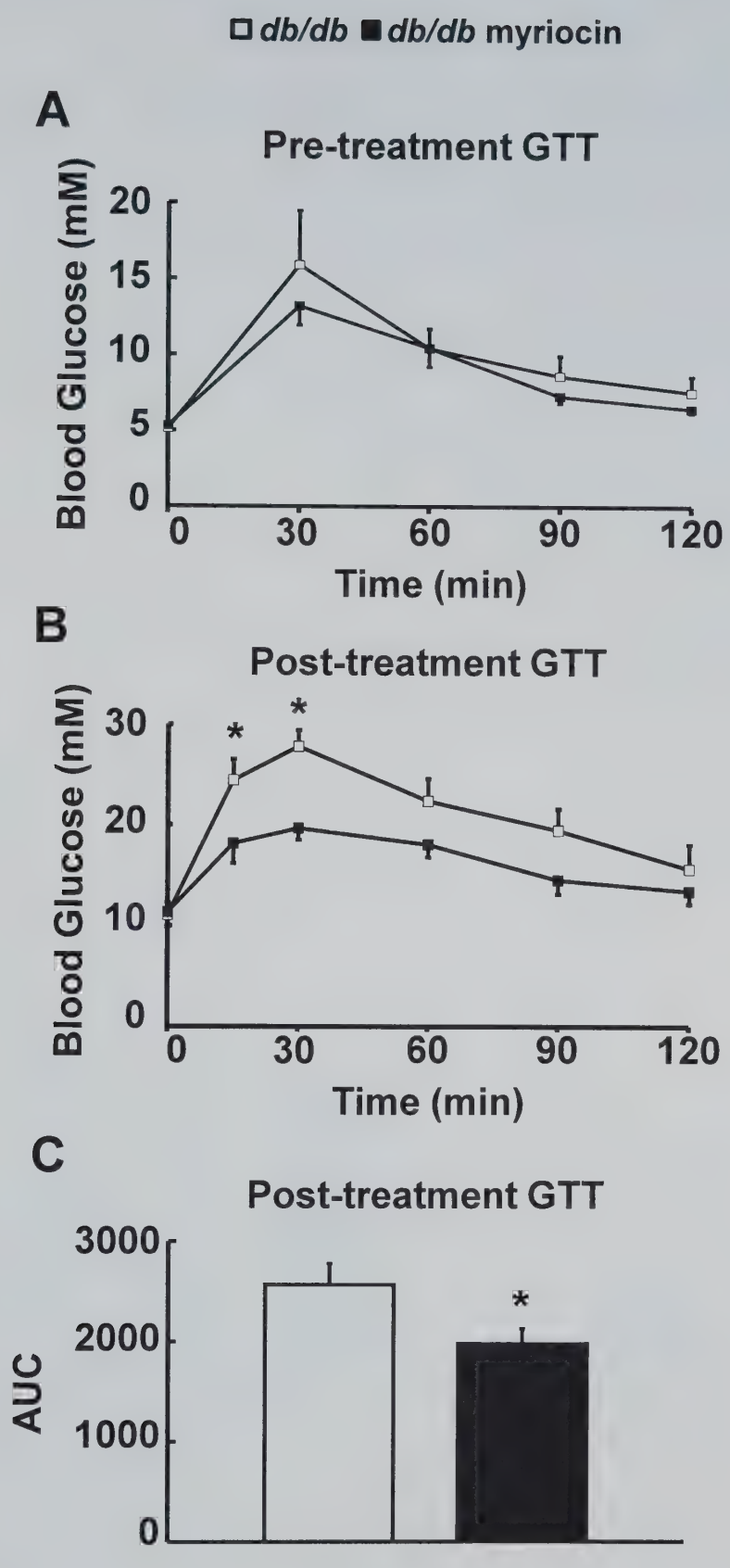
□ db/db ■ db/db myriocin
A
Pre-treatment GTT
Blood Glucose (mM)
20
15
10
5
0
0
30
60
90
120
Time (min)
B
Post-treatment GTT
Blood Glucose (mM)
30
20
10
0
*
*
0
30
60
90
120
Time (min)
C
Post-treatment GTT
AUC
3000
2000
1000
0
*

FIGURE 6-12

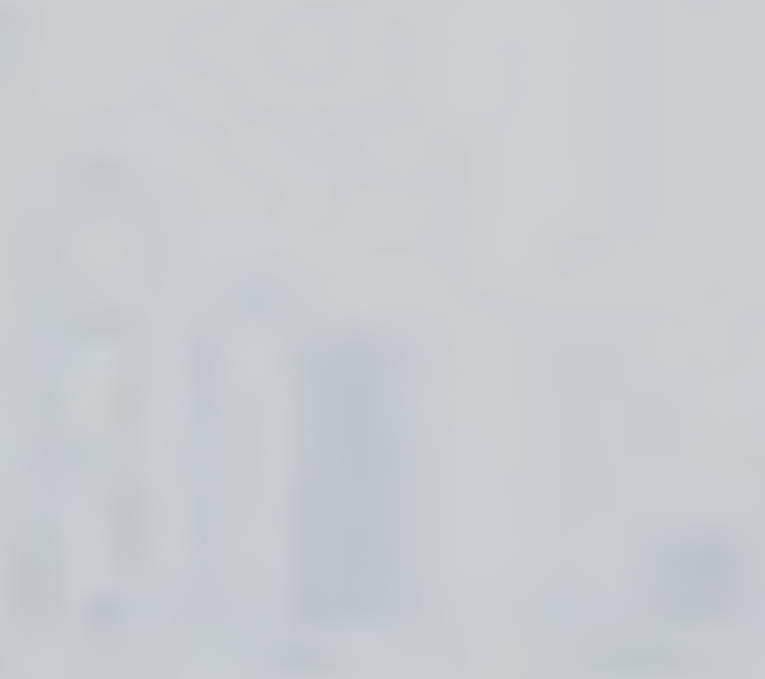

Figure 6-12: *Prevention of insulin resistance in db/db mice via myriocin treatment.*

A: Pre-treatment glucose tolerance test (GTT) in *db/db* mice at 6 wks of age. B: GTT in *db/db* mice treated with vehicle control or myriocin. C: Respective area under the curve for the post-treatment GTT in *db/db* mice. **D: ITT in *db/db* mice treated with vehicle control or myriocin. E: Fed and fasted plasma glucose levels in *db/db* mice treated with vehicle control or myriocin.** Values represent mean ± SE (n = 5-6). Differences were determined using a two-way ANOVA followed by a Bonferroni post-hoc analysis. $*P<0.05$, significantly different from the *db/db* control mice.

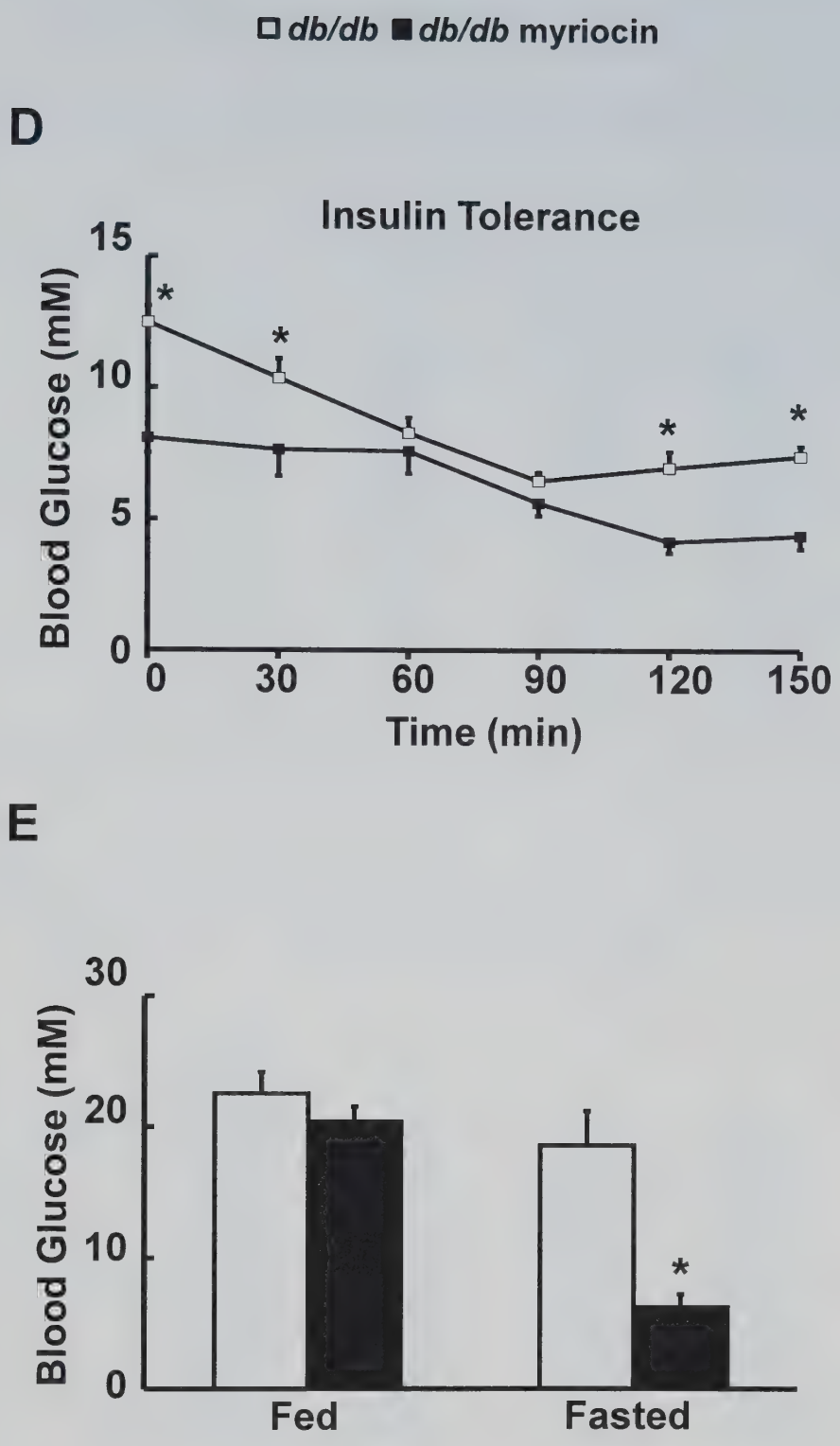
□ db/db ■ db/db myriocin
D
Insulin Tolerance
Blood Glucose (mM)
15
10
5
0
0
30
60
90
120
150
Time (min)
*
*
*
*
E
Blood Glucose (mM)
30
20
10
0
Fed
Fasted
*

FIGURE 6-12

Figure 6-13: *In vivo metabolic parameters, intramyocellular lipid metabolite profile, and insulin signaling in db/db mice treated with myriocin.*

A: Respiratory exchange ratio (RER), B: whole body oxygen consumption, C: heat production, and D: ambulatory activity in *db/+* heterozygous mice, and *db/db* mice treated with vehicle control or myriocin. E: Gastrocnemius triacylglycerol, F: long chain acyl CoA, G: diacylglycerol, and H: ceramide levels in *db/+* heterozygous mice, and *db/db* mice treated with vehicle control or myriocin. I: Insulin stimulated Akt phosphorylation at serine 473, and J: GSK3β phosphorylation at serine 9 in gastrocnemius muscle of *db/+* heterozygous mice, and *db/db* mice treated with vehicle control or myriocin. Values represent mean ± SE (n = 3-5). Differences were determined using a two-way ANOVA followed by a Bonferroni post-hoc analysis. $^{*}P<0.05$, significantly different from the *db/db* control mice. $^{\dagger}P<0.05$, significantly different from the *db/+* heterozygous mice.

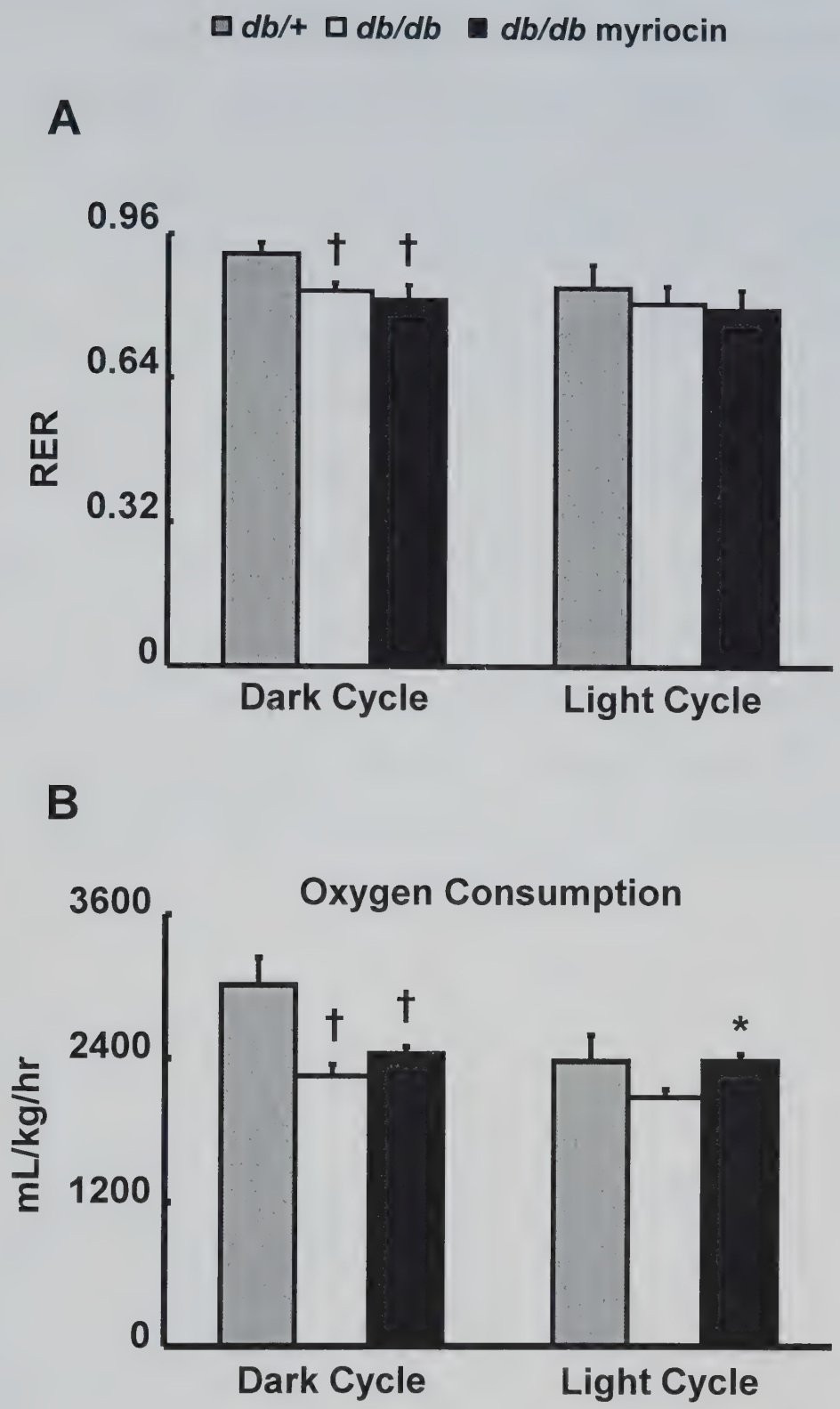
db/+ db/db db/db myriocin
A
0.96
0.64
0.32
0
RER
†
†
Dark Cycle
Light Cycle
B
Oxygen Consumption
3600
2400
1200
0
mL/kg/hr
†
†
*
Dark Cycle
Light Cycle

FIGURE 6-13

Figure 6-13: *In vivo metabolic parameters, intramyocellular lipid metabolite profile, and insulin signaling in db/db mice treated with myriocin.*

A: Respiratory exchange ratio, B: whole body oxygen consumption, **C: heat production, and D: ambulatory activity in *db/+* heterozygous mice, and *db/db* mice treated with vehicle control or myriocin.** E: Gastrocnemius triacylglycerol, F: long chain acyl CoA, G: diacylglycerol, and H: ceramide levels in *db/+* heterozygous mice, and *db/db* mice treated with vehicle control or myriocin. I: Insulin stimulated Akt phosphorylation at serine 473, and J: GSK3β phosphorylation at serine 9 in gastrocnemius muscle of *db/+* heterozygous mice, and *db/db* mice treated with vehicle control or myriocin. Values represent mean ± SE (n = 3-5). Differences were determined using a two-way ANOVA followed by a Bonferroni post-hoc analysis. $^{*}P<0.05$, significantly different from the *db/db* control mice. $^{\dagger}P<0.05$, significantly different from the *db/+* heterozygous mice.

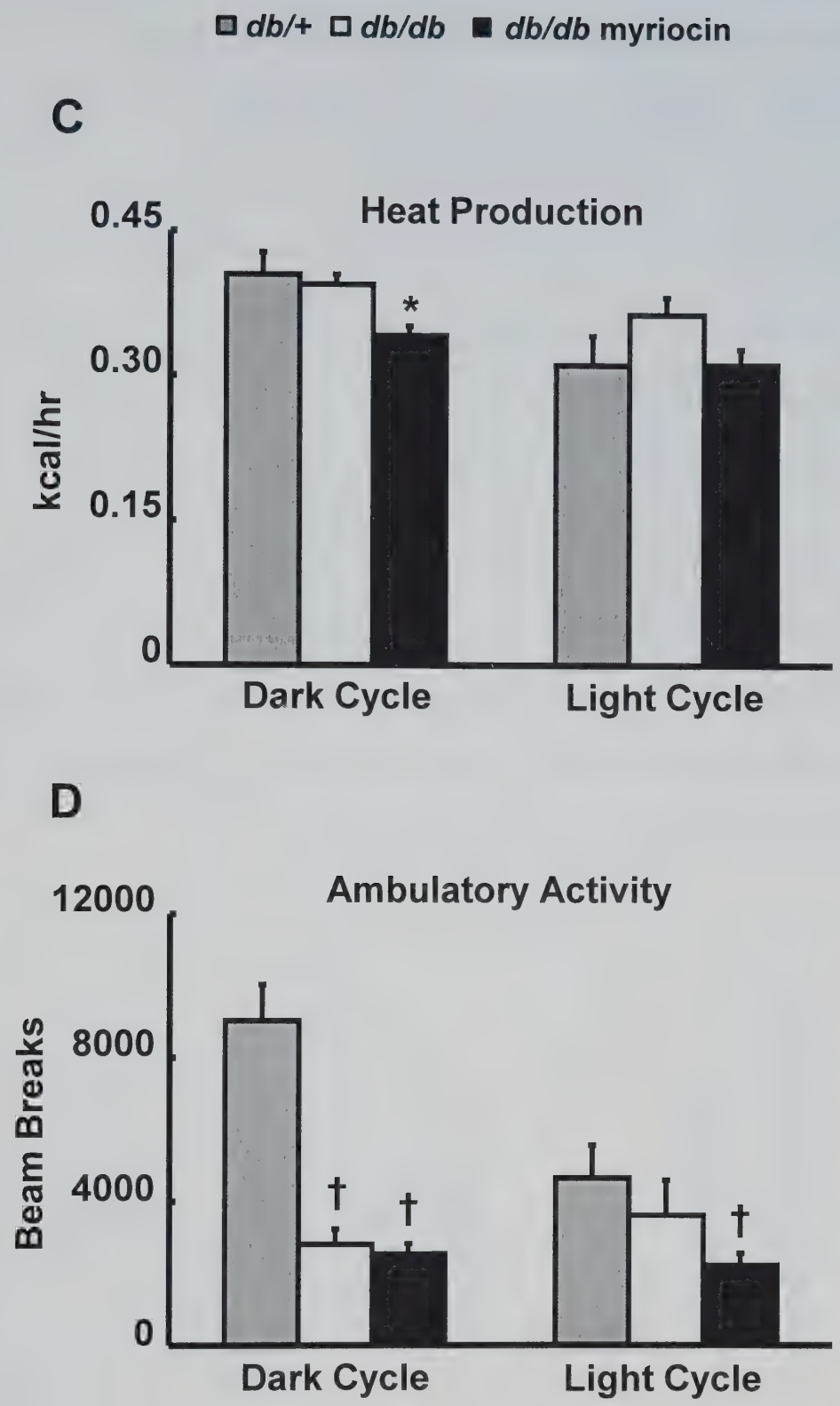
db/+ db/db db/db myriocin
C
Heat Production
0.45
0.30
0.15
0
kcal/hr
*
Dark Cycle
Light Cycle
D
Ambulatory Activity
12000
8000
4000
0
Beam Breaks
†
†
†
Dark Cycle
Light Cycle

FIGURE 6-13

Figure 6-13: *In vivo metabolic parameters, intramyocellular lipid metabolite profile, and insulin signaling in db/db mice treated with myriocin.*

A: Respiratory exchange ratio, B: whole body oxygen consumption, C: heat production, and D: ambulatory activity in *db/+* heterozygous mice, and *db/db* mice treated with vehicle control or myriocin. **E: Gastrocnemius triacylglycerol, F: long chain acyl CoA,** G: diacylglycerol, and H: ceramide levels in *db/+* heterozygous mice, and *db/db* mice treated with vehicle control or myriocin. I: Insulin stimulated Akt phosphorylation at serine 473, and J: GSK3β phosphorylation at serine 9 in gastrocnemius muscle of *db/+* heterozygous mice, and *db/db* mice treated with vehicle control or myriocin. Values represent mean ± SE (n = 3-5). Differences were determined using a one-way ANOVA followed by a Bonferroni post-hoc analysis. $^{\dagger}P<0.05$, significantly different from the *db/+* heterozygous mice.

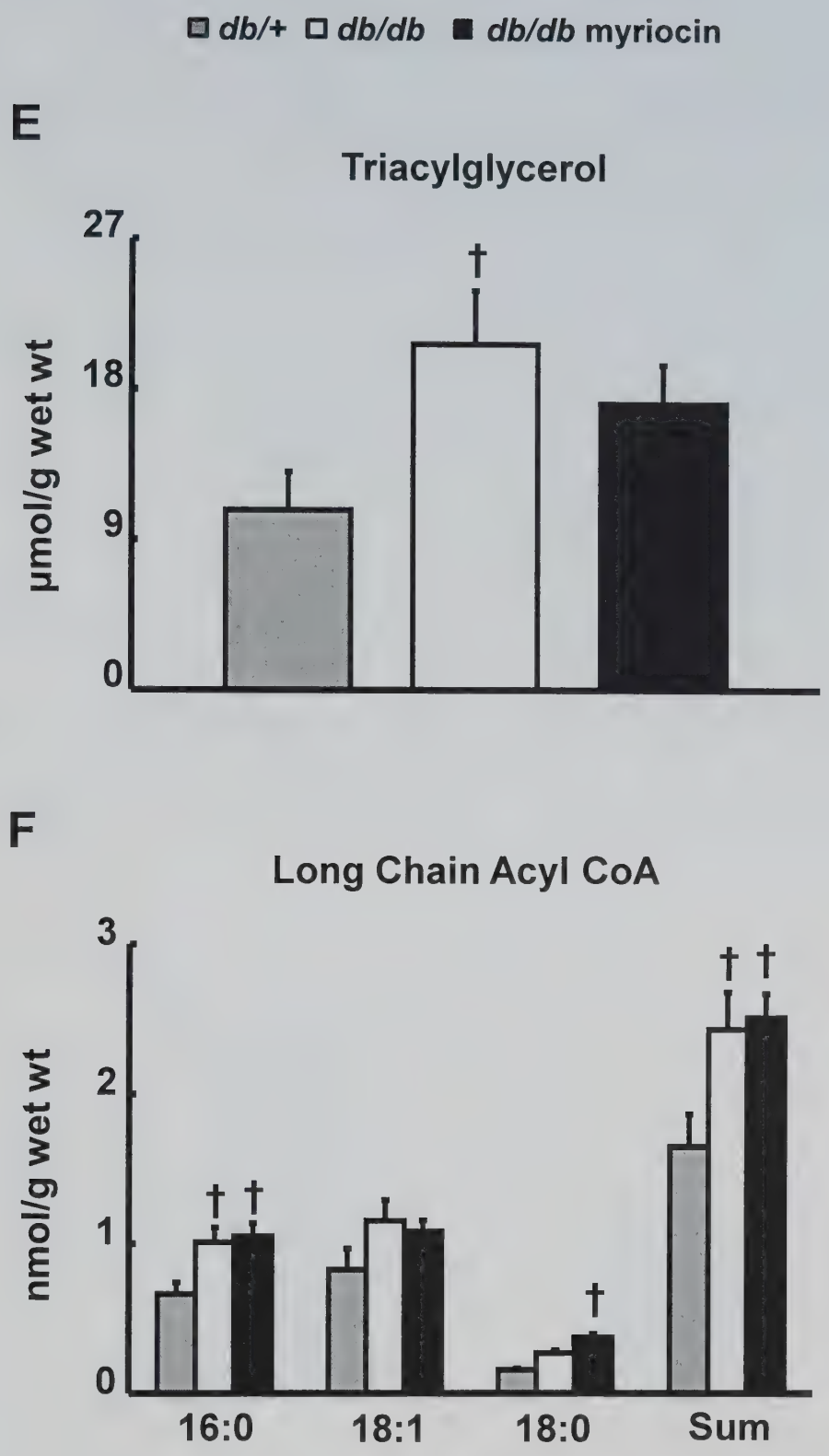
db/+ db/db db/db myriocin
E
Triacylglycerol
µmol/g wet wt
27
18
9
0
†
F
Long Chain Acyl CoA
nmol/g wet wt
3
2
1
0
† †
†
† †
16:0
18:1
18:0
Sum

FIGURE 6-13

Figure 6-13: *In vivo metabolic parameters, intramyocellular lipid metabolite profile, and insulin signaling in db/db mice treated with myriocin.*

A: Respiratory exchange ratio, B: whole body oxygen consumption, C: heat production, and D: ambulatory activity in *db/+* heterozygous mice, and *db/db* mice treated with vehicle control or myriocin. E: Gastrocnemius triacylglycerol, F: long chain acyl CoA, **G: diacylglycerol, and H: ceramide levels in *db/+* heterozygous mice, and *db/db* mice treated with vehicle control or myriocin.** I: Insulin stimulated Akt phosphorylation at serine 473, and J: GSK3β phosphorylation at serine 9 in gastrocnemius muscle of *db/+* heterozygous mice, and *db/db* mice treated with vehicle control or myriocin. Values represent mean ± SE (n = 3-5). Differences were determined using a one-way ANOVA followed by a Bonferroni post-hoc analysis. $*P<0.05$, significantly different from the *db/db* control mice.

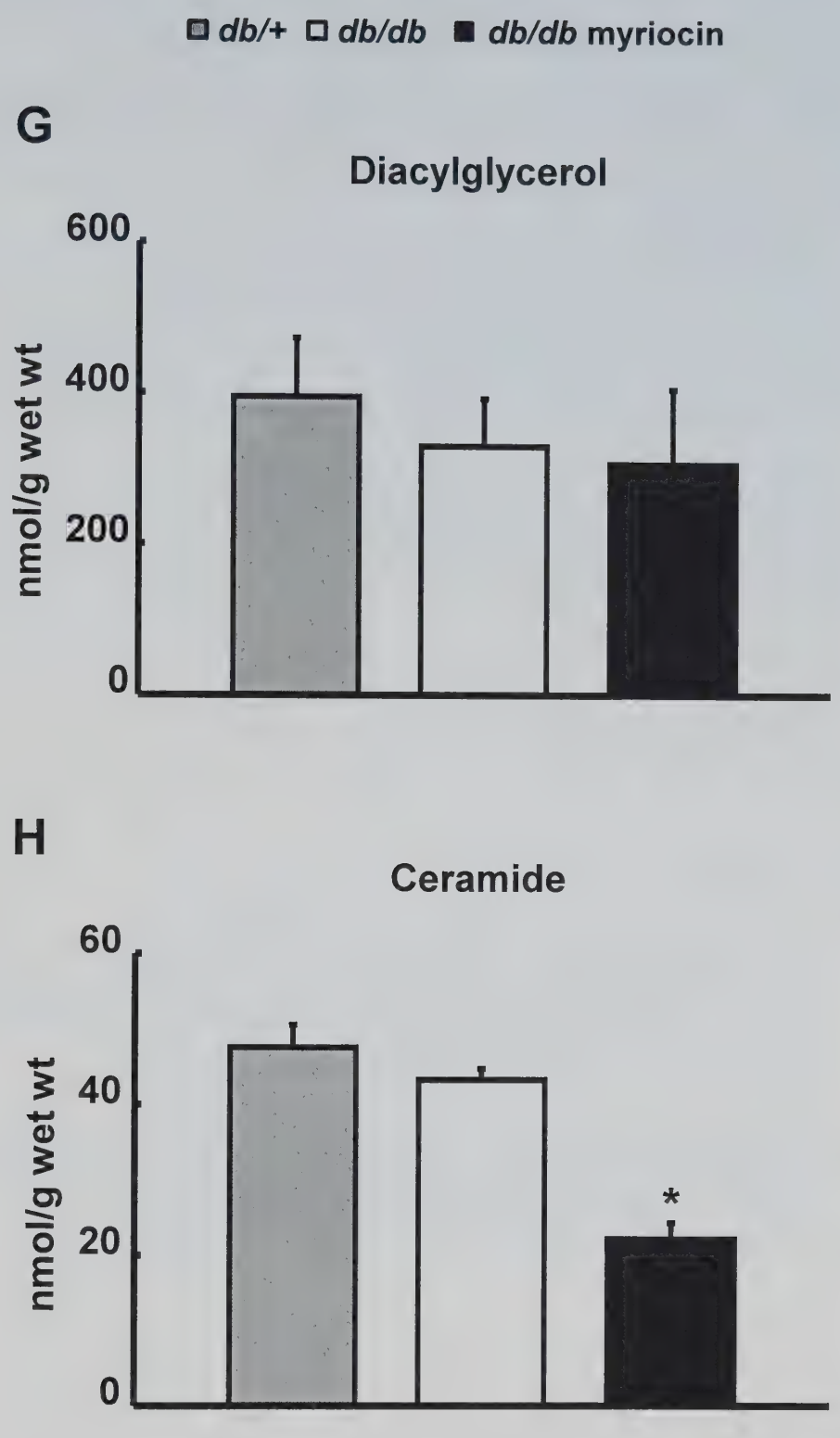
db/+ db/db db/db myriocin
G
Diacylglycerol
600
400
200
0
nmol/g wet wt
H
Ceramide
60
40
20
0
nmol/g wet wt
*

FIGURE 6-13

Figure 6-13: *In vivo metabolic parameters, intramyocellular lipid metabolite profile, and insulin signaling in db/db mice treated with myriocin.*

A: Respiratory exchange ratio, B: whole body oxygen consumption, C: heat production, and D: ambulatory activity in *db/+* heterozygous mice, and *db/db* mice treated with vehicle control or myriocin. E: Gastrocnemius triacylglycerol, F: long chain acyl CoA, G: diacylglycerol, and H: ceramide levels in *db/+* heterozygous mice, and *db/db* mice treated with vehicle control or myriocin. **I: Insulin stimulated Akt phosphorylation at serine 473, and J: GSK3β phosphorylation at serine 9 in gastrocnemius muscle of *db/+* heterozygous mice, and *db/db* mice treated with vehicle control or myriocin.** Values represent mean ± SE (n = 3-5).

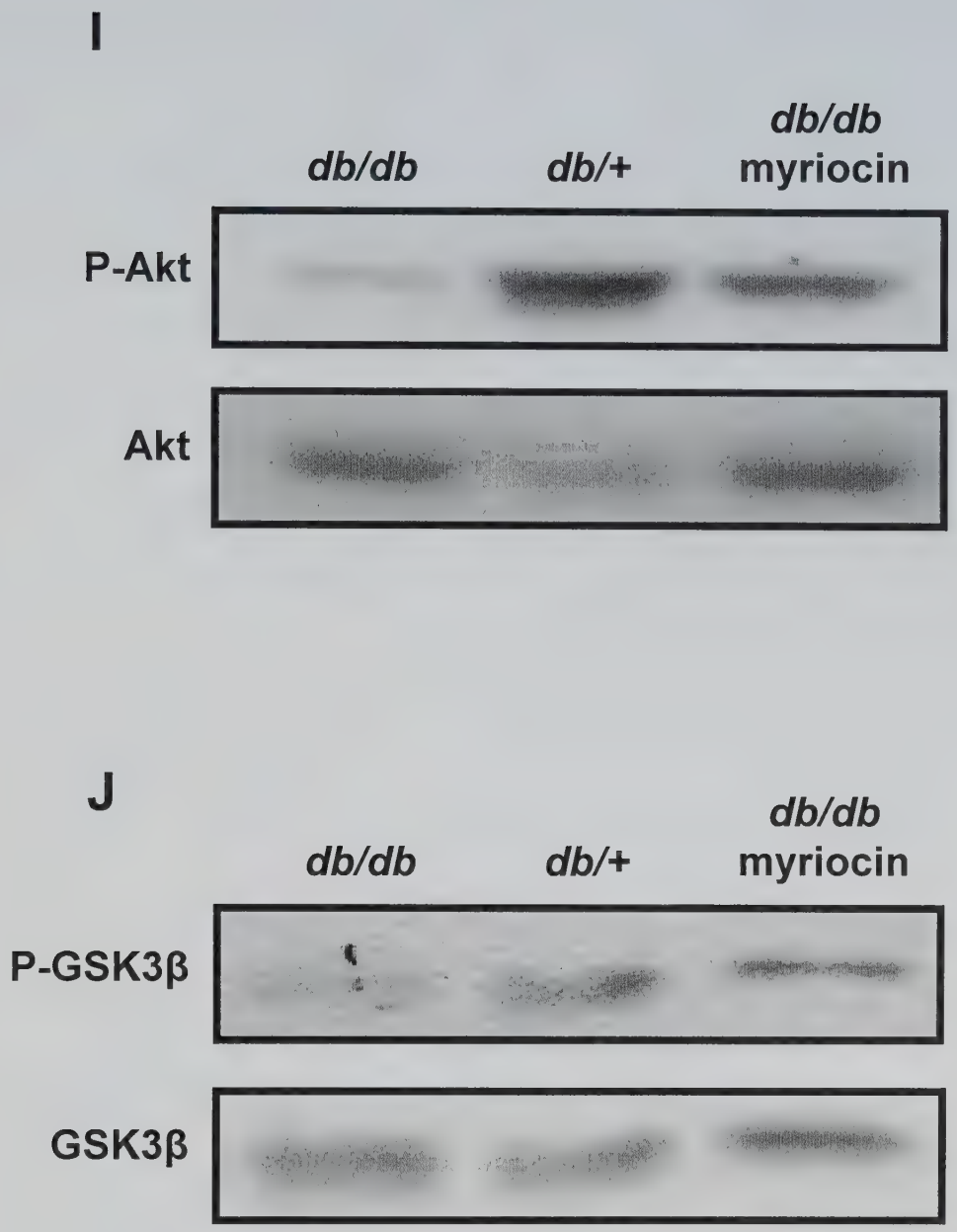
I
db/db
db/+
db/db
myriocin
P-Akt
Akt
J
db/db
db/+
db/db
myriocin
P-GSK3β
GSK3β

FIGURE 6-13

Figure 6-14: *Gluconeogenic capacity in obese-insulin resistant mice is not altered via myriocin treatment.*

A: Blood glucose levels during a pyruvate challenge in fasted, obese-insulin resistant mice treated with either vehicle control or myriocin. B: % change in blood glucose during the pyruvate challenge. Values represent mean ± SE (n = 4).

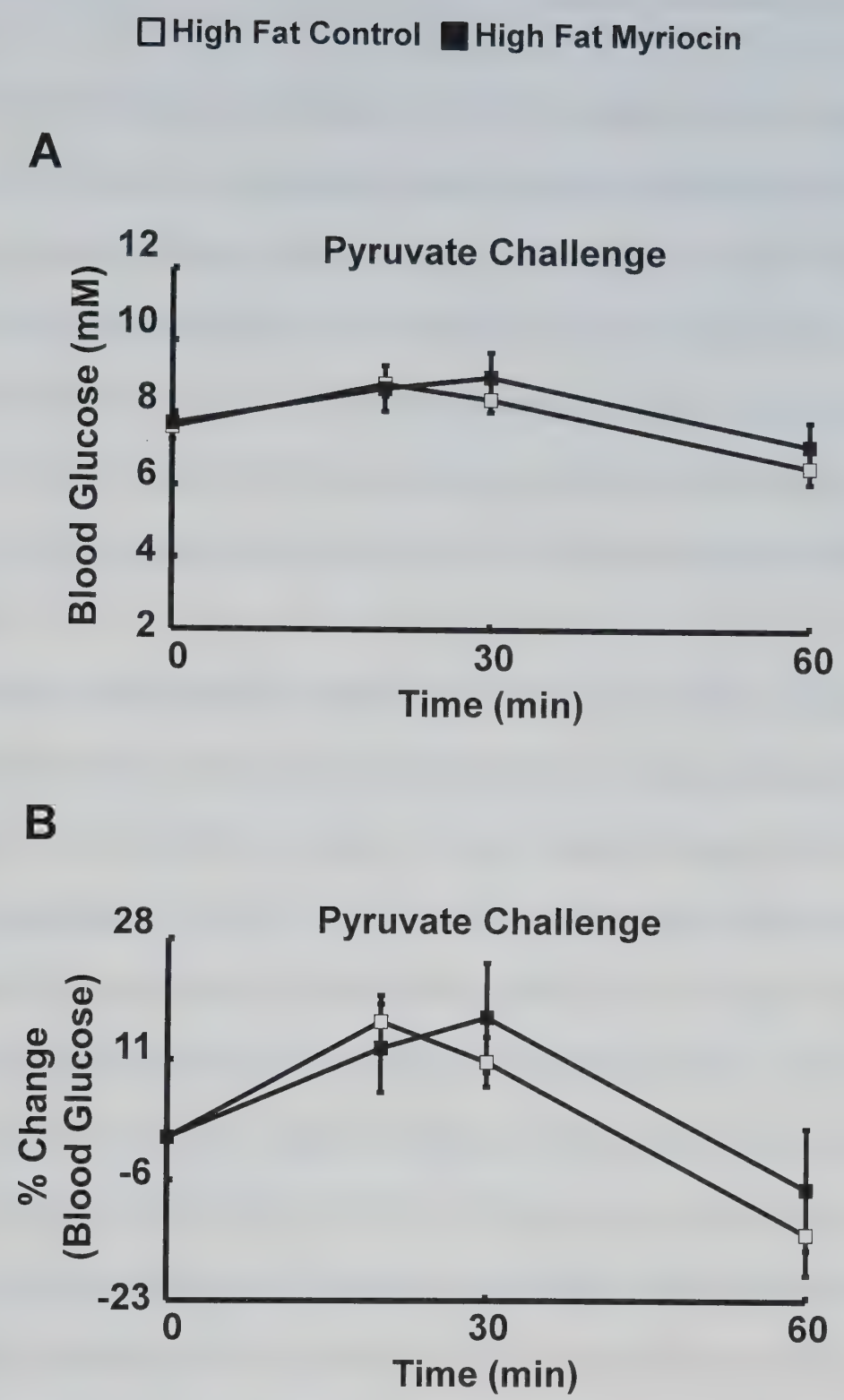
High Fat Control
High Fat Myriocin
A
Pyruvate Challenge
Blood Glucose (mM)
12
10
8
6
4
2
0
30
60
Time (min)
B
Pyruvate Challenge
% Change (Blood Glucose)
28
11
-6
-23
0
30
60
Time (min)

FIGURE 6-14

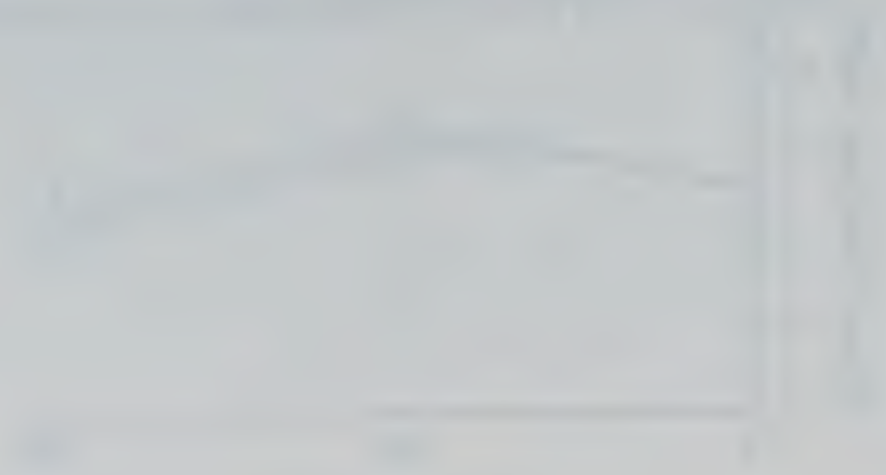

Our results show that inhibition of SPT 1 reduces *de novo* ceramide synthesis, which leads to a profound reversal of glucose intolerance and insulin resistance induced by chronic high fat feeding. Furthermore, we show that these improvements are dissociated from the other lipid metabolites believed to play a role in the insulin resistance process. Interestingly, obesity-induced insulin resistance in mice is associated with a detriment in aerobic exercise capacity and whole body oxygen consumption rates, both of which are reversed via SPT 1 inhibition.

Previous studies have postulated that skeletal muscle insulin resistance is caused by the intramyocellular cytosolic accumulation of lipid metabolites (TAG, long chain acyl CoA, DAG, ceramide, etc.) that negatively impact the insulin signaling cascade (64, 154, 281, 353, 367, 447). In particular, long chain acyl CoA and DAG have received considerable attention, due to their ability to activate the classical/novel protein kinase C signaling cascade, which can phosphorylate IRS proteins on serine residues, preventing their activation via the insulin receptor (64, 69, 188, 274, 367, 447). It is important to note however, that the vast majority (~95%) of acyl CoA esters are located inside the mitochondria (163, 325), suggesting that if long chain acyl CoA accumulation does play a role towards insulin resistance development, it is possible that mitochondrial, as opposed to cytosolic long chain acyl CoA, is the primary contributor. Although TAG has been shown in numerous studies to be elevated in muscle in association

with the development of insulin resistance, recent studies have shown that TAG may actually serve as a buffer, protecting the muscle against the accumulation of the more reactive lipid metabolite species (231, 310).

In regards to ceramide, data are mixed with its role in insulin resistance development, due to the fact that in some studies ceramide accumulation is not evident in muscle (69, 372), and in other studies where accumulation does occur, the relative increase in the ceramide pool is not that large (153, 395). However, a recent study by Holland *et al.* (153) has shed some light on this issue, as they demonstrated that ceramide accumulation in muscle is dependent on the type of diet fed to the animals. In particular, saturated fatty acids drive *de novo* ceramide synthesis in muscle via SPT 1, whereas unsaturated fatty acids cause insulin resistance via other mechanisms (153). Such findings may potentially explain why ceramide accumulation is not observed in studies of insulin resistance where the model employed is a lipid infusion, which consists primarily of unsaturated fatty acids (188). Furthermore, Holland *et al.* showed in their study that preventing *de novo* synthesis of ceramide via SPT 1 inhibition with myriocin prevented the development of glucose intolerance in obese Zucker rats, and prevented the palmitate-induced inhibition of insulin-stimulated 2-deoxyglucose uptake in isolated soleus muscle.

Interestingly, reductions in skeletal muscle ceramide accumulation may represent a potential explanation for the "exercise paradox" observed in man. Dube *et al.* (90) have shown that obese, insulin resistant men placed on an aerobic exercise training regime results in elevations of intramyocellular lipid and TAG

stores. However, marked reductions in muscle ceramide levels are observed, which may explain the enhanced insulin sensitivity of these men. Moreover, Bruce *et al.* (48) have also shown that the improved insulin sensitivity observed with exercise training in man is associated with a drop in muscle ceramide levels, and in particular, the saturated species. Animal studies of exercise have also yielded similar findings, as Dobrzyn *et al.* (88) have shown that exercise training of rats leads to a dramatic drop in the saturated species of ceramide in muscle, which is associated with an enhanced 2-deoxyglucose uptake. In addition, mice overexpressing DGAT1 in muscle are protected from high fat diet-induced insulin resistance and palmitate inhibition of 2-deoxyglucose uptake in isolated muscle, both of which are associated with an elevation of muscle TAG and drop in ceramide levels (231). Our results support these studies, as we show that obese, insulin resistant mice treated with myriocin had significant increases in intramyocellular TAG, long chain acyl CoA, and DAG, but a dramatic drop in ceramide content. Moreover, we observed a positive correlation with ceramide content and glucose intolerance, but not with any of the other lipid metabolites. We believe with this finding, in the setting of obesity, that ceramide may be more vital to the development of skeletal muscle insulin resistance than the other lipid metabolites. Support for this statement is also evident in culture models of ceramide accumulation, whereby inhibition of SPT 1 is able to prevent palmitate-induced insulin resistance in both human and rat L6 myotubes, despite elevated TAG and DAG levels (310, 312).

One of the most surprising findings of this study is that chronic high fat feeding results in a dramatic decline in whole body oxygen consumption rates. The vast majority of studies that have examined the effect of high fat feeding on whole body oxygen consumption via use of the CLAMS apparatus have reported elevations in oxygen consumption rates (226, 363). While the differences between their study and ours could be due to the duration or composition of the diet, we feel there are two possible explanations for this novel observation of ours. First, it has been reported that obesity-induced insulin resistance causes mitochondrial dysfunction that results from an impairment of fatty acid oxidative capacity (69, 383, 413, 447). Although it may be possible that our model of insulin resistance is inducing mitochondrial dysfunction, it is highly unlikely due to impairments in muscle fatty acid oxidative capacity, as the RER values in obese mice reported in this study are very close to 0.7, indicating that these animals have no trouble utilizing fat as an energy source. Nonetheless, other factors, such as mitochondrial content, protein expression of ETC complexes, or activity of these complexes, may account for potential mitochondrial dysfunction and the subsequent impairment of oxygen consumption rates observed in obese mice (37, 375). However, we did not observe differences in protein expression of cytochrome C of the ETC in any group (*data not shown*). Second, and potentially more relevant to the findings of this study, is that obesity-induced insulin resistance has been associated with elevated rates of incomplete fatty acid oxidation, which can arise when rates of fatty acid oxidation are disconnected from TCA cycle activity (200, 202, 280). This disconnect arises due to the

sedentary nature of obese individuals/animals, thus there is no demand for the TCA cycle to upregulate its activity to deal with the increased fatty acid supply that is being utilized as an energy source (200, 202, 280). If the TCA cycle is unable to accommodate the increasing acetyl CoA coming from fatty acid oxidation, reducing equivalents such as NADH and $FADH_2$ would not donate their electrons to the complexes of the ETC, accounting for the reduction in oxygen consumption rates.

Therefore, we feel that our observation of decreased whole body oxygen consumption rates in obese, insulin resistant mice, is consistent with elevated rates of incomplete fatty acid oxidation in muscle. Furthermore, we show that although CS activity is greater in muscle of DIO mice treated with myriocin, βHAD activity is similar between the two DIO groups, suggesting a disconnect between skeletal muscle fatty acid oxidation rates and TCA cycle activity in control treated DIO mice, again consistent with the incomplete oxidation of fatty acids (202, 280, 393). Higher muscle CS activity in myriocin treated DIO mice would ensure an increased delivery of reducing equivalents to the ETC, accounting for improvements in mitochondrial function and oxygen consumption, despite a lack of change in cytochrome C expression. Obesity-induced decrements in PGC1α protein expression might also explain impairments in mitochondrial function and oxygen consumption (200, 278, 376), and although not significant, we observed a trend towards a reduction in gastrocnemius PGC1α protein expression in control treated DIO mice ($P = 0.077$) that is not evident in myriocin treated DIO mice. Last, we have previously shown that MCD-/- mice

are protected from obesity-induced insulin resistance, which is associated with a reduction of incomplete fatty acid oxidation rates. Interestingly, we show here in this study that these exact same animals do not accumulate ceramide in their muscle following 12 wks of high fat feeding, leading to the very intriguing possibility that intramyocellular ceramide accumulation is linked to mitochondrial dysfunction and the incomplete oxidation of fatty acids observed with skeletal muscle insulin resistance.

Obesity-induced insulin resistance has been shown in a number of studies to impair insulin's actions on Akt, a key signaling molecule linking insulin to its effects on glucose homeostasis (12, 105, 312, 385). Here we show that insulin stimulated phosphorylation of Akt on serine residue 473 (indicative of Akt activity) is greater in myriocin treated obese, insulin resistant mice versus their control treated counterparts. Furthermore, insulin stimulated phosphorylation of the Akt downstream target, GSK3β, on serine residue 9, is also greater in obese mice treated with myriocin. These results are consistent with improved insulin signaling and sensitivity via myriocin treatment in obese mice.

It is important to note that the beneficial effects mediated by inhibition of SPT 1 and prevention of *de novo* ceramide synthesis could be mediated by liver effects in our animals. However, the vast majority of ceramides in the liver are unsaturated (339), as opposed to saturated. Thus, the inhibition of SPT 1 in the liver, which prevents *de novo* synthesis of ceramide from saturated fatty acids such as palmitoyl CoA, should not have as dramatic an effect in this tissue. As such, recent studies have shown that high fat feeding does not increase ceramide

levels in the liver (251). Moreover, we reported no difference during a pyruvate challenge of fasted, obese control or myriocin treated mice (Figure 6-14), suggesting that gluconeogenic capacity was not different between the 2 groups, and that the liver likely does not play a key role with the improved insulin sensitivity observed in myriocin treated mice. Regardless, we cannot rule out the possibility that the liver plays no role whatsoever with the benefit observed during myriocin treatment.

Finally, chronic low-grade inflammation has been shown in a number of studies to play a role in causing obesity-induced insulin resistance (157, 362, 416). Inflammatory and stress kinases, such as p38 MAPK and JNK have been proposed to be downstream mediators of this inflammatory effect, as inhibitors of both kinases are able to prevent high fat diet-induced insulin resistance (81, 151, 290, 385). Unexpectedly, the phosphorylation status of both p38 MAPK and JNK is not altered by DIO, nor is it altered by myriocin treatment, suggesting that inflammation may not be playing a role in our model of insulin resistance. It may also be possible that inflammation in our model is mediated by some other kinase, such as IKKβ (23, 149).

With regards to the findings in *db/db* mice, we report very similar findings to what we observed in the obesity-induced insulin resistant mice, and that treatment with myriocin also yielded a very similar beneficial profile. Interestingly, gastrocnemius ceramide levels, although reduced in myriocin treated *db/db* mice, did not differ between *db/+* lean and *db/db* control mice. This suggests, at least in this model, that perhaps ceramide metabolites, such as

glucosylceramide, are more important in mediating skeletal muscle insulin resistance than ceramide itself (7). Furthermore, the ceramide pool is under a dynamic process of synthesis and degradation (385), and although *de novo* synthesis of ceramide may be increased in these animals, a simultaneous increase in ceramide degradation would mask out any noticeable change.

In summary, we show that ceramide accumulation in skeletal muscle plays a key role during obesity-induced insulin resistance, while the other lipid metabolites, such as TAG, long chain acyl CoA, and DAG may not be as important. Importantly, inhibition of *de novo* ceramide synthesis in muscle is sufficient to reverse obesity-induced whole body glucose intolerance and insulin resistance. Furthermore, obesity-induced insulin resistance is associated with a reduction in whole body oxygen consumption rates and exercise capacity, both of which are also reversed via inhibition of *de novo* ceramide synthesis in muscle. Last, our finding that ceramide levels are not elevated in the muscle of *db/db* mice, but that inhibition of *de novo* ceramide synthesis still prevents insulin resistance development in *db/db* mice, suggests the possibility that ceramide metabolites may also play a role in this disease's progression.

CHAPTER 7.

Accumulation of ceramide contributes to the development of skeletal muscle insulin resistance in the obese JCR:LA-cp rat

---

My role in this work involved performing all experiments (except those noted below), as well as the writing of the manuscript. Panakkezhum Thomas performed the HPLC analysis of long chain acyl CoA and ceramide, Sandra Kelly and Shannon Lang assisted with the meal tolerance tests and indirect calorimetry experiments, and Wendy Keung determined the intramyocellular DAG content.

Manuscript Status: This manuscript is currently in preparation to be submitted to *the American Journal of Physiology: Endocrinology and Metabolism* for publication as an original article.

CHAPTER 7.

Accumulation of ceramide contributes to the development of skeletal muscle insulin resistance in the obese JCR:LA-cp rat

Abstract

It has been postulated that insulin resistance results from the accumulation of cytosolic lipid metabolites that impede insulin signaling. These lipid metabolites include long chain acyl CoA, diacylglycerol, and ceramide. *De novo* synthesis of ceramide is catalyzed via serine palmitoyl transferase-1 (SPT 1). Our goal was to determine if *de novo* ceramide synthesis plays a role in the development of insulin resistance in the JCR:LA-cp obese rat. 10-wk-old JCR:LA-cp obese rats were supplemented with either vehicle control or the SPT 1 inhibitor, L-cycloserine (360 mg/L), in their drinking water for a 2 wk period. Treatment of JCR:LA-cp obese rats with L-cycloserine significantly improved their plasma glucose (4.38 ± 0.30 vs. 5.50 ± 0.06 mM 30 min post-meal consumption) and insulin (11.56 ± 2.96 vs. 52.35 ± 6.60 ng/mL 30 min post-meal consumption) levels during a meal tolerance test. JCR:LA-cp obese rats demonstrated greater soleus ceramide content versus their lean heterozygous counterparts (36.9 ± 2.8 vs. 25.6 ± 2.9 nmol/g wet wt), which was prevented (36.9 ± 2.8 vs. 26.8 ± 1.7 nmol/g wet wt) via treatment with L-cycloserine. This reduction in ceramide content by L-cycloserine treatment did not alter the elevation of other lipid metabolites in soleus muscle of JCR:LA-cp obese rats. Finally, the improvement in insulin

sensitivity in L-cycloserine treated JCR:LA-cp obese rats was associated with enhanced glucose utilization as indicated by increased activity of Akt and PDH. Therefore, our results suggest that elevated ceramide levels contribute towards the development of insulin resistance in the JCR:LA-cp obese rat.

Numerous studies *in vivo* and *in vitro* have provided strong evidence that hyperlipidemia results in an accumulation of intramyocellular lipid-derived metabolites, which coincide with an impaired insulin response (353, 367). These lipid metabolites include TAG, long chain acyl CoA, DAG, and ceramide (353, 367, 385). These metabolites, and in particular, long chain acyl CoA and DAG, are believed to activate classical protein kinase C isoforms that phosphorylate and inactivate IRS proteins, preventing the insulin response at the level of Akt and GLUT4 translocation (353, 367).

In contrast, a number of recent studies have demonstrated clear disassociation between intramyocellular lipid metabolite accumulation and insulin sensitivity (231, 310, 312, 393). Thus, it is still up for debate as to the exact role that intramyocellular lipid plays in the development of skeletal muscle insulin resistance.

Of the aforementioned lipid metabolites, ceramide is an attractive candidate to be a culprit involved in mediating the skeletal muscle insulin resistance observed alongside obesity and type 2 diabetes, as it is elevated by both inflammation and lipid overload, linking two popular models of insulin resistance development (385). Numerous studies *in vivo* and *in vitro* demonstrate that ceramide accumulation inhibits insulin signaling and causes insulin resistance (153, 231, 310, 312). Moreover, Holland and colleagues have shown that inhibiting *de novo* synthesis of ceramide by pharmacological inhibition of SPT 1

can prevent insulin resistance caused by corticosteroids, saturated fats, and obesity (153). Pharmacological inhibition of SPT 1 in human muscle cells has also been shown to prevent the inhibition of insulin stimulated glycogen synthesis induced by palmitic acid (310). Finally, recent work in our lab has shown that inhibition of SPT 1 reverses insulin resistance in mice induced by chronic high fat feeding (unpublished data).

Our objective in this investigation was to determine if inhibition of *de novo* ceramide synthesis could prevent the development of skeletal muscle insulin resistance in the JCR:LA-cp rat. The JCR:LA-cp rat is a well-established animal model of obesity, hyperinsulinemia, and insulin resistance (20, 45, 333). The *cp* gene results in a leptin receptor mutation, resulting in a lack of functional leptin receptors in all tissues of homozygous JCR:LA-cp rats (431), causing these animals to develop insulin resistance between 4 and 12 wks of age.

Animal Studies

All animals received care according to the Canadian Council on Animal Care and the University of Alberta Health Sciences Animal Welfare Committee. 10-wk-old JCR:LA-cp lean heterozygous (*cp/+*) and JCR:LA-cp obese (*cp/cp*) rats supplemented with a standard chow/low fat diet (4% kcal from lard) were treated with the SPT 1 inhibitor, L-cycloserine, dissolved into the drinking water (360 mg/L) for a 2 wk period. This dose resulted in the animals consuming ~20 – 25 mg/day. At the end of the treatment protocol, animals were sacrificed via IP injection of sodium pentobarbital (12 mg) in the fed state in the middle of the dark cycle. Tissues were excised and immediately frozen in liquid N_2. Protocols for intramyocellular lipid metabolite accumulation, meal tolerance tests, plasma insulin levels, indirect calorimetry, immunoblotting, and statistical analysis are described in **Chapter 2** of this thesis.

JCR:LA-cp obese rats treated with L-cycloserine display improved insulin sensitivity during meal tolerance testing

JCR:LA-cp lean and obese rats were fasted overnight, before receiving a 5 g chow pellet during the middle of the dark cycle. Monitoring of plasma glucose levels during the meal tolerance test indicates that L-cycloserine treatment of JCR:LA-cp obese rats results in lower blood glucose levels (Figure 7-1A/B). Furthermore, determination of plasma insulin levels during the meal tolerance test also reveals a lowering in JCR:LA-cp obese rats treated with L-cycloserine (Figure 7-1C/D). Last, fasting plasma glucose and insulin levels are significantly lower in JCR:LA-cp obese rats treated with L-cycloserine, resulting in a lower HOMA score (Figure 7-1E). In summary, these results clearly suggest that L-cycloserine has protective effects against the development of insulin resistance in the JCR:LA-cp obese rat.

JCR:LA-cp obese rats display a severe impairment in whole body oxygen consumption rates that is not prevented via L-cycloserine treatment

Our previous results show that obesity-induced insulin resistance of mice caused by chronic high fat feeding is associated with a severe impairment in whole body oxygen consumption rates (unpublished data). Interestingly, inhibition of SPT 1 with an unrelated pharmacological inhibitor, myriocin, ameliorates whole body insulin resistance and restores the impairment in whole

body oxygen consumption rates (unpublished data). Supporting those findings, we show in this study that JCR:LA-cp obese, insulin resistant rats have a severe impairment in whole body oxygen consumption rates versus their lean counterparts (Figure 7-2A). However, in contrast, we show that the improvement in insulin sensitivity in JCR:LA-cp obese rats treated with L-cycloserine rats is not associated with a restoration of this impairment in whole body oxygen consumption rates (Figure 7-2A). Paralleling the impairment in whole body oxygen consumption rates, JCR:LA-cp obese rats demonstrate a severe impairment in whole body heat production, which is associated with a dramatic reduction in ambulatory activity, both of which are not improved via L-cycloserine treatment (Figure 7-2B/C). Because we have previously shown that JCR:LA-cp obese rats have significantly elevated plasma FFA and TAG concentrations, we anticipated that these animals would also show a significant decrease in their RER, indicating a preference for fatty acids as an oxidative energy source. Unexpectedly, we observe the opposite, as JCR:LA-cp obese rats display elevated RERs, which are not affected via L-cycloserine treatment (Figure 7-2D).

The improved insulin sensitivity in JCR:LA-cp obese rats treated with L-cycloserine is associated with an improvement in Akt and PDH phosphorylation

Obesity-induced insulin resistance has been associated with a reduction in the activity of Akt, a key signaling molecule regulating insulin's effects on

glucose homeostasis (417, 445). Supporting such proposals, we observe a reduction in Akt serine 473 phosphorylation (indicative of Akt activity (267)) in the soleus muscle of JCR:LA-cp obese rats, which is prevented in JCR:LA-cp obese rats treated with L-cycloserine (Figure 7-3A). Furthermore, phosphorylation at serine 9 of GSK3β, a key downstream target of Akt, shows a trend towards a reduction in the soleus muscle of JCR:LA-cp obese rats, which is prevented via treatment with L-cycloserine (Figure 7-3B). Examination of AMPK status in soleus muscle reveals no differences in threonine 172 phosphorylation of AMPK in JCR:LA-cp lean rats, JCR:LA-cp obese rats, and JCR:LA-cp obese rats treated with L-cycloserine (Figure 7-3C), paralleling our earlier work in this rat strain (20). Last, examination of the phosphorylation status of PDH, the rate-limiting enzyme of glucose oxidation, reveals a dramatic increase in PDH phosphorylation at serine 293 in the soleus muscle of JCR:LA-cp obese rats, indicative of an impaired PDH activity and reduction in skeletal muscle glucose oxidation rates (Figure 3D). Interestingly, treatment of JCR:LA-cp obese rats with L-cycloserine prevents this dramatic elevation of PDH phosphorylation (Figure 7-3D).

The improved insulin sensitivity in JCR:LA-cp obese rats treated with L-cycloserine is associated with a reduction in skeletal muscle ceramide levels

Examination of intramyocellular lipid metabolite accumulation reveals that L-cycloserine treatment has no effect on the elevation of soleus muscle TAG and long chain acyl CoA content observed in JCR:LA-cp obese rats versus their

lean counterparts (Figure 7-4A/B). Interestingly, L-cycloserine treatment has no effect on soleus muscle DAG content, and DAG content only shows a trend towards an increase in soleus muscle of JCR:LA-cp obese rats versus their lean counterparts (Figure 7-4C). As expected, ceramide content is significantly increased in soleus muscle of JCR:LA-cp obese rats versus their lean counterparts, which L-cycloserine treatment prevents (Figure 7-4D).

Figure 7-1: *L-cycloserine treatment improves insulin sensitivity in JCR:LA-cp obese rats.*

A: Supplementation of L-cycloserine in drinking water for 2 wks lowers plasma glucose levels following a meal tolerance test in JCR:LA-cp obese rats. B: Area under the curve (AUC) for plasma glucose levels during the meal tolerance test. C: Plasma insulin levels are also lowered in JCR:LA-cp obese rats treated with L-cycloserine supplementation in drinking water following a meal tolerance test. D: AUC for plasma insulin levels during the meal tolerance test. E: Fasting plasma glucose and insulin levels also reveal a decrease in the homeostasis model assessment score in JCR:LA-cp obese rats treated with L-cycloserine supplementation in drinking water. Values represent mean ± SE (n = 4-6). Differences were determined using a one-way or two-way ANOVA followed by a Bonferroni post-hoc analysis. $^{*}P<0.05$, significantly different from JCR:LA-cp lean heterozygous rats. $^{\#}P<0.05$, significantly different from JCR:LA-cp obese rats.

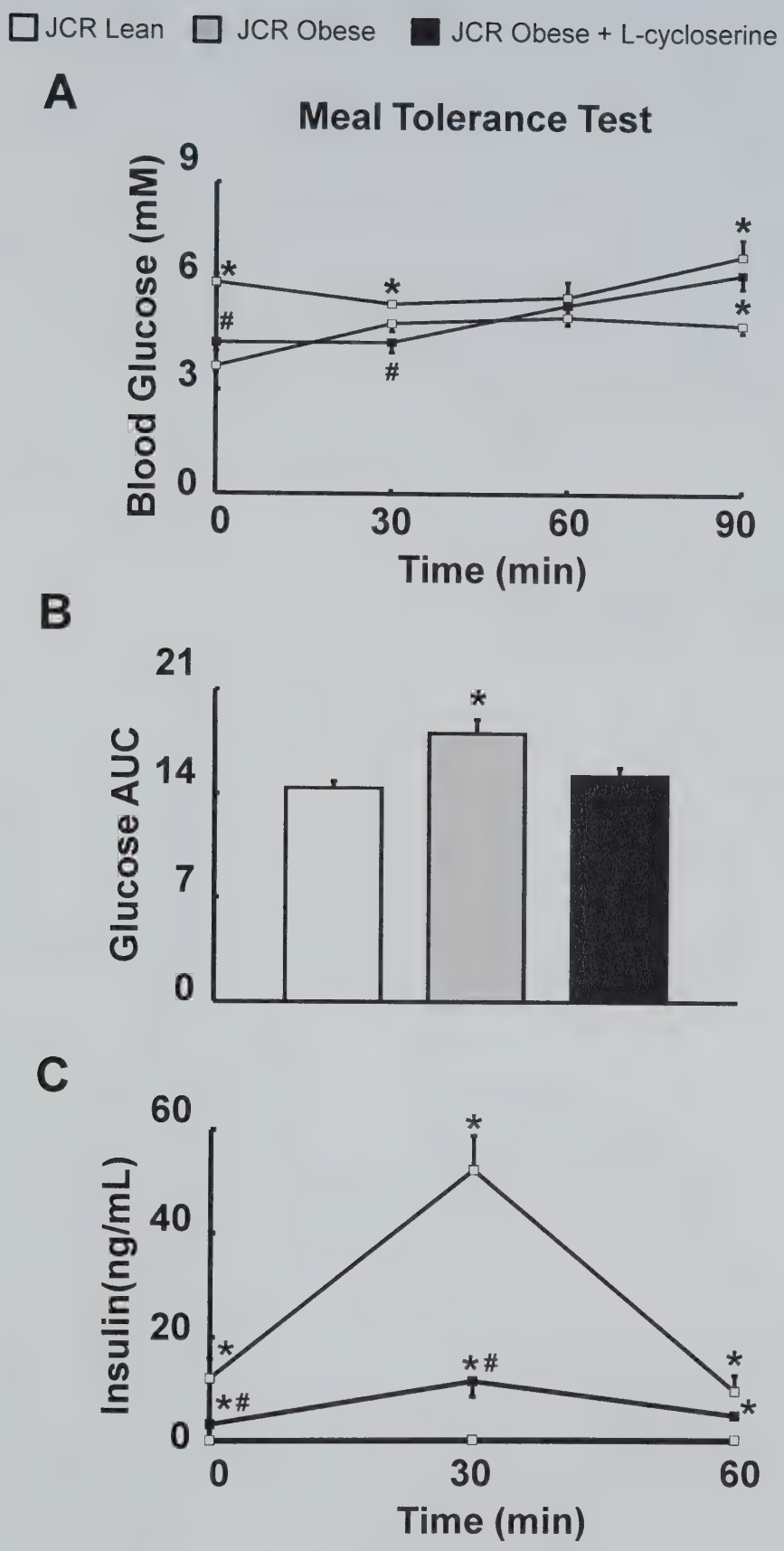
JCR Lean
JCR Obese
JCR Obese + L-cycloserine
A
Meal Tolerance Test
Blood Glucose (mM)
9
6
3
0
0
30
60
90
Time (min)
B
Glucose AUC
21
14
7
0
C
Insulin(ng/mL)
60
40
20
0
0
30
60
Time (min)

FIGURE 7-1

Figure 7-1: *L-cycloserine treatment improves insulin sensitivity in JCR:LA-cp obese rats.*

A: Supplementation of L-cycloserine in drinking water for 2 wks lowers plasma glucose levels following a meal tolerance test in JCR:LA-cp obese rats. B: Area under the curve for plasma glucose levels during the meal tolerance test. C: Plasma insulin levels were also lowered in JCR:LA-cp obese rats treated with L-cycloserine supplementation in drinking water following a meal tolerance test. **D: Area under the curve (AUC) for plasma insulin levels during the meal tolerance test. E: Fasting plasma glucose and insulin levels also reveal a decrease in the homeostasis model assessment score (HOMA) in JCR:LA-cp obese rats treated with L-cycloserine supplementation in drinking water.** Values represent mean ± SE (n = 4-6). Differences were determined using a one-way ANOVA followed by a Bonferroni post-hoc analysis. $^{*}P<0.05$, significantly different from JCR:LA-cp lean heterozygous rats. $^{\#}P<0.05$, significantly different from JCR:LA-cp obese rats.

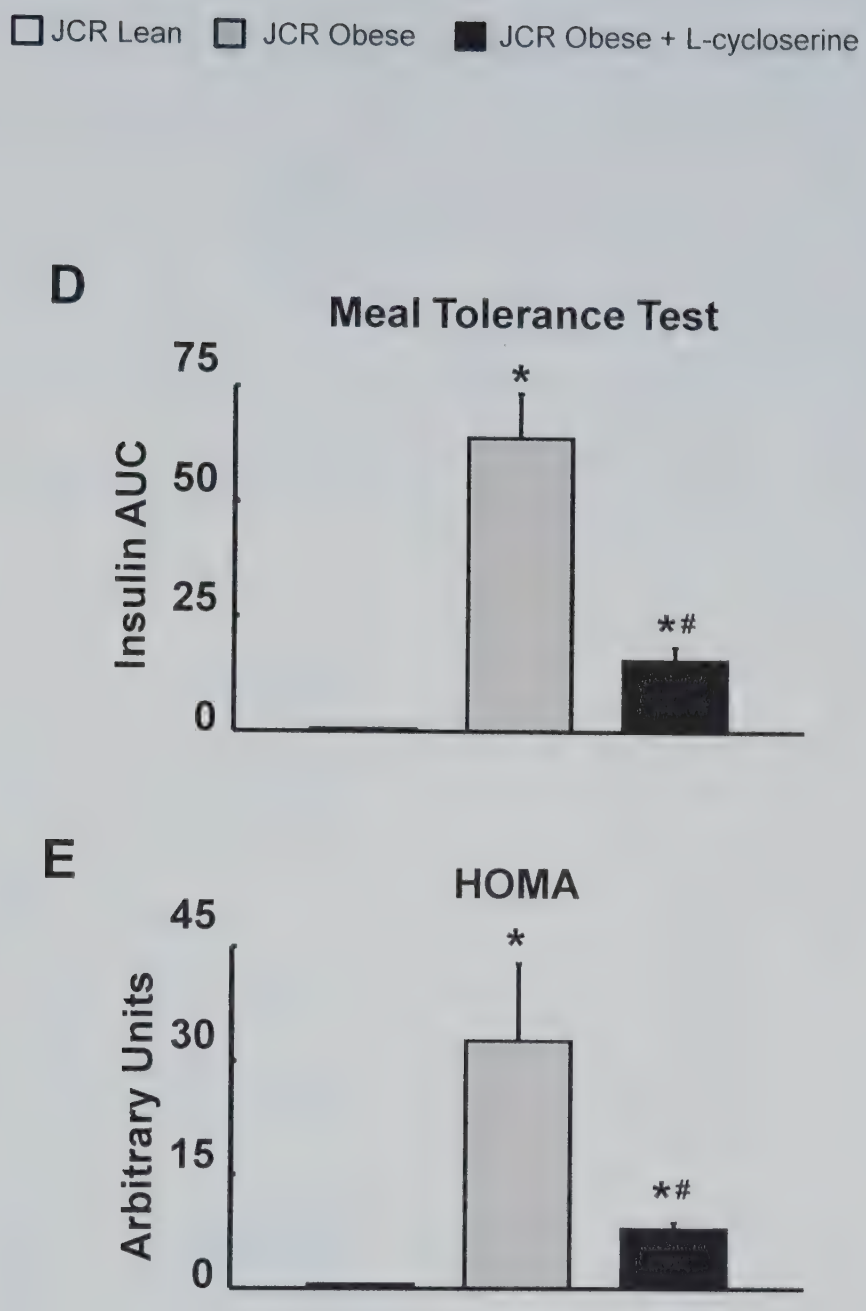
JCR Lean
JCR Obese
JCR Obese + L-cycloserine
D
Meal Tolerance Test
Insulin AUC
75
50
25
0
*
*#
E
HOMA
Arbitrary Units
45
30
15
0
*
*#

FIGURE 7-1

Figure 7-2: *L-cycloserine treatment has no effect on whole body oxygen consumption rates and heat production in JCR:LA-cp obese rats.*

A: Whole body oxygen consumption rates, B: heat production, C: ambulatory activity, and D: 24 hr respiratory exchange ratio (RER) in JCR:LA-cp obese rats treated with L-cycloserine supplementation in drinking water for 2 wks. Values represent mean ± SE (n = 6). Differences were determined using a one-way ANOVA followed by a Bonferroni post-hoc analysis. $*P<0.05$, significantly different from JCR:LA-cp lean heterozygous rats.

JCR Lean
JCR Obese
JCR Obese + L-cycloserine
A
O_2 Consumption
ml/kg/hr
1500
1000
500
0
B
Heat Production
kcal/hr/g body wt
0.0075
0.0050
0.0025
0
C
Ambulatory Activity
Beam Breaks
7500
5000
2500
0
*
D
RER
1.3
1.2
1.1
1.0
0.9
0.8
0.7
00:00 hr
6:00 hr
12:00 hr
18:00 hr
24:00 hr

FIGURE 7-2

Figure 7-3: *L-cycloserine treatment improves glucose utilization signaling in JCR:LA-cp obese rats.*

A: Supplementation of L-cycloserine in drinking water for 2 wks increases Akt serine 473 phosphorylation in JCR:LA-cp obese rats. B: GSK3β serine 9 phosphorylation, and C: AMPK threonine 172 phosphorylation are not altered in JCR:LA-cp obese rats versus their lean heterozygous counterparts. D: However, PDH phosphorylation is significantly increased in JCR:LA-cp obese rats versus their lean heterozygous counterparts, but restored to normal levels in JCR:LA-cp obese rats treated with L-cycloserine supplementation in drinking water. Values represent mean ± SE (n = 5-6). Differences were determined using a one-way ANOVA followed by a Bonferroni post-hoc analysis. $*P<0.05$, significantly different from JCR:LA-cp lean heterozygous rats.

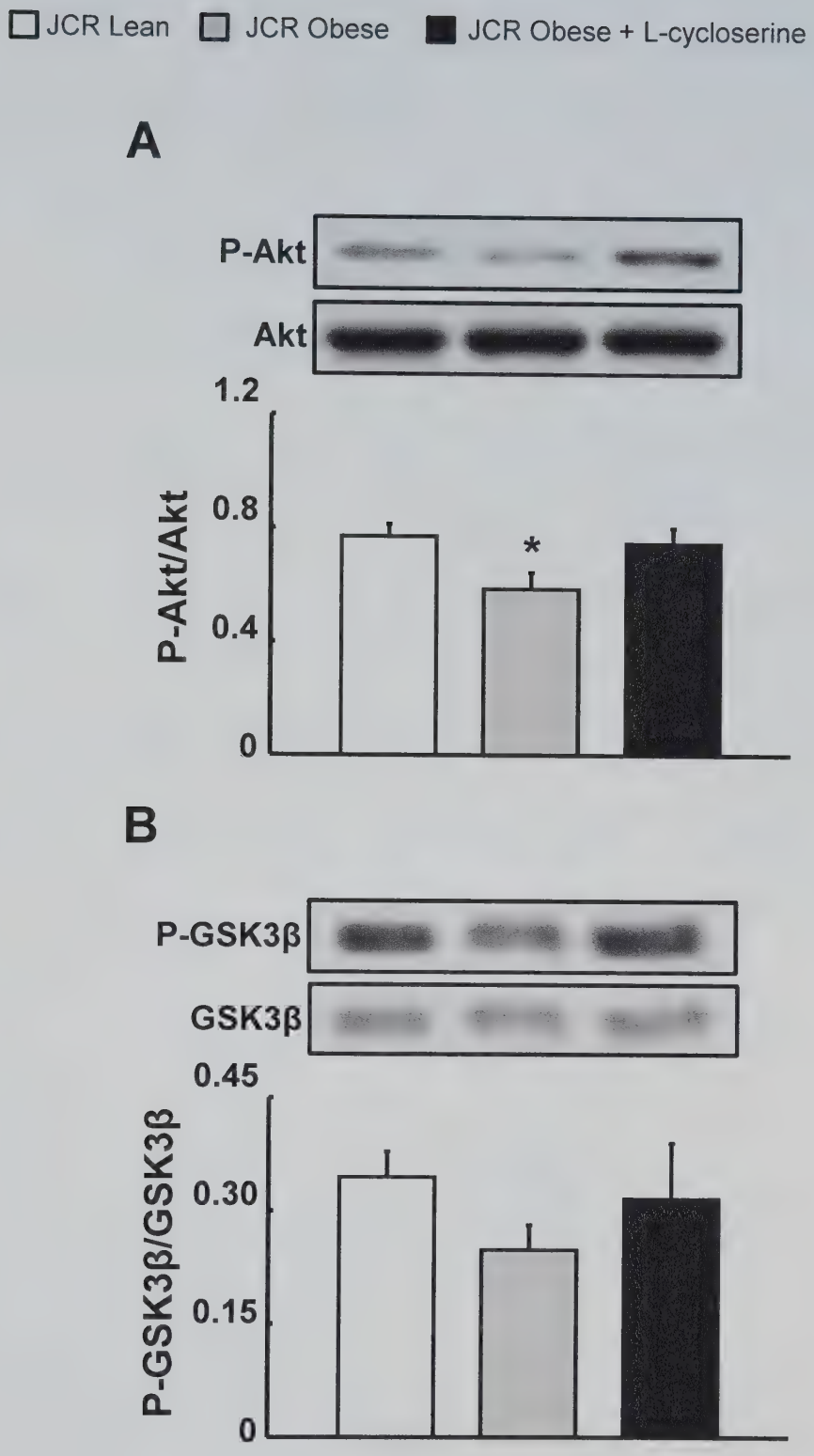
JCR Lean
JCR Obese
JCR Obese + L-cycloserine
A
P-Akt
Akt
1.2
0.8
0.4
0
P-Akt/Akt
*
B
P-GSK3β
GSK3β
0.45
0.30
0.15
0
P-GSK3β/GSK3β

FIGURE 7-3

Figure 7-3: *L-cycloserine treatment improves glucose utilization signaling in JCR:LA-cp obese rats.*

A: Supplementation of L-cycloserine in drinking water for 2 wks increases Akt serine 473 phosphorylation in JCR:LA-cp obese rats. B: GSK3β serine 9 phosphorylation, and **C: AMPK threonine 172 phosphorylation are not altered in JCR:LA-cp obese rats versus their lean heterozygous counterparts. D: However, PDH phosphorylation is significantly increased in JCR:LA-cp obese rats versus their lean heterozygous counterparts, but restored to normal levels in JCR:LA-cp obese rats treated with L-cycloserine supplementation in drinking water.** Values represent mean ± SE (n = 5-6). Differences were determined using a one-way ANOVA followed by a Bonferroni post-hoc analysis. $*P<0.05$, significantly different from JCR:LA-cp lean heterozygous rats.

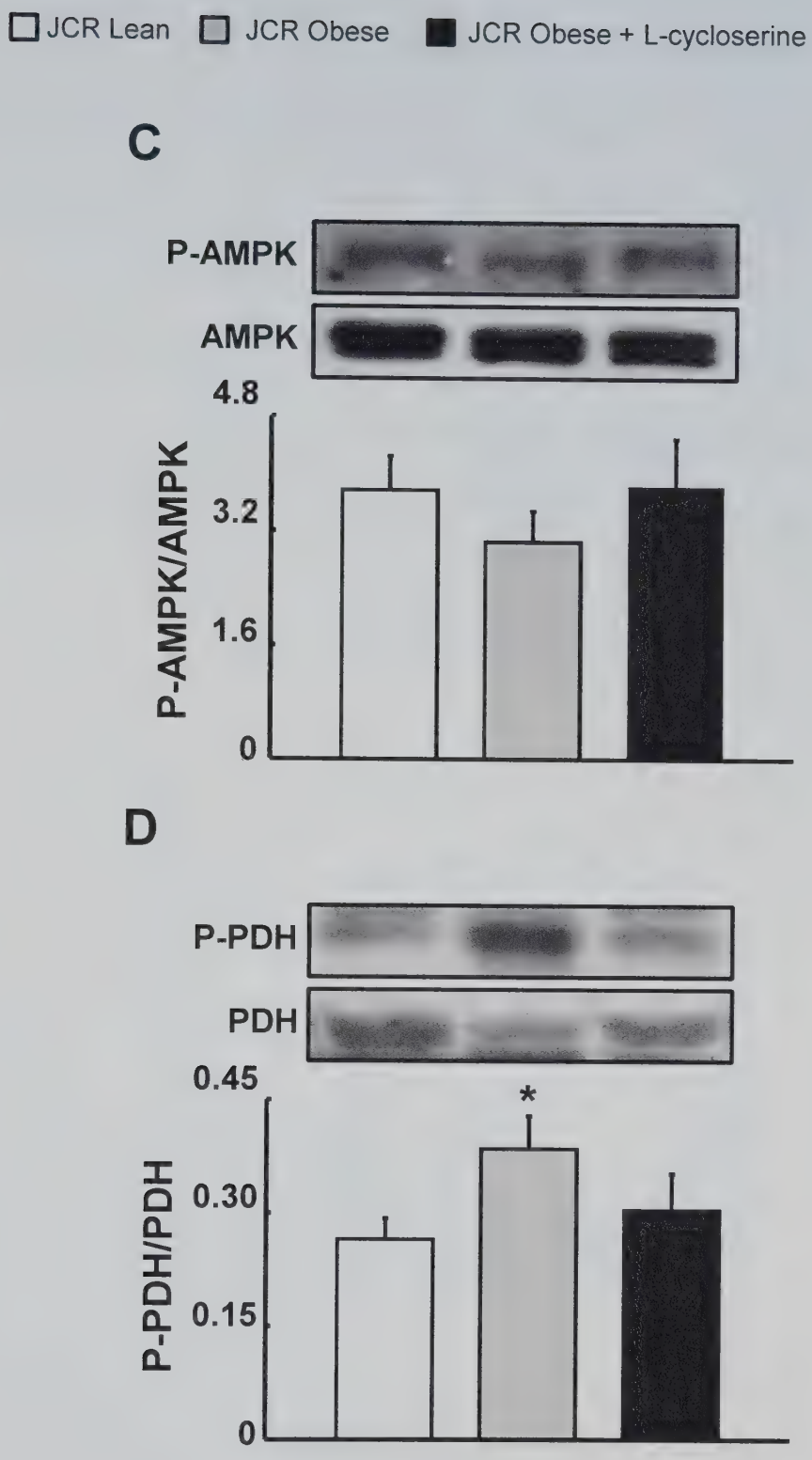
JCR Lean
JCR Obese
JCR Obese + L-cycloserine
C
P-AMPK
AMPK
4.8
3.2
1.6
0
P-AMPK/AMPK
D
P-PDH
PDH
0.45
0.30
0.15
0
P-PDH/PDH
*

FIGURE 7-3

Figure 7-4: *L-cycloserine treatment decreases the elevation of skeletal muscle ceramide levels observed in JCR:LA-cp obese rats.*

Supplementation of L-cycloserine in drinking water for 2 wks has no effect on soleus muscle A: triacylglycerol content, B: long chain acyl CoA content, and C: diacylglycerol content, but D: prevents the increase in ceramide content in JCR:LA-cp obese rats. Values represent mean ± SE (n = 5). Differences were determined using a one-way ANOVA followed by a Bonferroni post-hoc analysis. *$P<0.05$, significantly different from JCR:LA-cp lean heterozygous rats.

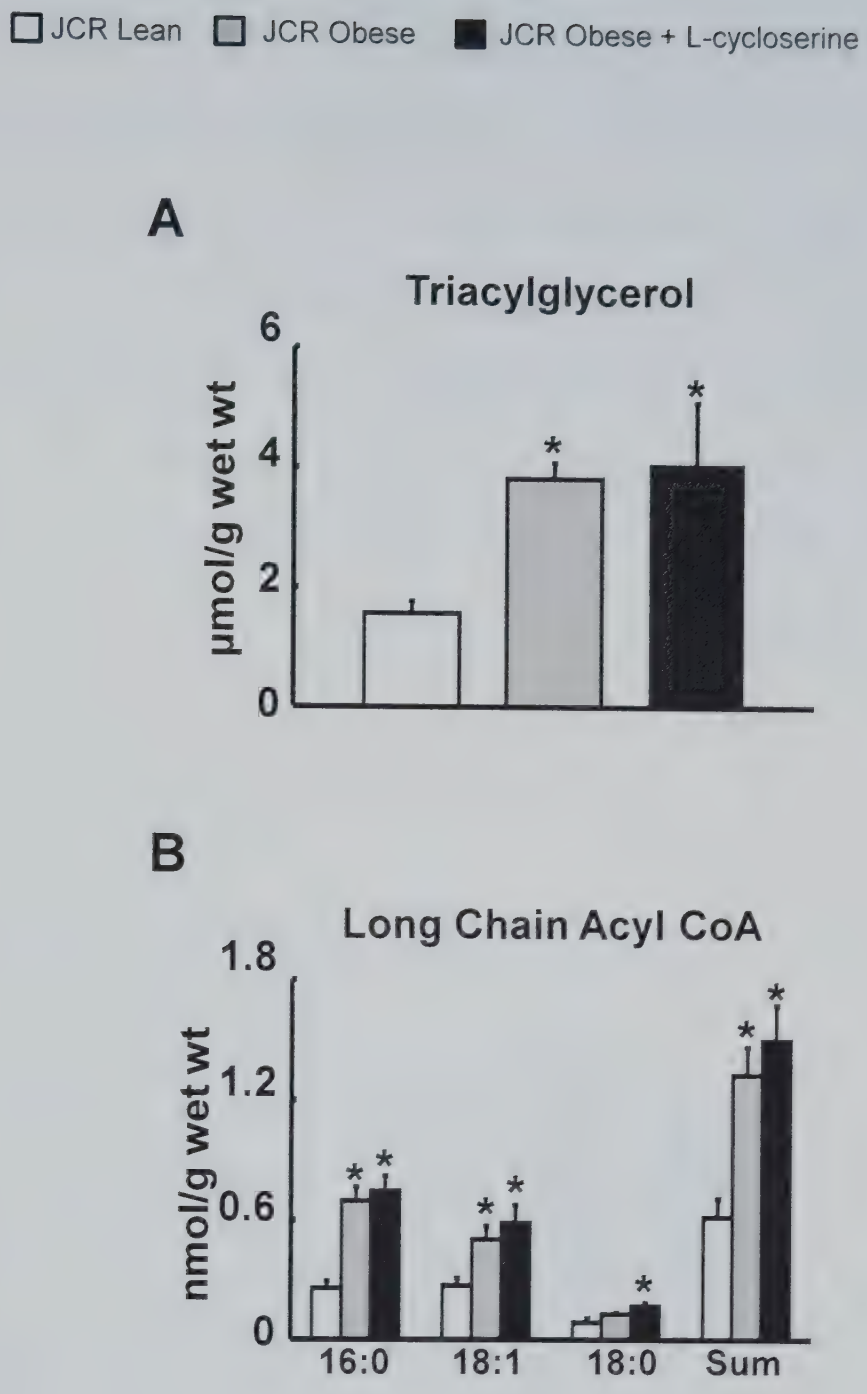
JCR Lean
JCR Obese
JCR Obese + L-cycloserine
A
Triacylglycerol
µmol/g wet wt
6
4
2
0
B
Long Chain Acyl CoA
nmol/g wet wt
1.8
1.2
0.6
0
16:0
18:1
18:0
Sum

FIGURE 7-4

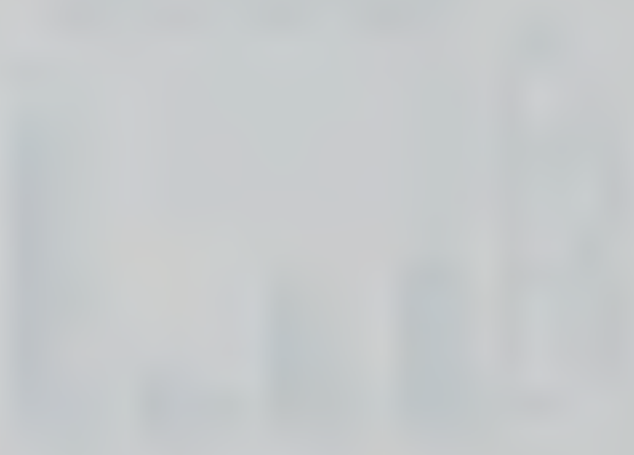

Figure 7-4: *L-cycloserine treatment decreases the elevation of skeletal muscle ceramide levels observed in JCR:LA-cp obese rats.*

Supplementation of L-cycloserine in drinking water for 2 wks has no effect on soleus muscle A: triacylglycerol content, B: long chain acyl CoA content, and **C: diacylglycerol content, but D: prevents the increase in ceramide content in JCR:LA-cp obese rats.** Values represent mean ± SE (n = 5). Differences were determined using a one-way ANOVA followed by a Bonferroni post-hoc analysis. $^{*}P<0.05$, significantly different from JCR:LA-cp lean heterozygous rats. $^{\#}P<0.05$, significantly different from JCR:LA-cp obese rats.

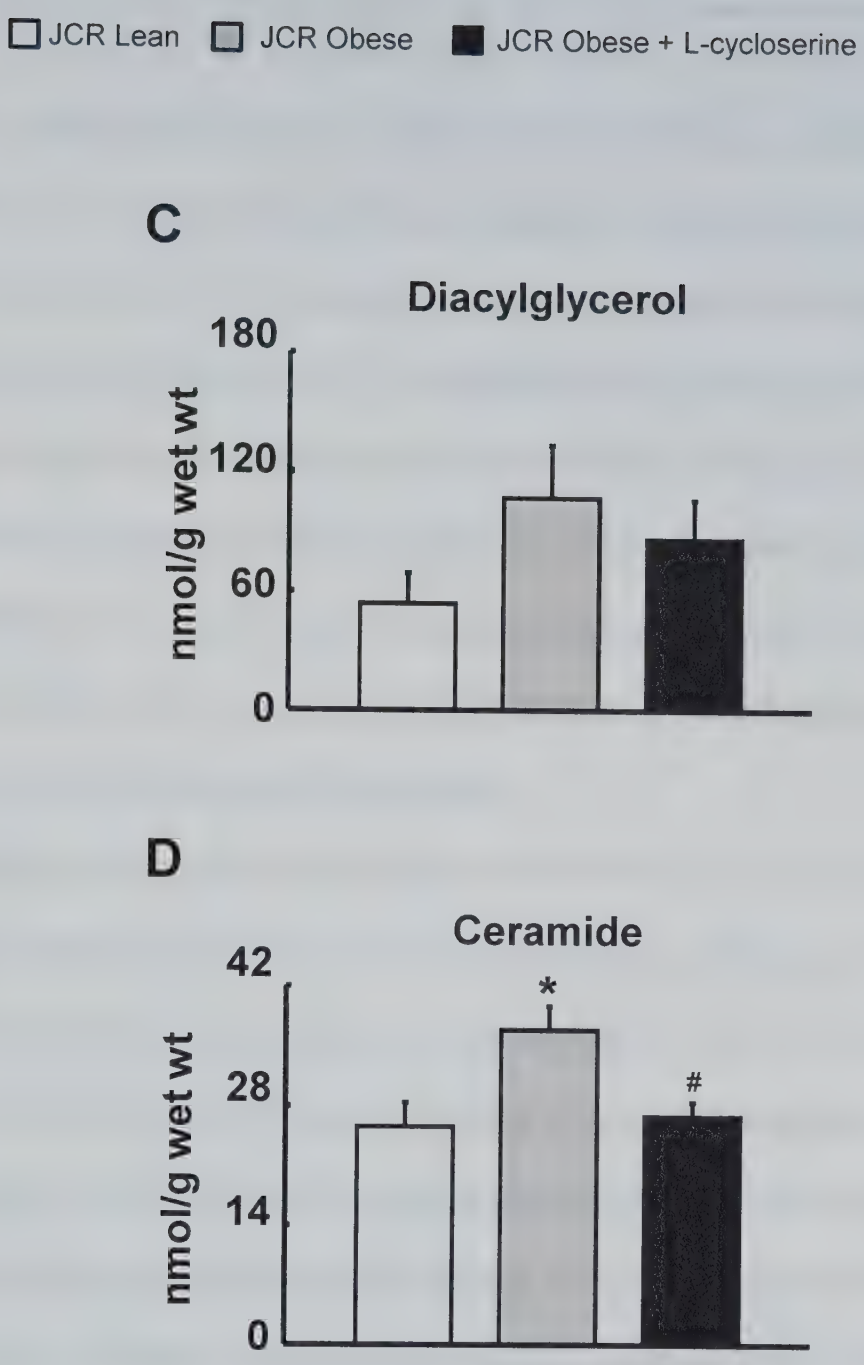
JCR Lean
JCR Obese
JCR Obese + L-cycloserine
C
Diacylglycerol
nmol/g wet wt
180
120
60
0
D
Ceramide
nmol/g wet wt
42
28
14
0
*
#

FIGURE 7-4

Our results reveal the novel observation that elevated skeletal muscle ceramide levels contribute towards the development of insulin resistance in the JCR:LA-cp obese rat. If *de novo* synthesis of ceramide was blocked via pharmacological inhibition of SPT 1, the progression of insulin resistance in the JCR:LA-cp obese rat was halted, even in the continuing presence of elevated levels of skeletal muscle TAG and long chain acyl CoA. The beneficial effects of SPT 1 inhibition in the JCR:LA-cp obese rat were associated with a restoration of Akt phosphorylation, and a reduction of PDH phosphorylation, highly suggestive of improved glucose utilization in these animals.

Previous studies from our laboratory and others have shown that TAG content is elevated in the skeletal muscle of the JCR:LA-cp obese rat (20, 333). However, treatment of these animals with MEDICA 16, an ATP-citrate lyase inhibitor that limits acetyl CoA supply to acetyl CoA carboxylase, a key enzyme in *de novo* fatty acid synthesis, improved insulin sensitivity, an effect associated with a decline in intramyocellular TAG content (333). Our results deviate from these findings, as intramyocellular TAG content remained elevated in JCR:LA-cp obese rats treated with L-cycloserine, despite the improvement in insulin sensitivity. It is important to note though, that other lipid metabolites, such as ceramide, were not examined in these previous studies (20, 333), and it is quite possible that intramyocellular ceramide levels were also significantly reduced in JCR:LA-cp obese rats treated with MEDICA 16. Regardless, our results support

a recent growing body of evidence revealing dissociation between skeletal muscle TAG content and insulin sensitivity, and support more recent proposals suggesting that the TAG pool in muscle may act as a protective buffer against other toxic lipid metabolites, such as ceramide and DAG (90, 231, 310, 355, 401). Furthermore, our results suggest that ceramide may be more important in the development of insulin resistance than either DAG or long chain acyl CoA in the JCR:LA-cp obese rat, as L-cycloserine treatment had no effect on their levels in soleus muscle from JCR:LA-cp obese rats. These findings were consistent with our previous studies in high fat fed mice, whereby ceramide was the only lipid metabolite that correlated with the development of glucose intolerance and insulin resistance (unpublished data).

Improved Akt phosphorylation in L-cycloserine treated JCR:LA-cp obese rats suggests improved insulin signaling in these animals, which has been shown to be impaired in a number of different models of obesity- or lipid-induced insulin resistance (153, 312, 357, 385). Moreover, PDH, the rate limiting enzyme of glucose oxidation, is rapidly inactivated by phosphorylation (300). We report here that PDH phosphorylation was robustly increased in soleus muscle of JCR:LA-cp obese rats versus their lean counterparts, indicative of a severe impairment in glucose oxidation in these animals. Interestingly, L-cycloserine treatment reduced PDH phosphorylation in JCR:LA-cp obese rats to levels seen in JCR:LA-cp lean rats. Combined, the increased Akt phosphorylation and reduced PDH phosphorylation suggest improved overall glucose utilization in JCR:LA-cp

obese rats treated with L-cycloserine, representing a possible mechanism mediating the improvement in insulin sensitivity.

Our previous observations have shown that mice subjected to DIO via chronic high fat feeding is associated with a robust decrease in the RER, and an impairment of both whole body oxygen consumption rates and heat production (unpublished data). Although our results in the JCR:LA-cp obese rat parallel our previous findings with an impairment of whole body oxygen consumption and heat production, we observed an unexpected increase in the RER in the JCR:LA-cp obese rat. As the RER approaches 1, its suggestive of a complete reliance on glucose oxidation as an energy substrate, and as it approaches 0.7, becomes suggestive of a complete reliance on palmitate oxidation as an energy substrate (104). Thus, initial interpretation of our data would suggest that the JCR:LA-cp obese rat relies primarily on carbohydrates such as glucose for its energy production. Such interpretations were not anticipated, as plasma TAG and FFA concentrations were dramatically elevated in the JCR:LA-cp obese rat (20, 22), and our previous findings and that of others have shown that high fat diets markedly lower the RER (287, 396), suggesting that obesity-induced insulin resistance is associated with a heavy reliance on fatty acids for energy production. The discrepancy in our findings, however, can be explained by the fact that the JCR:LA-cp obese rat is also a model of dramatically enhanced lipogenesis (100, 371). Severe increases in lipogenesis have been shown to increase the RER to values that can even exceed 1 (100, 371). Thus, although the JCR:LA-cp obese rat may primarily rely on fatty acids for energy production (241), the increased

lipogenesis of these animals may account for their increased RER, and caution should be taken with interpretation of this data.

In regards to the impairment in whole body oxygen consumption rates and heat production in the JCR:LA-cp obese rat, our results show that inhibition of SPT 1 with L-cycloserine did not prevent these effects. These results are in discordance with our previous findings, whereby myriocin, an unrelated SPT 1 inhibitor, restored whole body oxygen consumption rates and heat production in mice subjected to DIO (unpublished data). Such differences suggest that the effects of myriocin on whole body oxygen consumption rates and heat production are either independent of the reduction of ceramide content, or that model-specific differences in the JCR:LA-cp obese rat contribute to these impairments independent of ceramide accumulation.

Overall, our findings suggest that elevated intramyocellular ceramide levels contribute to the development and progression of insulin resistance in the JCR:LA-cp obese rat. Blocking *de novo* synthesis of ceramide via SPT 1 inhibition improved insulin sensitivity in the JCR:LA-cp obese rat, despite elevated intramyocellular TAG and long chain acyl CoA content. This increase in insulin sensitivity is associated with an enhanced Akt phosphorylation and reduced PDH phosphorylation, suggesting that SPT 1 inhibition improves overall glucose utilization in these animals. Thus, targeting SPT 1 to reduce skeletal muscle ceramide levels appears to be a novel exciting target for the treatment of obesity-induced insulin resistance.

CHAPTER 8.

Enhanced lifespan in mice deficient for malonyl CoA decarboxylase is associated with a switch in whole body energy metabolism from fatty acid to carbohydrate utilization

---

My role in this work involved performing all experiments (except those noted below), as well as the writing of the manuscript. Panakkezhum Thomas performed the HPLC analysis of long chain acyl CoA and ceramide, Sandra Kelly performed the ultrasound echocardiography, Cory Wagg performed the isolated working heart perfusions, and Wendy Keung determined the intramyocellular DAG content.

Manuscript Status: This manuscript is currently in preparation to be submitted to *Nature* for publication as a letter.

CHAPTER 8.

Enhanced lifespan in mice deficient for malonyl CoA decarboxylase is associated with a switch in whole body energy metabolism from fatty acid to carbohydrate utilization

Abstract

Aging is associated with the development of chronic diseases such as obesity, insulin resistance, and heart failure. A reduction in mitochondrial fatty acid oxidative capacity is believed to be a key factor contributing to the progression of these diseases (303). In order to address the contribution of impaired mitochondrial fatty acid oxidation to the development of these diseases with age, we monitored lifespan and the development of disease in mice deficient for malonyl CoA decarboxylase (MCD-/-), a model of reduced fatty acid oxidative capacity (202, 400). Here we show, contrary to popular belief, that lifelong deficiency of fatty acid oxidation in MCD-/- mice was associated with prolonged lifespan (~28% increase vs. wild type littermates). Furthermore, the prolonged lifespan in MCD-/- mice was associated with reduced whole body oxygen consumption rates, increased carbohydrate oxidation, and the accumulation of lipid metabolites in skeletal muscle. Interestingly, although fatty acid oxidation rates were decreased in hearts from MCD-/- mice, these mice had improved cardiac efficiency and no signs of cardiac dysfunction. Finally, aged MCD-/- mice displayed no signs of hepatic disease despite their reduction in oxidative

energy metabolism. Our findings highlight a paradigm shift with regards to reductions in fatty acid oxidation and the development of disease with age, and suggest that MCD may be a novel target in the battle against chronic disease in our elderly population.

Prolonging survival and improving overall health is of utmost importance in our constant battle to improve the quality of life in our elderly population. Recent studies have shown that aging is associated with the development of a number of chronic diseases, some of which include insulin resistance, type 2 diabetes, and cardiovascular disease (191, 318, 340, 352). In addition, a reduction in mitochondrial function, which manifests as a decline in fatty acid oxidative capacity, is believed to result in the accumulation of lipid metabolites in the cell, which contribute to the decline in insulin sensitivity and decline in cardiac contractile function observed with aging (303, 373).

MCD is an important enzyme in the regulation of fatty acid oxidation, by controlling cellular levels of malonyl CoA, a potent endogenous inhibitor of CPT 1, the rate-limiting enzyme of mitochondrial fatty acid oxidation (260, 405). Interestingly, we have shown that acute inhibition of MCD decreases fatty acid oxidation rates in the heart, which results in a subsequent increase in carbohydrate oxidation rates in the heart, and is associated with improved functional recovery during reperfusion following ischemia (93). We have also obtained similar results in a mouse model of MCD deficiency (MCD-/-) (95), and have shown that these mice are also protected against skeletal and cardiac muscle insulin resistance induced by chronic high fat feeding (202, 400).

Although MCD inhibition shows protection against many disease states when employed acutely, due to the profound findings showing that impaired

mitochondrial fatty acid oxidation rates contribute to disease progression in the elderly population (303, 353, 373), it became of utmost importance to monitor the effects of lifelong deficiency/inhibition of MCD. This was achieved by separating MCD-/- mice and their WT littermates into 2 cohorts. In one cohort, WT and MCD-/- mice were monitored until death to determine average lifespan, and in the second cohort, WT and MCD-/- mice were aged to ~70-75 wks of age, subjected to a number of different experimental procedures to monitor overall health, and then sacrificed for harvesting of tissues. We anticipated that contrary to current dogma, MCD-/- mice would not be candidates for the early development of chronic disease associated with aging.

Animal Studies

All animals received care according to the Canadian Council on Animal Care and the University of Alberta Health Sciences Animal Welfare Committee. WT or MCD-/- mice were placed on a standard chow/low fat diet (4% kcal from lard) and separated into two cohorts. In the first cohort, WT and MCD-/- mice were monitored until death to determine average lifespan. In the second cohort, WT and MCD-/- mice at 70-75 wks of age were subjected to a number of experimental procedures, including ITTs, *in vivo* whole body metabolic assessment via use of a CLAMS apparatus, ultrasound echocardiography, and exercise treadmill running. Once all *in vivo* physiological parameters were assessed, animals were euthanized via an IP injection of sodium pentobarbital (12 mg) in the fed state in the middle of the dark cycle. Tissues were excised and immediately frozen in liquid N_2 for biochemical analyses, while hearts were perfused in the isolated working mode to assess oxidative energy metabolism. Protocols for isolated working heart perfusions, assessment of energy metabolism, intramyocellular lipid metabolite accumulation, ITTs, indirect calorimetry, immunoblotting, and statistical analysis are described in **Chapter 2** of this thesis.

Aged MCD-/- mice have an enhanced lifespan that is associated with a reduction in whole body oxygen consumption rates and increased reliance on carbohydrates for energy metabolism

Unexpectedly, MCD-/- mice demonstrate an increase in lifespan by about 28% versus their WT littermates (Figure 8-1A). In addition, MCD-/- mice do not display any significant increases in the weight of their liver and adipose depots (Figure 8-1B-E). Plasma levels of TAG and insulin are similar between aged male WT and MCD-/- mice, as well as aged female WT and MCD-/- mice, except for a slight decrease in fed plasma TAG levels and a slight increase in fasted plasma insulin levels in aged female MCD-/- mice (Table 8-1). Lifelong partial deficiency of fatty acid oxidation in MCD-/- mice does not result in the development of glucose intolerance in aged male MCD-/- mice (Figure 8-2A), and the effects of insulin on blood glucose levels during an insulin tolerance test are maintained over a longer time course in aged male MCD-/- mice versus their WT littermates (Figure 8-2B). The effects of insulin on blood glucose levels during an insulin tolerance test are actually more profound in aged female MCD-/- mice (Figure 8-3A).

Use of a CLAMS apparatus reveals that the enhanced lifespan in MCD-/- mice is associated with increased carbohydrate oxidation as an energy substrate (Figure 8-2C), and a reduction in whole body oxygen consumption rates (Figure 8D). Similar results are seen in aged female MCD-/- mice, however the decline in

whole body oxygen consumption is not as dramatic (*data not shown*). Unexpectedly, we also observe a significant reduction in overall ambulatory activity in aged female MCD-/- mice versus their aged WT littermates (Figure 8-3B). The decline in whole body oxygen consumption rates is not accompanied via differences in skeletal muscle CS activity between aged male WT and MCD-/- mice (0.046 ± 0.007 vs. 0.047 ± 0.006 μmol/mg protein/min, *data not shown*), nor between aged female WT and MCD-/- mice (0.046 ± 0.012 vs. 0.057 ± 0.009 μmol/mg protein/min, *data not shown*). This is accompanied via similar skeletal muscle protein levels of PGC1α (7.45 ± 2.28 vs. 5.50 ± 1.47 and 3.86 ± 1.10 vs. 4.89 ± 2.00 arbitrary units in males and females, respectively, *data not shown*). These findings suggest that a decline in mitochondrial function or capacity is unlikely the cause for the reduced oxygen consumption in MCD-/- mice, and more likely indicate that an impaired ability to oxidize fatty acids is responsible for this effect.

Intramyocellular lipid metabolite accumulation in aged WT and MCD-/- mice

It has been proposed that a deficiency in mitochondrial fatty acid oxidation results in the cytosolic accumulation of lipid metabolites, such as TAG, long chain acyl CoA, DAG, and ceramide, which impede the insulin signaling cascade and lead to the development of insulin resistance (275, 353, 447). Interestingly, aged MCD-/- demonstrate no accumulation of TAG or ceramide levels in gastrocnemius muscle, but they do accumulate certain species of long

chain acyl CoA and show a trend towards an accumulation of DAG (Figure 8-2E-H). Although long chain acyl CoA and DAG accumulate in aged MCD-/- mice, insulin signaling at the level of Akt and GSK3 phosphorylation is similar to aged WT littermates (Figure 8-4). Such findings highlight a clear dissociation between reduced fatty acid oxidation rates, skeletal muscle lipid metabolite accumulation, and the development of insulin resistance, challenging current dogma.

Aged MCD-/- mice produce contractile work more efficiently and display no signs of cardiac dysfunction despite reduced fatty acid oxidative capacity

Aging is also associated with the development of cardiovascular disease such as heart failure (35), and it has been proposed that the decline in mitochondrial fatty acid oxidation in the heart with age contributes to the pathology of heart failure (364, 382). *In vivo* assessment of cardiac function in both aged WT and MCD-/- mice shows no decline in overall cardiac function with only minor signs of hypertrophy versus their young counterparts (Table 8-2). *Ex vivo* perfusion of aged male MCD-/- mice also reveals no decline in function versus their aged male WT littermates (Figure 8-5A). Measurement of oxidative metabolism in aged male mice reveals as expected, a significant reduction in fatty acid oxidation rates in hearts of MCD-/- mice, but interestingly, no compensatory increase in glucose oxidation rates (Figure 8-5B/C). Although we do not directly measure oxygen consumption in the hearts of aged male WT and MCD-/- mice, we have shown a strong correlation between oxygen consumption and TCA cycle acetyl CoA production (230). Therefore, by looking at the amount of work

performed by the heart per TCA cycle acetyl CoA molecule produced, we are able to obtain an index of cardiac efficiency, and demonstrate here that aged male MCD-/- mice have a dramatic improvement in cardiac efficiency (Figure 8-5D). Furthermore, an identical metabolic profile and improved cardiac efficiency is observed in aged female MCD-/- mice (Figure 8-6). Given that reductions in cardiac efficiency contribute to the development of cardiovascular disease (230, 382), it is possible that the improved cardiac efficiency in aged MCD-/- mice delays the progression of eventual cardiac disease in these animals, increasing their average lifespan.

Aged MCD-/- accumulate intrahepatic TAG, but not DAG, and show no signs of hepatic insulin resistance

One of the primary concerns with inhibition of MCD or fatty acid oxidation in general, is the potential for the development of hepatic steatosis and hepatic insulin resistance (15, 280, 447). As such, overexpression of MCD in the liver has actually been shown to have extremely positive effects on overcoming high fat diet-induced whole body insulin resistance (12). Nonetheless, aged male and female MCD-/- mice do not display an increase in total liver weight versus their WT littermates (Figure 8-1C/E). Although liver weights are identical between aged groups, we observe a unique profile with regards to the accumulation of lipid metabolites in aged male MCD-/- mice. These findings include elevated intrahepatic TAG levels, no change in long chain acyl CoA esters or ceramide content, and a significant decrease in DAG levels (Figure 8-7A-D).

This is of particular interest, as DAG has been shown in a number of recent studies to play a significant role in the development of hepatic insulin resistance (15, 251, 350), and may explain why MCD-/- mice show no signs of hepatic disease despite greater intrahepatic TAG content. Furthermore, the phosphorylation status of both Akt and the Akt downstream target, GSK3β, is not impaired in livers from aged MCD-/- mice (Figure 8-7E/F), suggesting that hepatic insulin sensitivity is not impaired in these animals.

Table 8-1: *Plasma parameters in aged WT and MCD-/- mice.*

	WT (Male) (n=5-6)	MCD-/- (Male) (n=5-6)	WT (Female) (n=5-6)	MCD-/- (Female) (n=4-6)
Fasted Glucose (mM)	5.8 ± 0.4	5.9 ± 0.4	5.2 ± 0.5	5.9 ± 0.4
Fed Glucose (mM)	7.5 ± 0.4	7.4 ± 0.4	6.3 ± 0.2	7.1 ± 0.2
Fasted Insulin (ng/mL)	0.45 ± 0.19	0.40 ± 0.04	0.28 ± 0.02	0.55 ± 0.12*
Fed Insulin (ng/mL)	0.91 ± 0.15	1.10 ± 0.27	0.52 ± 0.03	0.70 ± 0.18
Fasted TAG (mg/dL)	75.8 ± 4.2	79.9 ± 5.5	93.5 ± 4.8	82.1 ± 3.1
Fed TAG (mg/dL)	120.8 ± 7.0	129.7 ± 11.0	129.7 ± 2.2	105.4 ± 8.6*

Values represent means ± SE. Differences were determined using a two-tailed Student's *t*-test. *$P<0.05$, significantly different from sex-matched WT littermate. TAG = triacylglycerol.

Table 8-2: *MCD deficiency does not cause in vivo cardiac dysfunction in aged mice.*

	WT (Young) (n=5)	MCD-/- (Young) (n=5)	WT (Aged) (n=5)	MCD-/- (Aged) (n=5)
Tei Index	0.42 ± 0.02	0.44 ± 0.02	0.44 ± 0.02	0.44 ± 0.03
EF (%)	60.4 ± 4.2	62.4 ± 2.2	59.8 ± 3.2	62.3 ± 3.0
LVPW:d (mm)	0.74 ± 0.02	0.83 ± 0.06	0.76 ± 0.01	0.82 ± 0.02
LVID:d (mm)	4.10 ± 0.10	4.27 ± 0.08	4.43 ± 0.22	4.40 ± 0.09
LV Mass (g)	0.16 ± 0.01	0.17 ± 0.01	0.22 ± 0.01*	0.23 ± 0.01*
LV Mass/BW	0.60 ± 0.01	0.59 ± 0.01	0.69 ± 0.03*	0.70 ± 0.03*

In vivo cardiac function and ventricular wall measurements were assessed via ultrasound echocardiography (VisualSonics Vevo 770) in isoflurane anesthetized WT and MCD-/- mice (n = 5). Values represent means ± SE. Differences were determined using a two-way ANOVA followed by a Bonferroni post-hoc analysis. *$P<0.05$, significantly different from young counterpart. d = diastole, EF = ejection fraction, LV = left ventricular, LVID = LV internal diameter, LVPW = LV posterior wall.

Figure 8-1: *MCD-/- mice have a prolonged lifespan.*

A: Kaplan-Meier survival curve analysis of MCD-/- mice (n = 16, both males and females) and their WT littermates (n = 8, both males and females). B: Body weight, and C: organ weight in aged male WT and MCD-/- mice. D: Body weight, and E: organ weight in aged female WT and MCD-/- mice. Values represent mean ± SE (n = 7-10). Differences were determined via Kaplan-Meier survival curve analysis. **P*<0.05, significantly different from WT mice.

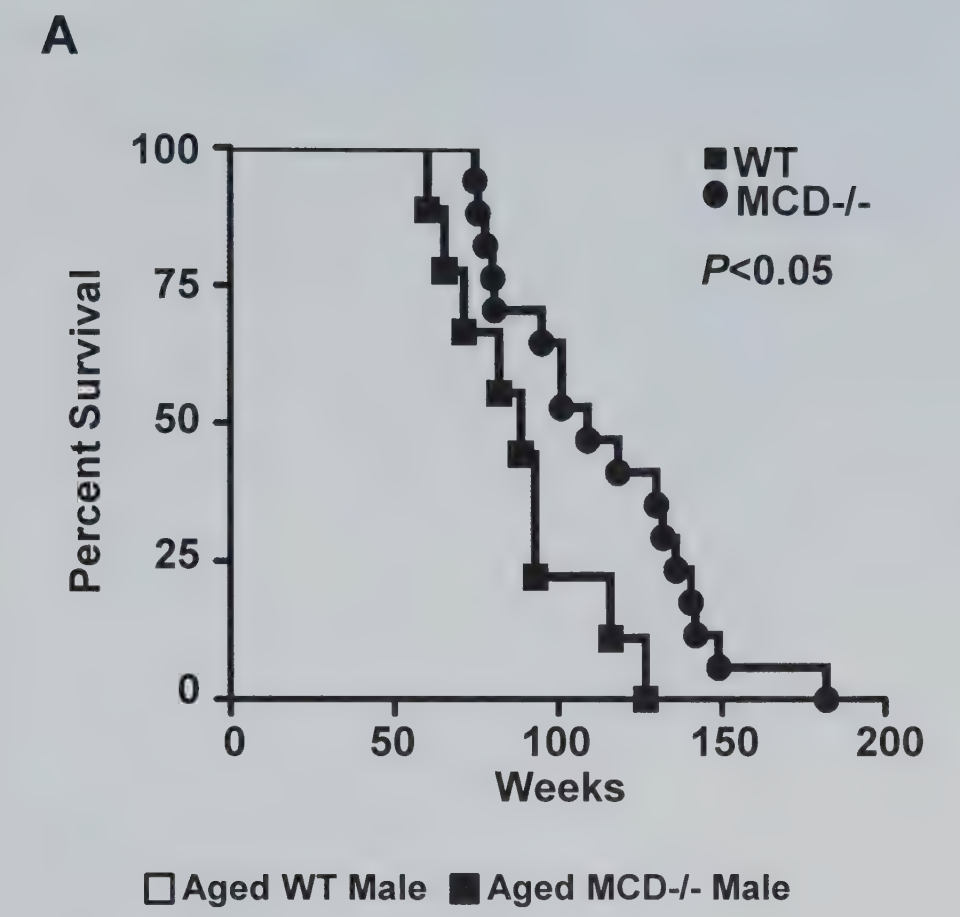
A
100
75
50
25
0
Percent Survival
0
50
100
150
200
Weeks
WT
MCD-/-
P<0.05
Aged WT Male
Aged MCD-/- Male
B
39
26
13
0
Body wt (g)
C
6
4
2
0
% of body wt
Liver
Epididymal Fat
Perirenal Fat

FIGURE 8-1

Figure 8-1: *MCD-/- mice have a prolonged lifespan.*

A: Kaplan-Meier survival curve analysis of MCD-/- mice (n = 16, both males and females) and their WT littermates (n = 8, both males and females). B: Body weight, and C: organ weight in aged male WT and MCD-/- mice. **D: Body weight, and E: organ weight in aged female WT and MCD-/- mice.** Values represent mean ± SE (n = 7-10). Differences were determined using a two-tailed Student's *t*-test. $*P<0.05$, significantly different from sex-matched WT littermate.

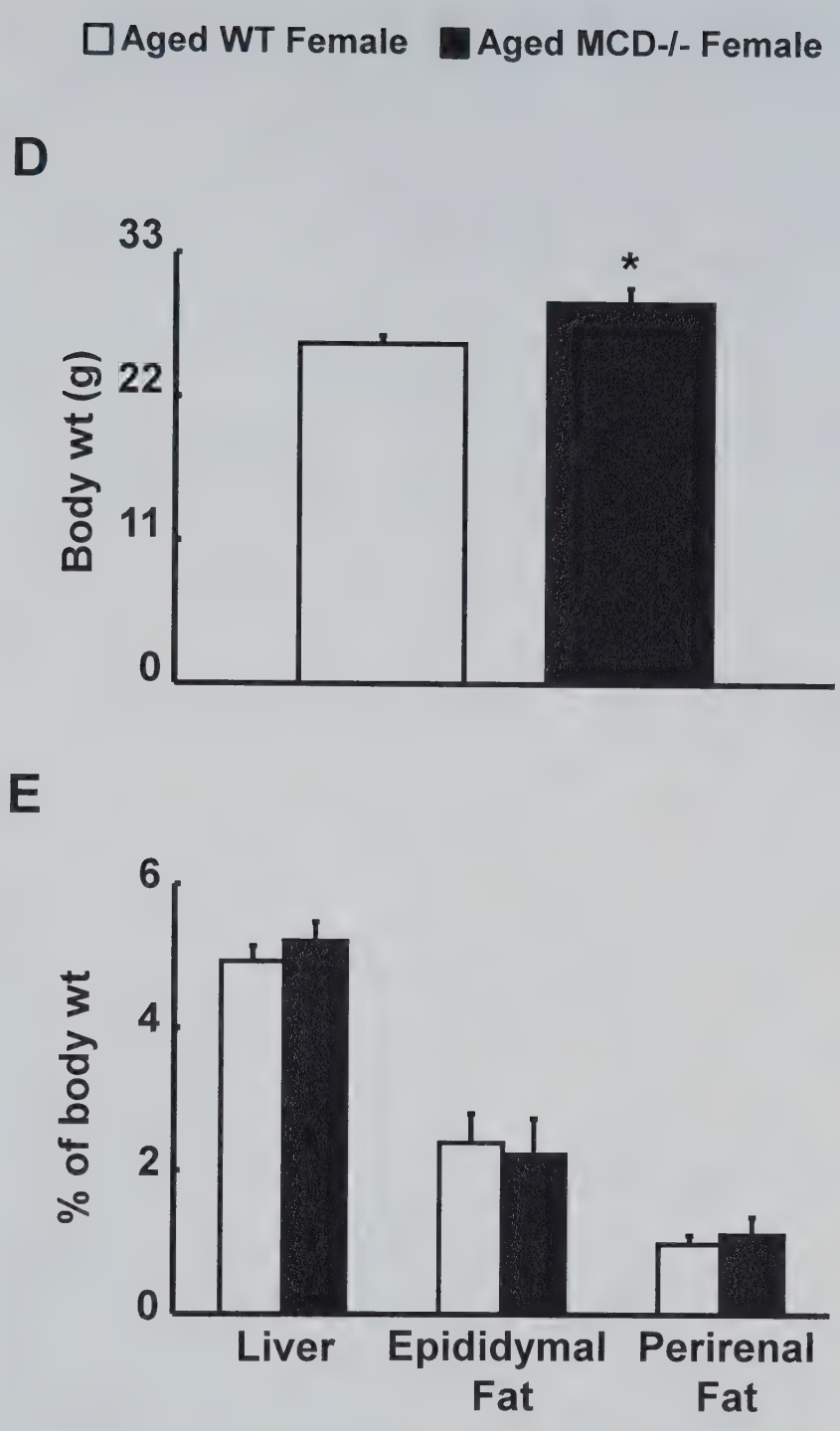
Aged WT Female
Aged MCD-/- Female
D
33
22
11
0
Body wt (g)
*
E
6
4
2
0
% of body wt
Liver
Epididymal Fat
Perirenal Fat

FIGURE 8-1

Figure 8-2: *Insulin sensitivity, oxygen consumption rates, and intramyocellular lipid metabolite accumulation in aged WT and MCD-/- mice.*

A: Glucose tolerance, and B: insulin tolerance in aged male WT and MCD-/- mice. C: 24 hr respiratory exchange ratio, and D: whole body oxygen consumption rates in aged male WT and MCD-/- mice. E: Triacylglycerol, F: long chain acyl CoA, G: diacylglycerol, and H: ceramide content in gastrocnemius muscle of aged male WT and MCD-/- mice. Values represent mean ± SE (n = 5-10). Differences were determined using a two-way ANOVA followed by a Bonferroni post-hoc analysis. $^{\dagger}P<0.05$, significantly different from respective 0 min time point.

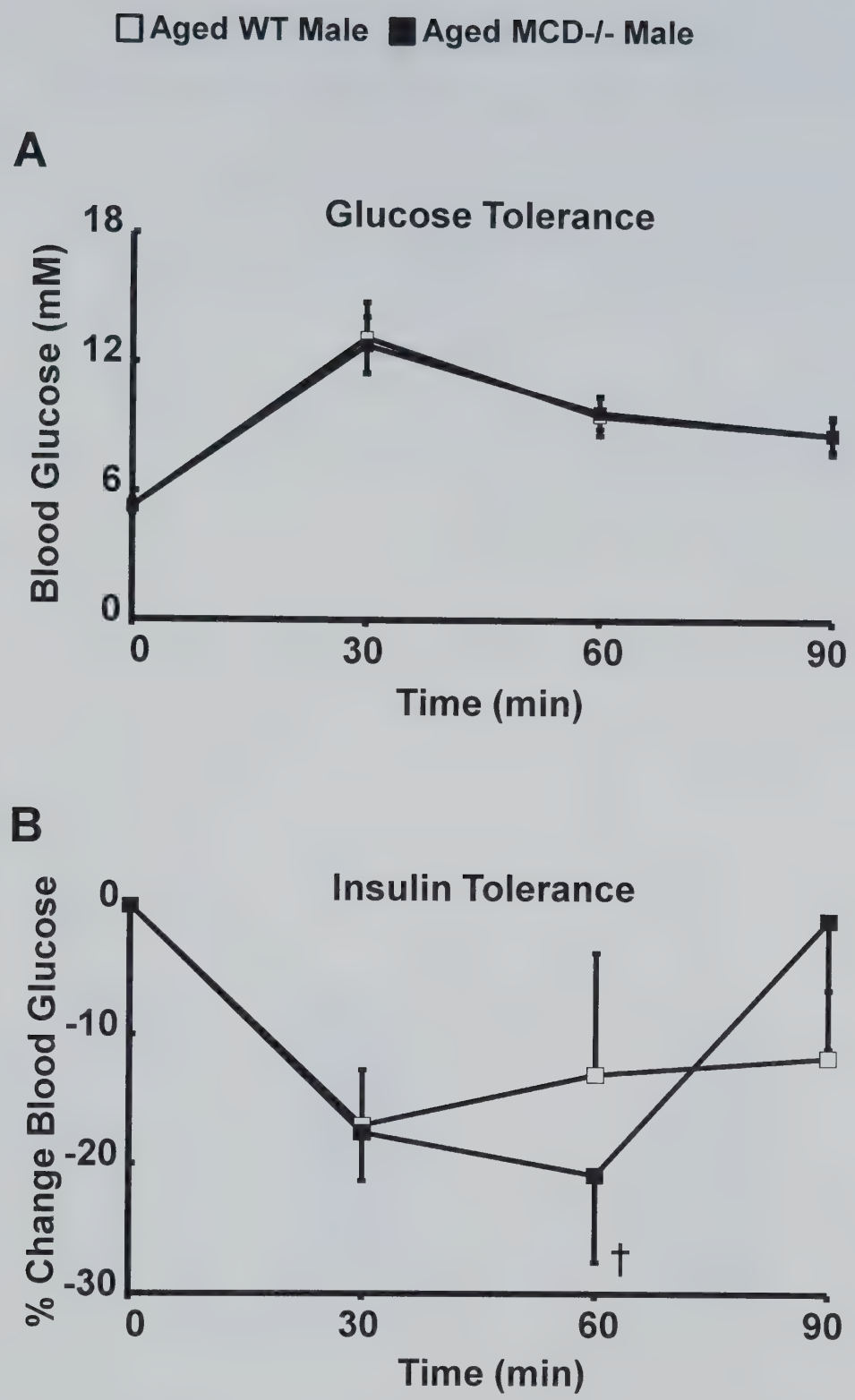
Aged WT Male
Aged MCD-/- Male
A
Glucose Tolerance
Blood Glucose (mM)
18
12
6
0
0
30
60
90
Time (min)
B
Insulin Tolerance
% Change Blood Glucose
0
-10
-20
-30
†
0
30
60
90
Time (min)

FIGURE 8-2

Figure 8-2: *Insulin sensitivity, oxygen consumption rates, and intramyocellular lipid metabolite accumulation in aged WT and MCD-/- mice.*

A: Glucose tolerance, and B: insulin tolerance in aged male WT and MCD-/- mice. **C: 24 hr respiratory exchange ratio (RER), and D: whole body oxygen consumption rates in aged male WT and MCD-/- mice.** E: Triacylglycerol, F: long chain acyl CoA, G: diacylglycerol, and H: ceramide content in gastrocnemius muscle of aged male WT and MCD-/- mice. Values represent mean ± SE (n = 5-10). Differences were determined using a two-way ANOVA followed by a Bonferroni post-hoc analysis. $*P<0.05$, significantly different from WT littermate.

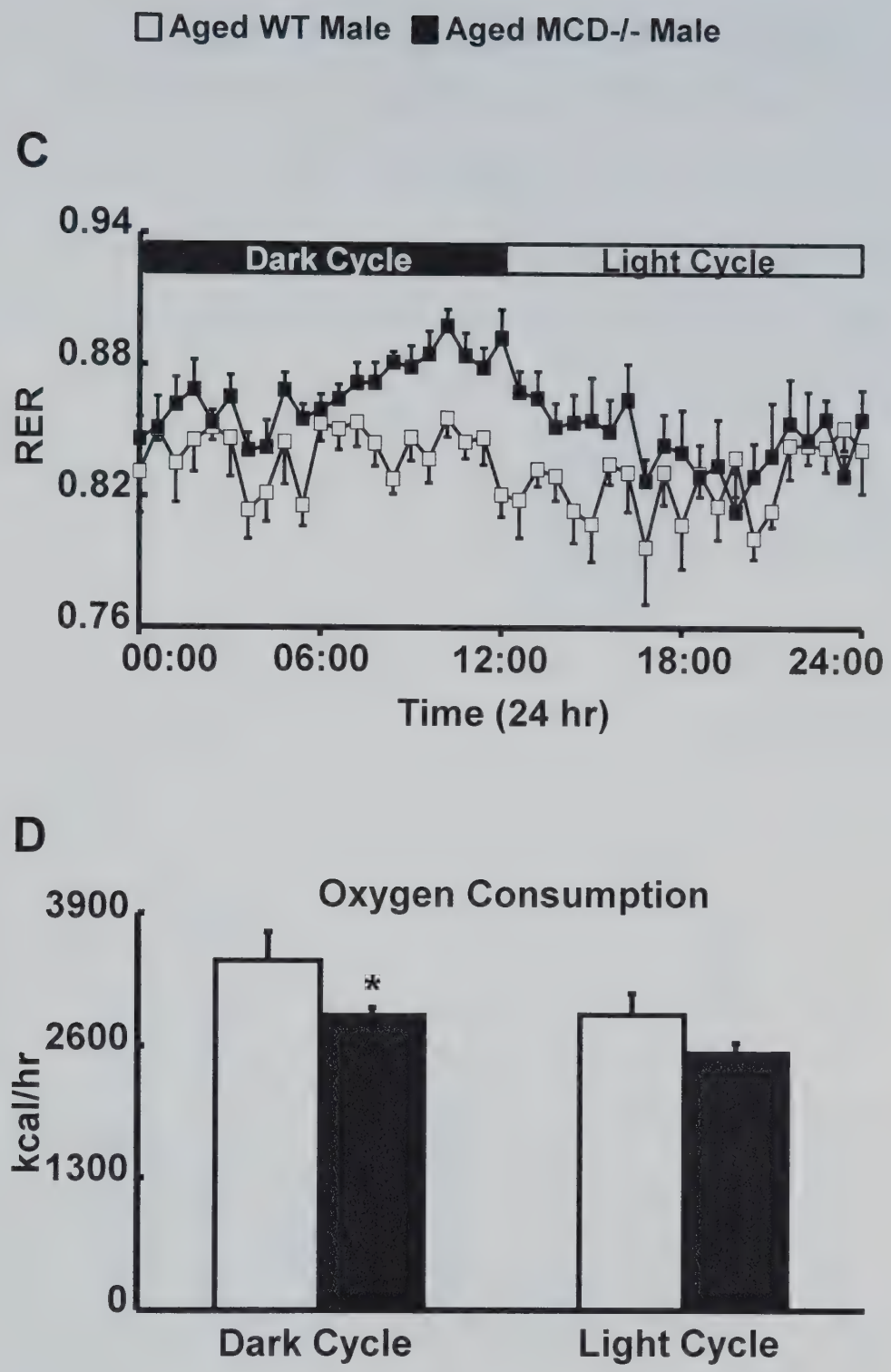
Aged WT Male
Aged MCD-/- Male
C
0.94
0.88
0.82
0.76
RER
Dark Cycle
Light Cycle
00:00
06:00
12:00
18:00
24:00
Time (24 hr)
D
Oxygen Consumption
3900
2600
1300
0
kcal/hr
*
Dark Cycle
Light Cycle

FIGURE 8-2

Figure 8-2: *Insulin sensitivity, oxygen consumption rates, and intramyocellular lipid metabolite accumulation in aged WT and MCD-/- mice.*

A: Glucose tolerance, and B: insulin tolerance in aged male WT and MCD-/- mice. C: 24 hr respiratory exchange ratio, and D: whole body oxygen consumption rates in aged male WT and MCD-/- mice. **E: Triacylglycerol, F: long chain acyl CoA,** G: diacylglycerol, and H: ceramide content in gastrocnemius muscle of aged male WT and MCD-/- mice. Values represent mean ± SE (n = 5-10). Differences were determined using a two-tailed Student's *t*-test. **P*<0.05, significantly different from WT littermate.

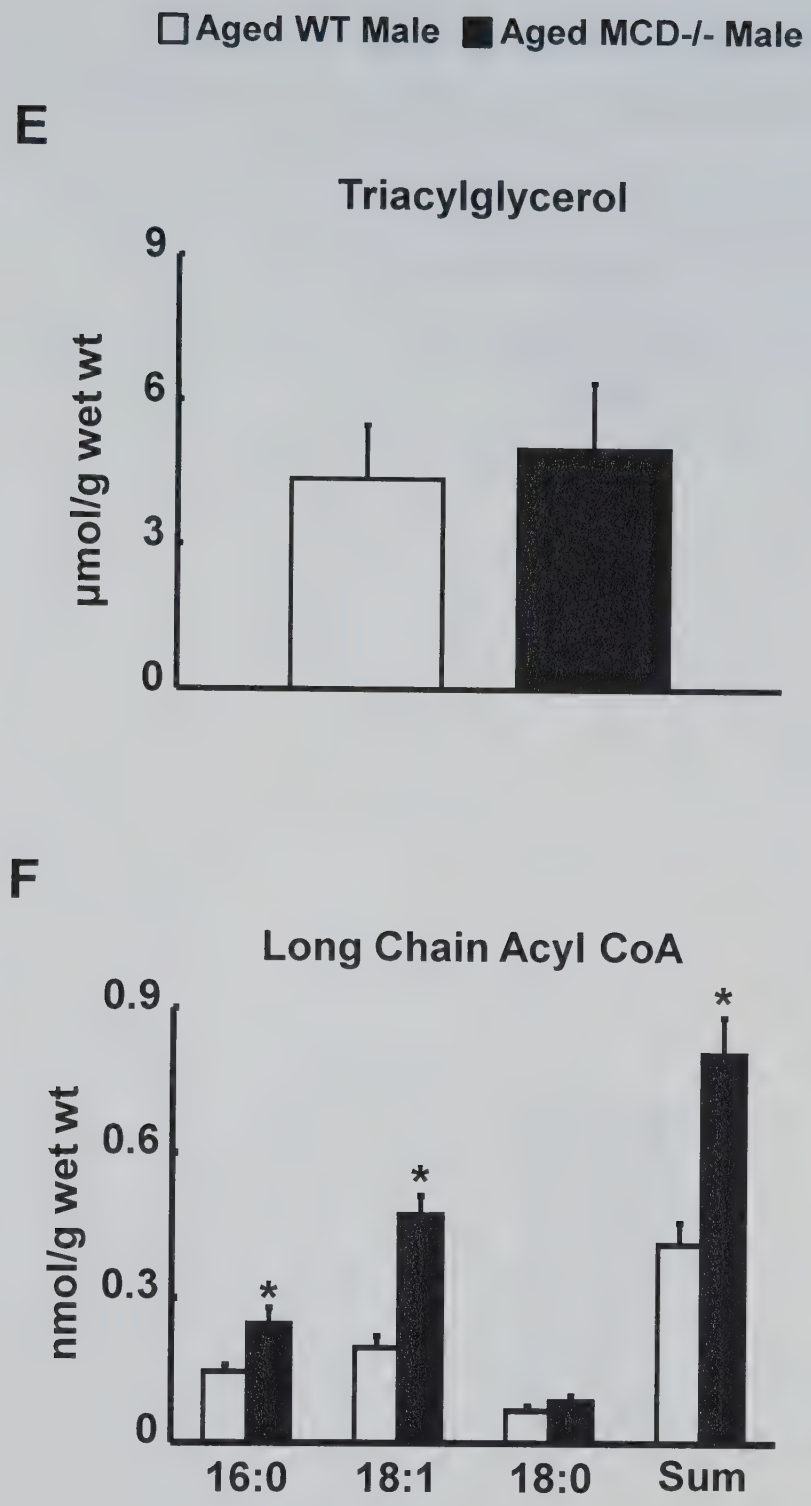
Aged WT Male
Aged MCD-/- Male
E
Triacylglycerol
µmol/g wet wt
9
6
3
0
F
Long Chain Acyl CoA
nmol/g wet wt
0.9
0.6
0.3
0
*
*
*
16:0
18:1
18:0
Sum

FIGURE 8-2

Figure 8-2: *Insulin sensitivity, oxygen consumption rates, and intramyocellular lipid metabolite accumulation in aged WT and MCD-/- mice.*

A: Glucose tolerance, and B: insulin tolerance in aged male WT and MCD-/- mice. C: 24 hr respiratory exchange ratio, and D: whole body oxygen consumption rates in aged male WT and MCD-/- mice. E: Triacylglycerol, F: long chain acyl CoA, **G: diacylglycerol, and H: ceramide content in gastrocnemius muscle of aged male WT and MCD-/- mice.** Values represent mean ± SE (n = 5-10).

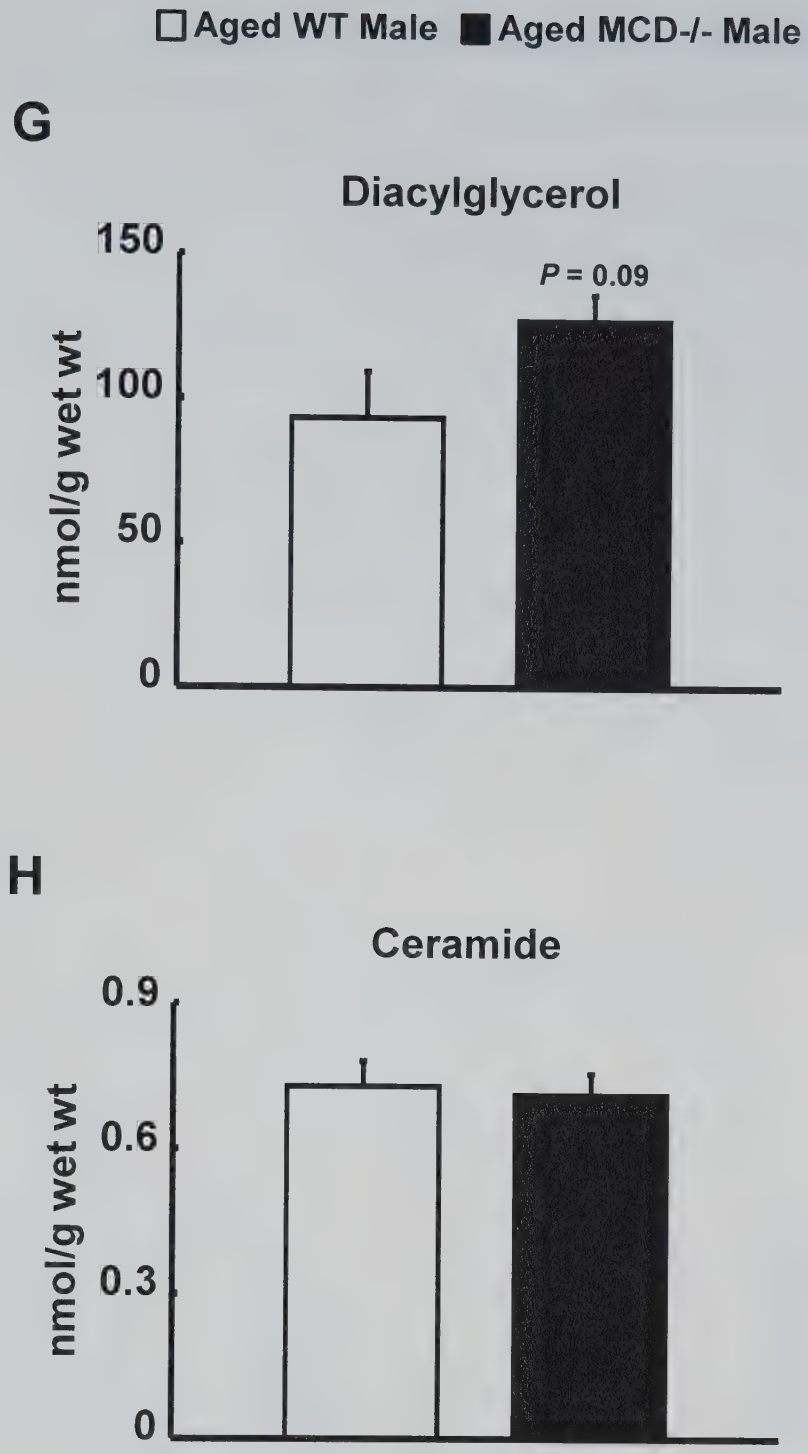
Aged WT Male
Aged MCD-/- Male
G
Diacylglycerol
150
100
50
0
nmol/g wet wt
P = 0.09
H
Ceramide
0.9
0.6
0.3
0
nmol/g wet wt

FIGURE 8-2

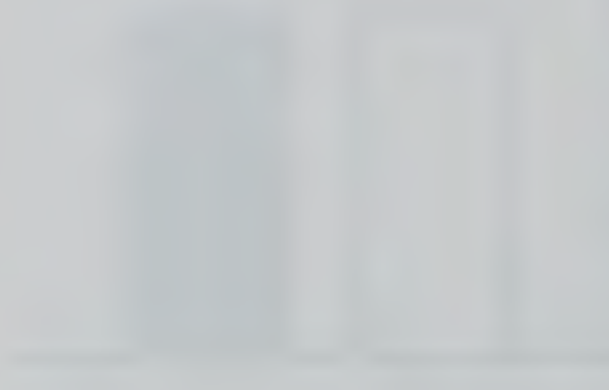

Figure 8-3: *Improved insulin tolerance in aged female MCD-/- mice.*

A: Insulin tolerance is improved in aged female MCD-/- mice **(It should be noted that after the 60 min time point, 3 of the aged female MCD-/- mice had to be removed from the experiment due to hypoglycemia (blood glucose below 2.0 mM), which skewed the average of the 90 min time point in the female MCD-/- mice)**. B: Despite these improvements in insulin sensitivity, aged female MCD-/- mice were less active than their WT littermates. Values represent mean ± SE (n = 6-7). Differences were determined using either a two-tailed Student's *t*-test or a two-way ANOVA followed by a Bonferroni post-hoc analysis. $*P<0.05$, significantly different from WT littermate.

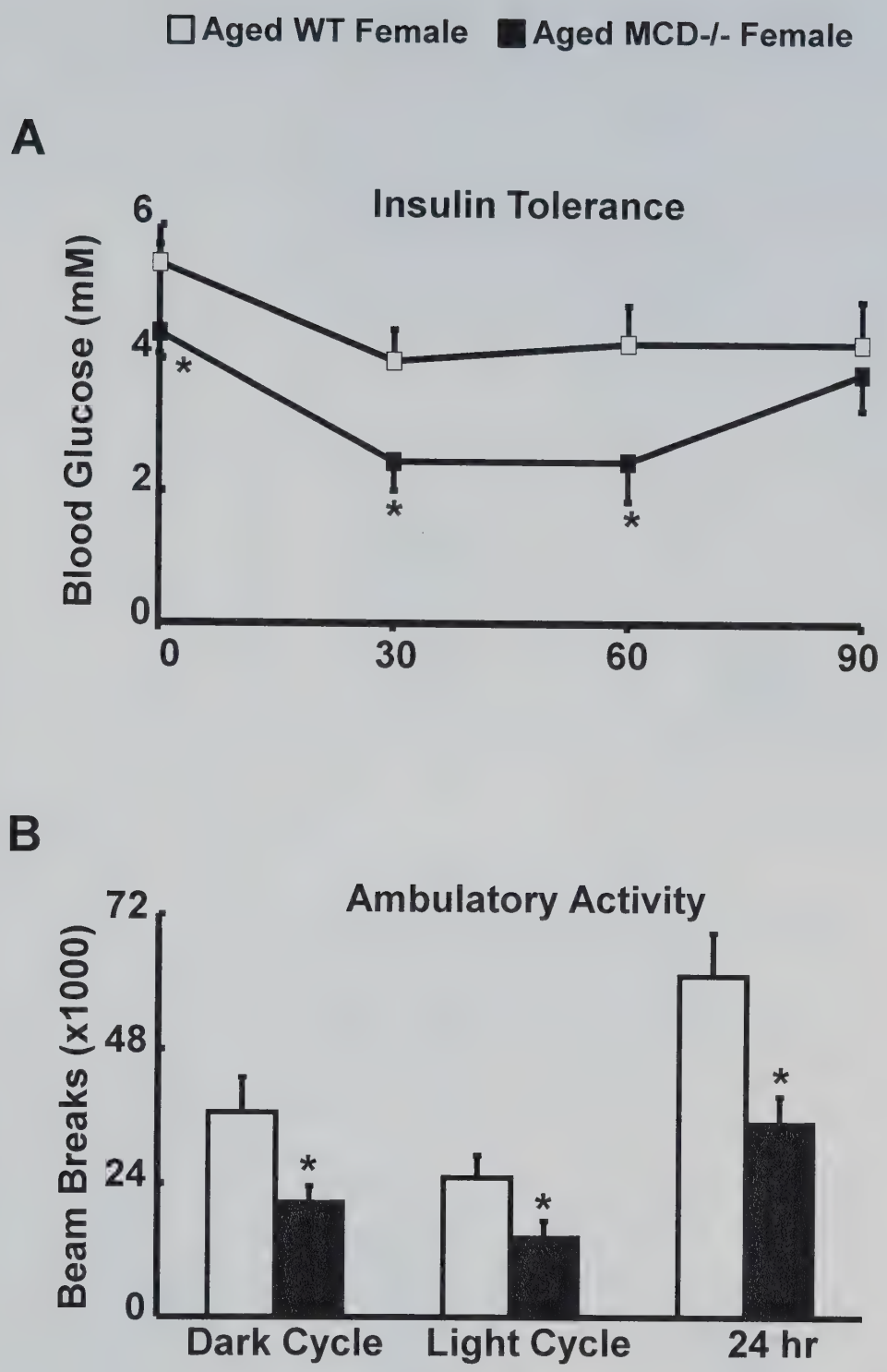
Aged WT Female
Aged MCD-/- Female
A
Insulin Tolerance
Blood Glucose (mM)
6
4
2
0
0
30
60
90
*
*
*
B
Ambulatory Activity
Beam Breaks (x1000)
72
48
24
0
*
*
*
Dark Cycle
Light Cycle
24 hr

FIGURE 8-3

Figure 8-4: *Insulin signaling pathway in aged male WT and MCD-/- mice.*

A: Akt serine 473 phosphorylation, and B: GSK3 serine 9 phosphorylation in gastrocnemius muscle of young and aged male WT and MCD-/- mice. Values represent mean ± SE (n = 5-6). Differences were determined by the use of a two-way ANOVA followed by a Bonferroni post-hoc analysis. $*P<0.05$, significantly different young, genotype-matched counterpart.

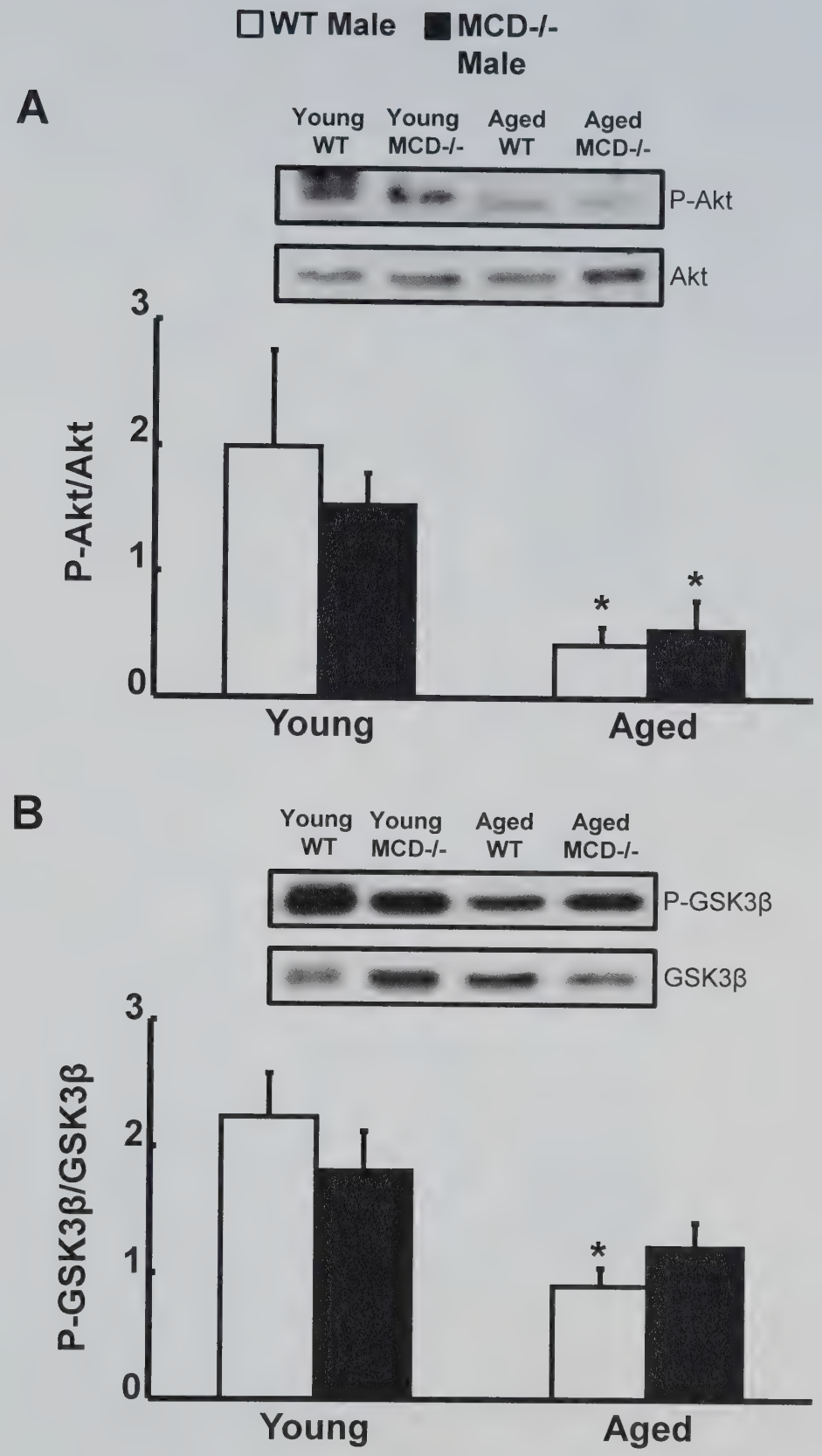
WT Male
MCD-/- Male
A
Young WT
Young MCD-/-
Aged WT
Aged MCD-/-
P-Akt
Akt
P-Akt/Akt
3
2
1
0
*
*
Young
Aged
B
Young WT
Young MCD-/-
Aged WT
Aged MCD-/-
P-GSK3β
GSK3β
P-GSK3β/GSK3β
3
2
1
0
*
Young
Aged

FIGURE 8-4

Figure 8-5: *Improved efficiency of contractile work in hearts from aged male MCD-/- mice.*

A: Cardiac power, B: palmitate oxidation rates, C: glucose oxidation rates, and D: efficiency in aged male WT and MCD-/- mice. Values represent mean ± SE (n = 8-10). Differences were determined using a two-tailed Student's *t*-test. **P*<0.05, significantly different from WT littermate.

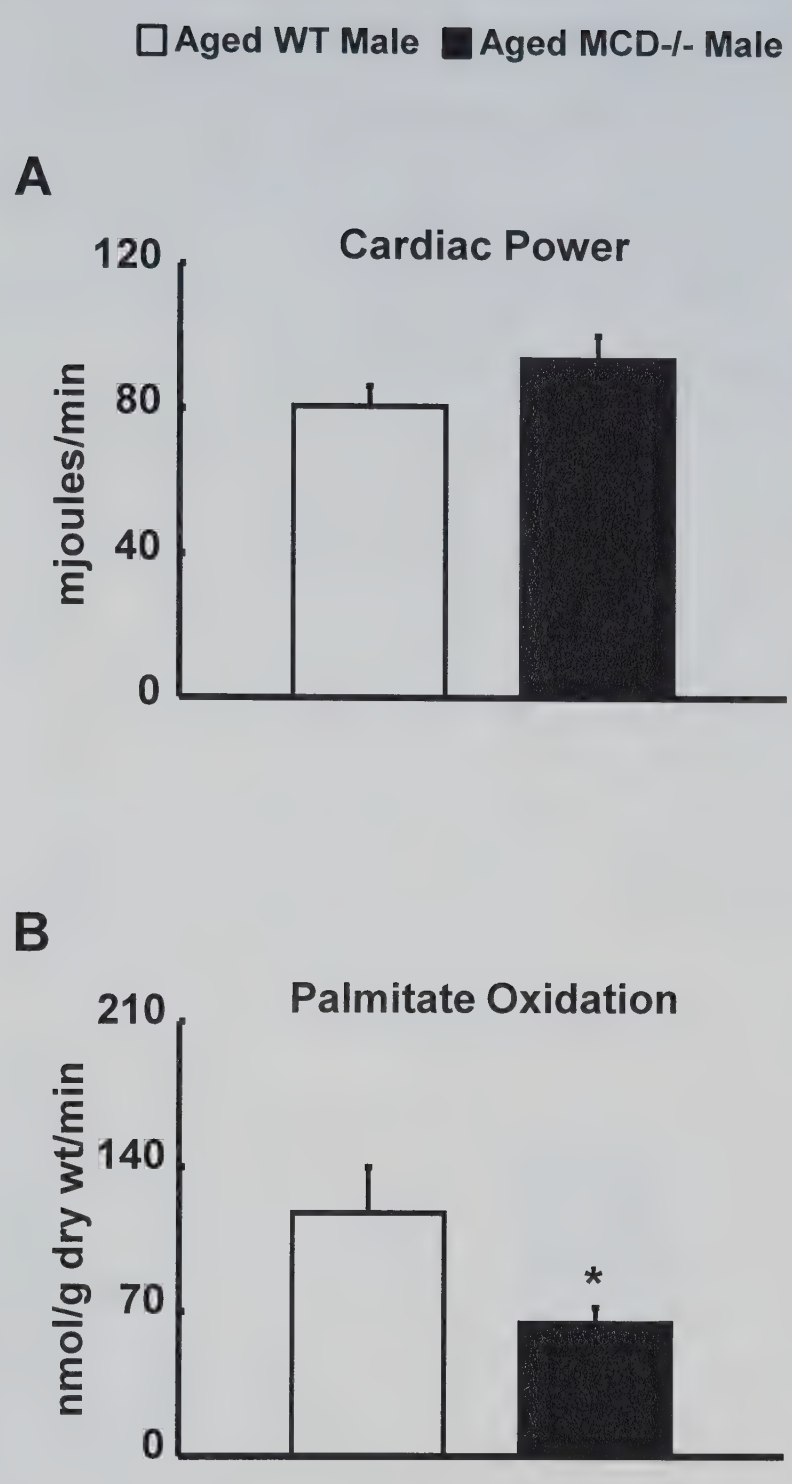
Aged WT Male
Aged MCD-/- Male
A
Cardiac Power
120
80
40
0
mjoules/min
B
Palmitate Oxidation
210
140
70
0
nmol/g dry wt/min
*

FIGURE 8-5

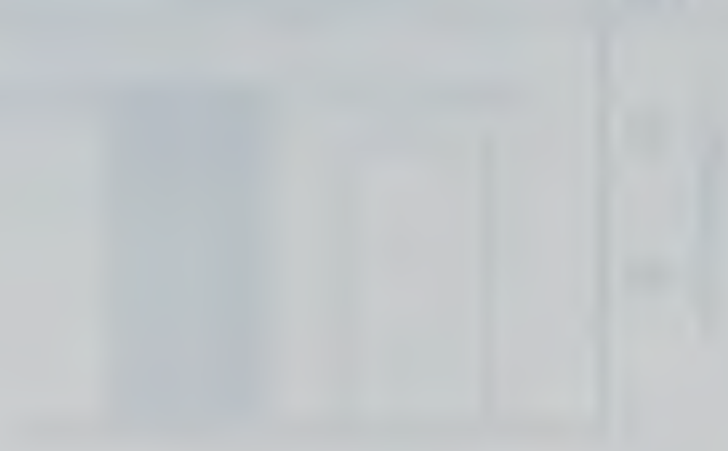

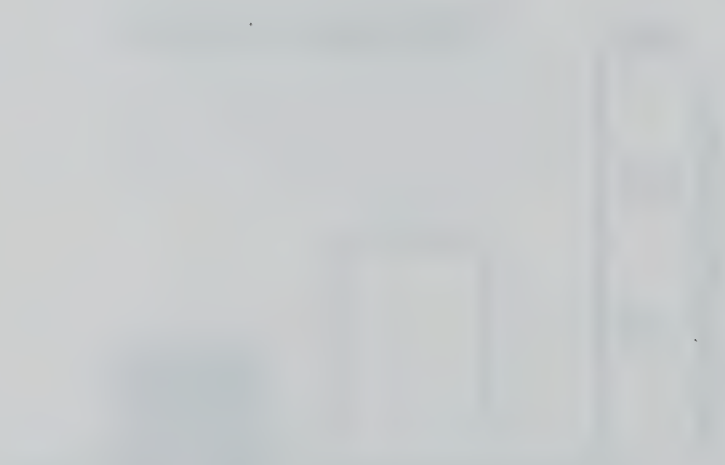

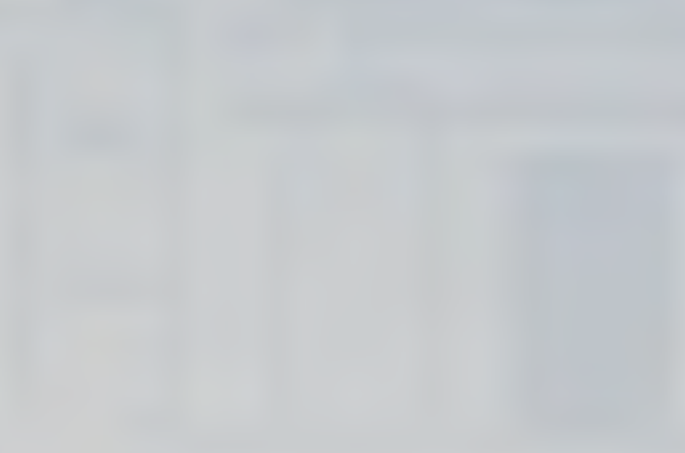

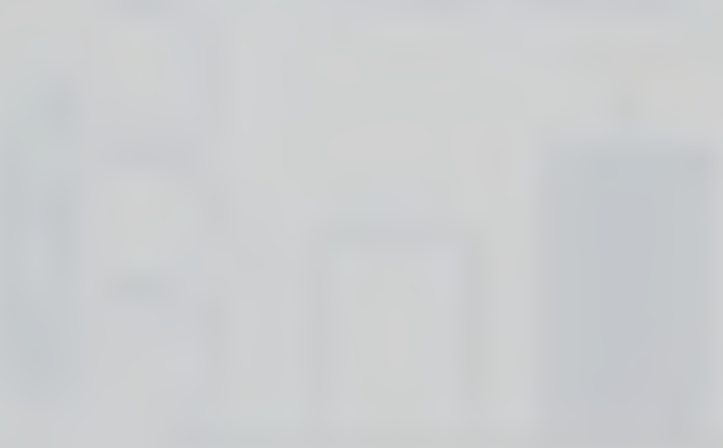

Figure 8-5: *Improved efficiency of contractile work in hearts from aged male MCD-/- mice.*

A: Cardiac power, B: palmitate oxidation rates, **C: glucose oxidation rates, and D: efficiency in aged male WT and MCD-/- mice.** Values represent mean ± SE (n = 8-10). Differences were determined using a two-tailed Student's *t*-test. **P*<0.05, significantly different from WT littermate.

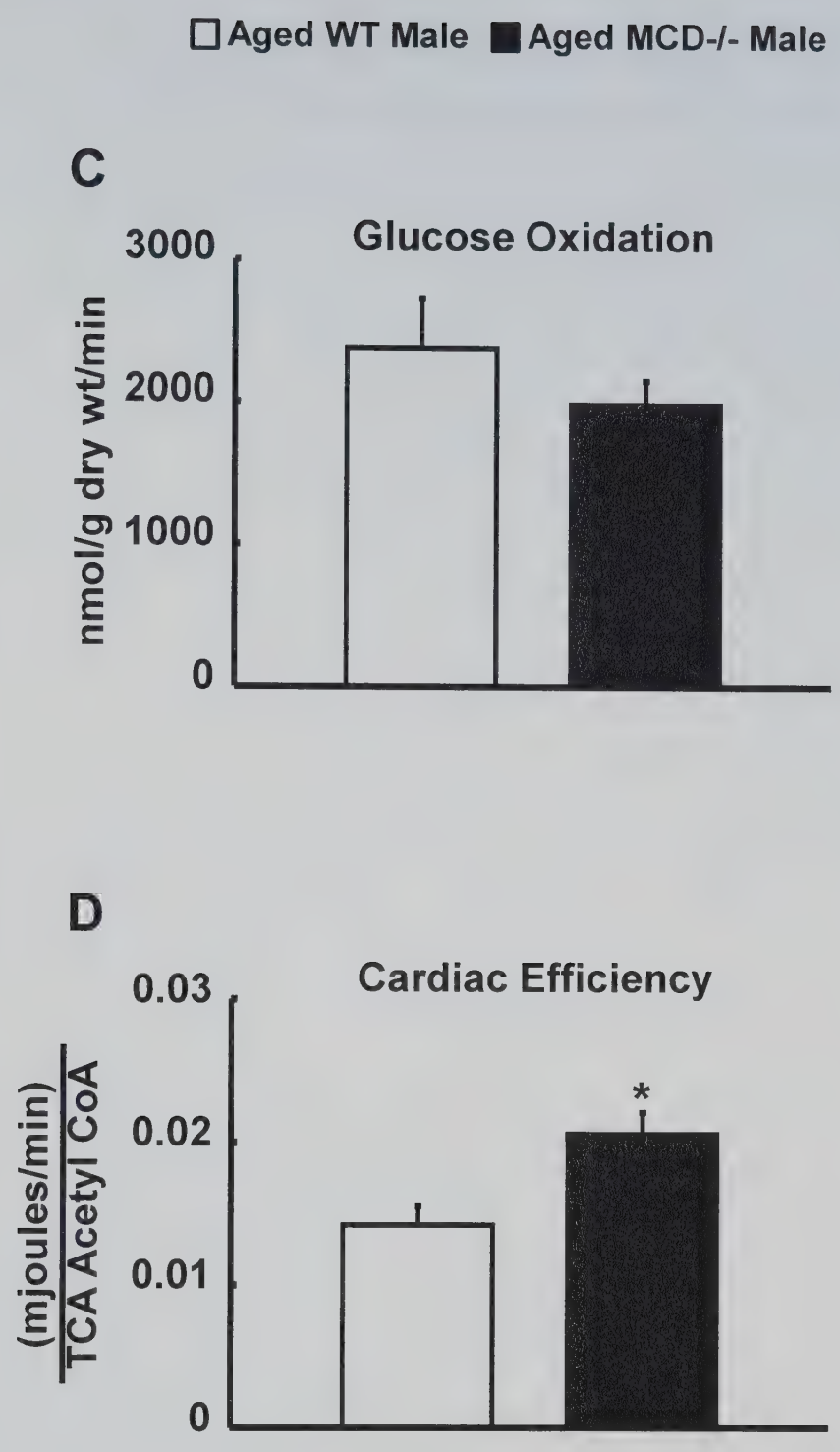
Aged WT Male
Aged MCD-/- Male
C
Glucose Oxidation
3000
2000
1000
0
nmol/g dry wt/min
D
Cardiac Efficiency
0.03
0.02
0.01
0
*
(mjoules/min)
TCA Acetyl CoA

FIGURE 8-5

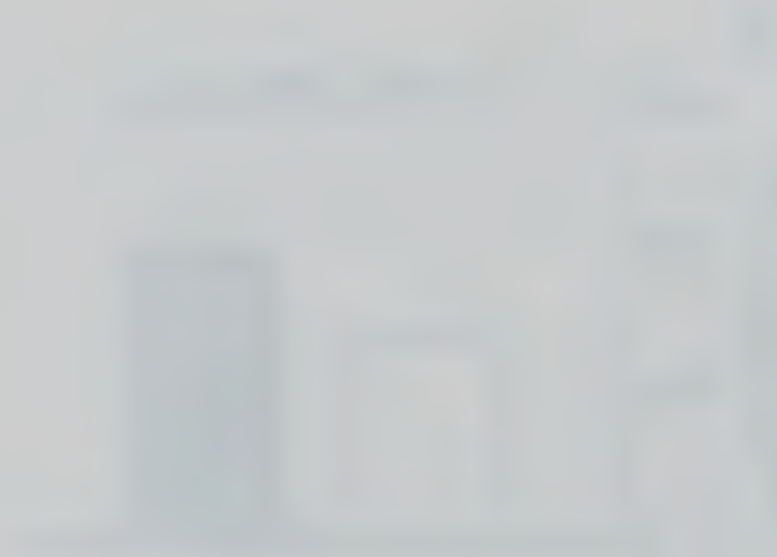

Figure 8-6: *Improved efficiency of contractile work in hearts from aged female MCD-/- mice.*

A: Cardiac power, B: palmitate oxidation rates, C: glucose oxidation rates, and D: efficiency in aged female WT and MCD-/- mice. Values represent mean ± SE (n = 8-10). Differences were determined using a two-tailed Student's *t*-test. **P*<0.05, significantly different from WT littermate.

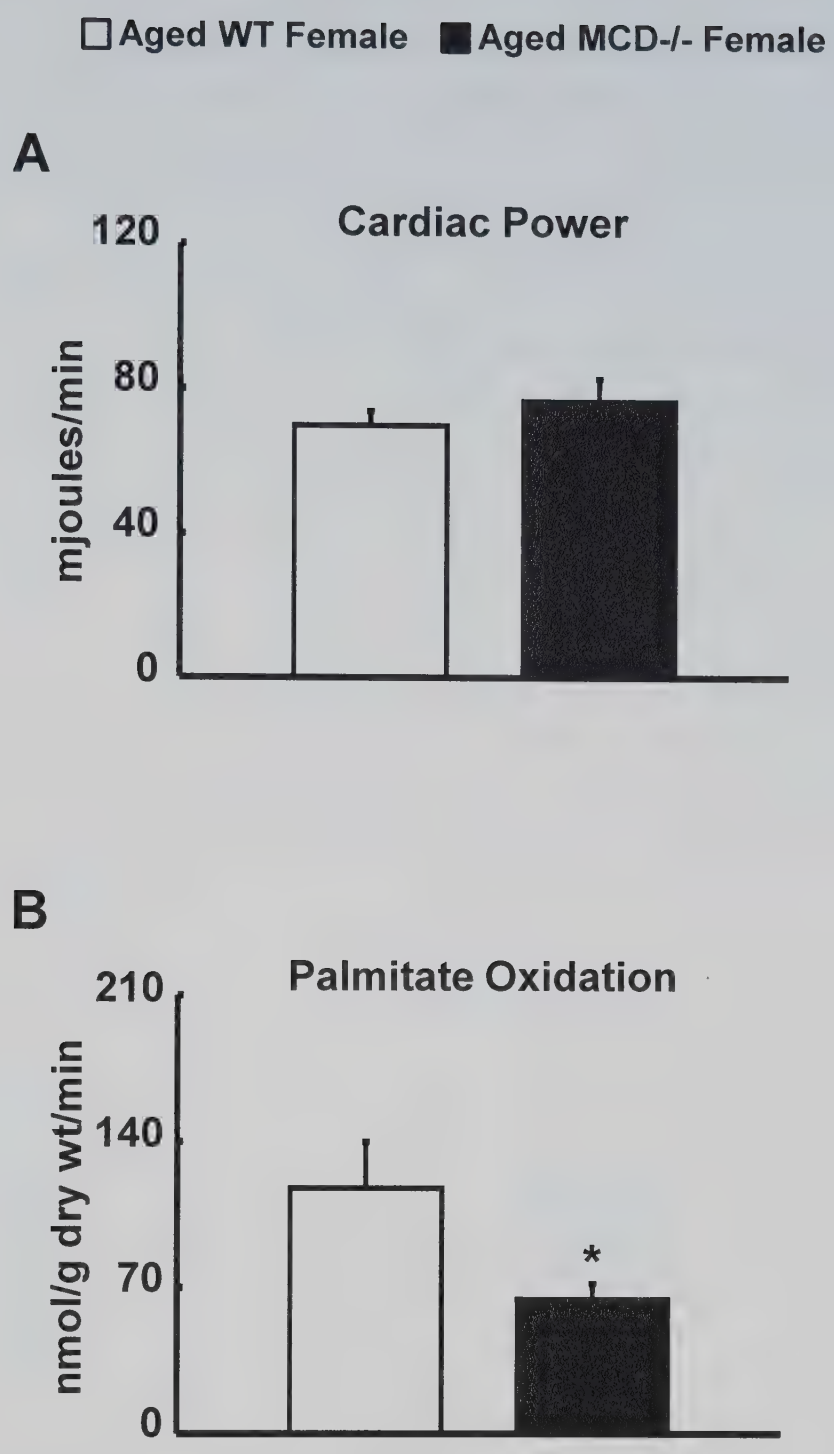
Aged WT Female
Aged MCD-/- Female
A
Cardiac Power
120
80
40
0
mjoules/min
B
Palmitate Oxidation
210
140
70
0
nmol/g dry wt/min
*

FIGURE 8-6

Figure 8-6: *Improved efficiency of contractile work in hearts from aged female MCD-/- mice.*

A: Cardiac power, B: palmitate oxidation rates, **C: glucose oxidation rates, and D: efficiency in aged female WT and MCD-/- mice.** Values represent mean ± SE (n = 8-10). Differences were determined using a two-tailed Student's *t*-test. **P*<0.05, significantly different from WT littermate.

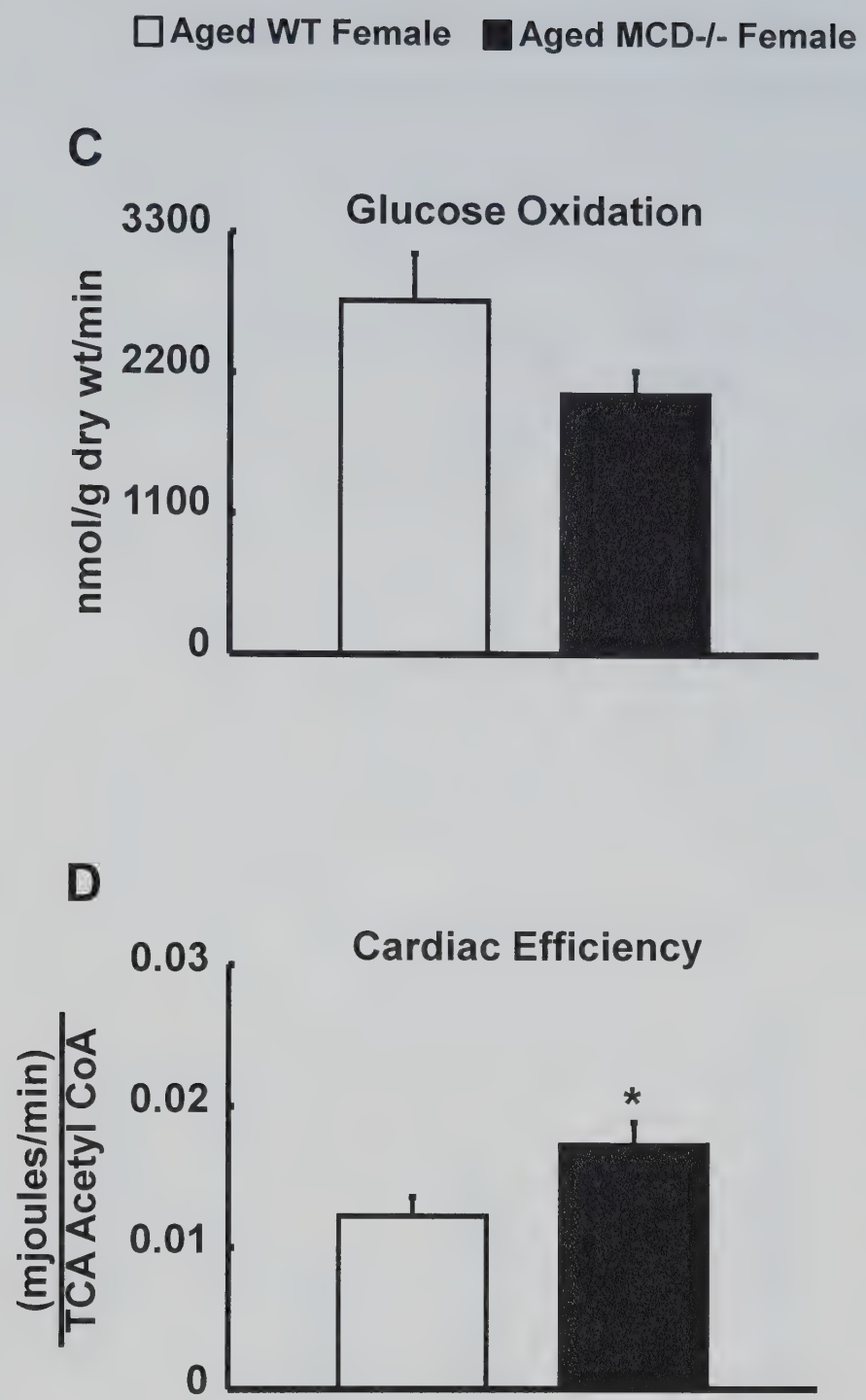
Aged WT Female
Aged MCD-/- Female
C
Glucose Oxidation
3300
2200
1100
0
nmol/g dry wt/min
D
Cardiac Efficiency
0.03
0.02
0.01
0
*
(mjoules/min)
TCA Acetyl CoA

FIGURE 8-6

Figure 8-7: *Intrahepatic lipid metabolite accumulation and hepatic insulin signaling in aged WT and MCD-/- mice.*

A: Triacylglycerol, B: long chain acyl CoA, C: diacylglycerol, and D: ceramide content in livers of aged male WT and MCD-/- mice. E: Akt serine 473, and F: GSK3β serine 9 phosphorylation in livers of aged male WT and MCD-/- mice. Values represent mean ± SE (n = 5-6). Differences were determined using a two-tailed Student's *t*-test. **P*<0.05, significantly different from WT littermate.

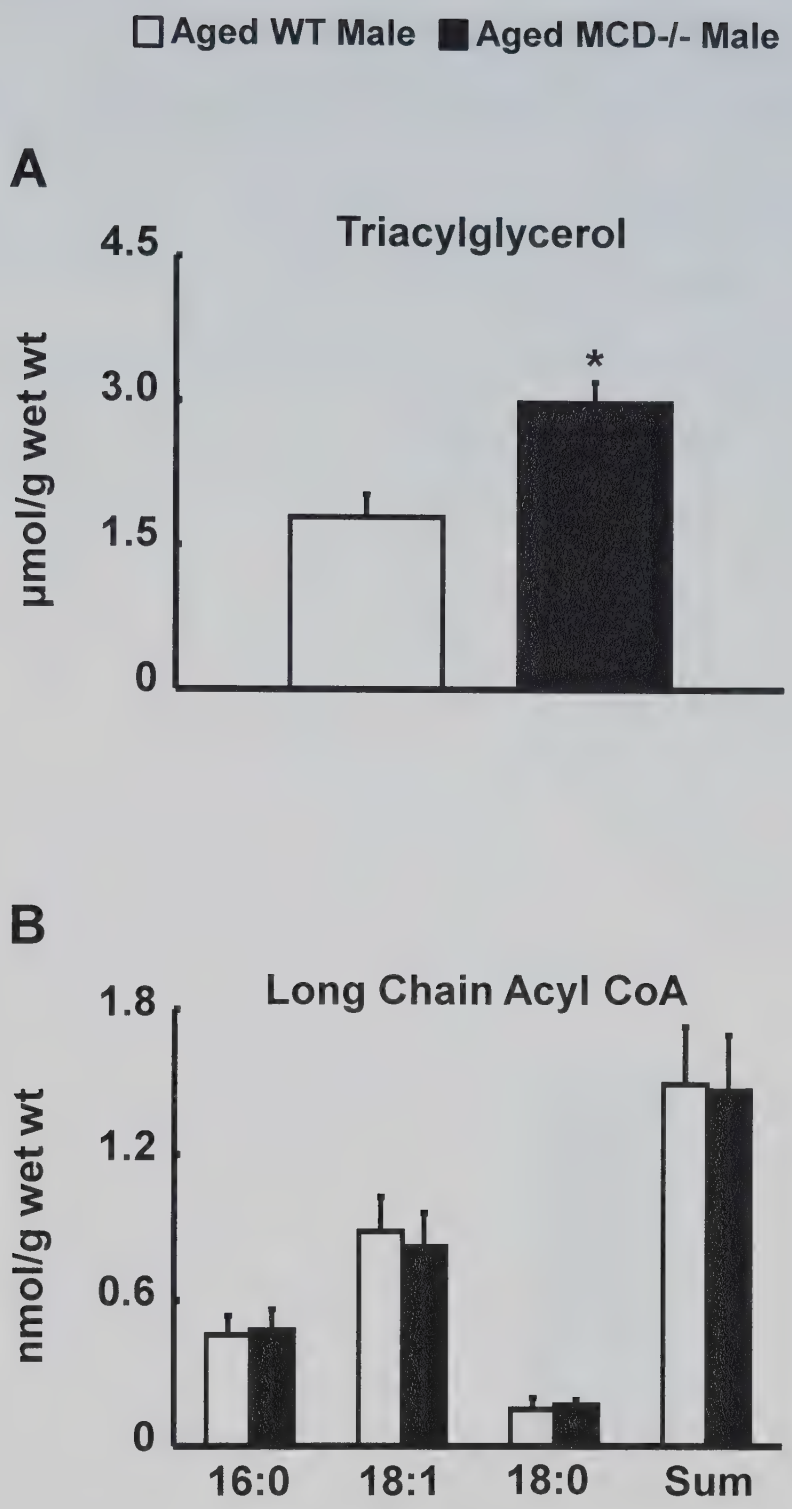
Aged WT Male
Aged MCD-/- Male
A
Triacylglycerol
µmol/g wet wt
4.5
3.0
1.5
0
*
B
Long Chain Acyl CoA
nmol/g wet wt
1.8
1.2
0.6
0
16:0
18:1
18:0
Sum

FIGURE 8-7

Figure 8-7: *Intrahepatic lipid metabolite accumulation and hepatic insulin signaling in aged WT and MCD-/- mice.*

A: Triacylglycerol, B: long chain acyl CoA, **C: diacylglycerol, and D: ceramide content in livers of aged male WT and MCD-/- mice.** E: Akt serine 473, and F: GSK3β serine 9 phosphorylation in livers of aged male WT and MCD-/- mice. Values represent mean ± SE (n = 5-6). Differences were determined using a two-tailed Student's *t*-test. **P*<0.05, significantly different from WT littermate.

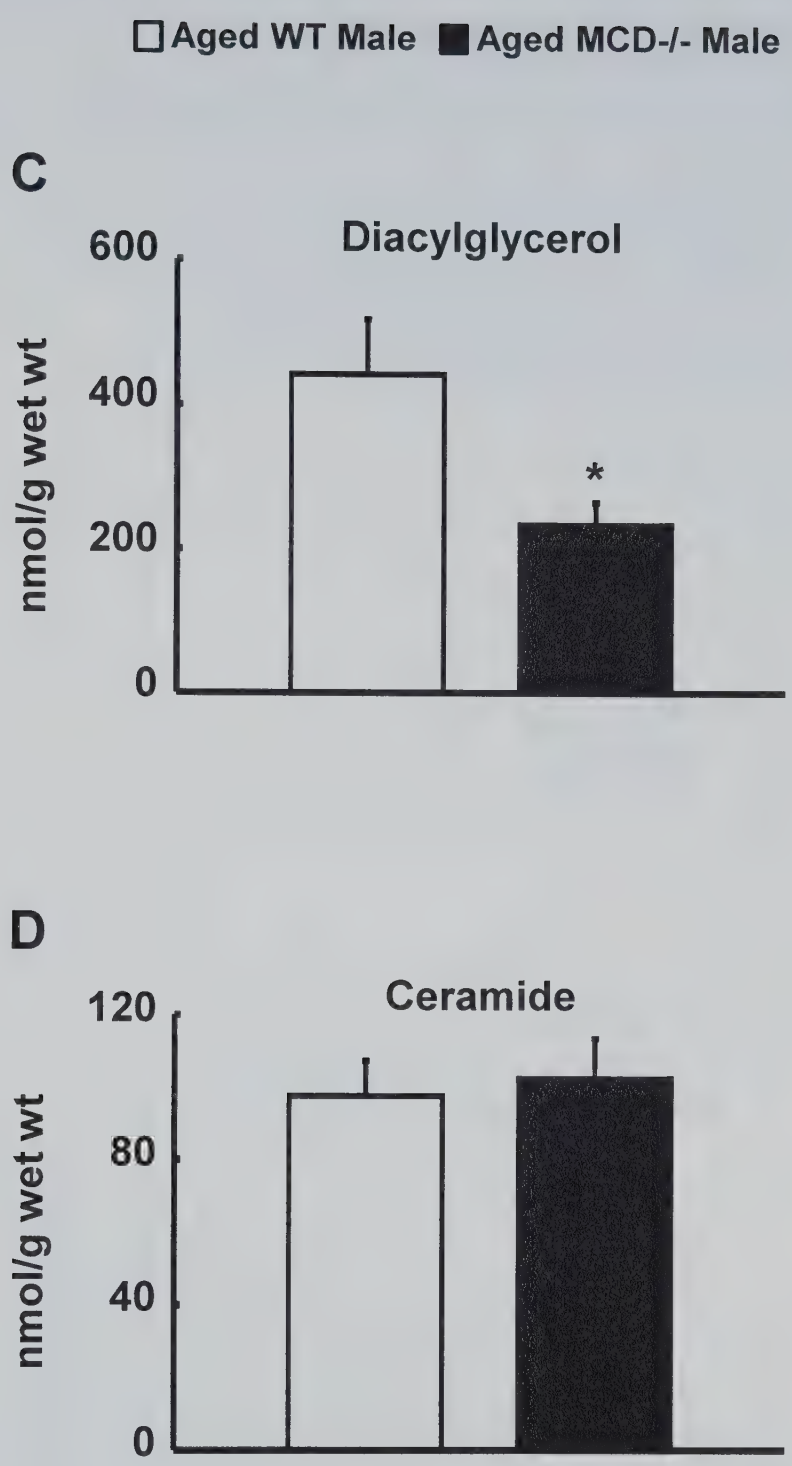
Aged WT Male
Aged MCD-/- Male
C
Diacylglycerol
600
400
200
0
nmol/g wet wt
*
D
Ceramide
120
80
40
0
nmol/g wet wt

FIGURE 8-7

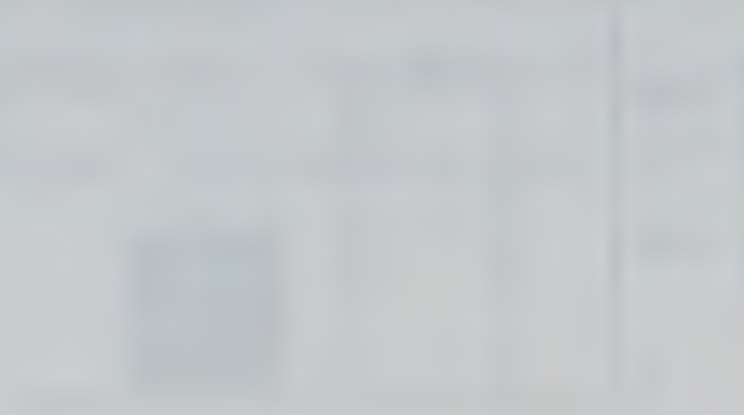

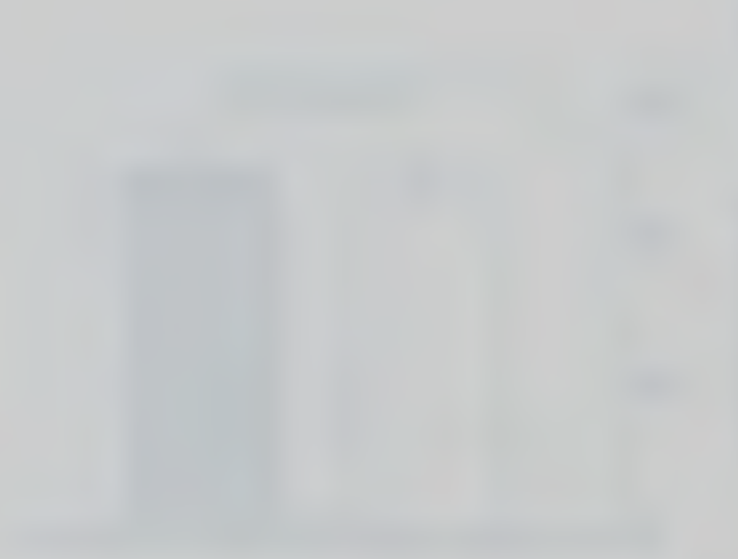

Figure 8-7: *Intrahepatic lipid metabolite accumulation and hepatic insulin signaling in aged WT and MCD-/- mice.*

A: Triacylglycerol, B: long chain acyl CoA, C: diacylglycerol, and D: ceramide content in livers of aged male WT and MCD-/- mice. **E: Akt serine 473, and F: GSK3β serine 9 phosphorylation in livers of aged male WT and MCD-/- mice.** Values represent mean ± SE (n = 5-6).

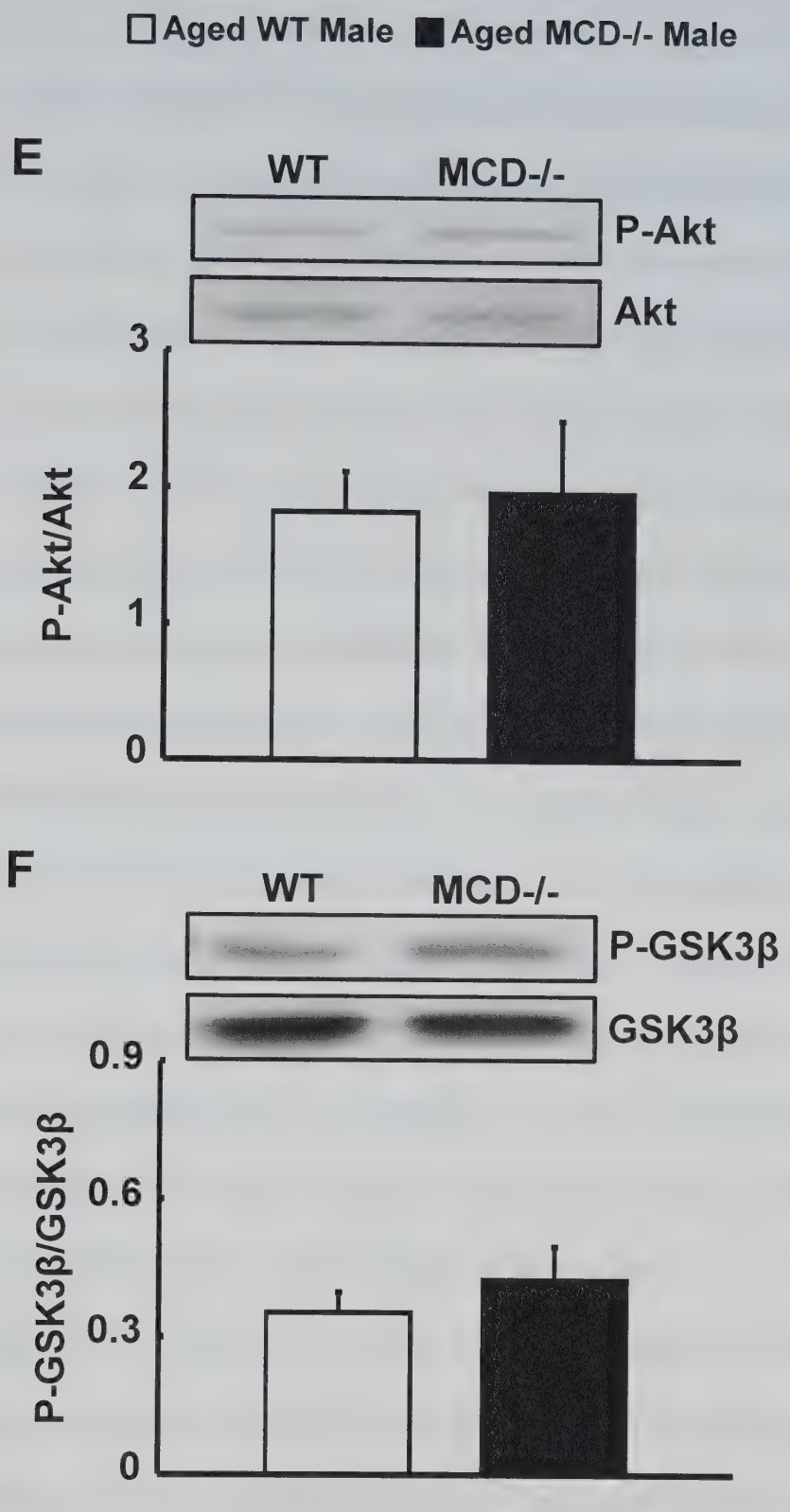
Aged WT Male
Aged MCD-/- Male
E
WT
MCD-/-
P-Akt
Akt
P-Akt/Akt
3
2
1
0
F
WT
MCD-/-
P-GSK3β
GSK3β
P-GSK3β/GSK3β
0.9
0.6
0.3
0

FIGURE 8-7

Recent studies postulate that an impairment in mitochondrial fatty acid oxidation is responsible for the accumulation of intramyocellular lipid metabolites that interfere with insulin signaling and contribute to the development of glucose intolerance and insulin resistance in our elderly population (99, 303, 305, 321). Furthermore, as an individual ages, he/she increases their risk of developing cardiovascular diseases such as heart failure, where it has also been postulated that an impairment in mitochondrial fatty acid oxidation leads to intra-myocardial lipid metabolite accumulation that contributes to contractile dysfunction (239, 373). Finally, the elderly population is often at risk of sedentary behavior and subsequent obesity (99), increasing the risk of developing hepatic steatosis and non-alcoholic fatty liver disease, which a reduction in mitochondrial fatty acid oxidation may also contribute towards (15, 280, 353, 447). Therefore, MCD-/- mice, which have decreased mitochondrial fatty acid oxidation rates and overall oxidative capacity, should be at an increased risk for developing insulin resistance, heart failure, and hepatic steatosis. All of these risks in combination would be expected to shorten the overall lifespan of these animals.

In contrast, MCD-/- mice displayed a significant increase in lifespan of ~30%, which was unexpected based on their lower overall oxidative capacity. However, we have previously shown that MCD-/- mice are actually protected from obesity-induced skeletal muscle and cardiac insulin resistance, which may arise from a reduction in the incomplete oxidation of fatty acids observed during

obesity (202, 400). The incomplete oxidation of fatty acids seen with obesity results from the TCA cycle not being able to keep up with the increased rates of acetyl CoA delivery arriving from the increased oxidation of fatty acids (200, 202, 280, 393). Interestingly, in the study by Petersen *et al.* (303) where it was demonstrated that a decreased oxidative metabolism contributes to the intramyocellular lipid metabolite accumulation and insulin resistance in elderly patients, TCA cycle activity was also reduced. Thus, it is possible that incomplete fatty acid oxidation contributes to the insulin resistance in elderly patients, and may explain why the effects of insulin on blood glucose levels are improved in aged MCD-/- mice. In accordance with this statement, a recent study in human patients has demonstrated increased rates of incomplete fatty acid oxidation in type 2 diabetic African-American women (6).

In regards to the increased risk of cardiovascular disease and heart failure in our elderly population, reductions in myocardial fatty acid oxidation in MCD-/- mice would be predicted to energy starve the heart and predispose them to the development of heart failure (239, 286, 382). In contrast, aged MCD-/- mice displayed no signs of cardiac dysfunction and actually showed an improved efficiency of converting energy metabolism into contractile work. This is in support of our previous findings showing that improving cardiac efficiency can improve functional outcomes following I/R (93, 229, 230, 233), and delays the progression to severe, decompensated heart failure in MCD-/- mice subjected to chronic ischemia via permanent LAD ligation (unpublished data). Furthermore, inhibiting myocardial fatty acid oxidation may also improve the efficiency of

contractile function by increasing the coupling of glucose oxidation and glycolysis, which decreases H^+ production from uncoupled glucose metabolism and subsequent intracellular acidosis (172, 229, 233). Unfortunately, we were not able to measure glycolytic rates in our isolated working heart perfusions, and cannot determine if this component also contributes to the improved cardiac efficiency observed in aged MCD-/- mice. Nonetheless, it is possible that improved cardiac efficiency in male MCD-/- mice delayed the eventual development of cardiovascular diseases such as heart failure with age, contributing to their prolonged lifespan.

Finally, another significant concern with an impairment in whole body fatty acid oxidation in the elderly population is that it may increase their risk of developing hepatic steatosis and non-alcoholic fatty liver disease (15, 353, 447). Surprisingly, liver weights were not different between aged WT and MCD-/- mice, and although intrahepatic TAG content was greater in aged MCD-/- mice, they had a subsequent reduction in intrahepatic DAG content. This finding is of particular interest, as DAG accumulation has been proposed to be a key player in the development of hepatic insulin resistance and the elevated rates of endogenous glucose production observed in elderly patients and those with type 2 diabetes (353). However, a recent study has shown a clear dissociation between lipid metabolite accumulation in the liver and the development of insulin resistance, as mice with a liver-specific overexpression of DGAT2 have increased TAG, long chain acyl CoA, DAG, and ceramide content, but no signs of insulin resistance (270). This may explain why there are no differences in hepatic insulin signaling

at the level of Akt and GSK3β phosphorylation between aged WT and MCD-/- mice, even though aged MCD-/- mice have a dramatic reduction in intrahepatic DAG content. In future studies, it will also be important to assess steatosis development in aged WT and MCD-/- mice via histological procedures such as oil Red O staining, and to also investigate their respective cholesterol and cholesterol ester content.

In conclusion, our results challenge the popular belief that chronic inhibition of fatty acid oxidation would accelerate the progression of chronic diseases with aging. Instead, we demonstrate that life long whole body deficiency of MCD is associated with normal insulin sensitivity, increased whole body carbohydrate utilization, a more efficient heart, and normal liver function. These parameters are present despite lower whole body oxygen consumption rates, lower fatty acid oxidation rates, and accumulating specific lipid metabolites in both muscle and liver. Coupled together with our previous data showing that MCD inhibition is associated with protection against I/R injury, and high fat diet-induced insulin resistance, we feel that our results illustrate an important paradigm shift, whereby chronic inhibition of fatty acid oxidation via targeting MCD, may have profound overall health benefits in our elderly population.

,

C12329